EFFECT OF COLLOIDAL INTERACTIONS IN THE FORMING OF LEAD MAGNESIUM NIOBATE CERAMICS

A Thesis Submitted to
Graduate School of Engineering and Sciences of
İzmir Institute of Technology
in Partial Fulfillment of the Requirements for the Degree of

DOCTOR OF PHILOSOPHY

in Chemical Engineering

by
Aylin M. DELİORMANLI

June 2007
İZMİR

We approve the thesis of **Aylin M. DELİORMANLI**

Date of Signature

……………………………………….. **13 June 2007**
Prof. Dr. Mehmet POLAT
Supervisor
Department of Chemical Engineering
İzmir Institute of Technology

……………………………………….. **13 June 2007**
Assoc. Prof. Dr. Erdal ÇELİK
Co-Supervisor
Department of Metallurgy and Materials Engineering
Dokuz Eylül University

……………………………………….. **13 June 2007**
Prof. Dr. Üner İPEKOĞLU
Department of Mining Engineering
Dokuz Eylül University

……………………………………….. **13 June 2007**
Assoc. Prof. Dr. Akın ALTUN
Department of Metallurgy and Materials Engineering
Dokuz Eylül University

……………………………………….. **13 June 2007**
Assoc. Prof. Dr. Sedat AKKURT
Department of Mechanical Engineering
İzmir Institute of Technology

……………………………………….. **13 June 2007**
Asst. Prof. Dr. Fikret İNAL
Department of Chemical Engineering
İzmir Institute of Technology

……………………………………….. **13 June 2007**
Prof. Dr. Devrim BALKÖSE
Head of Department
İzmir Institute of Technology

………………………………………..
Prof. Dr. M. Barış ÖZERDEM
Head of the Graduate School

ACKNOWLEDGMENTS

First of all, I would like to thank Prof. Dr. Mehmet Polat and Assoc. Prof. Dr. Erdal Çelik for their help, guidance and contributions during this study. I would also like to thank Prof. Dr. Jennifer A. Lewis for giving me the opportunity to work in her group at University of Illinois at Urbana-Champaign. I have benefited greatly from my interaction with her. In addition, I gratefully acknowledge the assistance rendered by the committee, namely Prof. Dr.Üner İpekoğlu, Assoc. Prof. Dr. Akın Altun, Assoc.Prof. Dr. Sedat Akkurt and Asst. Prof. Dr. Fikret İnal.

The successful completion of this work has been aided by a number of people at İzmir Institute of Technology and the University of Illinois. I would like to acknowledge the Prof. Dr. J.A. Lewis group members especially Dr. John Bukowski, Ranjeet Rao, and Summer Rhodes for their help and friendship. I would also like to thank Dr. James Smay and Dr. Alp Şehirlioğlu for their help and valuable comments.

Special thanks is given to Handan Gaygısız, Esra Tuzcuoğlu, Filiz Kurucaovalı and Sanem Kınal (İzmir Institute of Technology, Environmental Research Center) for their help with the total organic carbon analysis and inductively coupled plasma mass spectrometer measurements. I would also like to acknowledge the İzmir Institute of Technology, Materials Research Center members for their help with the scanning electron microscope analysis. I would like to thank Faruk Ebeoğlugil for his asistance with the impedance analyser measurements in Dokuz Eylül University. The grant for this project by the Scientific and Technological Research Center of Turkey is greatfully acknowledged.

Special thanks is given to Dildare Metin and Kamuran Günder for their friendship and support. Finally, I would like to thank my husband, Ahmet, for his help, support and patience. The succesful completion of this study would not have been possible without his constant love and encouragement.

ABSTRACT

EFFECT OF COLLOIDAL INTERACTIONS IN THE FORMING OF LEAD MAGNESIUM NIOBATE CERAMICS

Electrokinetic properties of lead magnesium niobate (PMN) powders in liquid medium are investigated in this thesis. Isoelectric point of aqueous PMN suspensions was determined as a function of solids concentration. Dissolution character of both Pb^{+2} and Mg^{+2} cations in PMN structure were examined as a function of pH. Poly(acrylic acid)-poly(ethylene) oxide PAA/PEO comb polymers were tested as the novel dispersant in this system and their effect on the stability and flow behavior of aqueous PMN suspensions was investigated. Stability and flow behavior were mainly studied by rheological measurements and sedimentation experiments as a function of pH and polyelectrolyte concentration. Adsorption of comb polymers onto PMN surface and their effect on the powder dissolution were also investigated. Results indicated that the PAA/PEO comb polymers impart stability to PMN suspensions over a wide pH range and ionic strength where pure PAA fails.

In the course of this study PMN powders were consolidated using two different wet shaping methods. First, PMN films were produced using aqueous tape casting method which is widely used in the manufacture of multilayer ceramic capacitors. Secondly, three-dimensional PMN lattices were produced using robocasting method. In the former case, the goal was to provide alternative recipes for the aqueous tape casting process to be utilized in industrial applications since the current technology is based on the organic solvent based techniques. Results showed that it was possible to produce high quality PMN films with thicknesses in the range of 10 to 250 µm using aqueous based tape casting process. In the latter case, the results showed that robocasting is a suitable technique for the preparation of three dimensional PMN ceramics.

Based on these results overall conclusion and the contribution of this study can be summarized as follows: The work carried out gives new insights into the manufacturing of PMN based ceramics using aqueous based techniques. Such improvements may bring benefits in the manufacturing of smaller electronic components employed in the personal computers and mobile phones and other consumer products in the near future.

ÖZET

KURŞUN MAGNEZYUM NİOBAT SERAMİKLERİN ŞEKİLLENDİRİLMESİNDE KOLLOİDAL ETKİLEŞİMLERİN ROLÜ

Bu tezde kurşun magnezyum niobat (PMN) tozlarının su içindeki elektrokinetik özellikleri incelenmiştir. Sulu PMN süspansiyonlarının izoelektrik noktası, katı konsantrasyonuna bağlı olarak elde edilmiştir. PMN'nin yapısındaki Pb^{+2} ve Mg^{+2} katyonlarının çözünme davranışı, pH'a bağlı olarak test edilmiştir. Çalışmada poliakrilik asit-polietilen oksit (PAA/PEO) komb polimerler, sulu PMN süspansiyonlarında alternatif dispersant olarak denenmiştir. Süspansiyon stabilitesi ve akış davranışı esas olarak reolojik ölçümler ve sedimentasyon deneyleri ile pH ve elektrolit konsantrasyonuna bağlı incelenmiştir. Çalışmada ayrıca komb polimerlerin PMN yüzeyine adsorpsiyonu ve bunun PMN`nin çözünmesi üzerindeki etkisi incelenmiştir. Sonuçlar, PAA/PEO komb polimerlerin PMN süspansiyonlarında geniş bir pH ve ionik şiddet aralığında stabilizasyon sağladığı ve aynı şartlar altında PAA'nın yetersiz kaldığını göstermiştir.

Çalışmada, PMN tozları iki farklı su bazlı döküm yöntemi ile şekillendirilmiştir. Öncelikle, genellikle çok katmanlı seramik kapasitörlerin üretiminde kullanılan bir yöntem olan şerit döküm ile PMN filmler üretilmiştir. Sonrasında, robotik döküm yöntemi ile üç boyutlu şekillerin üretimi gerçekleştirilmiştir. Şerit döküm deneylerinde amaçlanan, su bazlı şerit döküm yönteminin endüstriyel uygulamalarda kullanılması için alternatif süspansiyon reçeteleri üretmektir ki, mevcut teknolojiler büyük ölçüde organik solvent bazlı tekniklere dayalıdır. Sonuçlar, su bazlı şerit döküm yöntemi kullanılarak 10 μm ile 250 μm arasında şerit kalınlığına sahip yüksek kalitede PMN filmlerin üretilebileceğini göstermiştir. Robotik döküme ilişkin olarak, sonuçlar robotik döküm yönteminin üç boyutlu PMN seramiklerin üretimi için uygun bir yöntem olduğunu götermiştir.

Elde edilen deneysel verilere göre, çalışmanın genel sonuçları ve bilimsel alandaki katkısı şöyle özetlenebilir: Çalışma, PMN bazlı seramiklerin su bazlı yöntemler kullanılarak üretimine yeni bir bakış açısı getirmiştir. Bu gelişmelerin, kişisel bilgisayarlarda, cep telefonlarında ve diğer elektronik cihazlarda kullanılan parçaların daha üstün niteliklere sahip olarak üretilmesine katkıda bulunacağı düşünülmektedir.

DEDICATION

To Ahmet

TABLE OF CONTENTS

CHAPTER 4. PAA/PEO COMB POLYMER EFFECTS ON THE STABILITY OF LEAD MAGNESIUM NIOBATE SUSPENSIONS 96

APPENDICES

LIST OF FIGURES

LIST OF TABLES

CHAPTER 1

INTRODUCTION

With the advancement of several technologies such as nanotechnology, biotechnology and information technology, a growing interest has been emerging for smart materials. Smart material systems are non-living systems which integrate the functions of sensing, actuation, logic and control to respond adaptively to various changes in a useful and repetitive manner. Smart materials could be passive, responding to external change in a useful manner without assistance or they could be active with feedback capabilities (Su et al. 2001, Newnham and Ruschau 1991, Prasad et al. 1998, Lane and Craig 2000).

The piezoelectric and electrostrictive materials are smart materials and they can convert electrical energy into mechanical energy, or vice versa (Jordan and Qunaies 2001). Lead magnesium niobate (PMN) is an electrostrictive material that is characterized by a diffuse phase transition over a broad temperature range and a frequency dependent maximum in its relative dielectric permittivity. It is a relaxor ferroelectric such that the term relaxor refers to the significant decrease in dielectric constant with increasing frequency and it demonstrates very high dielectric constant around -10 to -5 °C (Fengbing et al. 2004, Kwon et al. 2001, Heartling 1999). Electrostrictive PMN, like piezoelectrics, exhibits a dimensional change upon the application of an applied electric field or electric polarization when mechanical stress is applied. However, it also exhibits a non linear response as opposed to the linear response of other piezoelectrics such as lead zirconate titanate. Electrostrictive materials have almost no hysteresis, a quick response time and high displacements with good reproducibility. These properties make them desired materials for micro-positioner and adaptive optic applications (Fanning 2000, Tzou et al. 2004, Shankar and Hom 2000).

PMN has numerous potential applications mainly as multilayer ceramic capacitors and electro-optic devices (Brailenau et al. 2004). Other applications include displacement actuators, motors, pumps, optical scanning systems, and vibration isolators. One specific application in optical devices is in the positioning of deformable mirrors, such as those employed in Hubble Space Telescope. PMN is arranged in an array on the back of the mirror surface, which can control the surface of the mirror reflection (Tzou et al. 2004). But the most important area of application for PMN is the production of multilayer capacitors (MLC) which greatly out numbers any other devices currently in production in the world with over 10 billion units annually produced (Adair et al. 2006). In such applications as mobile electronic equipment; cellular phones or portable personal computers, MLC dominates the market at present and is expected to play a major role in future (Pithan et al. 2005).

The use of PMN ceramics in various applications requires the use of different forms such as thin and thick films, fibers, composites or sintered bodies. In industry, colloidal powder processing is the predominant fabrication method to produce these electroceramic devices. Colloidal techniques play an important role in the wet shaping of ceramic bodies from particulate slurries. Tape casting and novel solid free form fabrication methods are commonly employed processes to produce thick films and three dimensional complex shapes for microelectronic applications (Luo 2005, Huei and Dogan 2000, Smay et al. 2002, Lewis 2006).

Tape casting is customarily the preferred method in manufacturing of multilayer electronic devices such as capacitors or actuators and requires properly prepared colloidal suspensions (Safari et al. 2006). The method consists of creating a thin layer of suspension on a carrier film via the doctor blade technique. The quality of these tape-cast layers is of fundamental importance in multilayer devices. Previous studies regarding the tape casting of PMN powders have basically relied on non-aqueous formulations (Yoon and Lee 2004). Few studies on this subject investigated the preparation of lead magnesium niobate-lead titanate suspensions in organic solvents such as methyl ethyl ketone, mesitylene and γ-butyrolactone, xylene, toluene, ethanol, isopropanol (Ogitani et al. 1998, Windlass et al. 2001, Vasanthakumari et al. 2005, Agarval et al. 1998). However, recent efforts, necessitated by environmental and economic concerns, are directed emphasize the use of aqueous tape casting formulations. While significant progress has been made in the aqueous tape casting of aluminum oxide (Gutierrez and Moreno 2001, Zhang and Binner 2002, Yuping et al. 2000), zirconia (Bitterlich et al. 2002, Chartier and Rouxel 1997), titania (Jingxian et al.2004) and other ceramics such as lead zirconate titanate (Galassi et al. 1997), barium strontium titanate, and barium titanate (Huei and Dogan 2000, Song et al. 2000, Jantunen et al. 2004, Zeng et al. 2004, Yoon and Lee 2004) scant attention has focused on PMN and other active electro ceramics. Hence, there is a need to develop concentrated stable suspensions and aqueous tape casting formulations for PMN.

On the other hand, solid free form fabrication (SFF) is used for manufacturing the electroceramic devices with complex shapes. It is a technique for manufacturing solid objects by sequential delivery of energy and/or material to specified points in space to produce the complex shape (Safari et al. 2006). This technique is also called "rapid prototyping" or "rapid manufacturing" (Teng et al.1988). Investigation of the colloidal properties and rheology of the ceramic suspensions is crucial for the ink-based SFF methods such as robotic deposition. Robocasting employs robotics to control the layer-wise deposition of the ceramic slurries through an orifice (Lewis 2000). Multiple layers are deposited, leading to the desired 3-D architecture. In order to maintain structural integrity while building a component, robocasting relies on the rheology of the deposited paste. The inks can be solidified either by a drying-induced pseudoplastic to dilatant transition or chemical gelation by polymeric aids (Smay 2002, Lewis 2006). The technique can be utilized for the fabrication of periodic lattices of rods, electronic ceramics components such as composites, novel designed actuators. Electronic ceramic devices composed of lead zirconate titanate, barium titanate and alumina have been successfully manufactured using robocasting method previously by many scientists (Cesarano et al.1998, Smay and Lewis 2001, Li and Lewis 2003). The robocasting has few challenges today and it has a high potential for future applications.

1.1. Scope of the Work

Studying the colloidal properties of the relaxor ferroelectric lead magnesium niobate is the main focus of this work. Detailed powder characterization, determining the effect of novel polyacrylic acid/polyethylene oxide PAA/PEO comb polymers and pure polyacrylic acid (PAA) on stability in concentrated PMN suspensions over a wide pH and ionic strength range, and attempts at producing actual PMN components were the main avenues of the work.

Based on these avenues, the specific objectives could be summarized as: 1) investigating the behavior of PMN powders in liquid medium, 2) understanding how PAA/PEO comb polymers influence the stability of concentrated aqueous PMN suspensions, and 3) manufacturing PMN layers and 3D shapes using tape casting and robocasting techniques. The work also attempt to provide guidelines for the colloidal behavior of multi-component oxide powders in liquid medium and wet shaping process.

1.2. Organization of the Thesis

This chapter provides a brief introduction to the area of research and the research objectives of this thesis. In Chapter two, a comprehensive literature review is presented. In Chapter three, the characterization of PMN/water system including the electrokinetic and dissolution behavior is reported. Effect of PAA/PEO comb polymer and PAA polyelectrolyte on the stability of PMN suspensions is given in Chapter four. Adsorption behavior of polyelectrolytes onto PMN surface and their effect on the solubility of PMN is also analyzed in the same chapter. Chapter five describes the aqueous tape casting of PMN films, including slurry formulations, drying behavior of green tapes and microstructural evolution during heat treatment. In Chapter six, preparation of PMN inks is examined for robocasting process. The chapter includes investigation the gelation mechanisms of PMN suspensions and preparation of 3D arrays for microelectronic applications. The key conclusions of the present work and the suggestions for future study are provided in Chapter seven. Finally, the Appendices outline Hamaker function and interaction potential calculations for PMN particles in absence and presence of polyelectrolytes.

CHAPTER 2

LITERATURE REVIEW

2.1. Piezoelectricity

In the 1880s, Pierre and Jacque Curie discovered some crystalline materials. When compressed they produce a voltage proportional to the applied pressure and when an electric field is applied across the material, they produce change of shape. This characteristic is called piezoelectricity. The name “piezo” is derived from the Greek, meaning “to press”. Therefore, piezoelectricity is the generation of the electricity as a result of mechanical pressure (Haertling 1999, Swartz 1990, Moulson and Herbert 1990).

During World War I, the French scientist, Paul Langevin, used the term piezoelectric. Subsequent work on ceramics in the late 1940's and 1950's led to their widespread application. The first commercial device to be made from piezoelectric barium titanate was a phonograph pickup and was produced in 1947. Piezoelectric lead niobate was discovered in United States in 1955 and then lead zirconate titanate (PZT) compositions were found. There are several piezoelectric ceramic compositions in common use today: barium titanate, lead zirconate titanate (and modified iterations such as PLZT), lead metaniobate and lead magnesium niobate (Swartz 1990, Haertling 1999, WEB_1 2007, WEB_2 2007).

In piezoelectric materials the relationship between mechanical parameter and electrical parameter is expressed by the following equations (Hu et al. 2004):

$$D_i = \sum d_{ij} T_j \text{ (Direct effect)} \tag{2.1}$$

$$S_i = \sum d_{ij} E_j \text{ (Converse effect)} \tag{2.2}$$

where S and D mechanical strain and electric displacement respectively. T and E are the mechanical stress and the electric field and d is the piezoelectric constant.

An understanding of piezoelectricity begins with the crystal structure of the material. A crystal is made up of negatively and positively charged atoms occupying specific positions in a repeating unit. All crystals can be divided into 32 point groups as it is shown in Figure 2.1 (Jordan and Qunaies 2001, Haertling 1999). From 32 point groups, 21 classes are noncentrosymmetric (a necessary condition for piezoelectricity to exist) and 20 of these are piezoelectric (Bellaiche 2002, Haertling 1999). If the material is noncentrosymmetric a net movement of the positive and negative ions produces electric dipoles such as polarization. Additionally, for materials that are piezoelectric the stress is the only means by which the dipoles are generated (Haertling 1999, Ravez 2000).

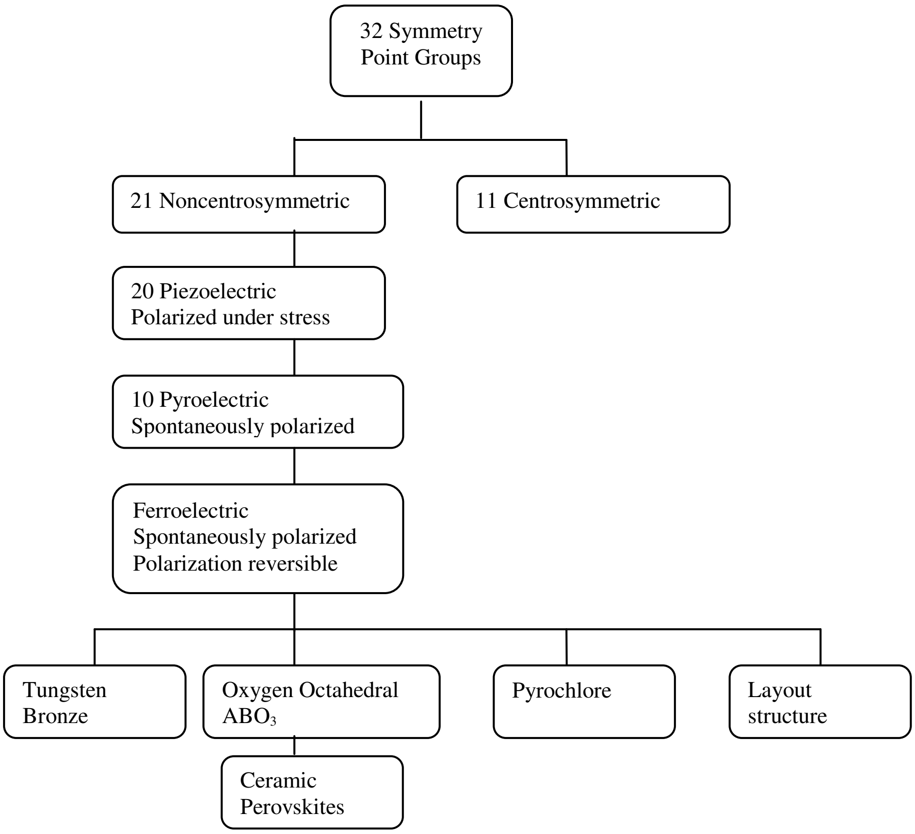

Figure 2.1. Interrelationship of piezoelectric and subgroups on the basis of symmetry. (Source: Haertling 1999)

2.2. Ferroelectric Ceramics

A class of piezoelectric materials is also ferroelectric. In contrast to the naturally occurring piezoelectric crystals, ferroelectric ceramics are of “polycrystalline” structure. The ferroelectricity is the ability of a material to retain an electric polarization in the absence of an applied electric field. This spontaneous polarization results from the alignment of internal dipoles within the crystal units of the ferroelectric material and it can be reoriented by an external electric field (Moulson and Herbert 1990, Ravez 2000).

Poling is very important for the application of polycrystalline ferroelectric ceramics since they do not possess any piezoelectric properties owing to the random orientations of the ferroelectric domains in the ceramics before poling. During poling, a DC electric field is applied on the ferroelectric ceramic to force the domains to be oriented or "poled" (see Figure 2.2). After poling the electric field is removed and a permanent polarization and remnant strain are maintained in the sample, and the sample exhibits piezoelectricity (Swartz 1990).

The ferroelectric materials have a transition temperature (the Curie temperature, Tc) where they undergo a structural phase change from a ferroelectric phase to a paraelectric with increasing temperature. Above the T_C, each perovskite crystal in the element exhibits a simple cubic symmetry with no dipole moment. At temperatures below the Curie point, however, each crystal has tetragonal or rhombohedral symmetry and a dipole moment. The dielectric permittivity often has a peak at Tc and linearly decreases according to the Curie-Weiss Law (Haertling 1999, Swartz 1990, WEB_2 2007).

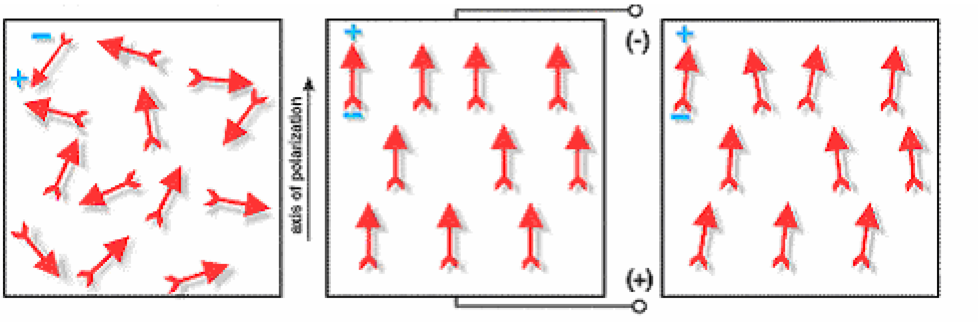

(a) (b) (c)

Figure 2.2. Schematic presentation of the poling in ferroelectric ceramics (a) unpolarized (b) polarized by an applied electric field (c) remnant polarization (Source: WEB_2 2007).

A very strong field could lead to the reversal of the polarization in the domain, known as domain switching. A consequence of the resistance to domain switching is that polarization in a ferroelectric is hysteretic, which is another important characteristic of ferroelectrics. A ferroelectric loop is shown in Figure 2.3. Generally the existence of the P-E loop is considered as evidence that the material is ferroelectric (Safari et al.1996).

The two characteristics of the P-E loop are the coercive field E_c and the remnant polarization P_r. E_c is the field at which the polarization is zero and P_r is the value of the polarization when the electric filed is zero. A loop is said to be saturated once the values of P_r and E_c no longer vary (Jordan and Quanies 2001, WEB_1 2007). A Sawyer-Tower circuit is commonly used to obtain a P-E loop. The ferroelectric hysteresis loops are both frequency and temperature dependent. Hysteresis loops come in all size and shapes and similar to fingerprint identify the material in a very special way.

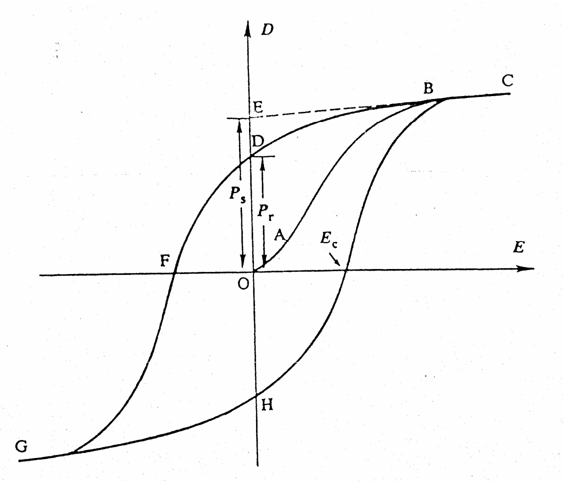

Figure 2.3. Polarization vs electric field (P-E) hysteresis loop for a typical ferroelectric crystal (Source: Safari et al. 1996).

Ferroelectric ceramics are used in broad range of electronic applications. These applications account for more than 50% of the total high technology ceramics market. Nonvolatile semiconductor memories, optical waveguide devices, spatial light modulators, capacitors for integrated circuits, pyroelectric devices and imaging sensors, micropositioners, actuators and micromotors are the examples of devices produced from ferroelectric materials (Goel and Tripathi 2001, Newhamn and Amin 1999, Kishi et al. 2003).

2.2.1. Electrical Properties

2.2.1.1. Dielectric Constant

The dielectric constant ε(F/m) is a measure of the charge stored on an electroded material at a given voltage. The dielectric constant of vacuum is $\varepsilon_0 = 8.85 \times 10^{-12}$ F/m. The relative dielectric constant (K) or relative permittivity (ε_r) is defined as the ratio of the permittivity of the material to the permittivity of free space and is dimensionless. The dielectric loss factor is defined as the tangent of the loss angle (tanδ) or the dissipation factor. The loss factor represents the ratio of the resistance of a parallel equivalent circuit of the ceramic element. The dielectric constant (ε_r) and dielectric loss factor (tanδ) can be measured using a standard impedance bridge or an impedance analyzer both of which provide a direct reading. High dielectric constants are desirable because they result in low impedance. Low dissipations are desirable because they result in low electrical losses (Su 1997, Moulson and Herbert 1990).

The relative permittivity is calculated from the measured values of capacitance and physical dimension of the specimen. The relations are expressed as:

$$\kappa^* = \varepsilon^*{}_r = \frac{\varepsilon^*}{\varepsilon_0} = \varepsilon'_r - j\varepsilon''_r = \left(\frac{\varepsilon'}{\varepsilon_0}\right) - j\left(\frac{\varepsilon''}{\varepsilon_0}\right) \qquad (2.3)$$

$$\tan\delta = \frac{\varepsilon''_r}{\varepsilon'_r} \qquad (2.4)$$

$$\varepsilon_r^* = \frac{t \times C}{\varepsilon_0 \times A} \qquad (2.5)$$

where K^* is the dielectric constant, ε_r^* is the relative permittivity, ε_0 permittivity of free space, t is the distance between the electrodes, C is the measured capacitance (Su 1997).

2.2.1.2. Piezoelectric Properties

The parameters to measure the electromechanical effects of piezoelectric materials are the piezoelectric charge coefficients, the piezoelectric voltage coefficients and the piezoelectric coupling factors (Jordan and Quanies 2001).

2.2.1.2.1. Piezoelectric Charge Coefficient

The activity of a piezoelectric material is quantified by the piezoelectric charge coefficient. The three most common of these are; d_{33}, d_{31}, d_{15}. These are commonly referred to as longitudinal mode, transverse mode and shear mode. Following equation give the relation between piezoelectric charge coefficient and the strain.

$$e_3 = d_{33}.E \tag{2.6}$$

where, e is the resultant strain and E is the applied electric field. High d-coefficients are desirable in materials utilized as actuators, such as in motional and vibrational applications (WEB_1 2007).

2.2.1.2.2. Piezoelectric Voltage Constant

The piezoelectric voltage constant, g, is the electric field generated by a piezoelectric material per unit of mechanical stress applied or, alternatively, is the mechanical strain experienced by a piezoelectric material per unit of electric displacement applied. The first subscript indicates the direction of the electric field generated in the material, or the direction of the applied electric displacement. The second subscript is the direction of the applied stress or the induced strain, respectively. The g coefficients are desirable in materials intended to be used a sensors, to produce voltage in response to mechanical stress (Jordan and Quanies 2001, Swartz 1990). The g –coefficient is related to the d coefficients by the following expression:

$$d_{33} = \varepsilon.g_{33} \tag{2.7}$$

2.2.2. Electrostriction

Electrostriction is a phenomenon in which a polarization produces a change in dimension of a material (Hood 1996). Piezoelectric materials display a strain that is proportional to the applied field. However, in electrostrictive materials the strain is proportional to the square of the applied field (see Figure 2.4). This means that a negative strain can not be generated (WEB_1 2007). In other words, the phenomenon of electrostriction is a second order piezoelectric effect (Fanning 2000). Corresponding equation is (Haertling 1999):

$$S=Q.P^2 \text{ (in terms of polarization)} \qquad (2.8)$$

Where Q is the electrostriction coefficients and P is the polarization. One of the most commonly used electrostrictive material is lead magnesium niobate with the chemical formula $Pb(Mg_{1/3}Nb_{2/3})O_3$, and solid solutions with lead titanate, $PbTiO_3$ (Fanning 2000). Materials such as PMN demonstrate large electrostriction strains (up to 0.1%) and are used widely in actuator applications (Cho et al. 2000). According to the Haertling electrostriction is due to the field activated coalescence of micropolar regions to macrodomains of the ferroelectric. The electrostriction effect in PMN can be explained on the basis of localized charge-transfer fluctuations. These fluctuations are coupled both to the soft lattice polarization and to lattice distortions (Haertling 1999, Vikhnin et al. 2003).

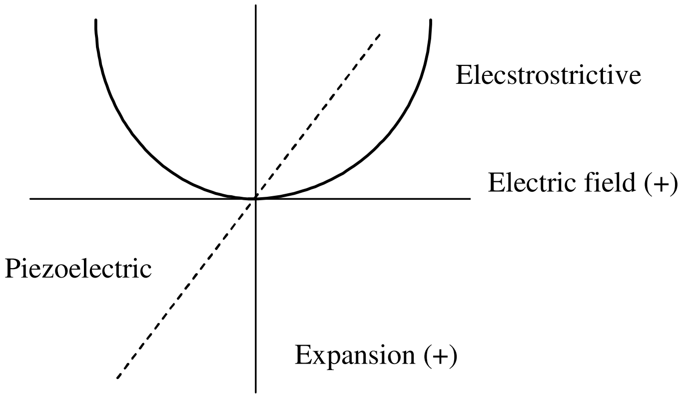

Figure 2.4. Displacement versus voltage curve of piezoelectric and electrostrictive materials.

2.2.3. Relaxors

Relaxor is a sub group of ferroelectrics. In relaxor systems, the dielectric response has a broad peak as a function of temperature, rather than a sharp peak in a normal ferroelectric, and a frequency dependent response (Cohen 2000). Therefore, relaxor ferroelectrics are characterized by a frequency dependent dielectric response which has a broad maximum as a function of temperature. In addition, relaxors possess a local polarization at temperatures above their dielectric maximum (Fanning 2000, Ravez 2000). The phase of the bulk material throughout the Curie temperature range from cubic to orthorhombic structure is responsible for the 0.1% volume expansion of the crystal lattice upon application of the electric field (Blackwood and Ealey 1993).

Relaxor ferroelectrics belong to the class of materials which show strong chemical disorder (Kircher and Bohmer 2002). They are generally expressed by $Pb\ (B_1, B_2)O_3$ with high permittivity and relatively small temperature coefficient (Kobune et al. 2004, Kelly et al. 1997).

PMN belongs to a class of relaxor ferroelectrics. Therefore, it exhibits a strong dispersion of dielectric permittivity with frequency and displays no macroscopic polarization even at temperatures well below the temperature of the maximum dielectric constant (Blackwood and Ealey 1993, Kim and Cha 1997). Because of the absence of the remanent polarization, PMN displays very little hysteresis above the Curie temperature range (Hood 1996). Relaxor behavior is very common among lead-based perovskites, suggesting that the “lone pair” electrons of Pb^{2+} play a role in the micro domain process, possibly by adjusting their orientations (Newnham et al. 1999).

2.2.4. Perovskite Structure

Many of the ferroelectric materials have perovskite-type structure which can be expressed mostly ABO_3 in formula (Schwartz 1997). The unit cell of perovskite structure is shown in Figure 2.5. In the structure A-site cations occupy the corners of a cube, while B-site cations sit in the body center. Three oxygen atoms per unit cell rest on the faces (Swartz 1990, Burton 2000). The lattice constant of these perovskites is always close to 4 Å due to the rigidity of the oxygen octahedra network and the well defined oxygen ionic radius of 1.35 Å. Another common ferroelectric structure is the layered perovskite structure which consists of a varying number of perovskite unit cells separated by an oxide layer. This structure is also found in many high Tc superconductors (Bhalla et al. 2000). The crystal structure of PMN is controversial and following models explain the order-disorder behavior observed in this material (Mathan et al. 1990)

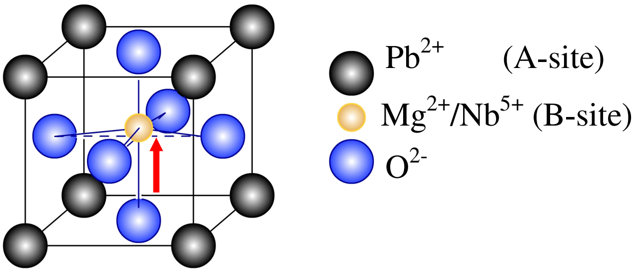

Figure 2.5. Schematic presentation of the PMN perovskite unit cell.
(Source: Adapted from Schwartz 1997)

2.2.4.1. Space Charge Model

According to this model ordered regions has an ordered Mg^{+2}: Nb^{+5} compositional distributions. The Mg^{+2}: Nb^{+5} (1:1) ordered region will have negative charge relative to the Nb^{+5} rich matrix. The disordered matrix around these ordered regions has to be Nb^{+5} rich to maintain the overall stoichiometry (Yan et al. 1998, Burton 2000).

2.2.4.2. Random-Site Model

In this model B`` sites are occupied by Nb^{+5} cations, and B` sites are occupied randomly by $2/3Mg^{+2}$ and $1/3Nb^{+5}$ cations, for the $Pb(Mg_{1/3}Nb_{2/3})O_3$ complex perovskite. The structural formula can be written as $Pb(Mg_{1/3}Nb_{1/3})_{1/2}Nb_{1/2})O_3$. This inherent randomless results in relaxor properties even for fully (1:1) ordered systems (Yan et al. 1998, Burton 2000, Fanning 2000).

2.3. Lead Magnesium Niobate

$Pb(Mg_{1/3}Nb_{2/3})O_3$ (PMN) is one of the most widely studied relaxor ferroelectric ceramic because of its superior dielectric constant, electrostrictive coefficient. PMN has a very high dielectric constant (ε_{max} = 15000-30000 at 1 kHz) near the room temperature (Fanning 2000, Swartz et al. 1990, Cho et al. 2000). Curie temperature of the material is about –10 °C (Gentil et al. 2004). Figure 2.6 show the frequency dependency of the dielectric constant of PMN at various temperatures.

It was first synthesized by Smolenskii and Agranovskaya in 1958 (Fanning 2000, Kircher and Bohmer 2002, Mohan et al. 2001). The study of relaxor materials continue in the early 1960`s with work on single crystal $Pb(Mg_{1/3}Nb_{2/3})O_3$ materials. More recent work in 1980`s with PMN based relaxor ceramics has led to their successful application as high strain electrostrictive actuators and high dielectric constant capacitors (Haertling 1999, Zhong et al. 2005).

The highest symmetry phase for PMN is cubic with P*m*3*m* space symmetry and lattice constant a=4.04 Å. PMN undergoes a diffuse phase transition with a maximum temperature, Tm, from -3 to -15 °C (Fitzgerald et al. 2000, Babooram et al. 2004). No structural change can be detected in PMN as it passes through the diffuse transition (Gu 2003). In its crystal structure, Pb^{+2} occupy the corner A-site and the B-site can be Mg^{+2} or Nb^{+5} (Swartz 1990). However, it does not exist with an idealized perovskite lattice structure as shown in Figure 2.5, where an ordered distribution of Mg(II) and Nb(V) ions in the next-nearest neighbor B-site octahedra exists (Fitzgerald et al. 2000). PMN has either partial or complete B-site disorder of the Mg(II) and Nb(V) B-site ions as it is discussed in the previous section. B-site cation order influences the crystallography, phase transitions and other physical properties. The broad diffused phase transition in PMN is due to the presence of two cations of very different ionic radii and the valences at the octahedral B-site of the perovskite (Das et al. 2003). The atoms are located in the ideal cubic sites but continually shift off these positions. The origin of these effects is a partial ordering of the PMN perovskite structure in which the niobium and the magnesium atoms of PMN alternate in position over only a few unit cells (usually 30–50 Å). Within these ordered regions, an external field acts upon fluctuating dipoles to make large electrostrictive motions (Newnham and Amin 1999).

PMN has temperature-sensitive micro domains that result from the many different “active” ion linkages in the disordered octahedral framework. Each NbO_6 octahedron may be bonded to zero to six other NbO_6 octahedra (with the remaining connections involving MgO_6 octahedra). Connections between these octahedra are assumed to be essential to ferroelectricity and high anisotropy coefficients. As the temperature decreases from the high-temperature paraelectric state, ferroelectric microdomains gradually coalesce to macrodomains, giving rise to a diffuse phase transformation. These polarization fluctuations are also dependent on bias field and the frequency used to measure the dielectric or piezoelectric constant. The dielectric constant drops off rapidly with increasing frequency (hence the name “relaxor”) because it takes time for the polarization fluctuations to respond (Newnham and Amin 1999, Egami et al. 1998).

The main problem in PMN production is the formation of a lead-niobate based pyrochlore phase with low dielectric constant (~200 compared to the 20000 for PMN single crystal) during the heating process (Costa et al. 2001). Although, the pyrochlore phase is composed mainly of PbO and Nb_2O_5 it may contain a small amount of MgO in the lattice. The ratio of Pb:Nb in the pyrochlore phase is less than or equal to the ratio of Pb:Nb=1.5 in the perovskite phase (Gu 2003). The pyrochlore can be formed by decomposition of the PMN perovskite phase as a consequence of PbO volatilization during sintering. The widespread method to synthesize pure perovskite was introduced by Swartz and Shrout in 1982, known as columbite method (Costa et al. 2001). In addition to mixed oxide method, solution synthesis methods such as sol-gel is used to synthesis high purity PMN powders and thin films (Wu and Liou 1995, Şakar-Deliormanli et al., Brailenau et al. 2004)

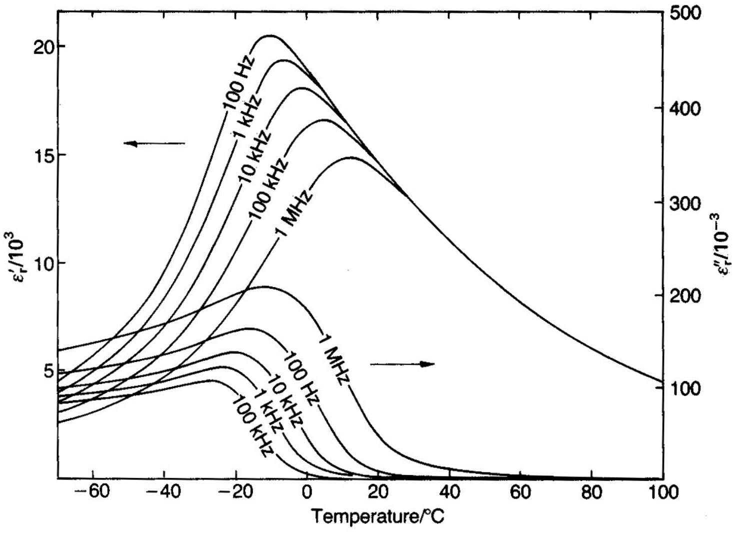

Figure 2.6. Dielectric constant (left) and dielectric loss (right) of the relaxor PMN as a function of temperature (Source: Fanning 2000).

PMN forms a solid solution with lead titanate (PT) as seen in Figure 2.7 providing many compositions that have excellent electromechanical properties (Kelly et al.1997). The composition near 0.9PMN-0.1PT, has a high dielectric constant (>20,000) and also has a very high electrostrictive coefficient ($3.6x10^{-16}$ m^2/v^2). The composition 0.65PMN-0.35PT has a very high piezoelectric coefficient of 560 $x10^{-12}$ C/N. Additionally, high electromechanical properties such as ~0.1% longitudinal strain and >0.03% transverse strain at 1 MV/m and 0.1 Hz have been reported (Cho et al. 2000).

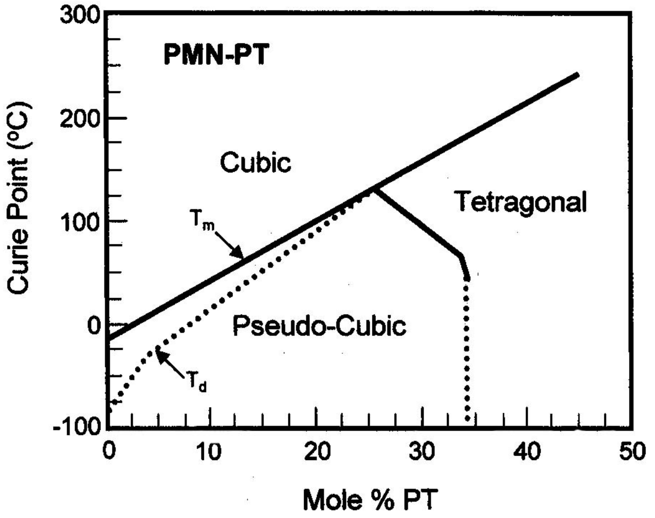

Figure 2.7. PMN-PT phase diagram.
(Source: Gu 2003)

Lucas and Petuskey investigated the ternary phase diagram of PbO- MgO-Nb_2O_5 at 1000 °C. Figure 2.8 show the phase diagram of this ternary system. Two ternary compounds were observed in the PbO–MgO–Nb_2O_5 system: $Pb(Mg_{1/3}Nb_{2/3})O_3$ and the cubic pyrochlore phase. In Figure 2.8, PMN is the perovskite phase, the black domain represents the pyrochlore (Py) solid-solution range, the light gray areas correspond to diphasic domains, and the dark gray area represents the extent of the liquidus at 1000°C (Lucas and Petuskey 2001).

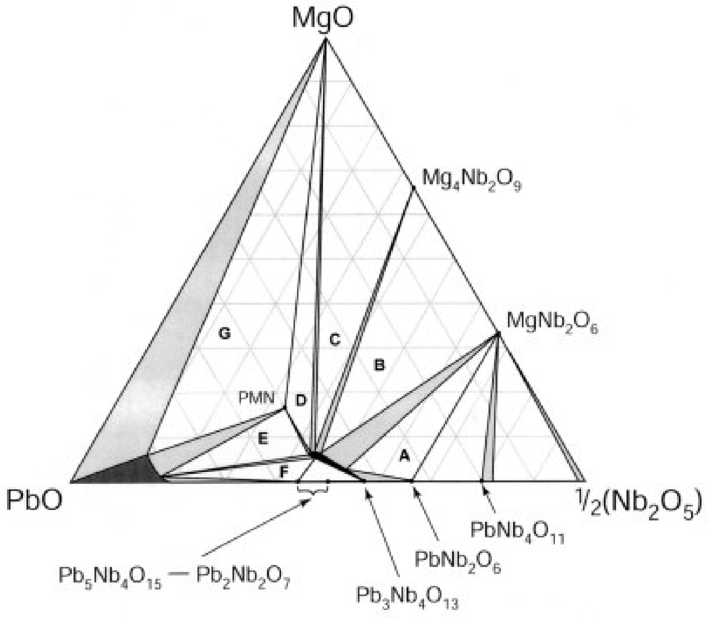

Figure 2.8. Ternary phase diagram of the PbO–MgO–Nb_2O_5 system at 1000°C (axes are given in cation fractions) (Source: Lucas and Petuskey 2001).

As conclusion, general properties of PMN ceramics are summarized in the following paragraph:

- Electrostrictive PMN exhibits a negligible hysteresis (<1%), which is essential in repeatedly locating and maintaining a set-point accuracy.
- PMN requires no poling, which means it remains stable with no aging or creep commonly found in piezoelectric devices.
- PMN has a very high elastic modulus (17×10^6 psi) which produces relatively high stiffness, enhancing the force/deflection capability.
- PMN actuators have negligible thermal growth because the thermal expansion coefficient dissipates very little power.

- PMN also has improved strain sensitivity that reduces the operating voltage below 150 V.
- PMN produces little or no electrical or magnetic interference with other components.

Accordingly, today PMN components have replaced many piezoelectric actuators used in precision apparatus because the PMN drift is less than 3% over two days compared with 10–15% of a comparable piezoelectric device under loading. Therefore, precision actuators and displacement transducers are ideal applications of PMN-based materials (Tzou et al. 2004, Shankar and Hom 2000).

2.4. Colloidal Processing of Ceramics

The solid-liquid dispersions within the particle size range of 1 nm to 1 μm are generally referred to as colloidal suspensions. On the other hand, systems in which a significant fraction of particles cover a range that is greater than the colloidal range, i.e. greater than 1 μm, are termed suspensions (Tadros 1986). Colloidal suspensions are used in widespread applications. Colloid based products include ceramics, inks, paints, cosmetics and pharmaceutical compositions (Shaw 2003, Lewis 2000). Agglomeration is a natural process for all ceramic powders because of the van der Waals forces. This is responsible for inhomogenities in microstructures that results in reduced mechanical and electrical properties.

On the other hand, colloidal processing methods can minimize the number of heterogeneities during fabrication due to use of stable particle suspensions. The colloidal processing approach for ceramic fabrication involves: 1) de-agglomeration and stabilization of colloidal suspensions 2) preparation of slurries that include other processing additives, with desired rheological properties 3) consolidation of the slurry to pack the particles to a high density 4) drying and densification by heat treatment (Su et al. 2001, Reed 1995, Rahaman 1995).

Therefore, by controlling the interparticle forces, the agglomeration between the ceramic particles can be prevented and this may result in improved ceramics with better final properties.

2.4.1. Origin of Surface Charge in Water

An interface may acquire an electrical charge by one or more of several mechanisms. The most common of which include (1) preferential solution of surface ions, (2) direct ionization of surface groups, (3) substitution of surface ions, (4) specific ion adsorption, and (5) charges deriving from specific crystal structures (Myers 1999, Reed 1995).

When a particle is immersed in an aqueous solution, it usually acquires a surface charge, either by adsorbing or desorbing ions according to some chemical equilibrium with the surrounding solution. For example, the surface of an oxide particle is hydroxylated when coming into contact with water, and undergoes proton association-dissociation reactions (Hunter 1995). As soon as the surface is exposed to water, chemical surface reactions take place between the oxygen ions and the water molecules resulting in a surface charge. The amount of surface charge depends on various parameters as the number of deprotonable surface sites per surface area and the acidicity / basicity of the oxide surface (Rezvan 2005). The deprotonation of the oxide surface is illustrated by Figure 2.9 using alumina as an example.

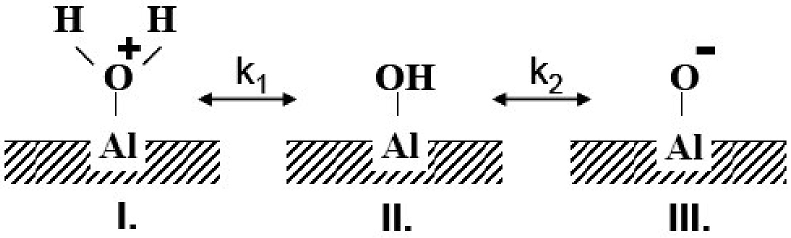

Figure 2.9. Reaction of water at the alumina surface: I. Protonated, II. Neutral, III. Deprotonated state (Source: Rezvan 2005).

The surfaces of metal oxides contain OH-groups which are amphoteric and can either take up a proton at low pH or leave one proton at a high pH. At low pH the surface is positively charged while at high pH the surface is negatively charged. At a certain intermediate pH level, the oxide surface is neutral and the point of zero charge can be expressed as a pH value. The PZC is usually measured in the presence of electrolytes. In many cases, one or both of the ions can adsorb on the surface. The PZC is then dependent on both the proper surface properties and also the content of the dispersion medium. If the medium does not contain any ions which specifically adsorb on the surface, the PZC is only dependent on the material in the colloidal particles. Such a PZC is known as a pristine point of zero charge (PPZC) (Holmberg et al. 2002).

As it is discussed before the net surface charge of a hydrous oxide is determined by the proton transfer and reactions with other cations and anions. In general, the net surface charge density of a hydrous oxide is given by:

$$\sigma_P = F\left[\Gamma_H - \Gamma_{OH} + \sum (Z_M\Gamma_M) + \sum (Z_A\Gamma_A)\right] \tag{2.9}$$

where σ_P is the net surface charge in Coulombs m^{-2}, F is the Faraday constant, Z is the valency of the sorbing ion, Γ_H, Γ_{OH}, Γ_M and Γ_A is the sorption densities of H,OH, metal ions and anions respectively. The point of zero charge can be given as where $\sigma_P=0$ (Stumm 1992).

The net proton charge, the charge due to binding of protons or H^+ ions is given by:

$$\sigma_H = F\left[\Gamma_H - \Gamma_{OH}\right] \tag{2.10}$$

The aquatic particles has electric charge and this charge is balanced by the charges in the diffuse layer which move freely in solution and remain near enough to colloid surface to create the effective (counter) charge σ_D that balances σ_P ,therefore $\sigma_P + \sigma_D =0$ .This is often referred to as isoelectric point. It is the point where particles do not move in an applied electric field (Stumm 1992).

2.4.2. Interactions in Colloidal Suspensions

Ceramic suspensions can be either stable or flocculated depending on the interactions between the colloidal particles. The total interparticle potential V_{tot} is given by the following equation:

$$V_{total} = V_{VDW} + V_{elec} + V_{steric} + V_{dep} \tag{2.11}$$

where V_{VDW} is the attractive potential energy due to long-range van der Waals interactions between particles, V_{elec}, is the repulsive potential energy arising from electrostatic interactions between charged particle surfaces, V_{steric} is the repulsive potential energy arising from steric interactions between particles coated with adsorbed polymers, and, V_{dep} is the potential energy created by the presence of nonadsorbed polymeric species in solution (Lewis 2000, Israelachvili 1991).

2.4.2.1. Van der Waals Interactions

The origin of van der Waals forces lies in the dipole or induced–dipole interactions at the atomic level. There are three major types of van der Waals forces: Debye, Keesom and London (Dispersion) forces. These three terms describe permanent dipole–induced dipole, permanent dipole–permanent dipole and induced dipole–induced dipole interactions. The London (Dispersion) force is always present, like the gravitational force, as it does not require the existence of permanent polarity or charge–induced polarity. The contribution of the van der Waals attraction to the total interaction depends to a large extent on the separation distance between the particles and the magnitude of the repulsive force at this separation (Tadros 1986, Larson 1999, Napper 1977, Rezvan 2005).

The strength of van der Waals forces increase for interactions between colloidal particles as typically each particle has a large number of atoms or molecules. But van der Waals forces are only effective over short distances of typically 0.2–3 nm which is the reason why colloidal suspensions do not coagulate instantly (Rezwan 2005).

In 1937 Hamaker, derived equations for these forces on the basis of additivity of van der Waals energies between pairs of atoms or molecules, and assuming these energies to be proportional to the inverse sixth power of the distance. Casimir and Polder introduced the influence of retardation at large separations (Overbeek 1977). The van der Waals interaction energy between two spherical interacting particles (see Figure 2.10) of the same material separated by a distance, H, is given by (Pashley and Karaman 2004):

$$V_{VDW} = -A_{121}.a / 12\ H \tag{2.12}$$

where A_{121} is the Hamaker constant .

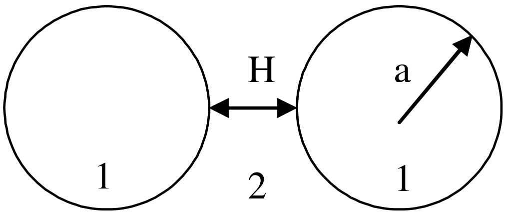

Figure 2.10. Diagram of two colloidal spheres separated by a distance H.

2.4.2.2. Electrostatic Interactions

The ions of opposite charge which are dissolved in water, known as counterions, are attracted towards the surface. However, they do not simply stick to the surface, but form a diffuse layer of charge adjacent to the surface due to the balance between their electrostatic and entropic energy. The surface charge plus the diffuse layer of opposite charge constitute an electric double layer. When two particles approach each other, the two double layers interpenetrate, causing a repulsive force between them. Figure 2.11 shows schematically the model including the Stern layer and diffuse double layer (Hunter 1995, Pashley and Karaman 2004, Rezvan 2005).

In Figure 2.11 the surface potential (ψ_0) is defined as the potential found at the surface (x_0). The zeta potential (ψ_ζ) is defined as the potential obtained at $x = x\zeta$. The zeta potential can be obtained from electro kinetic potential measurements such as electrophoresis but never directly the surface potential. However, at very low ionic strengths, the surface potential can be approximated by the zeta potential, that is $\psi_0 \approx \psi_\zeta$ (Hunter 1995).

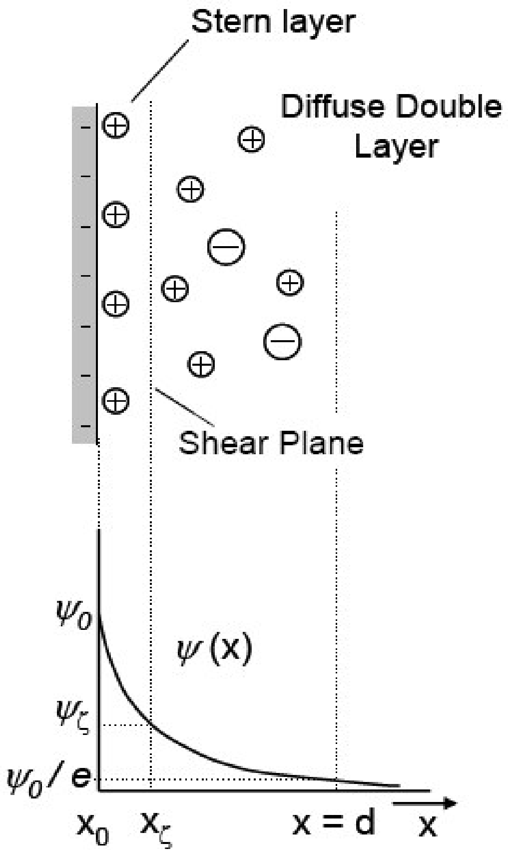

Figure 2.11. Schematic presentations of the electrical potentials develop through the electrical double layer (Source: Rezvan 2005).

Therefore, the stability of aqueous colloidal systems can be controlled by generating like-charges of sufficient magnitude on the surfaces of suspended ceramic particles. The resulting repulsive V_{elect} exhibits an exponential distance dependence whose strength depends on the surface potential induced on the interacting colloidal particles. (Lewis 2000, Kingery et al. 1976).

For the diffuse layer the Poisson-Boltzmann equation can be written in one dimension:

$$d^2\psi / dx^2 = - (e/\varepsilon)\Sigma\ z_i n_{io} \exp (z_i e\psi / kT) \qquad (2.13)$$

Where ψ is the potential at a distance x from the surface, ε is the permittivity of the medium, n_{io} is the bulk concentration of ions of charge zi, e is the electronic unit charge, k is the Boltzman constant and T is the absolute temperature. For the assumption of, low charge ($z_i e\psi / kT$)< 1 cases this equation can be written as:

$$\psi(x) = \psi_\delta \ \exp(-\kappa x) \tag{2.14}$$

In the low surface potential limit electrostatic potential between two particles is given by Derjaguin approximation:

$$V_{elect} = 2\pi\varepsilon_r\varepsilon_o a\varphi_0^2 \exp(-\ \kappa h) \tag{2.15}$$

where κ is known as the inverse Debye length (Overbeek 1977).

2.4.2.3. The DLVO Theory

The interaction potential in charged stabilized systems can be described approximately by the Derjaguin-Landau-Verwey-Overbeek (DLVO) theory (Myers 1999, Hunter 1995, Su 1997). DLVO theory determines the stability of a given colloid in a suspension through the balance between the repulsive and attractive forces as they approach each other. Figure 2.12 shows the total interaction potential graph of a system in the presence of electrostatic repulsive and van der Waals attractive terms (Ma et al. 2003, Yoshioka et al. 1997).

The sharp increase of Vr at very close approach is due to the repulsion between the electron clouds of atoms of the particles and is referred to as the Born repulsive energy. In the dispersed state, particles that exist in the suspension repel each other on close approach, provided the repulsive barrier is greater than k_bT. In the weakly flocculated state, particles aggregate in a shallow secondary minimum (well depth ~ 2–20 k_bT), forming flocs in suspension (Lewis 2000, Polat M and Polat H 2000).Yoshioka and co-workers reported that suspended particles coagulate when the minimum of the potential curve becomes smaller than -5 kT. The particles that are in weak flocculation have a tendency to disperse again, with aid of the mechanical energy when the value approximately above 5 kT (Yoshioka et al. 1997).

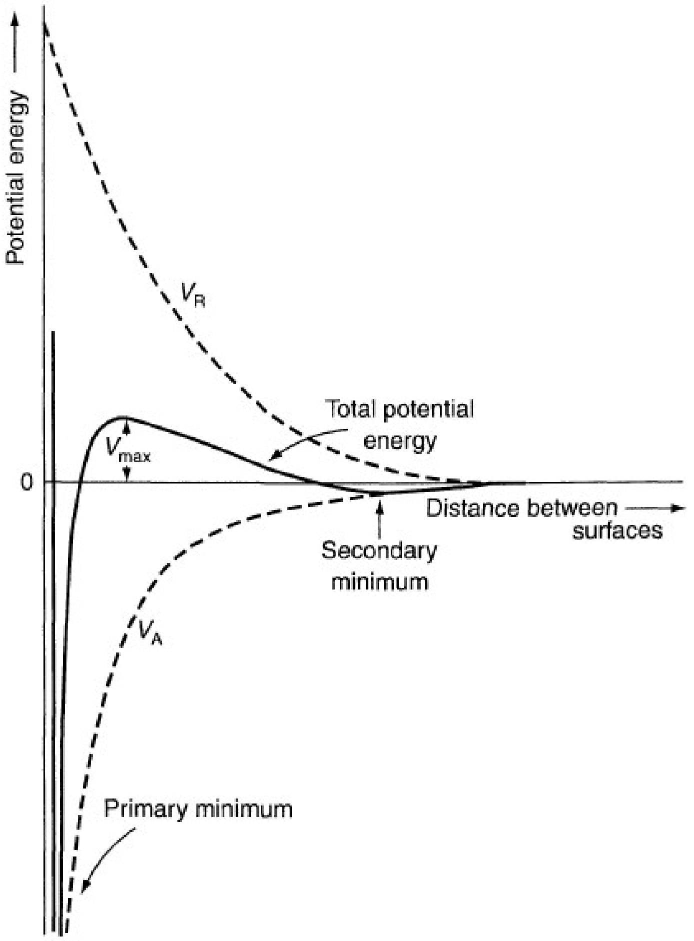

Figure 2.12. Schematic presentation of the total interparticle potential in the presence of attractive van der Waals and repulsive electrostatic forces. (Source: Adapted from Sato and Ruch 1980).

2.4.2.4. Steric Stabilization

When two particles with adsorbed polymer layers approach each other at distances of separation of their surfaces of less than twice the thickness of the adsorbed layer, interaction of two particles takes place (Sato and Ruch 1980). The degree of stabilization can be defined in terms of the energy change occurring during the interaction. The free energy of change for the interaction can be written as (Hesselink 1971):

$$\Delta G = \Delta H - T\,\Delta S \qquad (2.16)$$

where ΔH is the enthalpy change, ΔS is the entropy change and T is the temperature.

Steric stabilization can be achieved when one (or more) of the following conditions are met: good solvent conditions, good surface coverage, thick adsorbed layer, strongly bound adsorbed layer (Myers 1999). Good solvent conditions (When Flory Huggins parameter, $\chi < 0.5$) are desired because the interaction energy between the polymer chains is repulsive. The repulsive interaction arises since the polymer segments prefer to be surrounded by solvent rather than by other polymers. Therefore, good solvent conditions results in a greater coil size which yields a thicker layer. However, in poor solvent conditions ($\chi > 0.5$) the polymer prefers to be surrounded by itself rather than solvent because of the attractive interactions between segments (Ogden 1996, Netz and Andelman 2003). Effect of solvent quality on the polymer coil size is shown schematically in Figure 2.13.

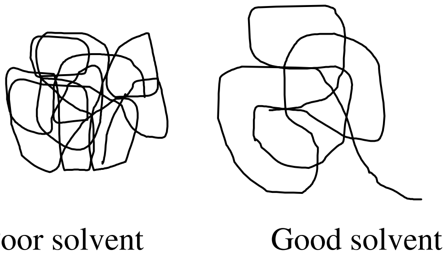

Figure 2.13. Schematic presentation of the effect of solvent quality on polymer coil size.

Linear polymer molecules in solution in general form random coils, which may be described as three-dimensional random walks in space. For "ideal" chains, consisting of non-interacting statistical units (segments), with molecular weight M, polymer in solution have a Gaussian segment density distribution and the coil radius of gyration is proportional to $M^{1/2}$. However, real segments have volume and interact with each other. For a pair of segments, an interaction (or excluded) volume can be defined in terms of the (effective) segment-segment interaction energy. In theta solvents (χ =0.5), chains behave "ideally". In better solvents, segments repel each other and a more realistic model for that case is a chain without self-intersections, the statistical analog of which is called a "self-avoiding walk". In this model radius of gyration is proportional to $M^{2/3}$ (Cohen-Stuart et al.1986, Napper 1977).

In concentrated solutions, coils overlap and interpenetrate so that the interaction between segments becomes even more important. In the "classical" polymer solution theory of Flory and Huggins, the thermodynamic properties of the solution were calculated assuming that, for the interaction of a segment with its surroundings, all other segments could be considered as "smeared out" (i.e., a segment would have the same probability of meeting a segment of its own chain as one from a different chain). This is referred to as a -mean field approach. As soon as chain overlap occurs, a polymer solution can be understood as a transient network with an average "mesh size", which depends on the extent of overlap and hence on the concentration. For distances smaller than the mesh size, the distribution of segments is correlated because segments interacting with each other will experience the full excluded volume. For distances larger than mesh size the correlation is lost because segments are screened from each other by other chains and the behavior is that of an ideal chain. The description of overlapping coils ("semi-dilute" solutions) in terms of mesh size is commonly referred to as the "scaling theory" of semi-dilute polymer solutions (Cohen- Stuart et al. 1986, Napper 1977).

Many theories have been proposed to explain the adsorption of charged polymers and steric stabilization mechanism (Vincent 1974). According to the Sato and Ruch most of these theories may be divided into two major categories. The first is the entropic stabilization theory and the second is the osmotic (or heat-mixing repulsion) stabilization theory (Sato and Ruch 1980, Shaw 2003).

In the entropic stabilization theory, it is assumed that the second surface approaching the adsorbed layer is impenetrable. Therefore, the adsorbed layer is compressed and the polymer segments contained in the interaction area loose configurational entropy. This reduction in entropy increases ΔG and this produce repulsion between the particles. In this theory the enthalpic interaction between the adsorbed molecules and the dispersion medium is neglected therefore the equation becomes, $\Delta G= -T.\Delta S$. The theory was first initiated by Mackor and van der Waals. Then Hesselink, Vrij and Overbeek described this entropic effect as the volume restriction effect (Overbeek 1977, Vincent 1974, Sato and Ruch 1980, Shaw 2003).

In contrast, the osmotic repulsion theory assumes that adsorbed layers can overlap each other when the two particles collide. It also assumes that no desorption occurs on collision. In this model the polymer segments are in contact with molecules of the dispersion medium. This contact is reduced as a result of the contact between the segments in the overlapped region and this result in the enthalpy of mixing, ΔH_{mix}. On the other hand, as a result of the segment concentration in the overlapped region, there is also reduction in the configurationally entropy of the adsorbed molecules. Therefore, the total free energy changes due to overlap of the adsorbed layers can be expressed as a function of both enthapic and entropic change (Hesselink et al. 1971):

$$\Delta G_M = \Delta H_M - T\,\Delta S_M \tag{2.17}$$

In other words, as the segment density increases the segment-segment interaction increases and the segment-dispersion medium interaction decreases. The change in the mixing free energy depends on the magnitude of these two interactions. Figure 2.14 show schematically the steric potential between two particles as a function of particle separation (Shaw 2003, Sato and Ruch 1980).

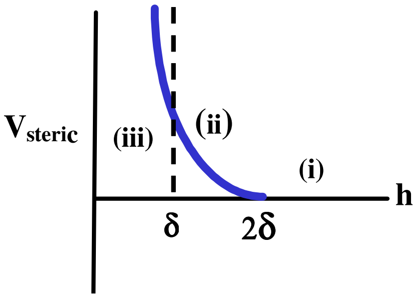

Figure 2.14. Schematic presentation of (i) h >> 2δ, no interaction, $V_{steric} = 0$, (ii) h ~ 2δ or less and $\delta < h \leq \delta$ repulsion due to entropic, mixing effects, (iii)h < δ repulsion due to mixing + strong repulsions due to elastic restoring forces.

To summarize, the interaction between the polymer chains on the particles may be separated into i) mixing effect that produces either repulsion or an attraction ii) an elastic effect that is always repulsive. The mixing effect is also described as osmotic effect, whereas the elastic effect is described as an entropic effect or volume restriction effect (Figure 2.15). The free energy of the polymeric interaction can be written as (Napper 1977, Rahaman 1995):

$$\Delta G_{steric} = \Delta G_{mix} + \Delta G_{elastic} \tag{2.18}$$

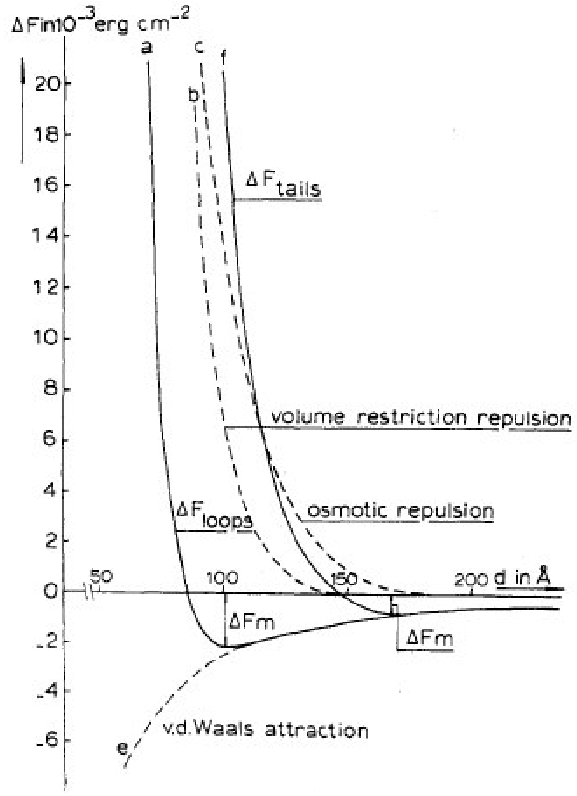

Figure 2.15. Total interaction potential graph that shows the effect of osmotic repulsion and volume restriction components (Source: Hesselink et al. 1971).

2.4.2.5. Depletion Interactions

This type of interactions arises when polymeric species are in the non-adsorbed state or free in solution (Lewis 2000). Depletion interactions can be attractive or repulsive, depending on the polymer concentration. At low concentrations, when particles approach each other at separation distances less than the effective coil diameter ($2R_g$) the coils are excluded from their gap. As a result, an osmotic pressure difference occurs between the surrounding bulk polymer solution and the pure solvent in the gap. This osmotic pressure difference drives the particles together and induces flocculation. On the other hand, at high polymer concentrations the coils will be begin to overlap in solution and prevent a close approach of particles hence will create stabilization (Blackman 1996, Vincent et al. 1986). The depletion potential depends on the size of the polymer and can be approximated by:

$$V_{depletion} = -\rho R_g kT \qquad (2.19)$$

Where ρ is the number density of the polymer, R_g is the radius of gyration of the polymer, k is the Boltzmann's constant, and T is the temperature.

Vincent and co-workers reported that addition of free (non-adsorbing) polymer chains to the continuous phase causes a weak, reversible flocculation occurs beyond some critical volume fraction of free polymer, however restabilisation occurs at an even higher volume fraction, of polymer (Vincent et al.1986). This is shown schematically in Figure 2.16.

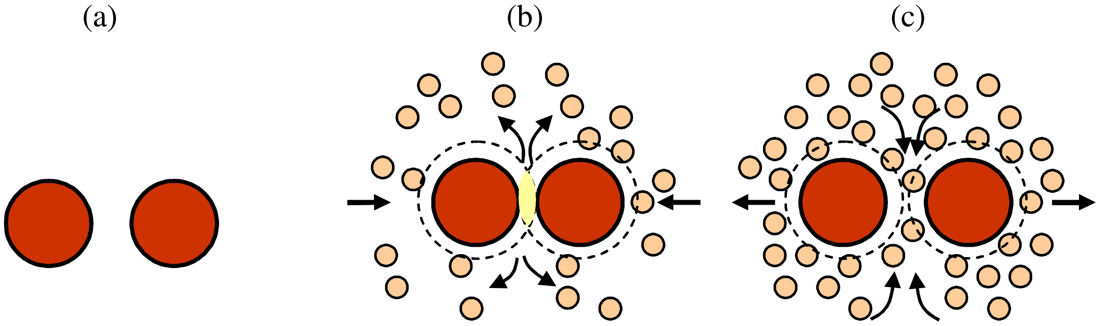

Figure 2.16. Schematic presentation of the interactions in the presence of free polymer (a) initial state (b) flocculated (c) restabilized.

2.4.3. Rheology of Colloidal Suspensions

Rheology plays an important role in the colloidal processing of ceramics. Control of the flow characteristics of suspensions is important for maintenance of their long-term physical stability and their application. This is especially crucial for the concentrated suspensions, in which the rheology of the system can be controlled by controlling the particle interactions (Kingery et al. 1976).

If the viscosity is independent of the shear rate (or the shear stress) the liquid is called Newtonian (Eqn. 2.20). For more complex systems such as colloidal suspensions viscosity is not independent of the shear rate and the behavior is called non-Newtonian (Larson 1999, Barnes et al. 1993).

$$\eta = \frac{\tau}{\dot{\gamma}} \tag{2.20}$$

Suspensions containing high concentration of particles may show shear thickening or dilatancy at high strain rates. Moderately concentrated suspensions of small elongated particles may show shear thinning or pseudoplasticity. Figure 2.17 describe the various flow behaviors in terms of viscosity and the shear stress as a function of shear rate. Shear thinning and shear thickening behavior can be described by (Barnes et al. 1993, Larson 1999, Shaw 2003):

$$\tau = K \dot{\gamma}^n \tag{2.21}$$

Where K is the consistency index and n is an exponent that indicates deviation from the Newtonian behavior. When n<1 suspension shows shear thinning flow and when n>1 flow described as shear thickening or dilatant (Macosko 1994). The flow behavior is described as plastic when the viscosity decreases with increasing shear rate after an initial threshold stress called the yield stress. The viscosity of most plastic materials is dependent on the shear rate and the flow behavior is often described by the power law relation (Barnes et al. 1993):

$$\tau - \tau_y = K \dot{\gamma}^n \tag{2.22}$$

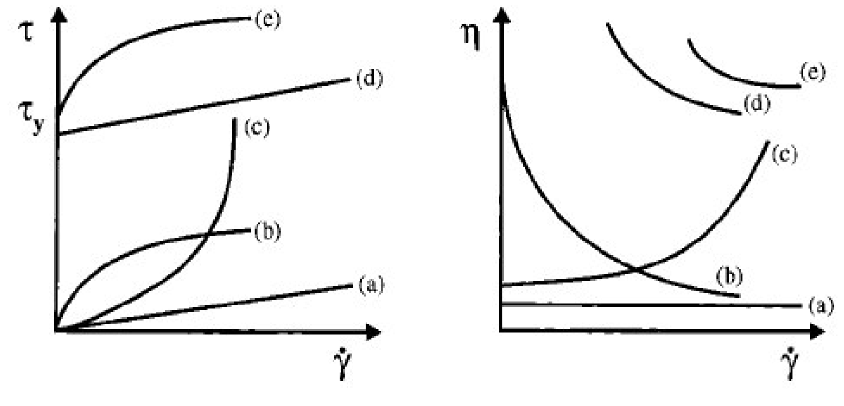

Figure 2.17. Types of rheological behaviour by colloidal dispersions: (a) Newtonian (b) Shear thinning (c) Shear Thickening (d) Bingham Plastic (e) Pseudo plastic with yield stress (Source: Lewis 2000).

2.4.3.1. Steady Shear Measurements

In the steady shear measurements one can control the shear stress by applying a torque (force) and measure the resultant displacement movement. On the other hand, it is also possible to control the shear rate by regulating the motor speed (movement) and measure the resultant torque. The sample is placed in rotational shear field at given shear rates and the resulting shear stress is measured by the instrument transducer as a torque signal (Barnes et al. 1993).

2.4.3.2. Dynamic Oscillatory Measurements

Viscoelastic behaviour can be characterized by the dynamic rheological measurements (or oscillatory techniques). Dynamic mechanical testing allows the sample to be subjected to a strain and the viscous and elastic properties of the sample to be measured simultaneously. During oscillation measurements, a frequency dependent shear stress or strain is applied to a suspension, and the shear moduli are obtained. The applied sinusoidal strain (γ) with a frequency (ω) and the resulting stress (τ) can be expressed as follows (Macosko 1994, Kim 1994):

$$\gamma = \gamma_0 \sin[\omega t] \tag{2.23}$$

$$\tau = \tau_0 \sin[\omega t + \delta] \tag{2.24}$$

$$\tau = \tau_0 \sin \omega t \cos \delta + \tau_0 \cos \omega t \sin \delta \tag{2.25}$$

where γ_0 is maximum amplitude of strain, τ_0 maximum amplitude of stress and δ is the phase angle. The stress can be considered to consist two components, one in phase with strain (ideal elastic material) and the other out of phase (purely viscous material). When these are divided by strain the modulus can be separated into real and imaginary components. The relationship between stress and strain is given as:

$$\tau = G^* \gamma \tag{2.26}$$

The complex modulus (the total energy required to deform the material) includes the complete information on the viscoelastic behavior.

$$G^* = G' + i.G'' \tag{2.27}$$

where G′ is the storage or elastic modulus, G″ is the loss or viscous modulus. The storage or elastic modulus is a measure of the energy stored and recovered in the material, on the other hand viscous or loss modulus is a measure of the energy lost as heat in the material through flow or deformation (Larson 1999, Barnes et al. 1993, Bitterlich et al 2002) Figure 2.18 show the oscillatory behavior of suspensions as a function of frequency. Absolute magnitude of the complex modulus can be written as the ratio of the maximum stress to the maximum strain (Barnes et al. 1993, Macosko 1994):

$$\left|G^*\right| = \frac{\tau_0}{\gamma_0} \tag{2.28}$$

From this value elastic and loss modulus values can be calculated using trigonometric relations:

$$\begin{aligned} G' &= \left|G^*\right| \cos\delta \\ G'' &= \left|G^*\right| \sin\delta \end{aligned} \tag{2.29}$$

Similarly tangent loss is an important parameter which is a measurement of the energy lost to the energy stored given as:

$$\tan\delta = \frac{G''}{G'} \tag{2.30}$$

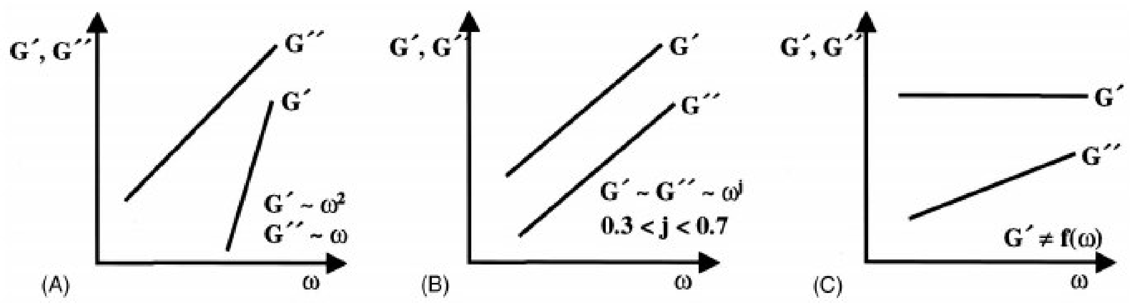

Figure 2.18. Oscillatory behavior as a function of frequency (A) liquid (B) gel (C) solid response (Source: Lewis 2000).

2.4.4. Interparticle Interaction Effects on Suspension Structure and Properties

2.4.4.1. Dispersed Systems

2.4.4.1.1. Hard Spheres

Hard sphere colloidal systems do not experience interparticle interactions until the point of particle contact (h=0) when the interaction is infinitely repulsive (Ogden 1996, Rahaman 1995, Barnes et al. 1993). The flow behavior dependence on volume fraction in dilute suspensions (volume fraction $\phi << 0.01$) is shown by the Einstein relation:

$$\eta_{rel} = \frac{\eta_{app}}{\eta_0} = 1 + 2.5\phi_s \qquad (2.31)$$

where η_{app} is the apparent viscosity of the suspension. Similarly the volume fraction dependent flow behavior at higher solids loadings ($\phi < 0.2$) is given by Batchelor equation:

$$\eta_{rel} = 1 + 2.5\phi_s + 6.2\phi_s^2 + o(\phi_s^3) \qquad (2.32)$$

However, the dependence of the low and high shear relative viscosity on solids loading is well described over a wide range of solids by Krieger-Dougherty relationship:

$$\eta_{rel} = \left[1 - \frac{\phi_s}{\phi_{\max}}\right]^{-[\eta]\phi_{\max}} \tag{2.33}$$

In addition the relative viscosity for hard sphere systems has been observed to scale with the Peclet number (Pe):

$$Pe = \frac{a^3 \eta_0 \dot{\gamma}}{k_b T} \tag{2.34}$$

Viscous forces begin to dominate when the Peclet number is at unity which correlates with the onset of shear thinning behavior (Ogden 1996, Rahaman 1995, Kim 1994).

2.4.4.1.2. Soft Spheres

They are particles covered with either an adsorbed polymer or electrostatic double layer. These layers can prevent direct contact of the particles. Stable soft sphere systems have exhibited flow behavior similar to that of hard sphere systems. Systems with thicker adsorbed layers exhibits significant deviations from hard sphere behavior because of the greater deformability of the stabilizing layer (Lewis 2000).

2.4.4.2. Strongly Flocculated Systems

These systems arise when particles aggregate in the deep primary minimum. The resulting structure is generally irreversible due to the large interparticle interaction energies ($V_{tot} >> 20\ k_bT$). These suspensions are characterized by strong shear thinning behavior as well as a yield stress and shear modulus (Buscall et al.1986, Rueb and Zukoski 1997).

At low solids loadings, $\phi_s < \phi_{gel}$, these suspensions exhibits weak shear thinning and no viscoelastic behavior. When $\phi_s > \phi_{gel}$ strongly flocculated suspensions demonstrates a yield stress and shear modulus that strongly depended on the volume fraction. The yield stress has a power law dependence on the solids loading and the particle size (Shih et al.1999, Rueb and Zukoski 1997):

$$\tau_y = \phi_s^{\ f} \tag{2.35}$$

$$\tau_y = a^g \tag{2.36}$$

Where f=2.5-3 and g= -2. It is also important to note that rheological properties of strongly flocculated systems are sensitive to shear history. After prolonged shear, yield stress and shear modulus decrease (Lewis 2000, Larson 1999).

The dependence of the elastic modulus (G') on solids volume fraction (ϕ) in particle gels has been described using a fractal gel model. Buscall and co-workers predicted that the elastic modulus (G') of a particulate gel increased in a power law relation with solids volume fraction (ϕ), according to $G' \sim \phi^{\mu}$ for $\phi \geq \phi_{gel}$, where the value of the critical scaling exponent (μ) differed for varying reaction pathways. Under reaction limited cluster growth conditions, $\mu = 4.5 \pm 0.2$, whereas for clusters formed under diffusion limited conditions, $\mu = 3.5 \pm 0.2$. These predictions were verified experimentally in strongly flocculated polystyrene lattices in which $\mu = 3.82$-4.06 depending on particle size, as illustrated in Figure 2.19, and in silica suspensions where $\mu = 4.0 \pm 0.5$ (Buscall et al. 1986, Morissette 1999*)*.

Yanez et al. found a similar volume fraction dependence of the elastic modulus, i.e., $G' \sim \phi^{4.75\pm0.25}$, in aqueous alumina suspensions in which the strength of the interparticle attraction was tailored via pH and salt additions (Yanez et al. 1996).

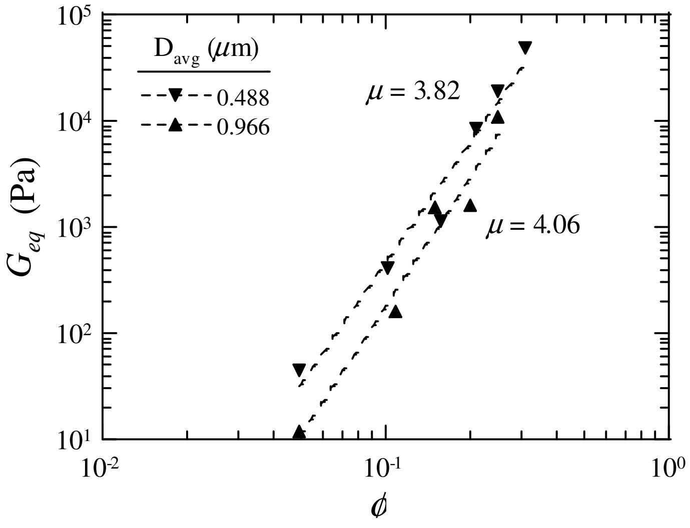

Figure 2.19. Steady–state elastic modulus as a function of solids volume fraction for electrolyte coagulated polystyrene lattices (Source: Morissette 1999).

2.4.5. Effect of Charged Polymers on the Stability of Ceramic Suspensions

Charged polymers with high molecular weights, called polyelectrolytes, can provide good dispersion of particles in aqueous systems through electrostatic stabilization (Hoogevan et al. 1996). On the other hand, steric stabilization generally occurs through the use of block or graft copolymers. Enhanced stabilization can be obtained by a combination of electrostatic and steric repulsion, known as electrosteric repulsion. In this case, the combined repulsive energy from the electric double layer and the steric interaction energy could eliminate the attractive van der Waals energy completely. A block copolymer with a charged anchoring chain and a water-soluble stabilizing chain can produce this effect, where the anchoring block ionically bonds to the oppositely charged sites on the particle surface (Rahaman 1995, Palmqvist et al. 2000).

2.4.5.1. Homopolymers

Homopolymers can be used as steric stabilizers. They often form trains and loops as well as tails because of their functional groups must attach to the particle and be well solvated (Slilaty 1995). The ionic strength and pH has a strong effect on the level of adsorption and on how polyelectrolyte adsorb. Under the conditions of low ionic strength electrostatic effects dominate adsorption, and the sign of the polymer and surface charge will determine the amount of adsorption. At high ionic strength, non-electrostatic effects such as hydrogen bonding and dipole interactions become more important because the electrostatics are screened by the high salt concentration. If the ionic strength increases too high the solvent quality may drop and increase adsorption, and further increase may cause polymer precipitation (Krsmanovic 2003, Vincent 1974, Napper 1977)

Polyacrylic acid (PAA) is a widely used polyelectrolyte used for the aqueous processing of ceramics (Cesarano III and Aksay 1988a, Das and Somasundaran 2001). It contains carboxylic acid groups one per monomer unit along its backbone. Similarly polymethacrylic acid (PMAA) is another dispersant that is commonly used in colloidal processing of ceramics. It contains carboxylic acid groups and methyl substutient on the backbone (Cesarano III and Aksay 1988b). PAA has carboxylic acid groups which become ionized above their p*K*a value of 5 (Kingery et al. 1976, Rahaman 1995), thereby promoting significant interactions with oppositely charged or neutral oxide surfaces. Alternatively, it undergoes a strong coulombic repulsion when interacting with like-charged colloidal surfaces (Whitby et al. 2003). Ionized the negatively charged carboxylic acid groups form an electrostatic repulsive barrier hence reduce the flocculation.

2.4.5.2. Comb Polymers

The comb polymers contain at least two types of side chains and are water soluble. The first type of side chain, referred to as ionizable, has moieties that ionize depending on the pH. These moieties can ionize to either cationic or anionic groups when they dissociate in the liquid. The second type of side chain referred to as nonionizable that does not ionize in the suspension (Larson 1999).

There are different methods to synthesize comb polymers but mainly two basic methods are known. The first pathway is to form a copolymer from a monomer or monomer unit having ionizable side chains and a monomer unit having nonionizable side chains (see Figure 2.20). By varying the ratio of the ionizable(m) to nonionizable(n) monomers combined to form the polymer. By maintaining a sufficient number of ionizable (hydrophilic) side chains, in relation to nonionizable side chains, the water solubility of comb polymer may be maintained (Lewis et al. 2006a).

The second general comb polymer synthesis method begins with a polymer having ionizable groups on the backbone that can be functionalized with nonionizable groups (cap). By capping a portion of the polymer's ionizable group with nonionizable a comb polymer may be formed (Lewis et al. 2006a).

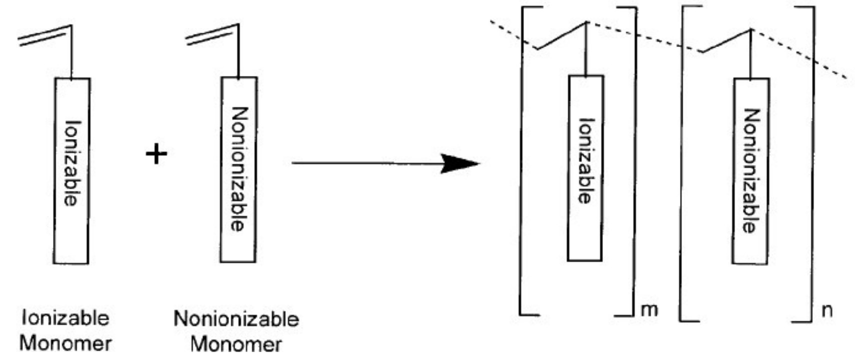

Figure 2.20. Schematic presentation of the synthesis method of comb polymers. (Source: Lewis et al. 2006a)

2.4.5.2.1. PAA/PEO Comb Polymers

Generally comb polymers made from the reaction of a hydrophilic polyacrylic acid backbone with polyethylene oxide caps (See Figure 2.21). By varying m,n, and/or o the molecular weight of the comb polymer and the ratio of the ionizable versus nonionizable side chains may be altered.

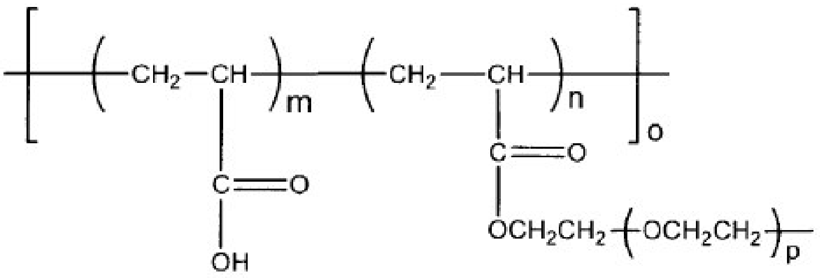

$$\left[\left(CH_2-\underset{\underset{OH}{|}}{\underset{C=O}{\underset{|}{CH}}} \right)_m \left(CH_2-\underset{\underset{OCH_2CH_2(OCH_2CH_2)_p}{|}}{\underset{C=O}{\underset{|}{CH}}} \right)_n \right]_o$$

Figure 2.21. Chemical structure of the PAA/PEO comb polymers. (Lewis et al. 2006a)

In addition to changing the atomic structure of the backbone and side chains, and the ratio of between the ionizable and nonionizable side chains (m versus n), the molecular weight of the backbone (determined by o) and the side chains (determined by

p) may be varied to control the suspension stability. Preferable ratios of ionizable to nonionizable side chains (m versus n) are from 10:1 to 2:1. Preferable average molecular weights of the backbone from 2000 to 10000. When polyacrylic acid backbones are used preferable values of p results in polyethylene oxide caps having average molecular weights from 100 to 5000 (Lewis et al. 2006a, Kirby 2003). PEO group of the comb polymer may contain alternative hydrophobic ethylene groups and hydrophilic ether linkages. The ether oxygen form hydrogen bonds with four water molecules. At low temperature, the polymer is soluble and as the temperature increases precipitation occurs (Sindel et al. 1999).

Acrylic based comb polymers are used as dispersants to increase the stability of colloidal suspensions containing multivalent or high concentrations of monovalent ions. Comb polymers comprising of neutral poly (ethylene oxide) (PEO) teeth attached at frequent intervals along a poly (acrylic acid) (PAA) backbone have been previously explored as dispersants for cement-based materials (Kirby and Lewis 2004).

Similarly, polyacrylic based superplasticizers with polyoxyethylene side chains have been used for the cement research previously by many scientists (Yamada et al. 2000). Yoshioka and co-workers performed interparticle potential calculations for the concrete system in the presence of PAA/PEO superplasticizers. According to their study the repulsive potential that is resulted from the electrostatic interactions were found negligible, which would allow cement particles to flocculate in the absence of steric contribution. Steric hindrance effects were found the dominant stabilizing mechanism in the system. Enhanced stability was observed with increasing adlayer thickness (Yoshioka et al. 1997).

Orth et al. demonstrated that a variety of water soluble poly (methacrylic acid)-(ethylene oxide) (PMAA-PEO) diblock copolymers could be used to formulate aqueous alumina suspensions with strongly repulsive interparticle potentials. They found that the diblock copolymers with a short PMAA anchor block and a long PEO block (block length ratio 10) were most effective for dispersing particles (see Figure 2.22). This can be expected since such compositions arrange the molecules in the desired “brush” conformation, which leads to an effective steric stabilization (Orth et al. 1997).

Palmqvist et al. used a water-soluble diblock copolymer, poly [(methacrylic acid)-*b*-(ethylene oxide)], to formulate alumina slurries that are dispersed over a wide range of pH through a combination of electrostatic and steric repulsion. They showed that the poly (methacrylic acid) blocks, a short chain (M_W 700 g/mol), interacts with the amphoteric alumina surface at pH 3 and acts as an anchor block. The nonionic PEO block only appears to have a steric function. At high pH, the polymer coated surface has a net negative charge due to the negative sites of the dissociated methacrylic acid units. This provides electrostatic repulsion at pH 9, which is the isoelectric point for pure alumina. The PEO chains extend from the surface and stabilize the alumina particles between pH 5 to 9 via an entropy-driven, steric repulsion (Palmqvist et al. 2000).

Adsorption behavior of PMAA-PEO diblock copolymers onto barium titanate was examined by Sindel et al. They found that in the presence of KNO_3 and $Ba(NO_3)$ increasing the concentration of electrolytes causes a reduction in extension of the PEO chains into the solution, but they did not observe any attractive forces (Sindel et al. 1999).

Similary, Kirby and co-workers studied the effects of PAA/PEO comb polymers on the stability of aqueous $BaTiO_3$ nanoparticle suspensions over a wide pH range in the presence and absence of monovalent and divalent salt species. They found that PAA/PEO comb polymers impart stability to $BaTiO_3$ suspensions over a wide range of pH and ionic strength conditions (Kirby et al. 2004).

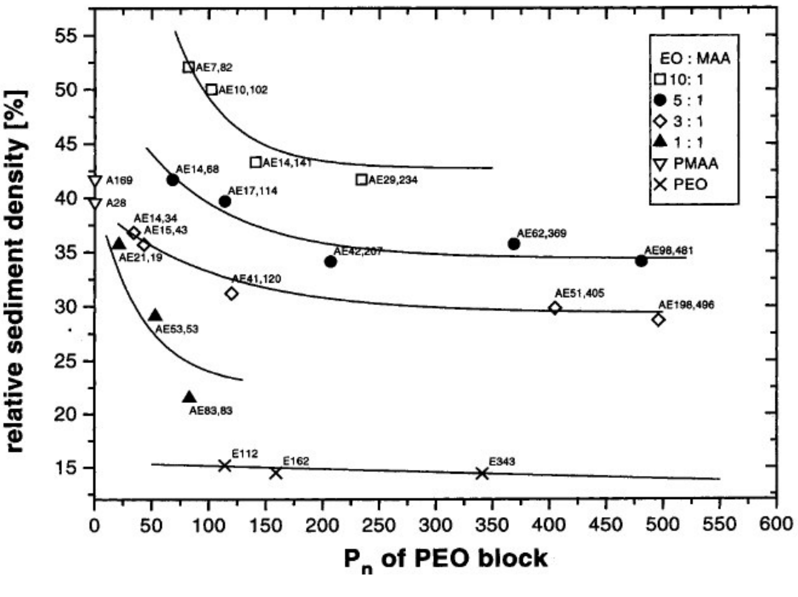

Figure 2.22. Al_2O_3 powder dispersing efficiencies of P[MAA-b-EO] block copolymers as probed by sedimentation tests (Source: Orth et al. 1997).

Withby et al. investigated the effects of PAA/PEO comb polymer on rheological properties and interparticle forces in aqueous silica suspensions. The comb polymer was found to adsorb more strongly under acidic than basic conditions, indicating that the

PAA backbone of the copolymer preferentially adsorbs onto silica surfaces with the PEO "teeth" extending out from the surface into the solution. In the presence of low concentrations of copolymer, the silica suspensions were stable due to electrostatic repulsions between the silica surfaces. At higher copolymer concentrations and under neutral and basic conditions, where the copolymer interacted only weakly with silica, the suspensions showed a transition from a dispersed to weakly flocculated state and attractive forces were measured between silica surfaces. The silica suspensions were stable at high copolymer coverage due to steric repulsions between the particles (Withby et al. 2003).

2.5. Shape Forming Methods

Ceramic components are formed by compacting a powder into the desired shape. The void space is eliminated with a high temperature heat treatment. Shape forming can be carried out by either pressing a dry powder mixed with a polymer binder or by injection molding the powder mixed into a polymer that imparts plasticity (Reed 1995, Kingery et al.1976).

Shape forming methods can also use slurries. Slurry methods for forming engineering shapes can be categorized as either consolidation methods or direct shaping methods. Consolidation methods start with slurry containing a low-volume fraction of powder, which is concentrated by either evaporation or pressure filtration (Table 2.1). Examples include tape casting to form thin sheets (by evaporation), slip casting to form thin walled bodies (capillary suction into a porous mold), and pressure filtration (Lange 2001, Reed 1995, Rahaman 1995). In direct shaping methods highly loaded ceramic suspensions are used to create three dimensional objects.

Dry powder pressing, slip casting, tape casting, extrusion and injection mouding are the conventional shape forming methods for the manufacturing of ferroelectric ceramics (Su et al. 2001). On the other hand, other methods have been developed for the fabrication of electroceramics are gel casting (Rak 2000, Guo et al.2003), viscous processing (Su et al. 2001, Su 1997), direct coagulation casting (Gauckler et al. 1999), electrophoretic deposition, pressure slip casting, temperature induced forming (Ewais et al. 2002) and novel solid free form fabrication techniques such as robocasting (Cesarano et al. 1998, Lewis 2000).

Table 2.1. Consolidation techniques used in ceramic processing.
(Source: Rahaman 1995, Lewis 2000, Ewais et al. 2002, Guo et al. 2003)

Forming method	Consolidation mechanism	Component shape
	DRY	
Dry pressing	Powder compaction (free flowing granules)	Small simple shapes
Isostatic pressing	Powder compaction (fragile granules)	Large,complex shapes
	FLUID REMOVAL	
Slip casting	Fluid flow into porous mold driven by capillary forces	Complex 3D, thin walled
Pressure filtration	Fluid flow trough porous filter driven by applied pressure	Simple, 3D
Osmotic consolidation	Fluid flow through a membrane	Simple, 3D
Tape casting	Fluid removal due to evaporation	Simple, 2D thin layers
Robocasting	Fluid removal due to evaporation	Complex, D
	PARTICLE FLOW	
Centrifugal consolidation	Particle flow due to applied gravitational force	Complex, 3D
Electrophoretic deposition	Particle flow due to applied electric field	Simple, 2D or 3D
	GELATION	
Aqueous injection molding	Organic gel forms in response to a temperature change	Complex, 3D
Gelcasting	Organic networks due to chemical reaction	Complex, 3D
Direct coagulation cast	Colloidal gel forms because of flocculation	Complex, 3D
Robocasting	Colloidal gel forms because of flocculation	Complex, 3D
Temp.induced forming	Colloidal gel forms because of flocculation	Complex, 3D

2.5.1. Tape Casting

Tape casting is a technique which is commonly used for the fabrication of ceramic sheets. The technique consists of deposition of a thin layer of a suspension on a carrier surface, generally using the doctor blade technique. After drying, a flexible green sheet is obtained with a thickness ranging from about 10 μ m to 1 mm (Kiennemann et al. 2005, Tian et al. 2007).

It was developed by G.N.Howatt in 1946. The method was originally developed for producing electronic ceramics such as insulating substrates and packages and multilayer capacitors. Since then, it is an important shaping technique used for the multi-layer capacitors, multi-layer ceramic packaging and solid oxide fuel cells

(Martinez 2002, Mistler 1998). Additionally, structural laminates, knives, membranes varistors, inductors, resistors, transducers, actuators, and sensors are examples of other applications for thin ceramics formed by tape casting (Blackman 1996, Seal et al. 2004, Bitterlich et al. 2002, Yoon and Lee 2004, Jantunen et al. 2004, Navarro et al. 2004).

Ceramic layers used in multilayer ceramic packaging have a dual purpose. They are the substrates which the circuit components are mounted and they also heat sink for the power dissipated from the circuitry. A cross sectional view of a multilayer ceramic capacitor is shown in Figure 2.23. The package contains several ceramic layers and conductive metal patterns connected between individual ceramic layers. A thermal conduction module produced by IBM contains up to 33 ceramic layers, 130m wiring, and 118 chips (Slilaty 1995, Kishi et al. 2003).

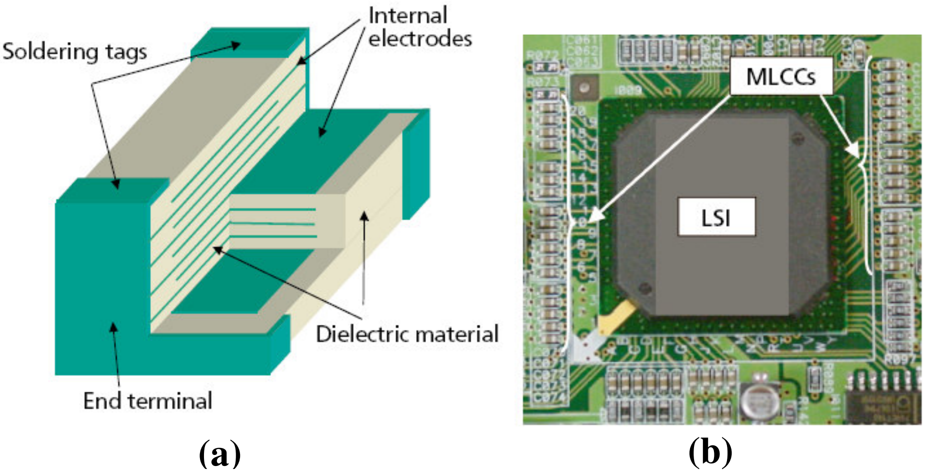

Figure 2.23. Schematic presentation of a) MLCC from cross sectional view b) Position of MLCC (Source: Kishi et al. 2003).

Tape casting process begins with preparation of a ceramic suspensions dispersed in a multicomponent solvent or water system. The tape thickness that can be achieved down to 5 µm with the today's technology. A diagram of the typical tape casting system is shown in Figure 2.24. Upon drying tapes are electroded, laminated and fired to produce multilayer ceramic components (Safari et al. 2002).

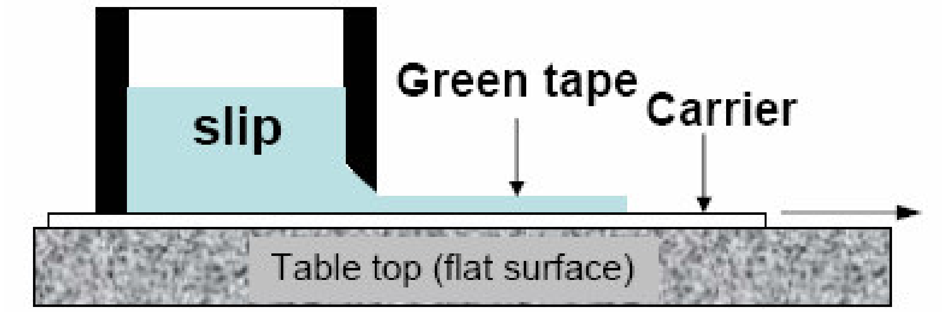

Figure 2.24. Schematic presentation of the tape casting process.

2.5.1.1. Development of Tape Casting Slurry Formulations

Tape cast films are produced from highly concentrated solvent based or aqueous suspensions. Previously non-aqueous formulations were commonly used because organic solvent based formulations offer good reproducibility, insensitivity to environmental changes and fast drying (Blackman 1996). However, heath and environmental considerations have motivated the researchers to developed aqueous based formulations. On the other hand, aqueous based tape casting formulations is not widely used by the industry due to their longer drying times, higher crack sensitivity. Therefore, there is still considerable interest to develop aqueous tape casting formulations to produce tapes with the desired properties.

In general, tape casting formulations must be designed to produce layers that satisfy the following criteria, (i) no defects (such as cracks, buckling) during drying, (ii) strength to allow manipulation of the dried sheets, (ii) microstructral homogeneity (iv) good lamination ability (v) high mechanical strength after sintering (Mistler et al. 1978, Rahaman 1995, Mistler 1998).

Aqueous tape casting suspensions generally composed of ceramic powder, dispersant, binder, plasticizer and water. In some cases, a wetting agent can be used in the formulations to enhance the spreading of the suspension on the carrier film. Furthermore, foaming agents can be used to reduce bubble formation that causes defects during drying. Aqueous tape casting suspensions can be optimized by investigating the flow behavior as a function of composition. At this stage, it is important to know the optimum amount of dispersant to obtain a stable suspension. Amount of binder and plasticizer additions should be carefully studied to achieve desired rheological properties (Cui et al. 2003, Hotza and Greil 1995).

The contents of solvent and organic additives in tape casting slurries should be as low as possible. Thus, the amount of solvent which has to be evaporated during drying and of organic additives, which have to be burnt out, is reduced. This minimizes the risk of defect formations (Chartier et al. 1999). But a low content of solvent results in highly loaded slurries with high viscosities. On the other hand, the viscosity of the slurries must be low enough in order to ensure a homogeneous flow during the tape casting process. In addition, the slurry should exhibit pseudoplastic behavior: during passing the blade, the viscosity is decreased due to shear forces, and immediately after the blade the viscosity increases rapidly to suppress uncontrolled flow and to prevent sedimentation of the ceramic particles. Thixotropy and any other time dependent behavior are undesired, because in this case the rheological behavior would be dependent on the pre-treatment of the slurry (Bitterlich et al. 2002, Seal et al. 2004, Slilaty 1995).

2.5.1.1.1. Binders

Among other processing agents binders are probably the most important processing additive in tape casting. They have important effects on green tape properties as strength, flexibility, and morphology. Many different binders have been used for making green ceramic tapes. The majority of these binders fall into two families: polyvinyls and polyacrylates (see Figure 2.25). The most familiar vinyl binders in tape casting are polyvinyl alcohol (PVA) and polyvinyl butyral (PVB). Acrylic latex binders are also widely used for tape casting as a water-soluble or emulsion type (Doreau et al.1998, Zhang and Binner 2002, Pagnoux et al. 1998). PVA and polyacrylates can be used for water-based system, while PVB can only be used for solvent-based system (Yoon and Lee 2004). Derivates of cellulose ethers such as hydroxyl ethyl cellulose and hydroxyl propyl methyl cellulose, also have been used in tape casting (Kristofferson et al. 1997, Kristofferson et al.1998, Cui et al.2003, Kiratzis and Luckham 1999).

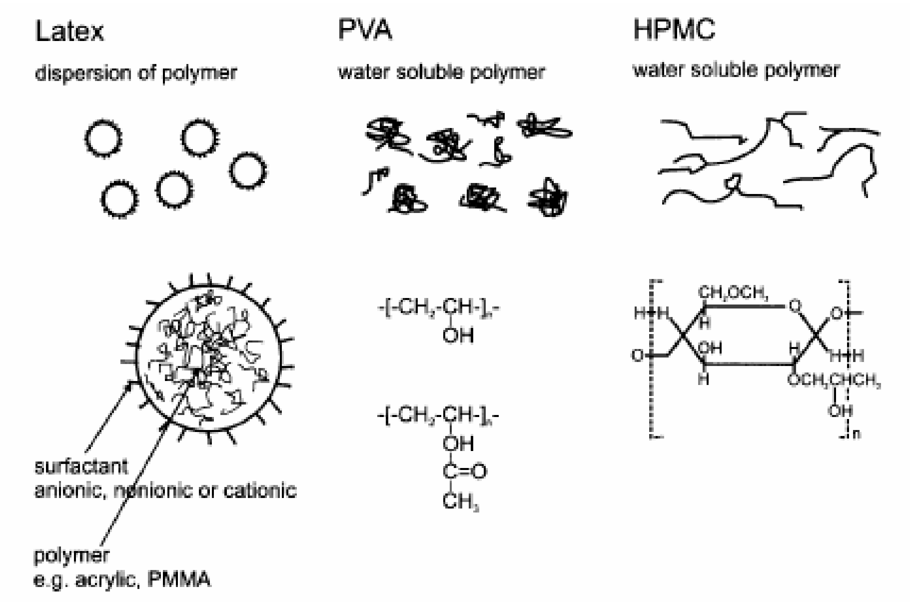

Figure 2.25. Schematic overview of the differences between the latexes, PVA and HPMC (Source: Kristofferson et al. 1998).

In tape casting process in addition to the dispersants and binders another important polymeric material used is the plasticizer. To either soften the binder polymer chains as a binder solvent and modify the binder glass transition temperature (Tg) or to lubricate the tape matrix by modifying interaction between binder polymer chains plasticizers are generally used in tape casting slurry formulations (Hotza and Greil 1995, Mistler et al.1978)

2.5.1.1.1.1. Latex Binders

A latex binder can be defined as a stable colloidal dispersion of a polymeric substance in an aqueous medium. The latexes used for tape casting are often acrylic and most common are those that are anionically stabilized. Acrylic latex-type binders have been identified as the best type of binder due to their low viscosity at high polymeric content and their internal plasticization. Furthermore, lamination is possible at room temperature using latex binders. Green tapes are obtained that are insensitive to air humidity, at the same time as they have a high quality with regard to surface smoothness, flexibility and green density. Important characteristics of the latex relevant to the processing are the latex particle size, the stabilization type of the latex and the type of the polymer (Kristofferson et al. 1998, Zhang and Binner 2002, Jablonski et al. 2004, Kristofferson and Carlström 1997).

In latex binders, buffers, typically ammonia, are added to maintain a pH between 8 and 10, for maximum dispersion stability of the acrylic polymer. Surfactants are a critical group of components, necessary to create the micelles for particle formation and long-term particle stabilization. Common surfactants are non-ionic (eg. alkyl phenol ethoxylates) and anionic (eg. sodium lauryl sulfate or dodecylbenzene sulfonate) that are typically added at 2 to 6 w%. These provide stability through electrostatic and steric hindrance mechanisms. Protective colloids also contribute to steric stabilization and are water-soluble natural or synthetic polymeric emulsifiers such as hydroxyethylcellulose and polyvinyl alcohol, added in 1 to 10 w% (Jablonski et al.2004).

The advantages of latex compared with the water soluble polymers such as PVA are their high polymer content at low viscosity, a low glass transition temperature (so there is no need for a plasticizer) and insensivity to moisture after drying. Disadvantage of latexes; they are insoluble after drying and that the surfactants may include alkali counter ions or impurities (Kristofferson et al.1998, Kristofferson and Carlström 1997).

Latexes form films upon drying when the water evaporates. At a certain stage the polymeric particles coalesce and form polymeric network. The formation of a film from a latex suspension can be divided in three stages. This is shown schematically in Fig 2.26. During stage I, because of the solvent evaporation volume fraction of the latex increases. This causes a network of particles that touching each other. In stage II, solvent evaporation continues and latex particles deform under the influence of interfacial forces until voids are completely removed. In stage III, polymer chain inter-diffusion occurs; continuous film forms and interfaces disappear (Martinez and Lewis 2002, Jablonski et al. 2004).

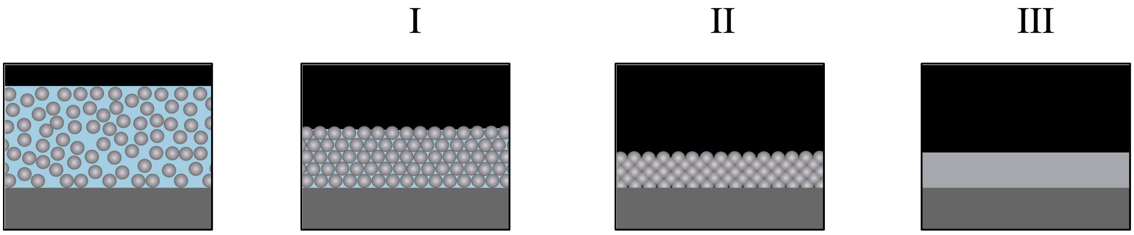

Figure 2.26. Schematic presentations that shows the drying sequences of acrylic latex binders (Source: adapted from Martinez 2002).

2.5.1.2. Drying of Ceramic Films

Drying of ceramic films is a complex process. After casting the film is in a super-saturated state which means that there is excess water to fill the pores between the particles. Therefore, ceramic particles move freely in the liquid phase under the influence of the Brownian motion and capillary flow. As the evaporation starts the solids loading of the film increases and it continuous until a particle of network forms that can support the capillary tension created by the liquid. This tension induces compressive stress on the solid network. Since the film adheres to the substrate, contraction is allowed only in the z direction, which results a stress in the x-y plane. The saturated state is reached when the water content equals to the pore volume and the radius of the menisci formed by the water is equal to the pore radius. As the evaporation proceeds large pores drain first from the particle network followed by the smaller pores. Further evaporation causes a pendular state and beyond this point water removal occurs by gas phase diffusion within the internal pore network (Chiu and Cima 1993, Scherer 1990, Scherer 1988, Rahaman 1995). Figure 2.27 shows schematically stages the drying of colloidal films.

The migration of colloidal particles during drying of droplets from colloidal suspensions (ϕ~0.001) was studied by Deegan and co-workers. Figure 2.28 demonstrates the optical image of a droplet containing 0.1 vol% solids (Deegan et al. 1997). Darker region near the edge indicates higher solids concentration. Similarly Figure 2.28 (b) shows the direction of particles as they stream from the center of the drop to the edge.

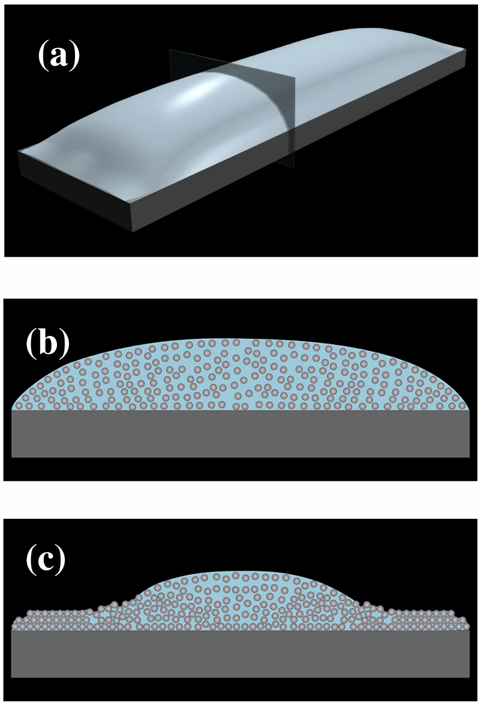

Figure 2.27. Schematic illustration of the shape evolution of ceramic films during drying (a) macroscopic view of deposited film (b) cross sectional view of the deposited film (c) cross sectional view of the film after drying partially (Source: Martinez 2002).

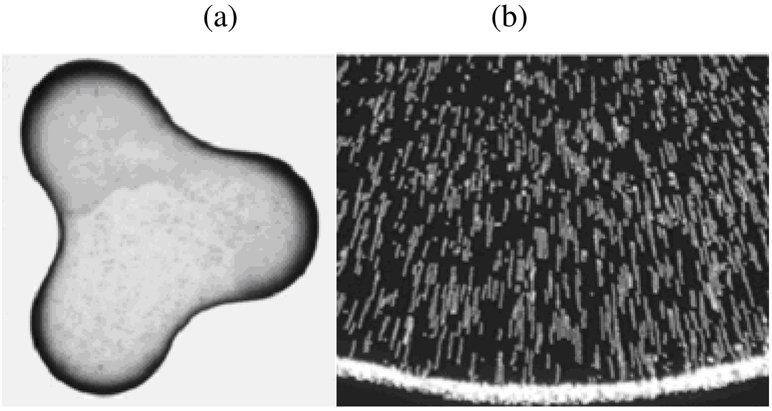

Figure 2.28. A ring strain of a) a drop of coffee dried to form a perimeter ring b) spheres in water during evaporation. Multiple exposures indicate the motion of microspheres (Source: Deegan et al. 1997).

Following paragraph summarizes drying stages of the films can be summarized as follows: Drying can be divided into three stages: (i) constant-rate period (CRP), (ii) first falling-rate period (FRP1), and (iii) second falling-rate period (FRP2). The first stage of drying is called the constant rate period (CRP), because the rate of evaporation per unit area of the drying surface is independent of time (Scherer 1990). In the CRP, the drying rate is controlled by external conditions. Fluid is supplied via capillary-driven transport to the external surface of the component, where evaporation takes place. As drying proceeds, large pores drain as fluid is drawn to smaller pores with higher suction potential. The drained pores may penetrate more into the materials interior. The transition to the FRP1 occurs when fluid can no longer be supplied to the external surface at a rate equivalent to the evaporation rate. In FRP1, evaporation occurs from the fluid menisci. As further evaporation occurs, fluid resides in isolated pockets, thereby marking the transition to FRP2. In FRP2, the remaining liquid is removed from the body by vapor-phase diffusion (Scherer 1990, Lewis 2000, Rahaman 1995).

2.5.2. Solid Free Form Fabrication

The continuous drive for producing near-net shape ceramic components has led to a new class of forming techniques known as solid freeform fabrication (SFF). Such techniques use computer-controlled robotics to build three-dimensional components in a layer-by-layer fashion (Cohen et al. 2006, Calvert and Crokett 1997, Brennan et al. 2003). Their advantages include the ability to tailor composition, greater process control and flexibility, reduced costs (i.e., there is no need for costly part specific tooling or molds), and improved performance and reliability. A number of SFF techniques, such as stereolithography (Griffith and Halloran 1996), selective laser sintering (Kumar et al. 2004) fused deposition (Safari et al. 2002), dip pen lithography (Xiaogong et al. 2002), electron beam lithography (Clendenning et al. 2004), laminated object manufacturing, 3D printing (Yoo et al.1995), and robocasting (Cesarano et al. 1998) for production of advanced ceramic components have been developed (Morisette 1999).

SFF was first applied to polymeric–based systems in the form of stereolithography (SLA). In SLA, a directed UV laser is rastered across the surface of a liquid monomer. The laser light induces solidification of the monomer via photo-polymerization, producing a solid layer of polymer at the surface of the part. The component is lowered into the bath, re-coated with fresh monomer, and re-exposed to create additional layers. This sequence is repeated until the part is complete. A schematic illustration of the SLA technique is provided in Figure 2.29 (Morissette 1999, Safari et al. 2006).

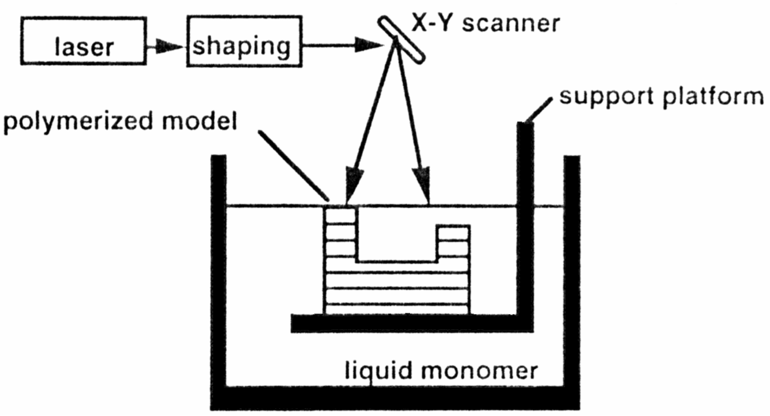

Figure 2.29. Schematic illustration of the stereolithography (SLA) process.
(Source: Morisette 1999)

SLA has been adapted to ceramic materials by Griffith and Halloran where ceramic powders are dispersed in a UV curable photopolymer. Scattering of the UV radiation in these highly turbid, concentrated suspensions results in reduced cure depths (d_c), where d_c decreases with increasing solids volume fraction and decreasing particle size. For example, typical cure depths in 30 v/o silicon nitride suspensions are 50-75μm. These limited cure depths result in reduced layer thickness and hence, extended build times (Morissette 1999, Griffith and Halloran 1996).

2.5.2.1. Ink Based Direct Writing Technology

Writing is the major means of generating arbitrary patterns on the surface of a substrate (Geissler and Xia 2004) Writing process can be carried out in different ways. Some of the direct writing techniques does not require any ink to generate the patterns but uses electric or magnetic field. In contrast, some of them require using a liquid like ink from an external source (Gratson 2005). Different ink writing techniques are highlighted in Table 2.2.

Formation of 3D structures requires controlling the lateral and vertical axes of the components. Therefore, it is generally more complex than the preparation of the 2D structures. 3D structures are commonly used in the microelectronic devices and their fabrication relies on the layer by layer (or multiple layer) fabrication scheme. In this case the critical issue is the accumulation of the defects as the number of layers increases and therefore the production cost. The technique such as photolithography that is commonly used in direct writing process is only capable of producing 1D or 2D patterns. It is still challenging to produce simplest 3D lattices using photolithography. Therefore alternative techniques are necessary to use for the fabrication of the 3D structures (Geissler and Xia 2004, Allahverdi and Safari 2004).

Table 2.2. Commonly used direct writing techniques.
(Source: Lewis and Gratson 2004, Dutta et al. 2001, Safari et al. 2002, Wu et al. 1996, Calvert and Crockett 1997, Cesarano et al.1998, Safari et al. 2006, Lewis 2006)

Technique	**Ink Design**	**Minimum Printed Feature Size**	**3D Periodic Structure**
Robotic Deposition	Concentrated colloidal gel	30 µm diameter	Yes
	Viscous polymer solution	200 µm diameter	Yes
	Concentrated polyelectrolyte complexes	< 1 µm	Yes
3D Printing	Binder solution printed on powder bed	170 µm lateral 45 µm depth	Yes
Ink jet Printing	Dilute and Concentrated fluid	20-70 µm lateral < 1 µm height	No
Fused Deposition	Thermoplastic polymer melt	100 µm diameter	Yes
Micropen Writing	Concentrated, shear-thinning colloidal fluid	25 µm diameter	No
Dip-pen Nanolithography	Dilute fluid	20 nm	No
Scanning Probe Contact Printing	Dilute fluid	< 500 nm	No
Reactive Extrusion Free Forming	Concentrated fluid	200 µm thickness	No

Ink-based direct-write techniques that enable 3D patterning of materials can be divided into two approaches: (1) droplet-based or (2) continuous (or filamentary) inks (see Figure 2.30) Direct ink-jet printing of ceramics and related approaches such as hot melt printing involve direct deposition using droplet based technique (Lewis 2002). Robotic deposition techniques such as robocasting, fused deposition and micropen writing uses continuous deposition approach (Lewis 2006).

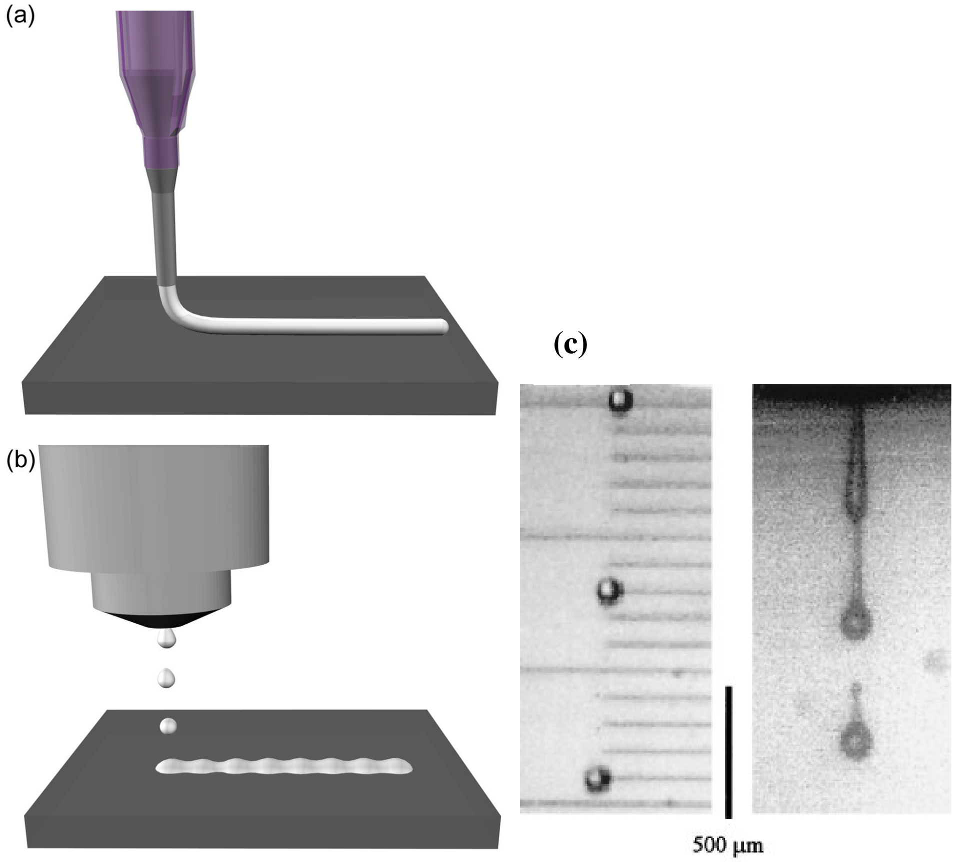

Figure 2.30. Schematic presentation of the a) continuous b) droplet based techniques (Source: Gratson 2005) c) picture of droplets used in ink jet printing (Source: Seerden et al 2001).

Direct ceramic ink jet printing is a fabrication technique where complex micro engineered parts are constructed from droplets of ceramic ink by an incremental building process (Mott and Evans 1999). Inkjet printing is familiar as a method for printing computer data onto paper or transparencies. Industrially, it is also widely used to print date information onto cans and bottles. The recent development of free-form fabrication methods for building parts layer-by-layer has led to interest in fabrication of multilayer parts and circuits by inkjet printing. The method have been used in the manufacture of organic transistors, light emitting diodes, ceramics, and biopolymer arrays (Figure 2.31) (Calvert 2001).

Fused deposition of ceramics (FDC) is an example of an layer manufacture technique. The technique is based on the idea of hot extrusion of ceramic-loaded polymer filaments through fine nozzles along pre-defined computer-controlled tool paths (Safari et al. 2002). Fused deposition of ceramics has also been used to make an array of novel actuators in the last decade. Actuators having different shapes such as tubes with straight, bellows, and curved wall geometry, spirals, telescoping, ovals, and mono morphs have been manufactured using FDC technique (Safari et al. 2006, Bandyobadhyay et al. 1997). However, as other injection molding techniques, FDC is limited by high binder contents which require extended burnout cycles prior to sintering. Also, current systems are not capable of multi-material deposition (Morissette 1999, Lewis 2006).

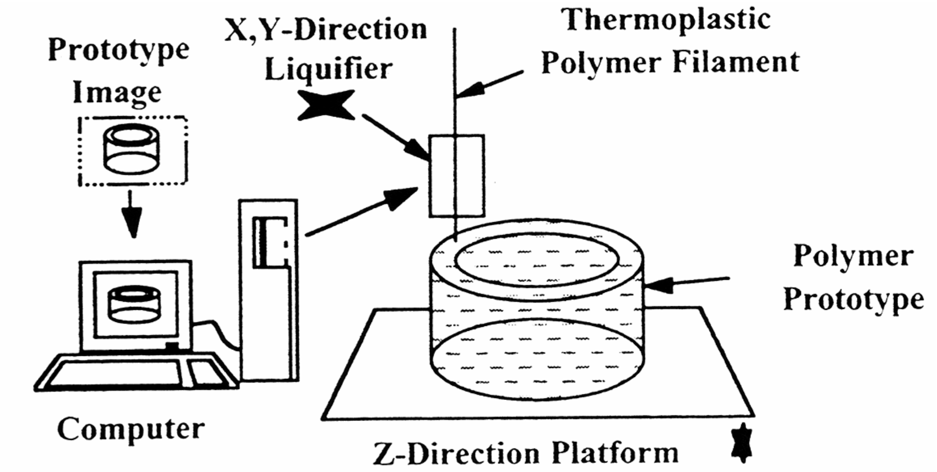

Figure 2.31. Schematic illustration of fused deposition of ceramics (FDC).
(Source: Morissette 1999)

3-D printing is an inkjet system writes a binder, such as polymer latex into a bed of ceramic powder. A layer of powder 100-150 µm thick is spread and then binder sprayed into the zone to be solidified as a stream of droplets. The method is excellent for coarser ceramic powders but is more difficult with fine, submicron powders where capillary forces become significant, and spreading the powder is difficult (Calvert and Crocket 1997).

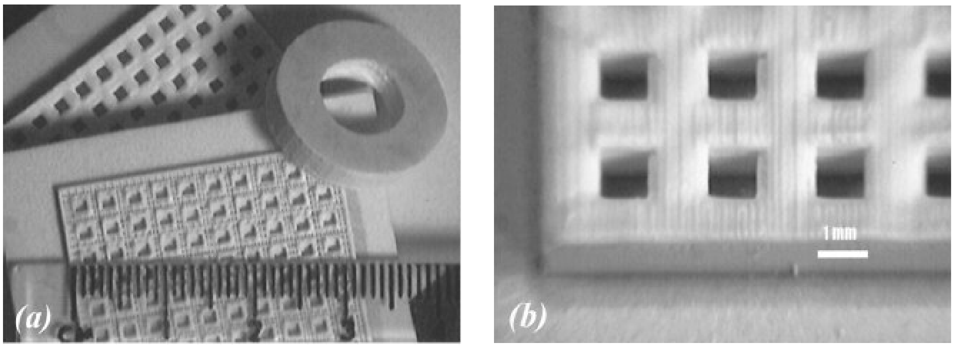

Figure 2.32. Structures produced by ink jet printing technique.
(Source: Seerden et al. 2001)

The micropen system is a computer-automated device for precision printing of ceramic slurries. The system uses a computer driven x-y stage for printing where the print pattern is defined by a CAD instruction file. The system is also capable of laying down multiple materials in a single layer, which cannot be done with conventional tape casting techniques. However, because the work piece needs to support the force of the pen, any underlying slurry layer must be dried before printing on top of it. Therefore, the system is not suitable for continuous processing of structures, in contrast to other rapid prototyping techniques for structural components (Dimos et al. 1999).

2.5.2.1.1. Robocasting

Robocasting or robotic deposition, involves the layer-by-layer deposition of concentrated colloidal inks in a predefined pattern (Li and Lewis 2003). The technique developed at Sandia National Labs in New Mexico, USA, and utilizes highly concentrated particulate slurries with a minimal amount of organic binders or polymeric gels (Safari et al. 2002, Cesarano et al. 1998). It is a free form fabrication technique and uses robotics to control layerwise deposition of ceramic slurries through an orifice (Figure 2.33) for near net shape processing (Cesarano et al. 1998). The build platform moves relative to the dispensing tip while material is being extruded. A computer generated model of a part usually contains surface information. It is imported into a slicing program which mathematically slices the model into sequential horizontal layers, and the hardware specific tool path for each layer is created. This tool path file then is downloaded into the printing device hardware, which fabricates the model layer by layer, following the specified path (Li and Lewis 2003).

This direct write assembly technique is capable of producing 3D periodic structures consisting rods with different geometrical shapes such as cylindrical, square, hexagonal (Rao et al. 2005). It has been utilized for the fabrication of periodic lattices of rods; intricate performs for piezocomposites, 3D microvascular networks and multimaterial composites (Therriault et al. 2005, Wu et al. 1996, Gratson et al.2006).

In robocasting the inks are typically formulated from colloidal or polymeric building blocks suspended or dissolved in a liquid to create a stable, homogeneous ink with the desired rheological behavior. In contrast to other freeform fabrication techniques such as gel casting or direct coagulation casting, robocasting does not require organic polymerization reactions or solidification of a polymeric melt for the solid transformation. In order to maintain structural integrity robocasting relies on the rheology of the deposited paste (Safari et al. 2002, Safari et al. 2006, Lewis 2006). The important rheological parameters for a given ink design include its apparent viscosity, yield stress under shear and compression, and viscoelastic properties (Gratson 2005, Cesarano et al.1998).

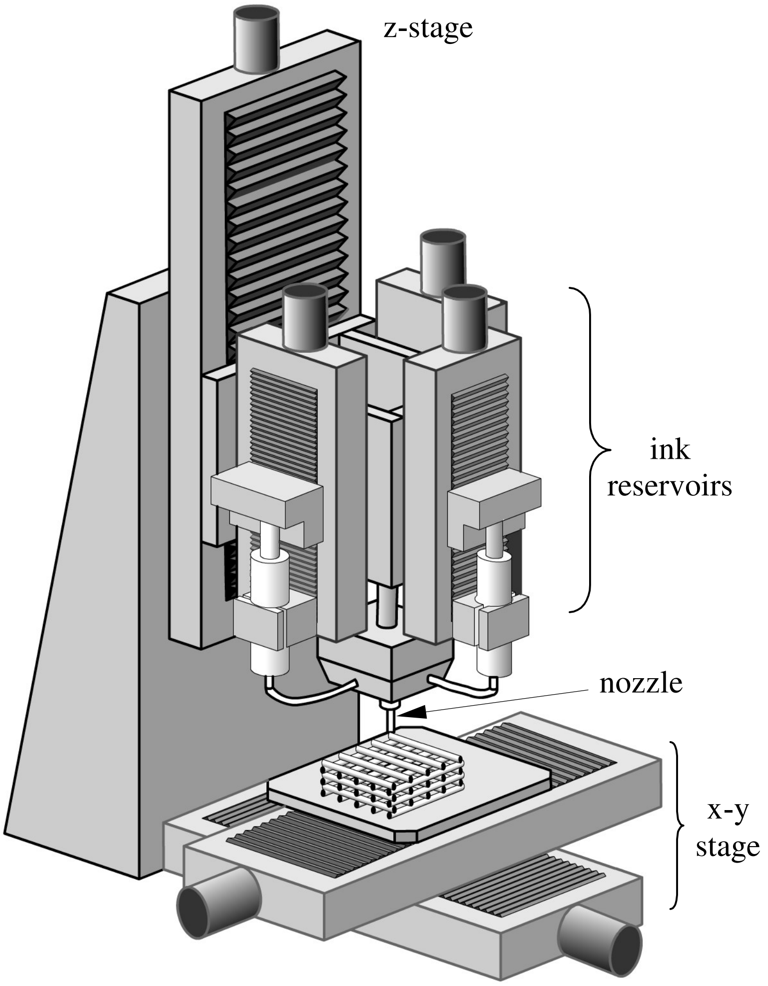

Figure 2.33. Schematic illustration of the first generation robotic deposition apparatus used in the directed assembly of concentrated particle inks. Inks are housed in individual syringe reservoirs mounted on the *z*-axis motion stage, and deposited through a cylindrical nozzle (diameter ranging from 10 µm to 1 mm) onto a moving *x*-*y* stage (Source: Li 2005, Smay 2002).

2.5.2.1.1.1. Colloidal Inks for Robotic Deposition

Colloidal inks developed for the robotic deposition of the 3D periodic structures must satisfy two important criteria. Primarily, they must able to flow through deposition nozzle and then set immediately to keep the shape retention. Second, they must contain high colloid volume fractions to minimize drying induced shrinkage. In other words, the particle network must be able to resist compressive stresses arising from capillary tension (Lewis et al. 2006a, Lewis 2002, Lewis 2006).

Therefore, the design of inks that are capable of flowing through deposition nozzles of varying size and then "setting" immediately to facilitate shape retention of the deposited features is crucial in direct writing techniques (Gratson 2005, Cesarano et al.1998). The preparation of colloidal inks requires control of the colloidal forces. The first stage of the ink preparation is to generate highly concentrated stable dispersions. The fluid-to-gel transition can be promoted by tuning pH towards the particle's isoelectric point, or increasing ionic strength or addition of cationic polyelectrolyte (Nadkarni and Smay 2006) as it is shown Figure 2.34.

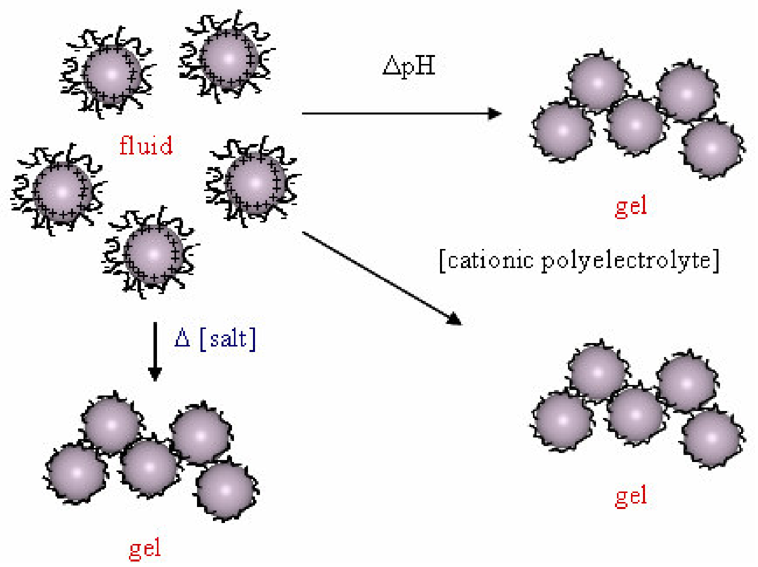

Figure 2.34. Schematic illustration of the fluid-to-gel transition in PMN inks.
(Source: Adapted from Smay et al.2002b)

Gelation denotes transition from a liquid (sol) to a solid (gel) state that occurs in the absence of fluid removal. During this process discrete species in solution undergo growth as gelation proceeds. Such species grow until at least one cluster known as the percolating (or spanning) cluster reaches a critical size on the order of the sample dimensions. At the sol-gel transition dramatic changes in the viscoelastic properties of the system are observed (Morissette et al. 2002).

Cesarano et al. developed colloidal inks designed to solidify via a drying-induced pseudoplastic-to-dilatent transition. As it is shown in Figure 2.35, robocasting work closely to the dilatant transition However, difficulty in controlling drying kinetics limits their applicability for creating 3D structures with high aspect ratio walls or spanning elements (Cesarano et al. 1998).

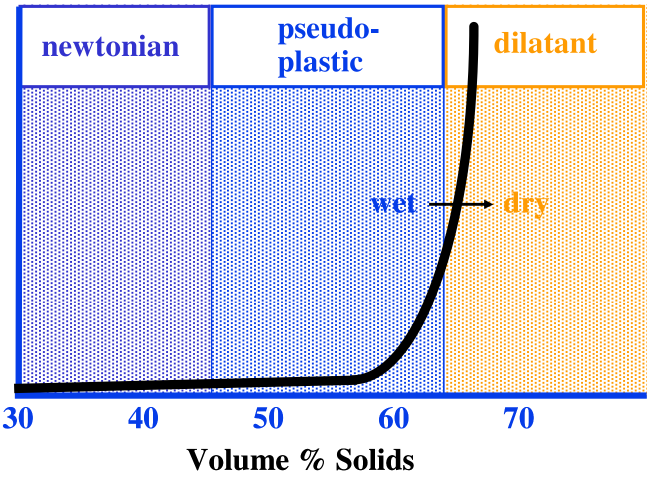

Figure 2.35. Schematic showing the viscosity versus volume percent solids behaviour for alumina slurries (Source: Cesarano et al. 1998).

Li and Lewis produced barium titanate nanoparticle inks for robotic deposition. In the study first, well dispersed barium titanate suspensions were produced using PAA as dispersant. Then the fluid to gel transition was performed by adding monovalent or divalent salt species to generate the desired viscoelastic response. A dramatic rise in elastic properties was observed in the phase transition by divalent salt additions such as Zn-acetate. They showed that unlike the monovalent counterions that only screen the negatively charged COO^- groups, divalent counterions such as Zn^{+2} can promote the aggregation through the ion briding effects between PAA adsorbed on the particle surface (see Figure 2.36) (Li and Lewis 2003).

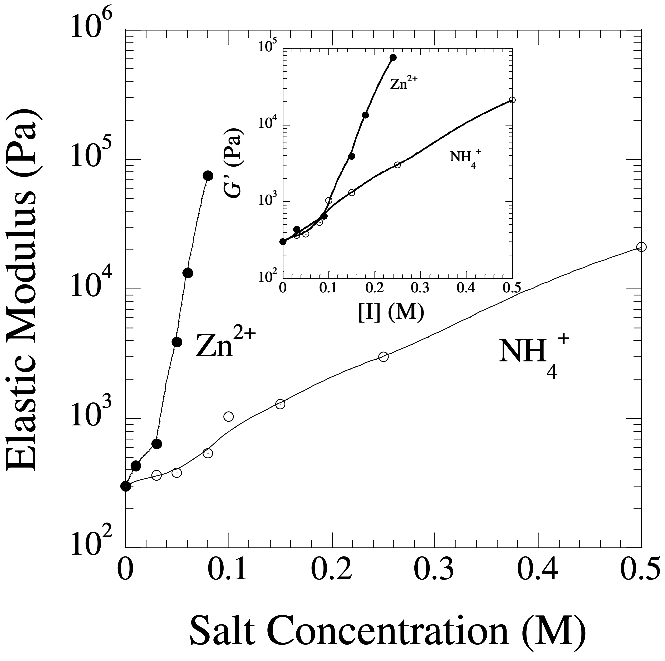

Figure 2.36. Equilibrium elastic modulus of 50 vol% $BaTiO_3$ nanoparticle inks with monovalent and divalent salt additions (Source: Li and Lewis 2003).

Similarly, Smay and co-workers prepared lead zirconate titanate (PZT) colloidal inks to produce 3D structures with robotic deposition. In the study particle gelation was induced by lowering the pH via HNO_3 titration. The rheological behavior of concentrated inks showed strong pH dependence. Each ink displayed marked shear thinning behavior with increasing viscosity as pH decreased as it is shown in Fig 2.37 (Smay et al. 2002a).

The elastic properties of the colloidal gel inks depend both on the particle concentration and interparticle potentials. The viscoelastic colloidal gels are formed whose shear elastic modulus (*G'*) and shear yield stress (τ_y) increase by orders of magnitude due to strengthened interparticle attractions, as given by the following scaling relationship (Larson 1999):

$$y = k\left(\frac{\phi}{\phi_{gel}} - 1\right)^x \tag{2.37}$$

where *y* is the elastic property of interest (shear yield stress (τ_y) or elastic modulus (*G'*)), *k* is a constant, ϕ_{gel} is the colloid volume fraction at the gel point, and *x* is the scaling exponent (~ 2.5). The equilibrium mechanical properties of colloidal gels are governed by two parameters: ϕ, which is proportional to their bond density, and ϕ_{gel}, which scales inversely with bond strength.

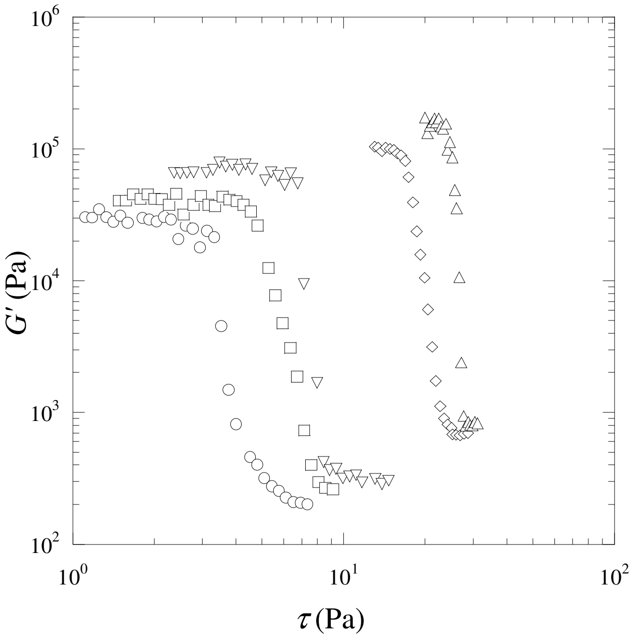

Figure 2.37. Elastic modulus as a function of applied shear stress for colloidal inks of varying pH = 8.05 (○), 7.6 (□), 7.2 (▽), 6.85 (◇), and 6.15(△) (Source: Li and Lewis 2003, Smay et al. 2002a).

On the other hand, extrusion of colloidal gels through a fine deposition nozzle is a complex dynamic process. When stressed beyond its yield point (τ_y), a colloidal gel exhibits shear thinning flow behavior due to the attrition of particle-particle bonds within the gel, as described by the Hershel-Bulkley model (Larson 1999):

$$\tau = \tau_y + K\dot{\gamma}^n \tag{2.38}$$

where τ is the shear stress, n is the shear thinning exponent (< 1), K is the viscosity parameter, and $\dot{\gamma}$ is the shear rate. Below τ_y, G' is independent of applied stress (i.e., the system resided in the linear viscoelastic region). Above τ_y, interparticle bonds rupture leading to a sharp decrease in G', thus facilitating flow (Gratson 2005).

The ink flows through the nozzle when a pressure gradient (ΔP) is applied along the length and a radial shear stress (τ_r) develops:

$$\tau_r = \frac{r\Delta P}{2l} \tag{2.39}$$

where r=0 at the center axis and r=R at the nozzle wall. Depending on the velocity profile and stability of the ink plug or laminar flow may develop in the nozzle (Lewis 2006).

Smay and Lewis investigated the elastic properties of the inks to retain the shape of 3D structures. For 3D structures with spanning features, which are comprised of cylindrical rods, by using a supported beam with distributed load model, the ink's minimum elastic modulus can be estimated by the following relationship:

$$G' > 1.4\rho_{\mathrm{eff}}\, gs^4 D \tag{2.40}$$

where ρ_{eff} is the effective ink density, g is the gravity constant, D is the diameter of the rod, d is the spanning distance between two rods, and s is the normalized spanning distance ($s = d/D$, $s > 1$ for spanning structures) if the maximal allowable rod deflection is assumed as 5 % of the rod diameter (Smay and Lewis 2001, Smay et al. 2002a).

2.5.2.1.1.2. Fabrication the 3-D Structures Using Polyelectrolyte and Colloidal Inks

In robocasting concentrated ink is housed in the syringe immersed in a reservoir. The reservoir generally contains oil to avoid rapid evaporation. Then the ink is deposited onto a substrate. A three dimensional structure to be assembled is virtually sliced into layers, and deposition tool paths are calculated using a computer-aided design (CAD) program. Figure 2.38 shows schematic illustration of a typical robotic deposition process

In this approach, inks are extruded through a fine cylindrical nozzle (or orifice) to create a filamentary element that is patterned layer-by-layer. By controlling ink rheology, three-dimensional structures that consist of continuous solids and high aspect ratio (e.g. parallel walls) or spanning features can be constructed. Lewis and coworkers recently developed several inks, including highly concentrated colloidal, nanoparticle, and polyelectrolyte inks, capable of direct writing complex three-dimensional structures with minimum feature sizes ranging from hundreds of microns to the submicron scale (Lewis and Gratson 2004, Lewis 2006).

Simple tetragonal and face centered tetragonal structures are the most commonly used designs (see Figure 2.39). It is also possible to produce various lattice designs such as radial and triangular structures using robocasting. Some of these structures are shown in Figures 2.40 to 2.44. In printing process the layers of the 3D structure are deposited sequentially, starting from the bottom layer. After the printing operation, the structure is dried and sintered to obtain a dense product (Nadkarni and Smay 2006, Smay 2002).

In robocasting it is also possible use polyelectrolyte inks such polyacrylic acid-polyethylene imine (PAA-PEI) complexes to produce 3D lattices (Gratson 2005). 3D microperiodic polyelectrolyte structures may find potential application as direct cell-scaffolds, photonic, microfluidic, or low-cost microelectromechanical devices (MEMs). The development of a fluid ink that flows through fine deposition nozzles, and then rapidly solidifies in a coagulation reservoir is central in patterning these structures (Lewis 2006, Wu et al 1996). Gratson et al. demonstrated the direct-write assembly of three-dimensional microperiodic structures using fluid inks that flow through microscale deposition nozzles (~1 μm in diameter or less) and rapidly solidify in a coagulation reservoir (Gratson et al. 2006)

Additionally, polymer structures are generally used to fabricate the hollow rods prepared from different materials. For example, it is possible to coat the 3D polymeric structures with silica using chemical vapour deposition process. Polymer burn out reveals the thin silica layer produced through CVD (Figure 2.41). Similarly ceramic-polymer composites can be successfully prepared using robotic deposition process. Figure 2.42 shows the picture of PZT-epoxy composite produced by robocasting (Lewis 2006, Smay 2002).

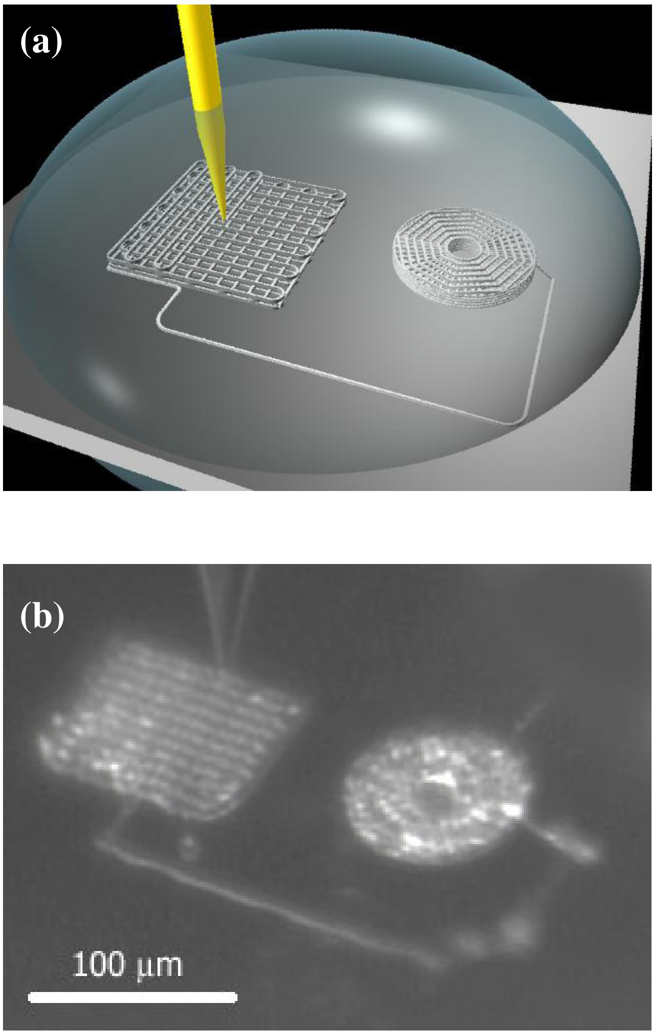

Figure 2.38. (a) Schematic drawing of the robocasting process. A concentrated ink is housed in the syringe immersed in a coagulation reservoir and deposited onto a substrate. (b) Optical image acquired in situ during the deposition process that reveals the actual features illustrated in (a) (Source: Lewis and Gratson 2004).

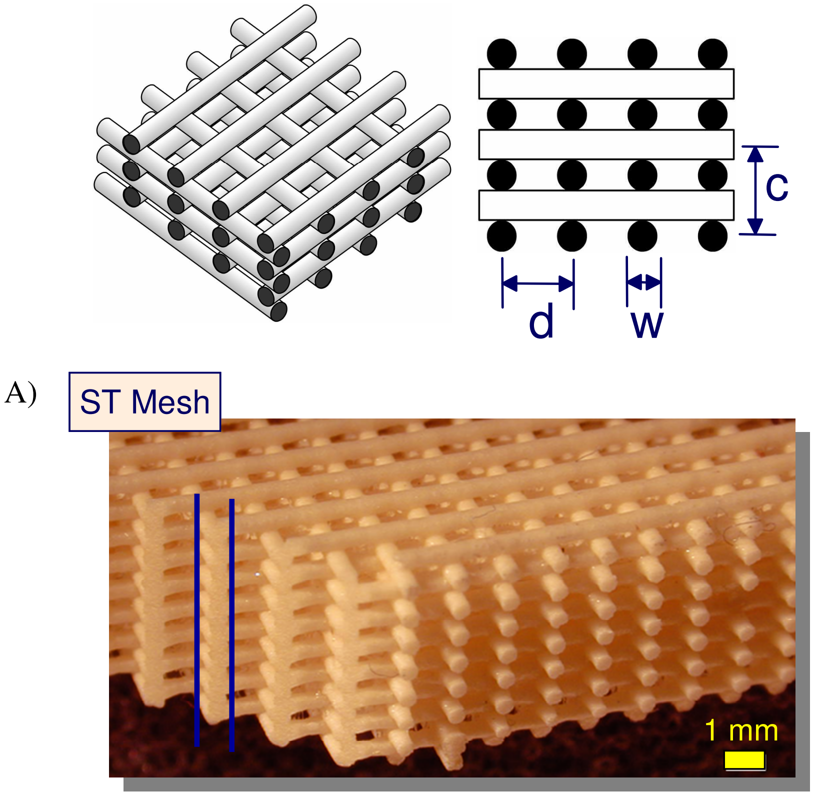

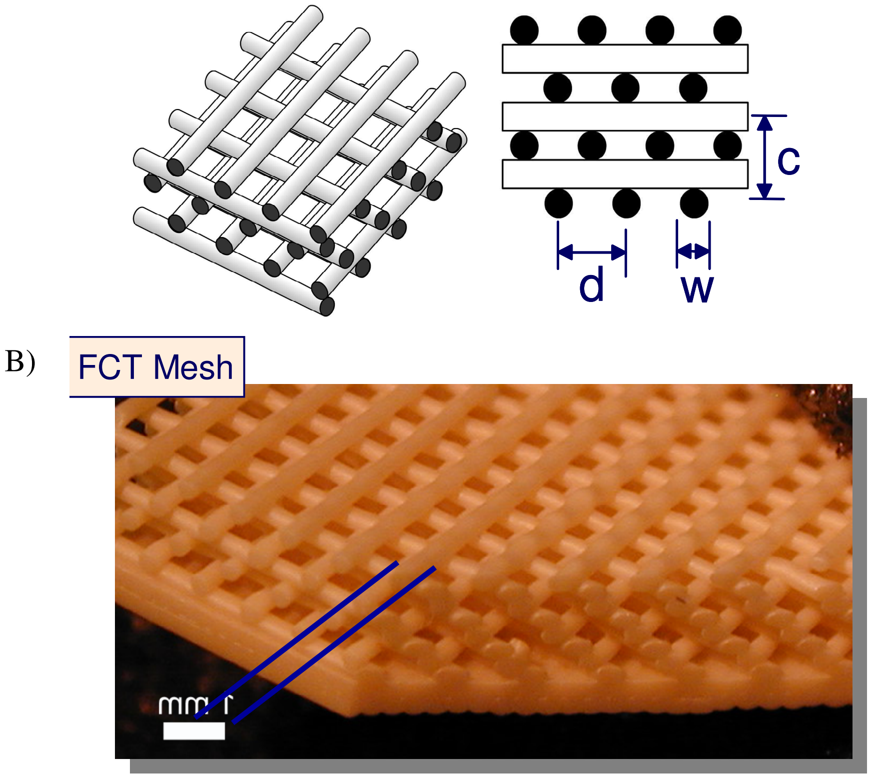

Figure 2.39. Two types of lattice structures designed for robotic deposition a) simple tetragonal structure b) face centered tetragonal structure (Source: Smay 2002).

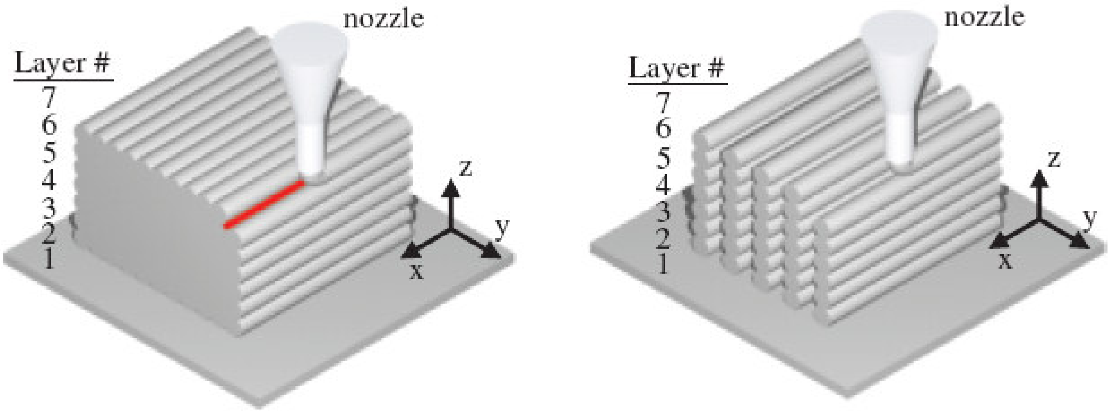

(a) Space filling solid

(b) High aspect ratio walls

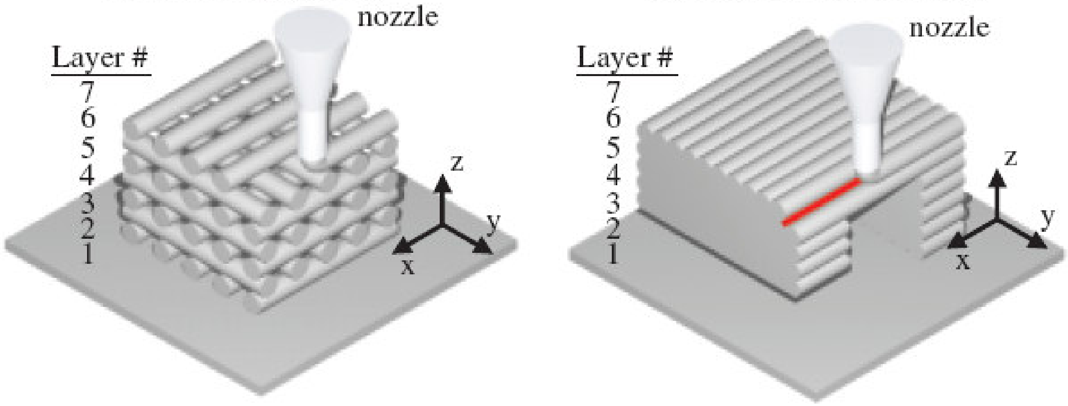

(c) Spanning (lattice)

(d) Cantilever and floating

Figure 2.40. Possible structural features that can be manufactured using direct write assembly (Source: Lewis et al. 2006b).

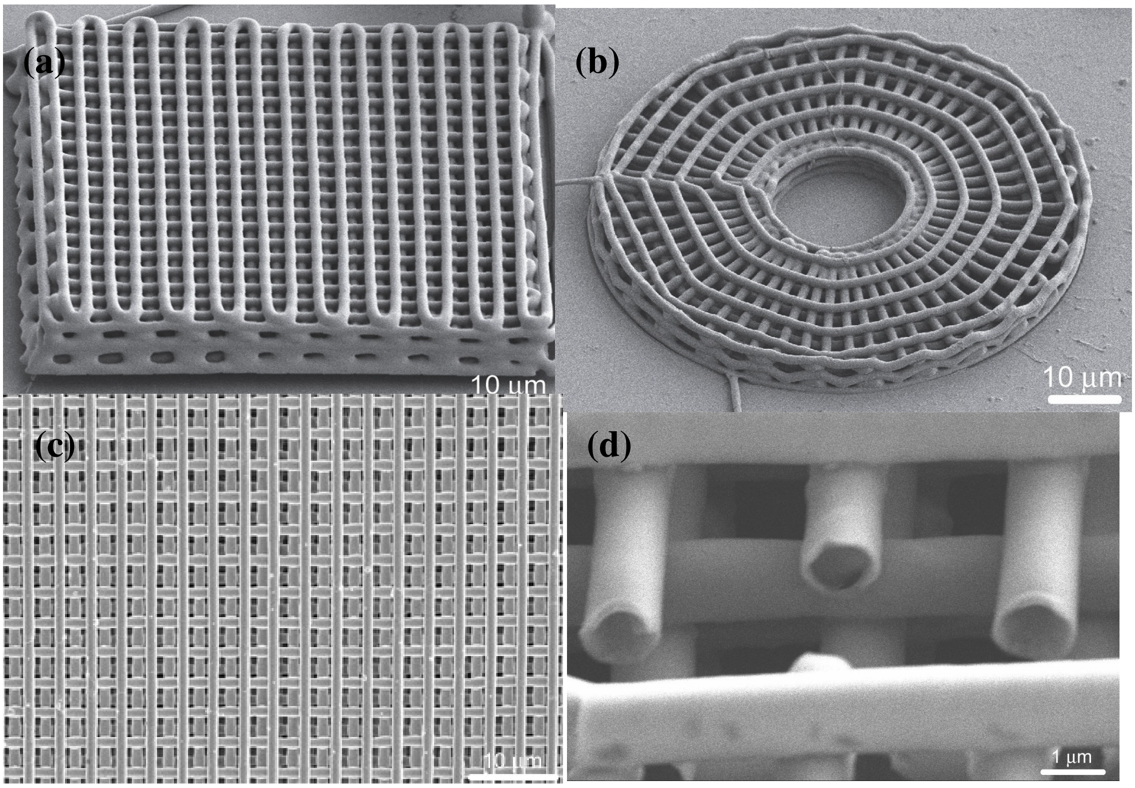

Figure 2.41. SEM images of 3D micro-periodic structures (filament diameter ~ 1 µm) prepared by PAA-PEI polyelectrolyte inks: (a) FCT lattice (10 layers, 4 µm road width), (b) radial array (5 layers),c) *rw* = 4 µm, 16 layers (d) fracture surface in a silica scaffold after polymer burn out revealing the thin silica layer produced through CVD (Source: Gratson and Lewis 2005).

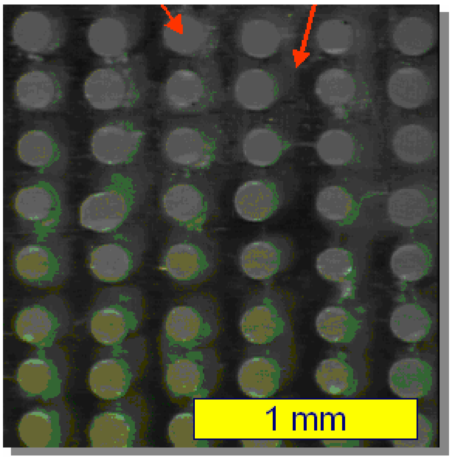

Figure 2.42. PZT-epoxy composites, rod diameter 175 µm
(Source: Smay 2002).

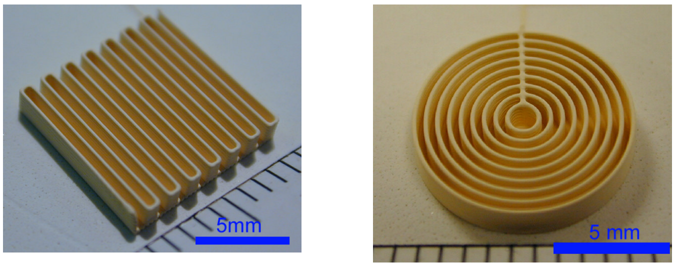
Linear Array 1 (0.5mm spacing)

Annular Array 1 (0.5mm spacing)

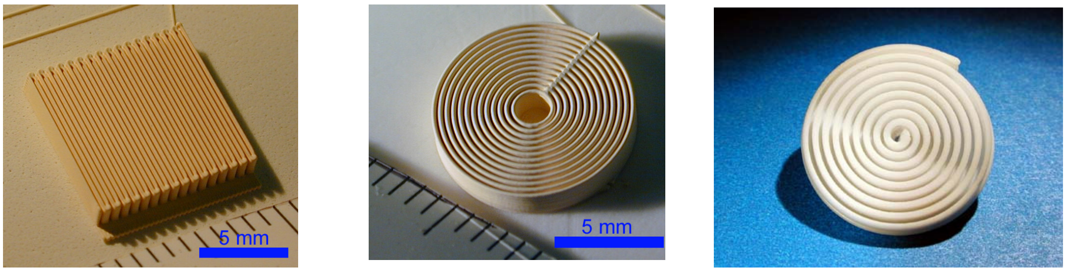
Linear Array 2 (0.3mm spacing)

Annular Array 2 (0.3mm spacing)

Figure 2.43. PZT and alumina high aspect ratio wall structures.
(Source: Smay 2002)

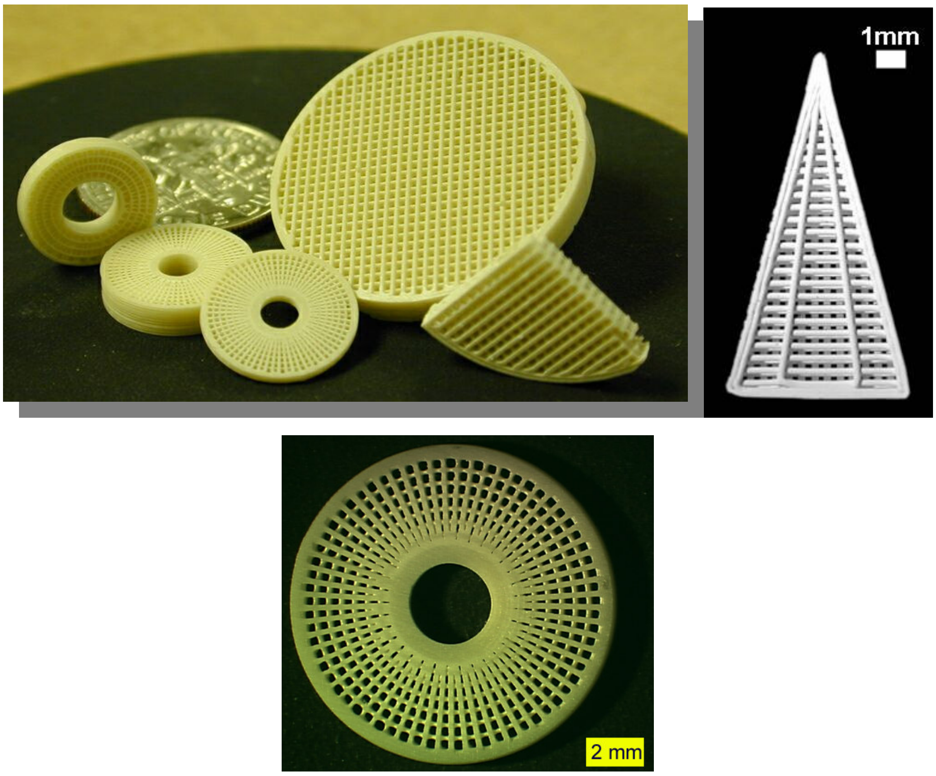

Figure 2.44. Various lattice designs prepared by PZT and alumina.
(Source: Smay 2002, Lewis 2002, Lewis 2006)

CHAPTER 3

PROPERTIES OF LEAD MAGNESIUM NIOBATE POWDERS IN WATER

3.1. Introduction

The leaching of perovskite materials in water is a major issue in colloidal processing (Nesbitt et al.1981). The contact with water may affect the final properties of the ceramics produced by wet shaping methods. Perovskite materials such as lead magnesium niobate (PMN) have the general chemical formula of ABO_3. In perovkites the cation at the A site is generally soluble in water whereas the B site cation is only slightly soluble overall the practical pH range. Therefore, A site cation undergoes incongruent dissolution leaving an interface which is relatively rich in the B site cation. Because of this fact, determination of the isoelectric point of the perovskite materials such as PMN can not be made by titration of the stock suspensions at a single solid loading (Adair et al. 2006).

The isoelectric point (IEP) is an important parameter in ceramic systems since it determines the stability of the colloidal particles in liquid medium. It is the pH value at which the apparent charge of the particles is zero (Stumm 1992). Ions in solution form a charged layer opposite in sign to that on the oxide, which is called the inner Helmholtz layer. Another layer, which consists of both the positive and negative ions and extends beyond the inner Helmholtz layer, is called diffuse layer. The boundary between these two layers is the shear plane and the difference in the electrical potential between the shear plane and the bulk solution is called the zeta potential (Zhou et al. 2003). The zeta potential depends on the surface charge density and the double layer thickness. The pH at which the zeta potential is zero is the IEP of the material (see Figure 3.1) (Houbenov 2005). The electrostatic repulsion between the interacting particles is eliminated at IEP. Under such a condition, particles become unstable and tend to coagulate.

Ceramic oxides generally have well defined and characteristic IEP values (Lopez et al. 2000). On the other hand, it is possible for a powder to exhibit multiple

pH_{iep} values, due to specific adsorption, dissolution, and/or precipitation reactions (Paik et al. 2002, Paik et al. 2003).

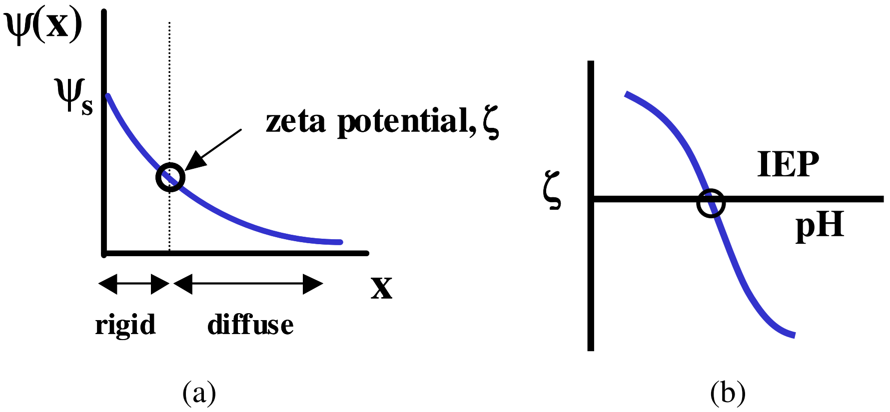

Figure 3.1. Schematic presentation of (a) zeta potential and (b) determination of IEP as a function of pH.

The zeta potential of colloids can be measured by methods based on electrokinetic (electrophoresis, electroosmosis, streaming potential and sedimentation potential) or electroacustic methods (Sabate et al. 2000). The conventional micro-electrophoresis method consists of setting up an electrical potential gradient in a cell and tracking the movement of micron size particles in solution using a microscope. One of the limitations of this method is that the size of the particles should be in the range 0.1 to 1 μm. Recent developments of this method are laser Doppler approach and the electrokinetic sonic amplitude (ESA) technology (Zhou et al. 2003).

The manufacturing of multilayer electronic devices composed of PMN generally involves a colloidal process which requires preparation of colloidal suspensions. However, the behavior of PMN particles in water medium is yet to be clarified. The few studies on this subject include the preparation of lead magnesium niobate-lead titanate (PMN-PT) suspensions in solvents other than water (Windlass et al. 2001, Vasanthakumari et al. 2005) whereas detailed work is present on barium titanate system in water (Paik and Hackley 2000). Therefore, understanding the PMN-H_2O system essential in producing high quality PMN ceramics.

In this study isoelectric point of PMN suspensions were determined as a function of pH and solids loading using Doppler based micro-electrophoresis and ESA techniques. The solubility characteristics of the cations that constitute PMN were examined as a function of suspension pH and solids concentration. Effect of cation leaching on the surface bond formation and the microstructure of the PMN powders after heat treatment was investigated.

3.2. Experimental

3.2.1. Materials

Lead magnesium niobate, $Pb(Mg_{1/3}Nb_{2/3})O_3$ powder which was produced by combustion spray pyrolysis method provided by Praxair Specialty Ceramics, WA, USA. Powder purity is 99.9% as reported by the manufacturer. Bulk density (Helium pycnometer Micromeritics 1330, Norcross, GA, USA), and the BET surface area (Micromeritics ASAP 2400, Norcross, GA, USA) of the powder are measured to be 7.967 g/cm^3 and 1.168 m^2/g, respectively. Particle size distribution of the powder was obtained using a particle size analyzer (Horiba CAPA-700, Tokyo, Japan) and the d_{50} of the powder was measured to be 2.03 µm (Figure 3.2). Other materials used in the work are Niobium (V) oxide (Alfa Aesar, 99.9% metal basis), Lead (II) oxide (Alfa Aesar 99.9%), and Magnesium oxide (Mallinckrodt AR, Analytical reagent, Paris). Crystal structure of the PMN powder was identified using X-ray diffraction technique (Philips X`pert PRO). Morphology was investigated using Scanning electron microscope (Philips, XL-30S, FEG). Figure 3.3 show the microstructure and the crystal phase of the PMN powder used in the study.

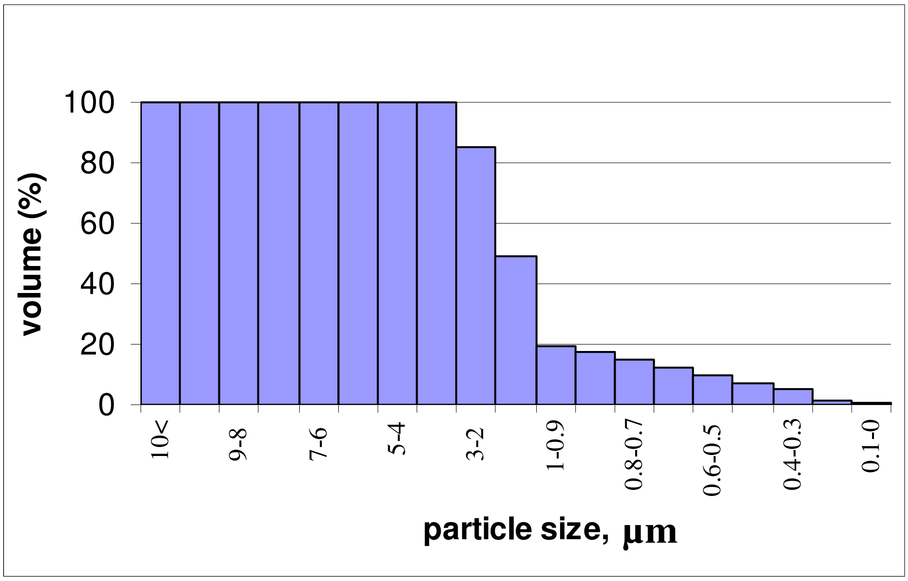

Figure 3.2. Particle size distribution of the PMN powder used in the study.

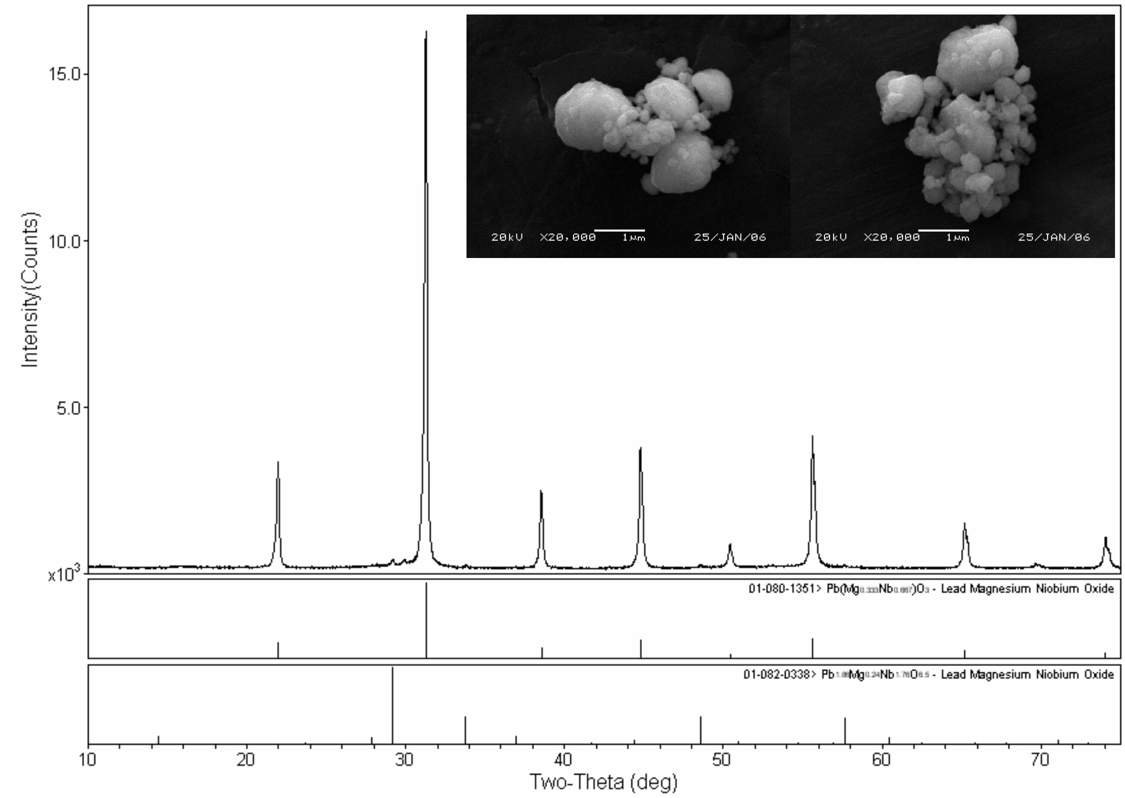

Figure 3.3. XRD pattern and the SEM micrographs of the PMN powder used in the study.

3.2.2. Method

3.2.2.1. Suspension Preparation

Lead magnesium niobate suspensions were prepared at different solids loadings in water. Suspensions was ultrasonicated (F550 Sonic Dismembrator, Fisher Scientific, pardubice, Czech Republic) for 2.30 minutes using a 1s on/off pulse sequence. The suspension pH was adjusted using 1 M solutions of HNO_3 and NH_4OH. Suspensions were magnetically stirred for 24 hours at room temperature prior to measurements. Since the addition of simple electrolytes do not affect the IEP (eventough it affects the magnitude of the zeta potential), no care was taken to control the electrolyte concentration such as by using a background electrolyte.

3.2.2.2. Solubility Behavior of PMN in Water

The solubility of PMN powder in aqueous medium was investigated using inductively coupled plasma–atomic emission spectroscopy (ICP-AES Varian Liberty Series II) and inductively coupled plasma mass spectroscopy (ICP-MS Agilent, 7500 Series) as a function of pH and solids concentration. Suspensions prepared at different solids loadings according to the procedure described in the previous section were centrifuged (Beckman, Avanti J-25 I) at 4000 rpm for 1 hour to obtain a clear supernatant. Supernatants were further filtered from 0.02 μm microfilters to eliminate any possible particles in solution. The amounts of Pb^{+2}, Mg^{+2} and Nb^{+5} in particle-free supernatants were measured.

3.2.2.3. Zeta Potential Measurements

Measurements were performed using two different techniques namely microelectrophoresis and electroacustic method.

3.2.2.3.1. Electrophoresis Method

Zeta Potential measurements were performed using a zeta sizer (3000 HS, Malvern Instruments, Worcestershire, UK) with aqueous dip cell apparatus whose electrodes were properly cleaned before each measurement to avoid contamination. The device uses the microelectrophoresis technique for the zeta potential determination. Since this technique allows measurements only in dilute suspensions, samples were diluted prior to measurement using sedimentaion and then a small amount of sediment redispersed with the supernatant. The measurements were periodically checked against a calibration standart with a zeta potential of -50 mV(± 5). Experiments were performed in triplicate, and the results given are the average of 10 measurements.

Micro-electrophoresis system is a cell with electrodes at either end to which a potential is applied. Particles move towards the oppositely charged electrode, their velocity is measured and expressed in unit field strength as their mobility. The system uses the Laser Doppler Velocimetry (LDV) to measure the velocity of particles moving through the fluid in an electrophoresis experiment. In the system to make an electrophoretic mobility measurement, laser beams of are caused to cross at a particular point in the cell. Particles in the cell are illuminated by these beams (WEB_3 2007).

According to the electrophoresis theory when an electric field is applied across an electrolyte, charged particles suspended in the electrolyte are attracted towards the electrode of opposite charge. Viscous forces acting on the particles tend to oppose this movement. When equilibrium is reached between these two opposing forces, the particles move with constant velocity. The velocity is dependent on the strength of electric field or voltage gradient, the dielectric constant, the viscosity of the medium and the zeta potential. The velocity of a particle in a unit electric field is referred to as its electrophoretic mobility. Zeta potential is related to the electrophoretic mobility by the Henry equation:

$$U_E = \frac{2\varepsilon\xi}{3\eta} . f\left(Ka\right) \tag{3.1}$$

Electrophoretic determinations of zeta potential are most commonly made in aqueous media and moderate electrolyte concentration. f (Ka) in this case is 1.5, and this is the value used in the Smoluchowski approximation (Zhou et al. 2003):

$$U_E = \frac{\varepsilon\xi}{\eta} \tag{3.2}$$

Therefore calculation of zeta potential from the mobility is straightforward for systems that fit the Smoluchowski model, i.e. particles larger than about 0.2 microns dispersed in electrolytes containing more than 10^{-3} molar salt (WEB_3 2007). In this work, f (Ka) value was taken as 1.5 through the measurements.

3.2.2.3.2. Electroacoustic Method

Zeta potential of concentrated suspensions were also determined by electrokinetic sonic amplitude measurements using an electroacoustic analyzer (ESA-9800, Matec Applied Sciences, Northborough, MA, USA). The solids loadings in this case were 0.1, 5 and 10 vol%. The ESA apparatus (see Figure 3.4) makes use of the so-called electroacoustic effect and a high frequency AC voltage in the order of 1 MHz is applied to the suspension. If particles carry any electrostatic charge they will oscillate around the position of rest. Such an oscillation generates a pressure wave in the liquid which can be detected and correlated to the zeta potential. The amplitude of the wave is dependent on the magnitude of the charges on the particle surface, the particle concentration and amplitude of the electric field. The ESA is detected and converted to a voltage with a piezoelectric transducer. Relation between the electrokinetic sonic amplitude and zeta potential can be given as (Graule and Gauckler 1993, Ushifusa and Cima 1991):

$$\mu_d = \frac{ESA}{\phi.\Delta\rho.c} \tag{3.3}$$

$$\xi = \frac{ESA}{\varepsilon.\phi.\Delta\rho.c} G(\alpha)^{-1} \tag{3.4}$$

$$G(\alpha) = \left[1 - \frac{i\,\alpha\left(3 + \frac{2\Delta\rho}{\rho}\right)}{9\left(1 + (1-i)\sqrt{\frac{\alpha}{2}}\right)} \right]^{-1} \qquad (3.5)$$

where Δρ is density difference, c is the velocity of sound in suspension, η is the liquid viscosity, a is the particle radius, w is the angular frequency, ρ is the particle density and $\alpha = wa^2 \rho / \eta$.

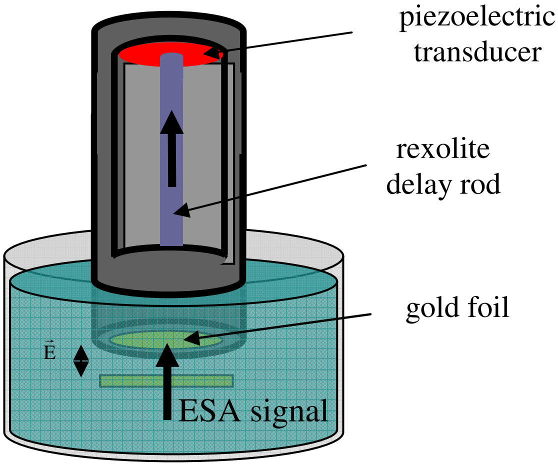

Figure 3.4. Schematic presentation of the ESA analyzer.

Since the technique capable of measuring the zeta potential of concentrated suspensions samples were prepared without any dilution. To ensure dispersion the suspensions were ultrasonicated for 2.5 minutes using ultrasonic horn (550 Sonic Dismembrator, Fisher Scientific) prior to measurements. The ESA measurements were checked against a 10 vol% Ludox suspension having a zeta potential of -38 mV. Experiments were performed in triplicate, and the results given are the average of 10 measurements.

3.2.2.4. Microstructure and Phase Analysis

Structural bonds on the PMN powder after aging in water at different conditions were analyzed using Fourier Transform Infrared Spectroscopy (FTIR-8201, Shimadzu).

Microstructure and crystal structure of the PMN powders aged in water at different conditions prior to a heat treatment at 1100 ºC for 2 hours (heating rate, 5 ºC/min) was examined using a scanning electron microscope (Philips, XL-30S, FEG) and X-ray diffractometer (Philips, X`pert Pro), respectively.

3.3. Results and Discussion

3.3.1. Cation Dissolution in PMN/Water System

In the study, cation dissolution from the PMN surface was examined primarily as a function of solution pH. Figure 3.5 and Table 3.1 show the amount of cation concentration in solution after 24 hours stirring. The graph depicts that the lead and magnesium ion concentrations increases with decreasing pH. Especially the Pb^{+2} concentration increases dramatically in the acidic region and reaches 12,620 ppm at pH 2. Though the Mg^{+2} dissolution was also pH dependent the dissolution rate was almost an order of magnitude smaller compared to that observed with Pb^{+2} at low pH values. But it was observed that Mg^{+2} dissolution is significant at neutral pH values. On the other hand, Nb^{+5} showed rather low dissolution under the same conditions. The Nb^{+5} concentrations in the acidic region were below the detection limit of the analyzing device. Therefore, it is concluded that PMN behaves both like as an insoluble oxide and a partially soluble inorganic salt. Insoluble oxide can be approximated to the Nb_2O_5 component, whereas the salt is in the form of PbO and MgO in the PMN structure.

Previously, Neubrand et al. investigated the dissolution of Ba^{+2} ions from the barium titanate in water. They found that the amount of barium leached increases as the pH decreases. In fact the increase in the dissolved metal ion concentration with decreasing pH considered to be a general behavior for most perovkites in water (Neubrand et al. 2000). However, in Pb-Mg-Nb-H_2O system both A site cations Pb^{+2} and Mg^{+2} are soluble that makes the surface chemistry more complex compared to other perovskites such as $BaTiO_3$ and PZT.

Table 3.1. Cation concentration in PMN Suspensions at room temperature.

pH	Cation Concentration (ppm)		
	Pb	**Mg**	**Nb**
2	12,620	844	-
4	2228	407	-
6	90	300	0.0013
8	80	249	0.0044
10	54.82	31.17	0.005

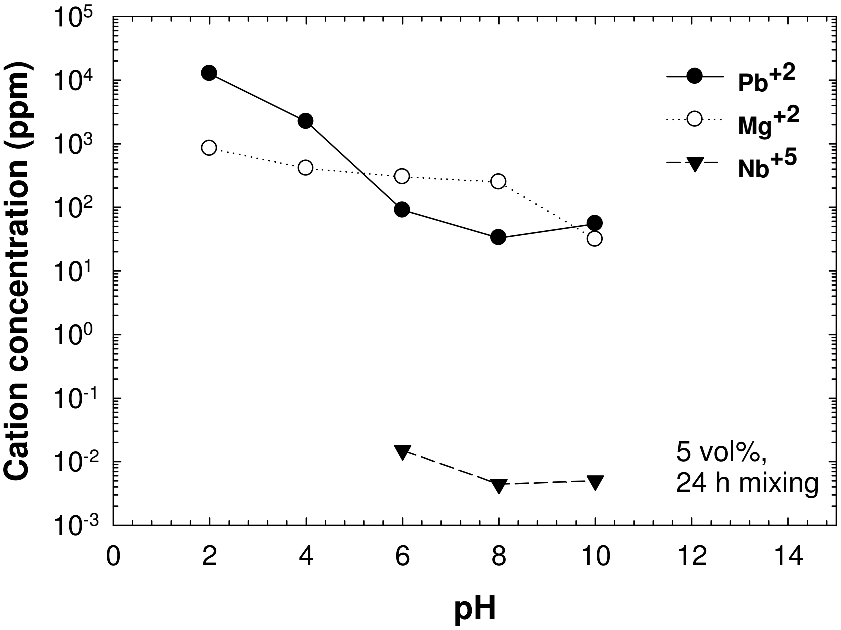

Figure 3.5. Cation concentration in PMN suspensions (5 vol%) after 24 hours mixing as a function of pH.

Cation dissolution from PMN surface was also investigated at some other solid concentrations namely 0.1, 1 and 10 vol%. Results are given in Figures 3.6 to 3.8. According to Figures 3.6 and 3.7, Pb^{+2} ion concentration increases dramatically starting from pH 6 for low solids loading suspensions. However, the increase in cation concentration for higher solids loading suspensions was rather low. The dissolution percentage of Pb^{+2} and Mg^{+2} as a function of solid concentrations is drawn in Figure 3.9.

Results showed that cation dissolution from PMN surface increases as the solid concentration decreases. Previously, Paik and Hackley investigated the dissolution of barium titanate in water as a function of solid concentration and obtained a similar result. In barium titanate/water system, Ba^{+2} ions dissolve from the surface, like in the case of PMN (Paik and Hackley 2000, Lopez et al. 1997).

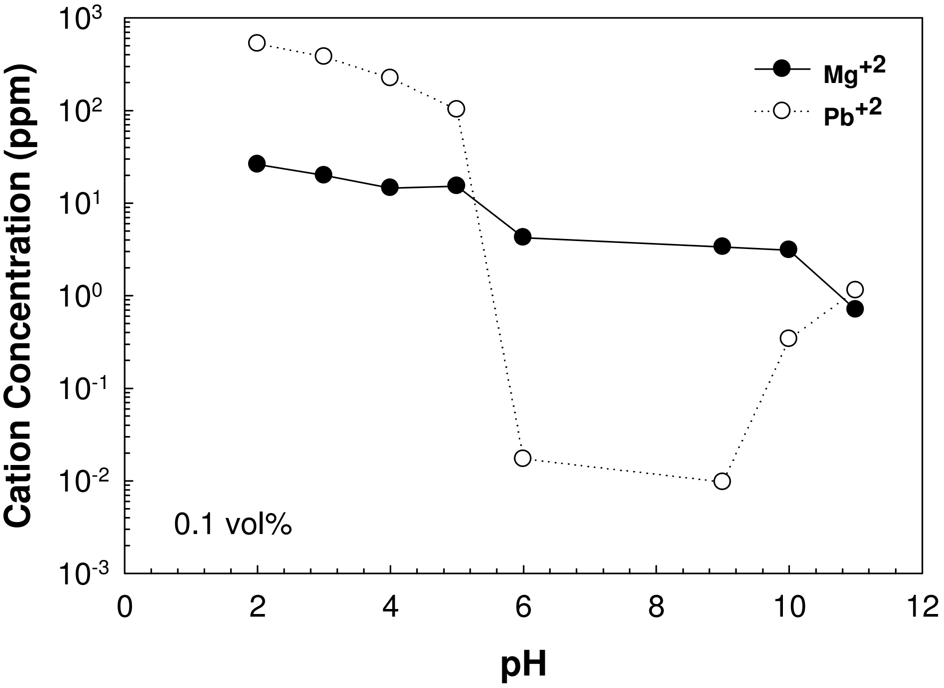

Figure 3.6. Cation concentrations in 0.1 vol % PMN suspensions as a function of pH.

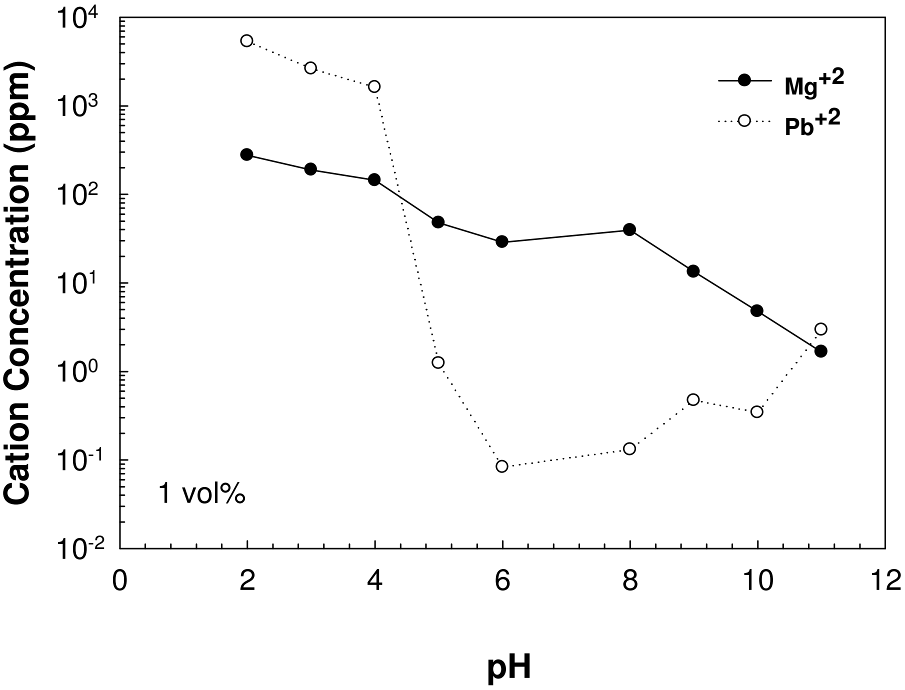

Figure 3.7. Cation concentrations in 1 vol % PMN suspensions as a function of pH.

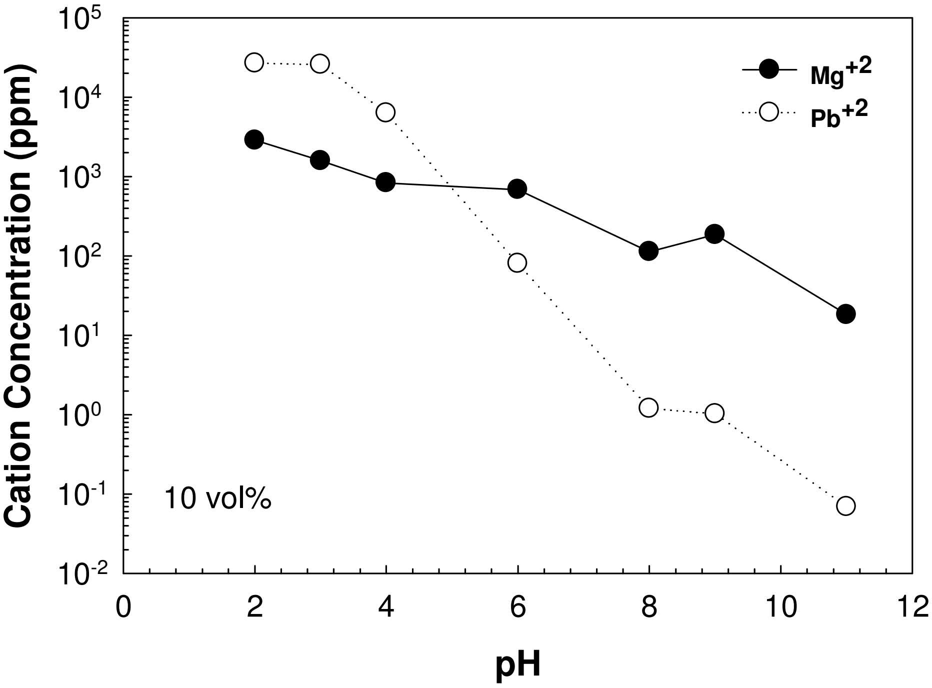

Figure 3.8. Cation concentrations in 10 vol % PMN suspensions as a function of pH.

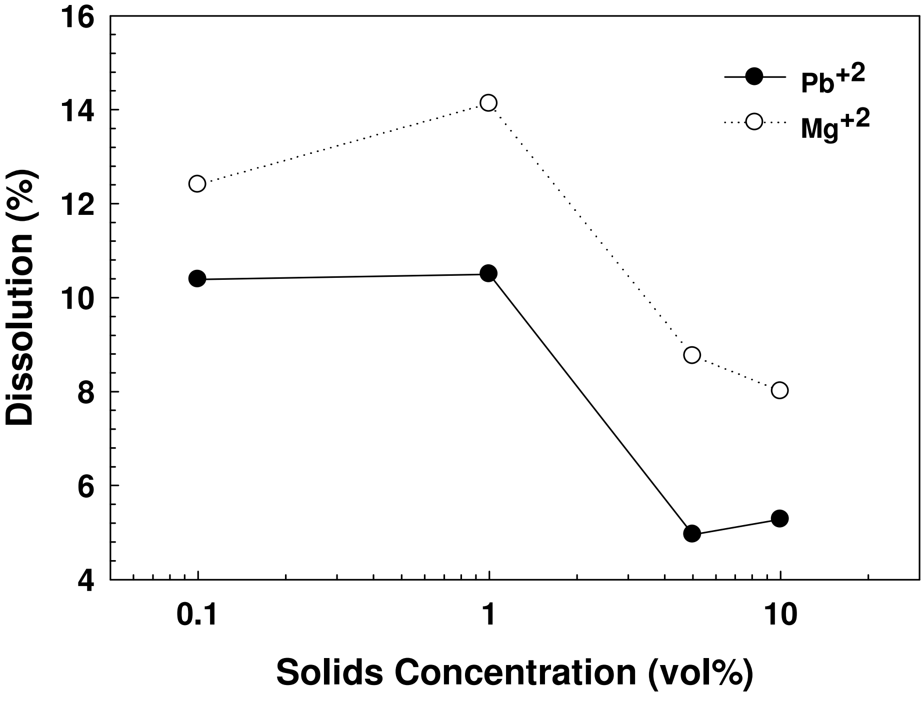

Figure 3.9. Cation dissolution from PMN surface as a function of solids concentration, pH 2.

Paik and Hackley modeled the dissolution behaviour of $BaTiO_3$/water system using following equations:

$$h = (2Dt)^{1/2} \tag{3.6}$$

where h is the growth of the leached ion layer thickness over the time (t), D is the diffusion coefficient for the leached ions. Ratio of the total reactive surface area to the solution volume (S/V) can be written as:

$$S/V = A.\rho \frac{\phi}{1-\phi} \tag{3.7}$$

where ρ is the bulk solid density (g/cm^3), A is the specific surface area (cm^2/g) and ϕ is the volume fraction of the solid. Diffusion coefficient can be given by:

$$\sqrt{D} = \frac{2k}{(C_1 - C_2)S/V} \tag{3.8}$$

where C_1-C_2 is the concentration difference across the dissolved ion layer. If we insert diffusion coefficient to the Equation (3.6), following equation can be obtained (assume $C_1 >> C_2$) (Paik and Hackley 2000):

$$\frac{h_1}{h_2} = \frac{(S/V)_2}{(S/V)_1} = \frac{\phi_2}{\phi_1}\frac{1-\phi_1}{1-\phi_2} \tag{3.9}$$

Figure 3.10 shows schematically the reactive surface layer grown on a solid particle.

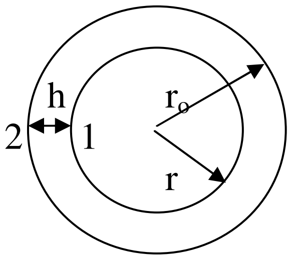

Figure 3.10. Schematic presentations the formation of a dissolved surface layer on a particle.

According to this model, surface layer on PMN particles dispersed in acidic environment will be thicker in dilute suspensions compared to the concentrated suspensions because the rate of dissolution in concentrated suspensions is inhibited by the high S/V ratio.

Figure 3.11 displays the kinetics of the Pb^{+2} and Mg^{+2} dissolution at pH 6 and 9. Results show that the dissolution rate of both cations were nearly constant at pH 9 within the time period studied. However, dissolution rates were quite different at pH 6. The lead concentration reaches considerable levels immediately after the powder addition and decreases gradually with time. The decrease in the Pb^{+2} ion concentration in solution phase may be attributed to the re-adsorption of the free Pb^{+2} ions onto the hydrated PMN surface. As it is described in previous figures, at pH 6 dissolution of Pb^{+2} and Mg^{+2} ions were higher compared to the dissolution rate at pH 9. On the other hand, Mg^{+2} ion concentration gradually increases with time at pH 6 and reaches a maximum after 24 hours, showing a decrease for longer contact times. Accordingly, it is possible to conclude that Mg^{+2} and Pb^{+2} ions show different behavior after they dissolve from the PMN surface. Mg^{+2} and Pb^{+2} ions possibly form complexes with the –OH ions in water.

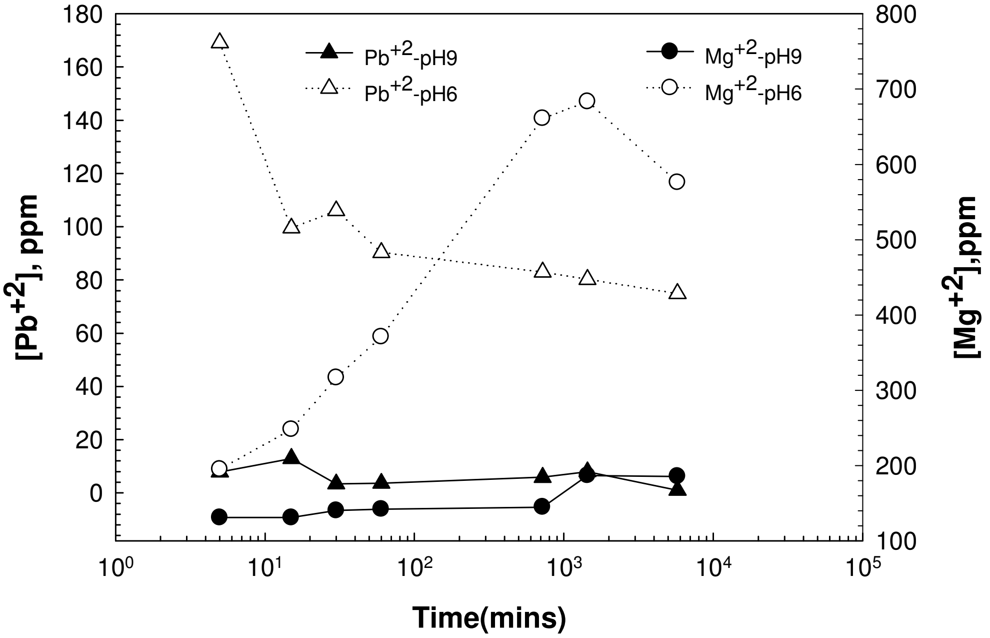

Figure 3.11. Dissolved Pb^{+2} and Mg^{+2} concentrations as a function of stirring time.

Figure 3.12 shows the variation in the natural pH of the PMN suspension (5 vol %) as a function of stirring time. An increase was observed in pH from 9.5 to 10.9

in 2 hours. Similarly Figure 3.13 displays the variation in pH of PMN suspensions after initial pH adjustments. The increase in the pH of the PMN suspensions from pH 6 to pH 8.6 as a function time may be attributed to the complex formation between the cations (especially Pb^{+2}) dissolved from PMN surface and the –OH ions in water. Figures 3.14 and 3.15 demonstrate the formation pH of various lead and magnesium hydroxides. According to this picture, formation of PbOH or $Pb_4(OH)_4^{+4}$ may responsible for the rapid increase in pH of the PMN suspension (pH $_{\text{initial}}$: 6).

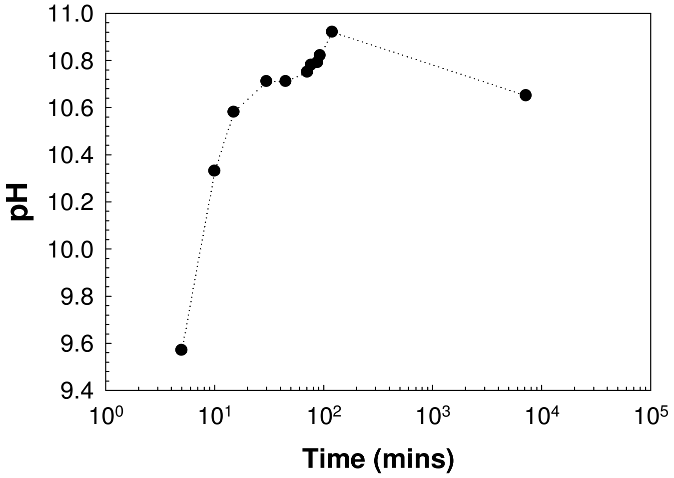

Figure 3.12. The pH of PMN suspension (5 vol%) as a function of stirring time. pH_{water}: 6.63.

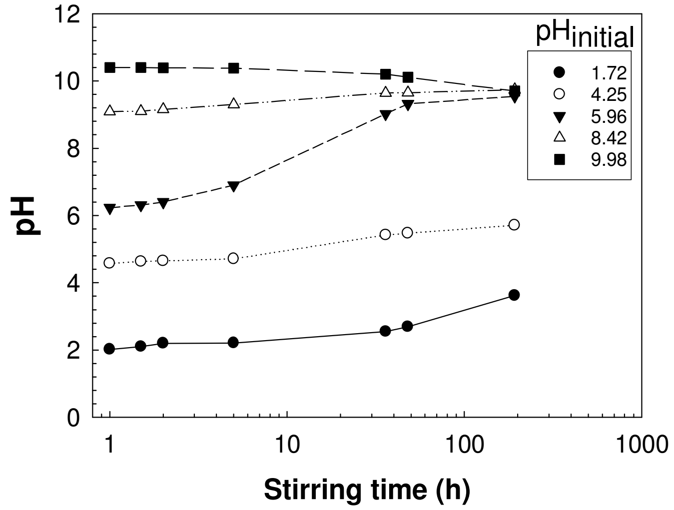

Figure 3.13. Variation in pH of PMN suspensions (1 vol%) as a function of stirring time.

The Figure 3.13 also shows that the suspensions most probably consume the protons from solution. This may be attributed to the adsorption of protons from solution onto the PMN surface which should yield a positive surface charge at these low pH values. Such increase in the pH due to consumption of protons must be associated by the cation dissolution from the PMN surface at the acidic pH range. Such effect would be more pronounced with increasing solids content.

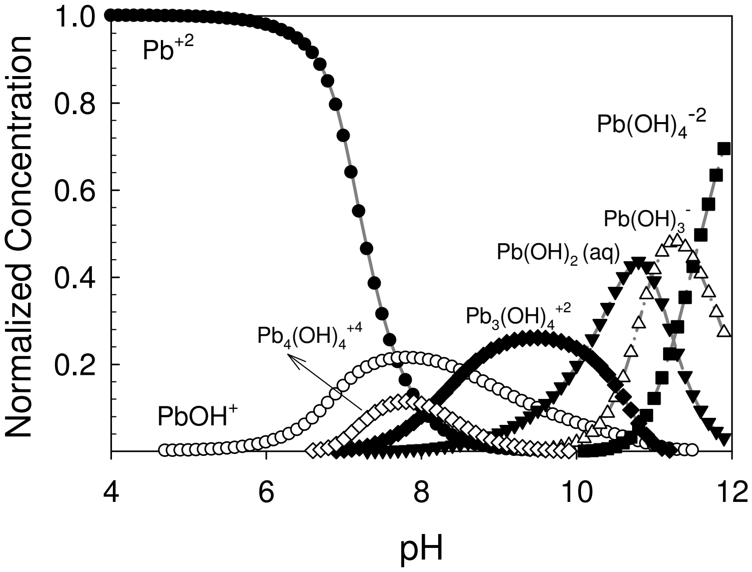

Figure 3.14. Normalized concentrations of various lead compounds as a function of suspension pH, obtained by Visual MINTEQ ver. 2.12.

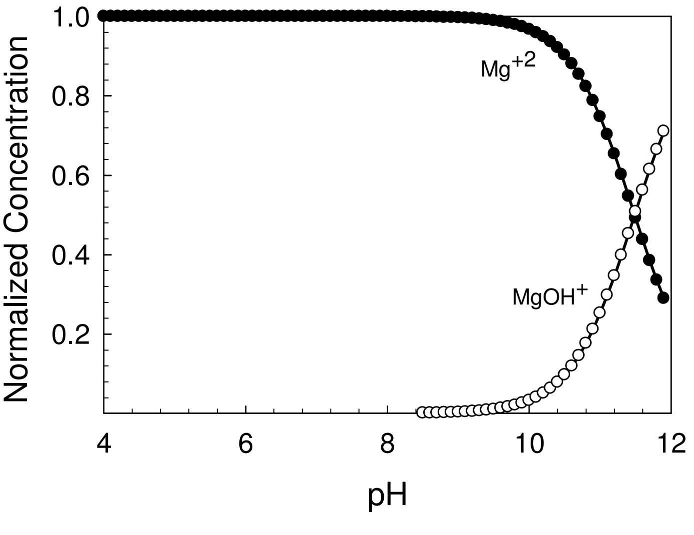

Figure 3.15. Normalized concentration of magnesium hydroxide as a function of suspension pH, obtained by Visual MINTEQ ver. 2.12.

Adair and co-workers reported the dissolution types dictated by the ceramic materials and solution pH. According to their study, type 1 dissolution describes the uniform surface decomposition of single component metal oxides such as alumina or silica. In contrast, types 2, 3, and 4 dissolutions are typical of thermodynamically unstable systems (see Figure 3.16) (Adair et al. 2006).

The most multi-component metal oxides such as barium titanate generally follow incongruent type dissolution but the dissolution mechanism strongly depends on the pH. In the current study similar to barium titanate system in absence of any surface carbonates it is possible to assume that the Pb-Mg-Nb-H_2O system undergoes incongruent dissolution with selective leaching and form a protective passive film on the solid surface in the pH range between pH 2 to 10. However, unlike to the barium titanate in PMN system niobium oxide reach matrix does not totally dissolve below pH 2. Because measurements showed that solubility of Nb^{+5} very low compared to other cations in PMN and increases with increasing pH.

The dissolution process for PMN can be explained based on the previous study of Paik and Hackley for barium titanate system. Accordingly, the dissolution process can be divided into three stages. First, incongruent dissolution in the first few minutes after initial contact with the acidic solution followed by a mass transport limited second step. In this step Pb^{+2} and Mg^{+2} must diffuse out through a growing reactive surface layer. In the final stage, dissolution slows considerably and following possibilities may arise: (1) a steady-state equilibrium concentration is reached, (2) a thick the depletion layer forms and leads to passivation or (3) the particles are completely converted to Nb^{+5} rich phase (Paik and Hackley 2000, Paik et al. 2002, Paik et al. 2003).

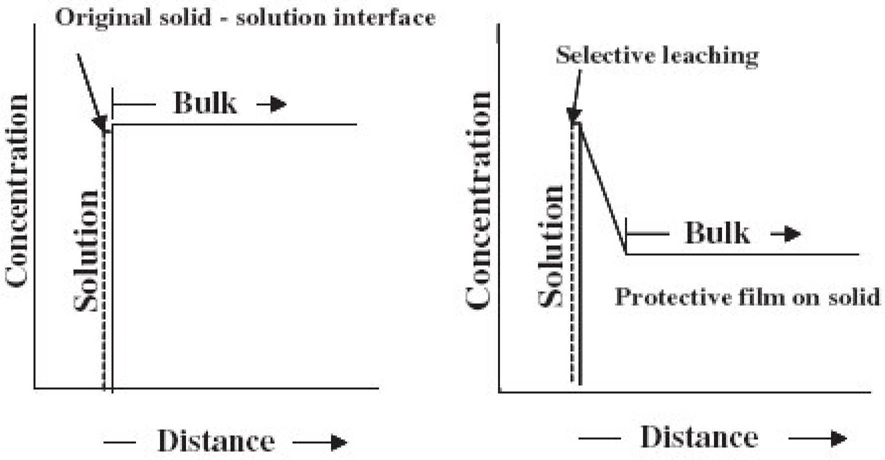

a) **Type I** **b) Type II**

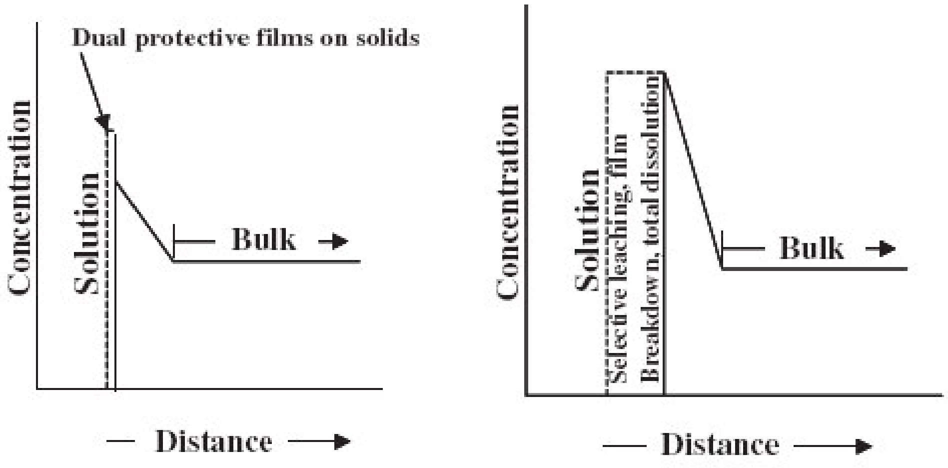

c) Type III **d) Type IV**

Figure 3.16. Dissolution types observed in ceramic materials.
(Source: Adair et al. 2006)

3.3.2. Aging Behavior of PMN in Water

Figure 3.17 depicts the FTIR spectra of the PMN powders aged in water at different conditions. In the figure the vibrational band over the range of 3200-3700 cm^{-1} indicates the –OH groups in the sample. The band over the range of 500-900 cm^{-1} corresponding the metal oxygen bonds (Beng et al. 1999). According to the spectra, there is no surface carbonate formation in samples treated in water.

Wang et al. analyzed the DRIFT spectra of the $BaTiO_3$ and PZT powders after aging in water for several days. They observed surface carbonate formation which is shown at 1450 cm^{-1} and 1400 cm^{-1} for BT and PZT, respectively (Wang et al. 2000).

Surface carbonate formation is an important problem faced during the aging of perovskites in water.

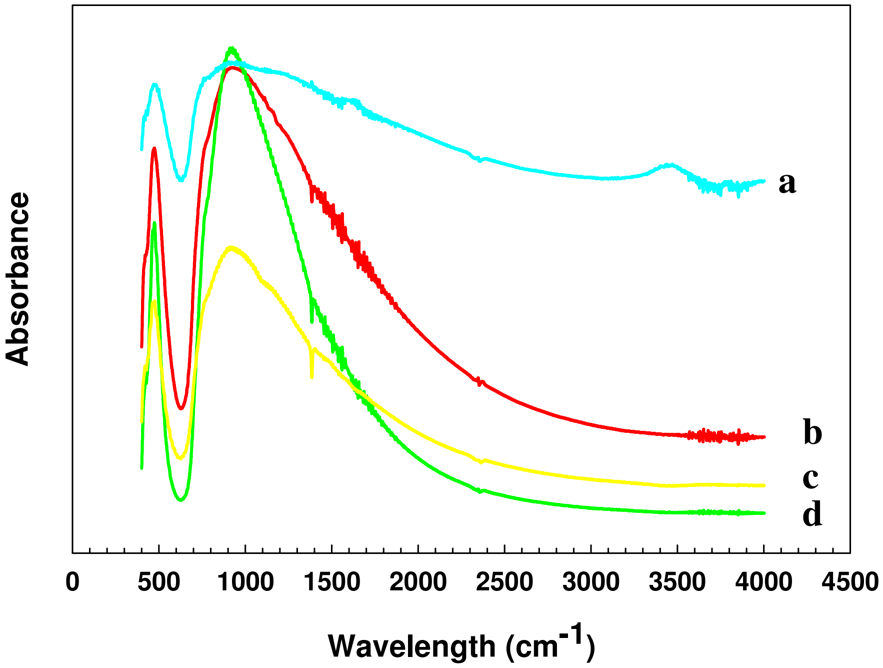

Figure 3.17. FTIR spectra of PMN powders aged in water, 10 vol% a) no water treatment b) 24h, pH 6 c) 4 days pH 9 d) 24h, pH 9.

It is also known that local chemical inhomogeneties play an important role in abnormal grain growth in the perovskite structures exposed to the aqueous environment. Additionally, formation of broad distribution of the grain sizes may affect the desirable electric properties (Adair et al. 2006). Figures 3.18 and 3.19 show the SEM micrograph and XRD spectra of the PMN powders aged in water at different conditions followed by calcination at 1100 °C for 2 hours. It is clear from these figures that there is no significant difference between the microstructures of the powder aged in water at pH 9 for 4 days and as-received powder. However, XRD pattern reveals that the formation of a small pyrochlore peak in the powder aged for 24 hours at pH 6. As it is discussed in previous section, starting form pH 6, especially the Pb^{+2} dissolution from PMN surface reaches considerable levels. This may cause some deviation from the exact stoichiometry and formation of pyrochlore.

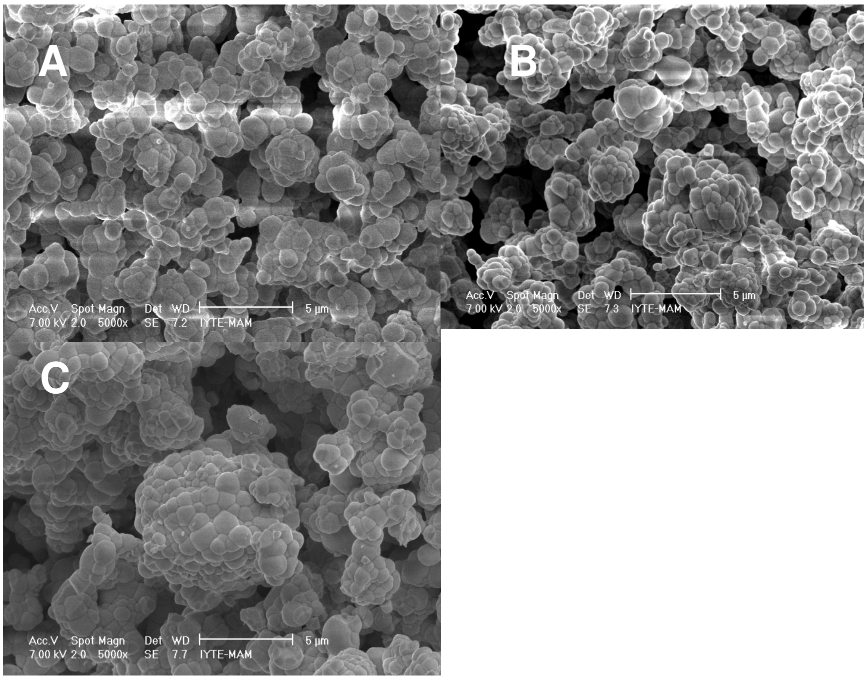

Figure 3.18. SEM micrographs of the PMN powders aged in water (10 vol%) followed by a calcination at 1100 ºC for 2 hours. a) no water treatment b) 4 days mixing at pH 9 c) 24 hours mixing at pH 6.

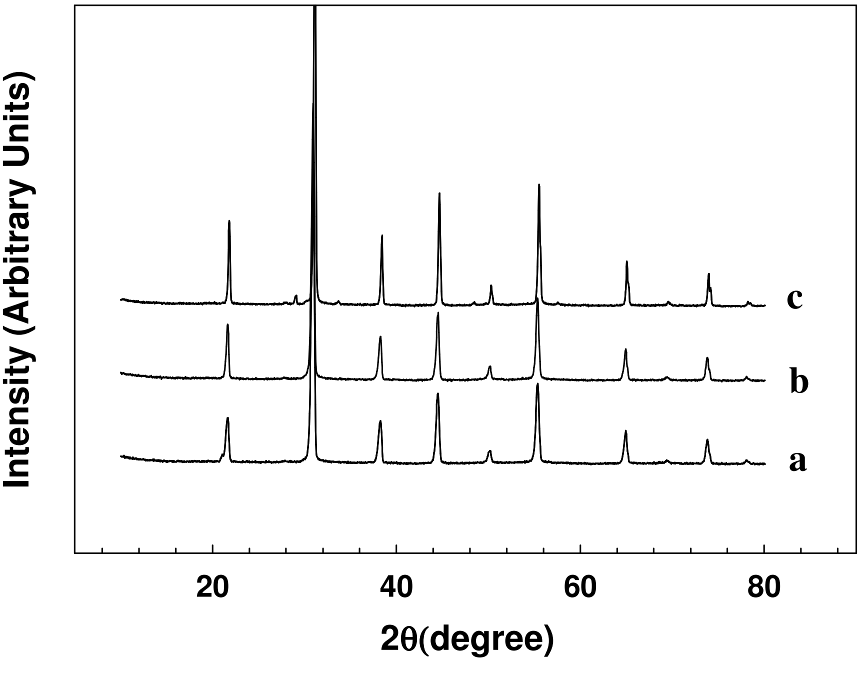

Figure 3.19. XRD diagrams of the PMN powders treated in water (10 vol %) followed by calcination at 1100 ºC a) no water treatment b) 4 days mixing, pH 9 c) 1 day mixing pH 6.

3.3.3. The Isoelectric Point of PMN

The Figures 3.20 and 3.21 show the variation in the IEP of PMN as a function of solids loading obtained by micro-electrophoresis and electroacustic methods, respectively. Table 3.2 summarizes the IEP values obtained by two different methods. Although slight differences were observed in the IEP in general values obtained using both methods were in good agreement with each other. The agreement between micro-electrophoresis and electrokinetic sonic amplitude techniques at the overlap solids concentration of 0.1% serves to validate the methodology. As it was described in the previous section electrophoresis method requires the use of extremely dilute suspensions, in contrast zeta potential of concentrated suspensions can be measured using electroacustic method. However, in the current study samples for the electrophoresis technique were prepared by dilution from concentrated suspension. Therefore, IEP value, reflect only the solid-liquid interfacial chemistry and should be independent of the technique used to measure it. Using both techniques, it was found that IEP increased with increasing solids concentration.

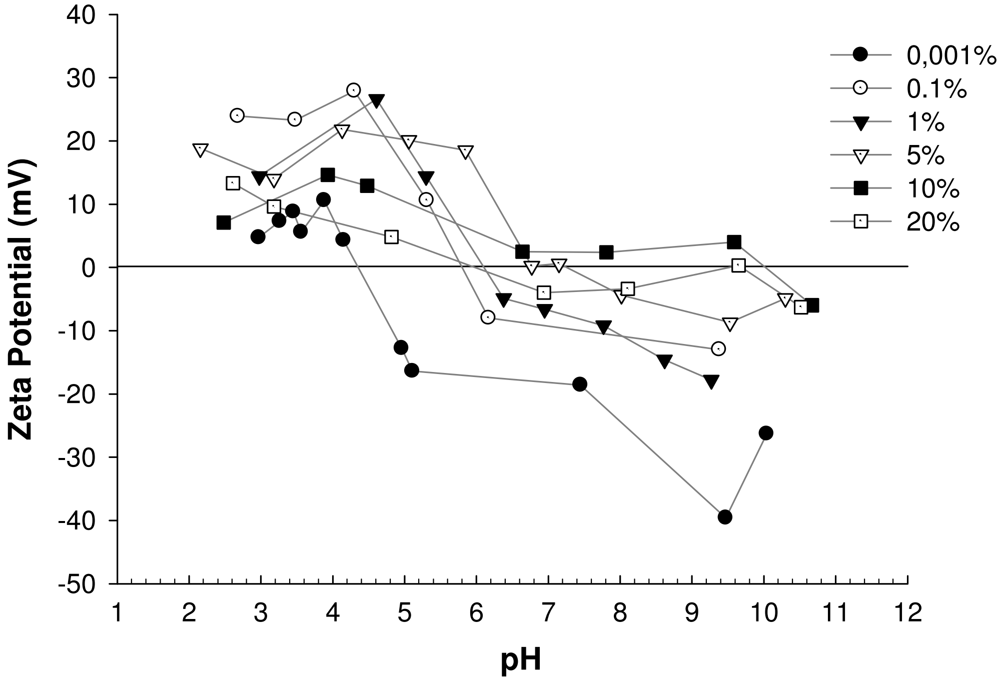

Figure 3.20. Zeta potential of PMN suspensions as a function of pH and solids concentration (by electrophoresis technique).

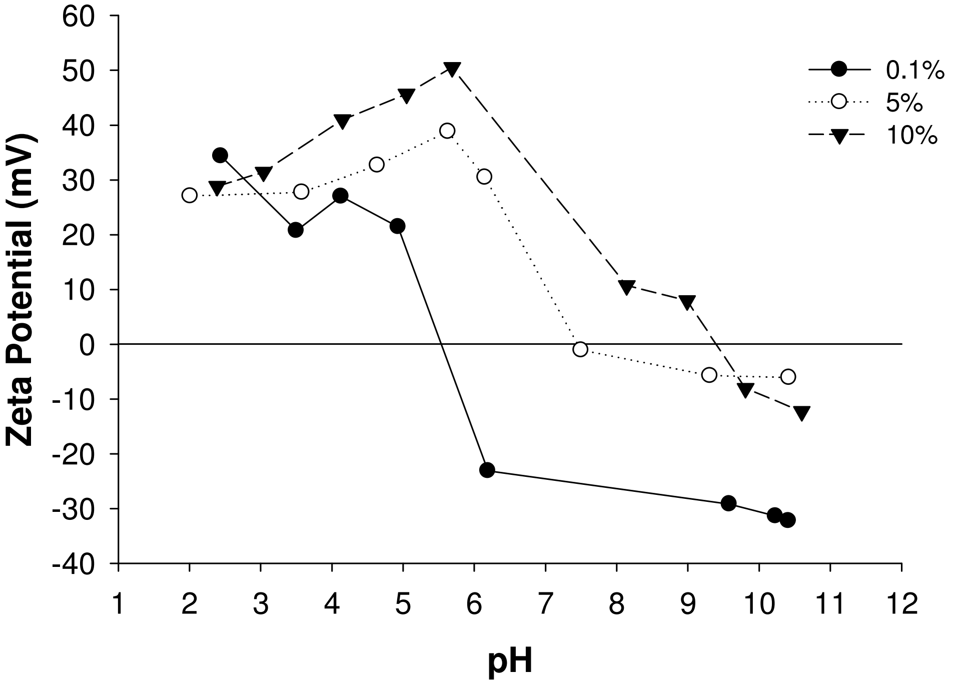

Figure 3.21. Zeta potential of PMN suspensions as a function of pH and solids concentrations (by electroacoustic technique).

Table 3.2. IEP of PMN suspensions at different solids concentrations.

	IEP	
Solids Concentration (vol%)	Microelectrophoresis	Electrokinetic sonic amplitude (ESA)
0.001	4.4	-
0.1	5.8	5.6
1	6.1	-
5	7.1	7.5
10	10	9.6
20	9.7	-

The shift in the IEP of PMN to lower pH values at low solid concentrations can be explained based on the solubility considerations. When the PMN is suspended in water a surface layer will be developed around the particle due to ion dissolution. Specifically, the surface layer forms because of mass-transport limited incongruent dissolution (Paik and Hackley 2000). Without the mass transport limitation, the entire particle would be converted to the Nb oxide at sufficiently low pH and low solids concentration. The thickness of that layer is determined by both the pH to which it is subjected and the surface-to-volume ratio of the solid phase. A lower pH increases the dissolution rate and also accommodates a higher solubility limit for the dissolving A-type cations. Essentially, an Nb oxide-rich corona develops around a core of unmodified perovskite material. The thickness and level of depletion of A-type cations in this corona determines the "acidity" of the particles. That is, the greater the depletion and the thicker the depletion layer, the lower the IEP, until the IEP approaches that of the more acidic Nb oxide. The solids concentration effect is due to the fact that at higher solids, more particle surface is available for dissolution to occur (i.e., a higher S/V ratio, for a given particle size). This means that the pH-determined solubility limit of the dissolving cations will be reached more quickly and with less depletion of cations from any given particle thus the apparent IEP will not shift as much from the native material. At lower solids, the depletion zone of all particles in the suspension must increase in order to reach the same solubility limit for a given pH, since the S/V ratio within the suspension is now reduced. This results in a greater (acidic) shift in the IEP.

As Pb^{+2} and Mg^{+2} ions are depleted from the PMN surface as a result of incongruent dissolution the surface begin to resemble the Nb_2O_5. The IEP of oxides that constitute the PMN were measured and results are shown in Figure 3.22. In the current study the IEP of native niobium oxide is determined at pH 2.6. Previously, Kosmulski have been reported the IEP of niobium oxide at pH 4.5 (Kosmulski 1997). Therefore, the shift in the IEP of PMN suspensions to lower pH values may also be explained by the formation of an Nb_2O_5 rich structure at low solids concentrations. Measured isoelectric points of native oxides that constitute the PMN and the values reported in the literature are tabulated in Table 3.3.

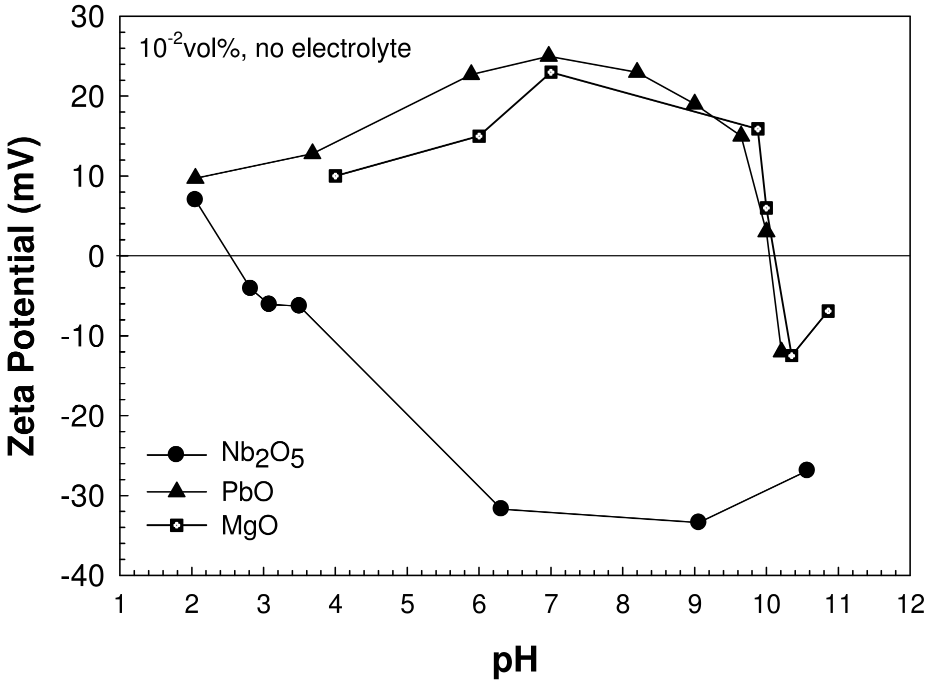

Figure 3.22. Isoelectric points of individual oxides that constitute the PMN structure.

Table 3.3. Isoelectric point of individual oxides in the composition of PMN.

Oxides	IEP	Reference
PbO	10 10.1	 This study
MgO	12 10-12 10.2	Lewis 2000 Bourikas 2005 This study
$Mg(OH)_2$	10	Luo 2005
Nb_2O_5	2.6-2.8 4.1 2.6	Luo 2005 Kosmulski 1997 This study

Mobility measurements were performed using Matec ESA 9800 to investigate the change in dynamic mobility of PMN suspensions as a function of time. Figure 3.23 demonstrates the mobility curves for the suspension prepared at 0.1 vol % at pH 8 and pH 2. Measurements were also made at 5 vol% to understand the effects of solids concentration on the dynamic mobility. It is clear that, the mobility increases with time for the dilute suspension (0.1 vol %) at pH 2. On the other hand, the mobility of the PMN suspension at 5 vol% was nearly constant through the measurement. This behavior can be attributed to the higher dissolution rate of lead and magnesium ions in dilute suspension compared to the more concentrated suspension.

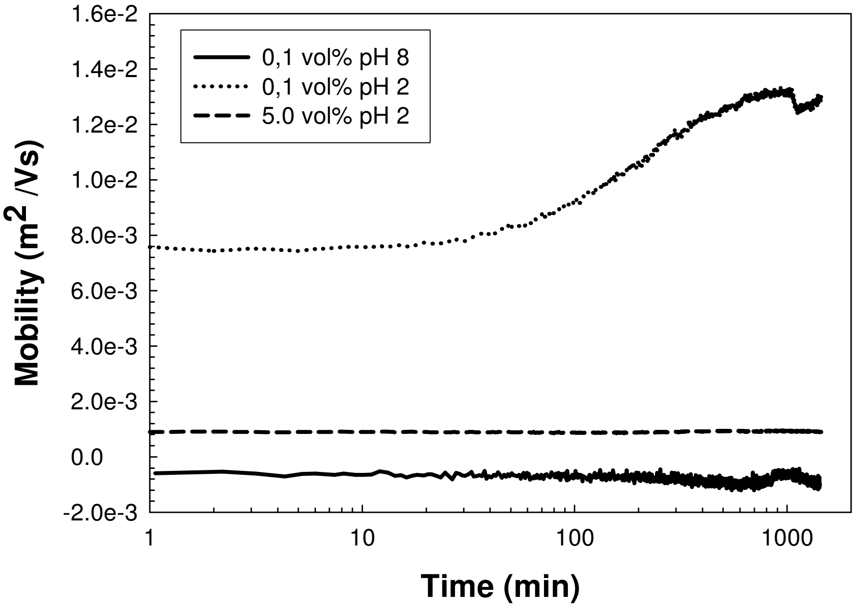

Figure 3.23. Dynamic mobility of PMN suspensions as a function of stirring time.

3.3.4. Effect of Electrolytes on the Isoelectric Point

It is known that simple inorganic electrolytes can have a significant impact on zeta potential. The effect depends on the relative valence of the ions and on their concentration. The influence of background electrolytes on the electrokinetic behaviour of PMN suspensions were investigated using KNO_3, KCl, and $MgCl_2$ as a function of electrolyte concentration. Figures 3.24 and 3.25 display the effect of KNO_3 and $MgCl_2$ on the IEP of PMN suspensions, respectively. The IEP of PMN shows no significant change in the presence of KNO_3 but shifts to higher pH values in the case of $MgCl_2$ depending on the electrolyte concentration. At the concentration of 10^{-3} M $MgCl_2$, IEP remains around pH 7 but at higher concentrations of $MgCl_2$ an inflection point develops and the IEP disappears and zeta potential becomes positive over pH range 2-11. This may be attributed to the deposition of the Mg^{+2} ions to the PMN surface which makes the surface positive. In other words, when the $MgCl_2$ concentration is increased, the zeta potential of PMN becomes positive due to specific adsorption of Mg^{+2} ions.

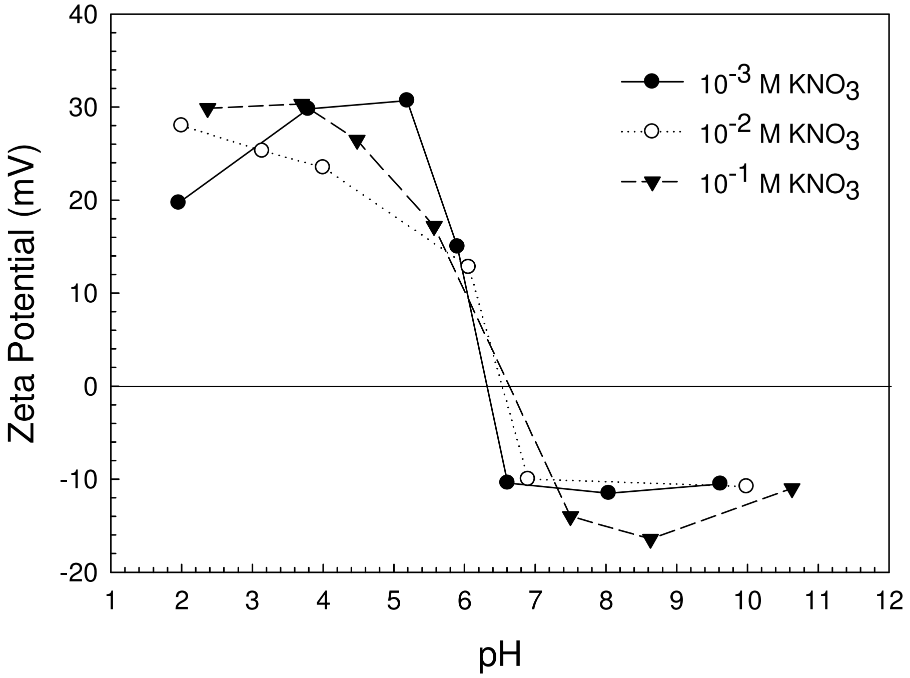

Figure 3.24. Effect of KNO_3 on the IEP of PMN suspensions at 1 vol %.

It is also known that adsorption of metal ions to the hydrous oxide surfaces may inhibit the dissolution of the oxide powder. Surface complex formation of a metal ion to the oxygen donor atoms of the functional groups of a hydrous oxide is in principle similar to complex formation in homogeneous solution (Stumm 1992). Lopez et al. investigated the effect of Ba^{+2} additions on the zeta potential of $BaTiO_3$ suspensions. They observed a marked shift of the IEP towards higher pH values with increasing Ba^{+2} concentrations. Additionally, the zeta potential values at pH higher than the IEP were significantly less negative than those of suspensions without added Ba^{+2} (Lopez et al. 2000).

On the other hand it was interesting to observe that in the presence of KCl the surface charge of the PMN powders was negative at high electrolyte concentrations (Figure 3.26). In that case it is possible to consider the effect of Cl^{-1} ions in the system. Kosmulski investigasted the chloride adsorption onto alumina as a function of pH. He found that adsorption of chloride on to oxide surface at constant pH and ionic strength is independent of temperature (Kosmulski 1993). Therefore, adsorption of Cl^- ions onto PMN is a possible explanation for the behavior observed in Figure 3.26.

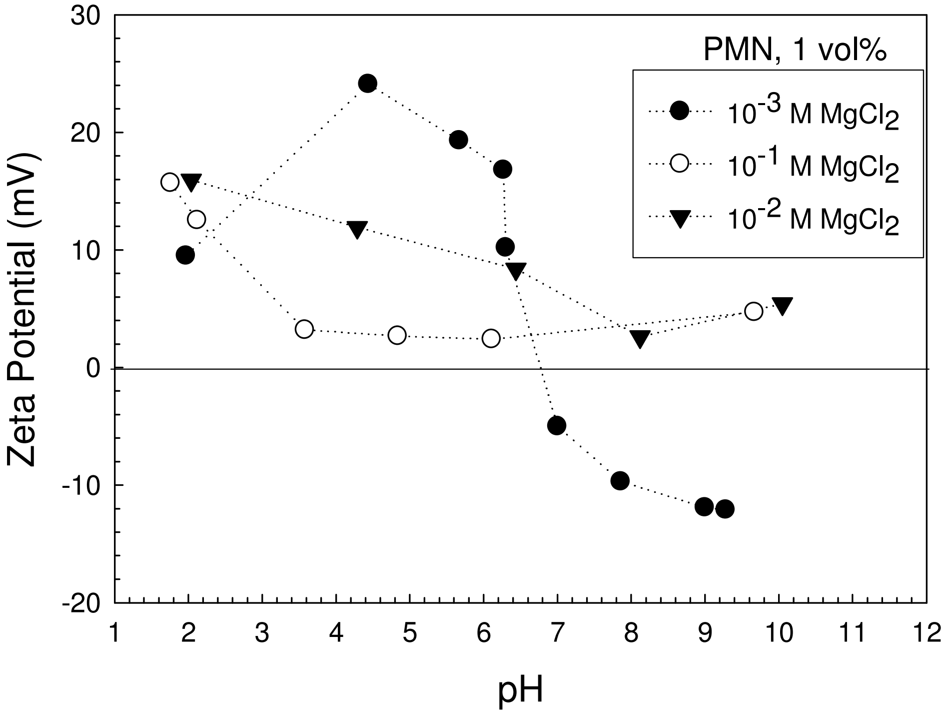

Figure 3.25. Effect of $MgCl_2$ on the IEP of PMN suspensions at 1 vol %.

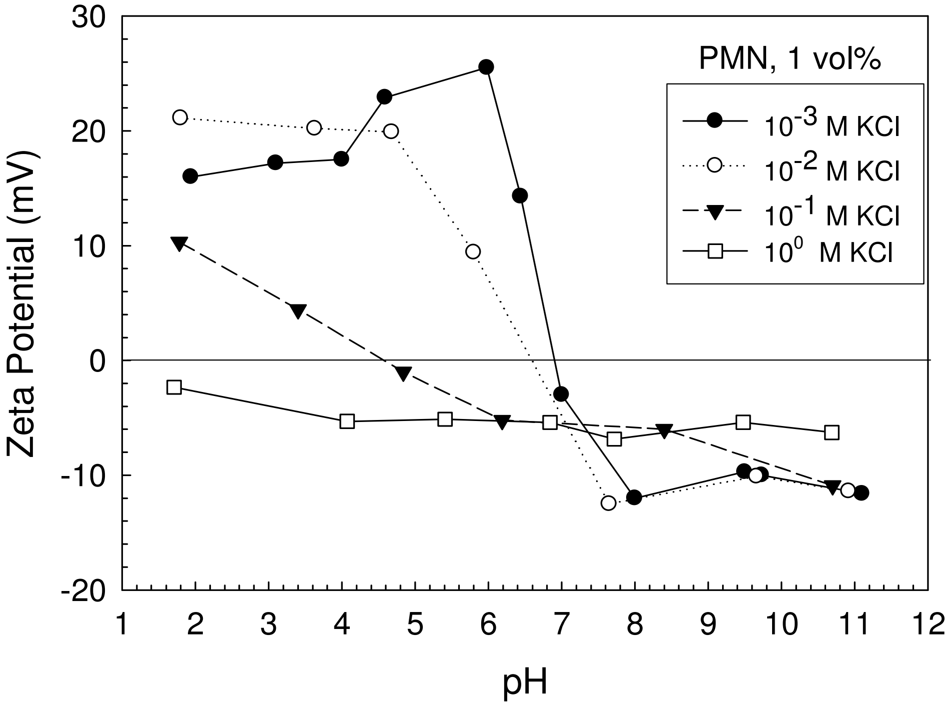

Figure 3.26. Effect of KCl on the IEP of PMN suspensions at 1 vol %.

CHAPTER 4

PAA/PEO COMB POLYMER EFFECTS ON THE STABILITY OF LEAD MAGNESIUM NIOBATE SUSPENSIONS

4.1. Introduction

There is a considerable interest for the colloidal processing of perovskite ceramic materials in recent years because of their applications in electrical and electronic devices (Adair et al. 2006, Li and Jean 2002, Windlass et al. 2001). Lead magnesium niobate is an important perovskite material in this area because of its high dielectric constant and electrostrictive properties. It has some applications as the multilayer ceramic capacitors (MLCC), actuators, transducers and micropositioning devices (Tzou et al. 2004, Moulson and Herbert 1990). However, colloidal properties of aqueous PMN suspensions have not been investigated yet. Therefore, it is essential to study the behavior of the PMN powders in liquid medium and also prepare highly stable PMN suspensions which is crucial in wet shaping processes.

Colloidal processing involves manipulation and control of the interparticle forces in the precursor dispersion before and during forming (Shqau 2004, Reed 1995). Colloidal processing of perovskite ceramics is challenging mostly due to ion dissolution from the surface of the ceramic oxide. In the case of PMN we observed that Pb^{+2} and Mg^{+2} ion dissolution significantly increases with decreasing pH and causes build up of these ions in the solution (see Chapter 3). This behavior limits the pH range of the suspensions and the dispersant selection to prepare stable suspensions.

Widely used polyelectrolyte dispersants such as polyacrylic acid (PAA) contain ionizable carboxylic acid groups along their backbone (Cesarano and Aksay 1988a, Hackley 1997). These groups dissociate and form negatively charged carboxylate groups at high pH. Furthermore, PAA dispersant systems are less effective in high ionic strength suspensions especially those containing multivalent ions (Kirby et al. 2004). Because multivalent ions interfere with the electrostatic repulsive barier and cause flocculation. Therefore, there is need to discover novel dispersants that can reduce flocculation for suspensions containing multivalent ions.

In this study it was intended to investigate the colloidal properties PMN powders in liquid medium and investigate the effect of polyacrylic acid/polyethylene oxide (PAA/PEO) comb polymers as novel dispersant in this system. The main purpose was to prepare highly concentrated stable suspensions, which is prequest for many wet shaping methods such as tape casting and novel 3D patterning methods such as robocasting.

The aqueous tape casting and robocasting of the PMN suspensions is the topic of the next chapters. In this chapter our concern is to investigate the effect of PAA/PEO comb polymers on the stability and flow behavior aqueous PMN suspensions. As a benchmark, further experiments were performed using pure PAA.

4.2. Experimental

4.2.1. Materials

Lead magnesium niobate, $Pb(Mg_{1/3}Nb_{2/3})O_3$ powder produced by combustion spray pyrolysis method provided by Praxair Chemicals (USA). Properties of the powder are reported in Chapter three.

Polyacrylic acid graft polyethylene oxide comb polymers PAA/PEO (W.R. Grace and Co- Connecticut, Cambridge, MA) were tested in the study as novel dispersant for the aqueous PMN suspensions. These comb polymers consists an anionic PAA backbone with ionizable carboxylic acid group (COO^-) per monomer unit and charge neutral PEO teeth grafted onto the backbone at random intervals through ester linkages. Figure 4.1 shows the chemical structure of the comb polymer used in this study. In order to investigate the effect of comb polymer architecture on the dispersion behavior PMN suspensions different PAA/PEO comb polymers were tested having different molecular weight, carboxylic acid to ester linkage ratio. For comparison purposes experiments were also performed using pure PAA (Polyscience Inc., Warrington, PA). Table 4.1 shows the properties of the comb polymers and PAA used in the study.

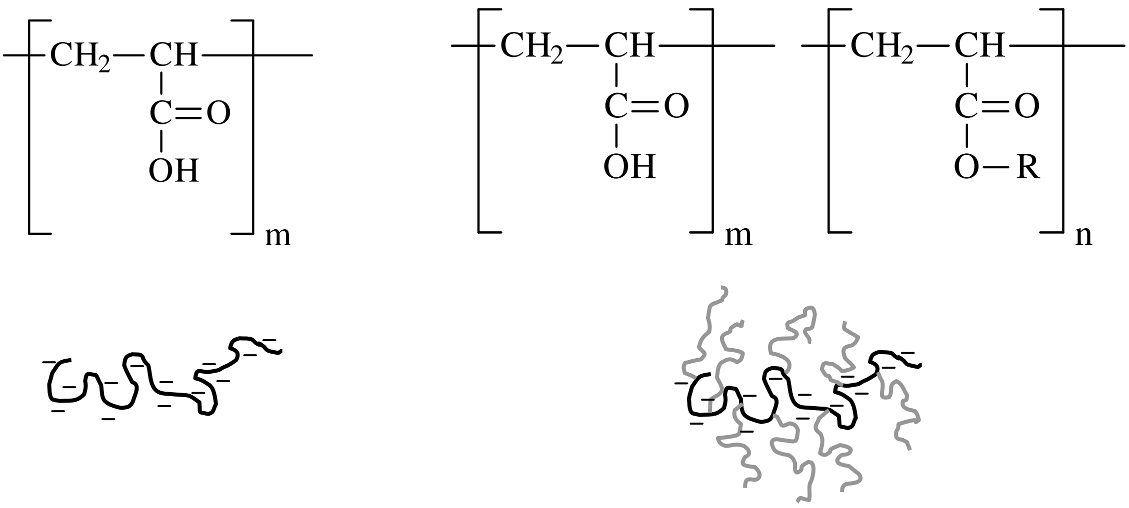

(a) (b)

Figure 4.1. Chemical structure of (a) PAA and (b) PAA/PEO comb polymers R= $(CH_2CH_2O)_x$-CH_3 , x=45 for PAA/PEO(2000).

The GPC molecular weight data of comb polymers (PAA/PEO2000 and PAA/PEO1000) shown in Table 4.1 was obtained from previous study of Kirby and Lewis 2004. In their study Mw of the comb polymers were measured using gel permeation chromatography (GPC).

Table 4.1. Properties of the PAA and PAA/PEO comb polymers used in the study.

PAA/PEO Architecture	PAA Mw (g/mole)	PEO Mw (g/mole)	Acid:ester	COO^- groups	GPC Mw (g/mole)	Theoretical Mw (g/mole)
Pure PAA	5000	-	-	69	-	5000
PAA/PEO360	5000	360	3:1	52	-	13583
PAA/PEO400	5000	400	3:1	52	-	14537
PAA/PEO1000	5000	1000	3:1	52	23360	22850
PAA/PEO1000	5000	1000	7:1	61	18040	15300
PAA/PEO2000	5000	2000	7:1	61	25800	25600

4.2.2. Method

4.2.2.1. Solution Preparation

Dilute polymer solutions were prepared by adding an appropriate amount of polymer to deionized water. The pH was adjusted using either a 0.1 *M* HNO_3 or 0.1 *M* NH_3OH solution. These polymer solutions were magnetically stirred for 0.5 h to allow for equilibration. 1M of KNO_3, KCl, $MgCl_2$, $LaCl_3$ salt solutions were prepared by dissolving KNO_3, KCl , $MgCl_2•6H_2O$ (Fisher Chemicals, Fair Lawn, NJ) and $LaCl_3$ (Fisher Chemicals, Fair Lawn, NJ) in deionized water. These salt solutions were used to vary the monovalent, divalent, or trivalent salt concentration of the polymer solutions. To investigate the complexation behaviour of Pb^{+2} with polyelectrolytes, lead (II) acetate trihydrate, ($Pb(CH_3COO)_2.3H_2O$, 99.5%, Riedel-de Haen) was used as the Pb^{+2} source. After adjusting the ionic strength, the solutions were magnetically stirred for another 0.5 h for equilibration.

4.2.2.1.1. Potentiometric Titrations

The ionization behavior of PAA and PAA/PEO comb polymers were studied by potentiometric titrations. The pH of the dilute polymer solutions (around 0.02 g/ml) were measured as a function of titrant (2.5 M NaOH) addition. The pH response was measured using a pH meter (Orion, model 250-A). From the plot of pH versus moles of base added, the steepest slope region was found. A line was drawn through this region, and the first point that falls on this line called alpha (fraction of the ionized groups).

4.2.2.1.2. Dynamic Light Scattering

Dynamic light scattering (DLS) measurements (Zetasizer 3000HS, Malvern Instruments Ltd., United Kingdom) were carried out on dilute polymer solutions, (5 mg/ml and pH 9) of varying salt concentration to determine their hydrodynamic radius (R_H) as a function of counterion concentration. A refractive index, n, of 1.53, and 1.47 was used in the scattering experiments for PAA, PAA/PEO2000, respectively. CONTIN algorithm was used for the data analysis.

The DLS unit utilizes a He-Ne laser at a wavelength of 632.8 nm with a laser power of 10 mW. The scattered light was collected at an angle of 90°. A virgin polystyrene cuvette was used for each measurement. In DLS a beam of monochromatic light passes through the sample under study. When the beam passes through the colloidal dispersion, the particles or droplets scatter some of the light. As a result of Brownian motion, neighboring particles within the illuminated zone will cause constructive and destructive interference of the scattered light. This interference gives rise to the intensity fluctuations of the scattered light which contains information about the particle motion. The time-dependent fluctuations in the scattered intensity are measured by a suitable detector such as a photomultiplier. Analysis of the time dependence of the intensity fluctuation yields the diffusion coefficient of the particles. The diffusion coefficient can then be used to calculate the hydrodynamic radius of the particles via the Stokes Einstein equation (WEB_3 2007).

4.2.2.1.3. Solution Turbidity

The turbidity of dilute polymer solutions of varying pH and salt concentration was measured by a turbidimeter (Model WTW 555, Germany). Dilute polymer solutions of varying pH and salt concentration (KNO_3, KCl, $MgCl_2$, and $LaCl_3$) were prepared as described in previous section (4.2.2.1).

Turbidity is an optical property that causes light to be scattered and absorbed rather than transmitted in straight lines through the sample. The turbidimeter used in this study measure the light scattered at an angle to the incident light beam and then relate this angle scattered light to the samples turbidity (Sadar 1998). It is a type of nephelometric turbidimeter and measure 90° scatter (see Figure 4.2). Turbidity measured in this way is stated in nephelometric turbidity units (NTU). In the current study turbidity measurements were performed using nephelometric ratio method and results were recorded in terms of NTU with ±2 of value or ± 0.01 NTU accuracy.

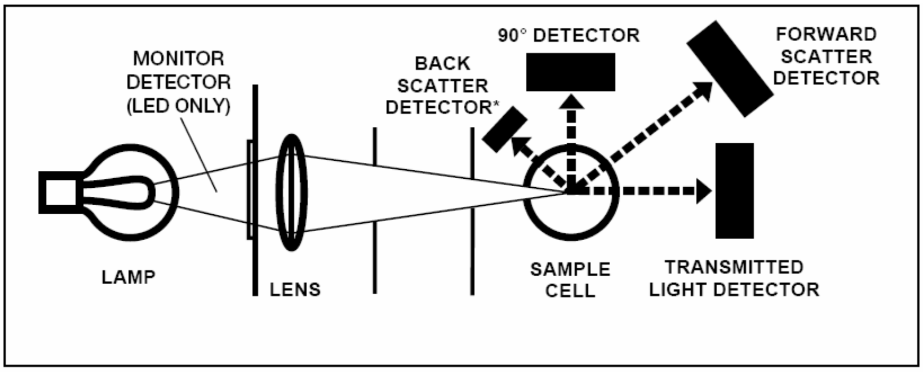

Figure 4.2. Principle used in the WTW turbidimeter.
(Source: Sadar 1998)

4.2.2.1.4. Critical Micelle Concentration

Critical micelle concentration of PAA and PAA/PEO comb polymers were determined using viscosity and surface tension measurements. For the viscosity measurements pH of the solutions were adjusted to pH 9 and solutions were allowed to stir for 30 minutes prior to measurements. Measurements were performed using a stress controlled rheometer (Bohlin CS-50) with C14 cup and bob geometry at a constant temperature of 25 ºC.

Surface Tension measurements were performed using a tensiometer (Kruss-Digital K 10ST) using Do Nouy ring method. Platinum ring geometry was heated in a flame until it glowed red before each measurement to eliminate the contamination.

4.2.2.2. Suspension Preparation

Lead magnesium niobate suspensions were prepared at different solids loading, ϕ, in presence and absence of PAA/PEO comb polymers and PAA. After PMN powder was added the stock solution of polymeric dispersant, the suspension was ultrasonicated (F550 Sonic Dismembrator, Fisher Scientific, pardubice, Czech Republic) for 2.30 minutes using a 1s on/off pulse sequence. The suspension pH was adjusted using HNO_3 and NH_4OH solutions. Suspensions were magnetically stirred for 24 hours at room temperature prior to measurements.

4.2.2.2.1. Solubility Behavior of PMN in Water

The solubility of PMN powder in aqueous medium was investigated using inductively coupled plasma mass spectrometer (ICP-MS Agilent, 7500 Series), as a function of pH and polyelectrolyte concentration. Suspensions prepared at 10 vol% according to the procedure described in the previous section were centrifuged (Rotofix 32, Hettich Zentrifugen) at 4000 rpm for 1 hour to obtain a clear supernatant. Supernatants were further filtered from 0.02 μm microfilters to eliminate any possible particles in solution. The amounts of Pb^{+2} , and Mg^{+2} in particle-free supernatants were measured by ICP-MS.

4.2.2.2.2. Zeta Potential Measurements

Zeta Potential measurements were performed using a zeta sizer (Malvern 3000 HS, UK) with aqueous dip cell apparatus whose electrodes were properly cleaned before each measurement to avoid contamination. The device uses the laser Doppler microelectrophoresis technique for the zeta potential determination. The observed velocity divided by the strength of the applied electrical field is a direct measure of the electrophoretic mobility, μ, of the particles examined. The zeta potential can then be calculated from the mobility, μ, using the Smoluchowski relation.

Since this technique allows measurements only in dilute suspensions, samples (20 vol%) were diluted prior to measurement using sedimentaion and then a small amount of sediment redispersed with the supernatant. The measurements were periodically checked against a calibration standart with a zeta potential of -50 mV(± 5).

4.2.2.2.3. Rheological Measurements

Flow behavior of PMN suspensions in the absence and presence of PAA and PAA/PEO comb polymers were studied using a stress controlled rheometer (Bohlin CS-50, Sweden). The Bohlin rheometer works with a unique drag cup motor that applies torque to the fluid sample. This torque is transmitted through the measurement geometry to the fluid sample with the help of a frictionless air bearing. The applied torque induces shearing into the sample and the resultant displacement is measured with a highly sensitive optical angular position transducer.

Double gap (24/27)-co axial cylinders geometry (see Figure 4.3) was used through the measurements to avoid settling of the PMN powders. Suspensions were prepared at 20 vol% and measurements were performed as a function of pH and dispersant concentration at 25 ºC.

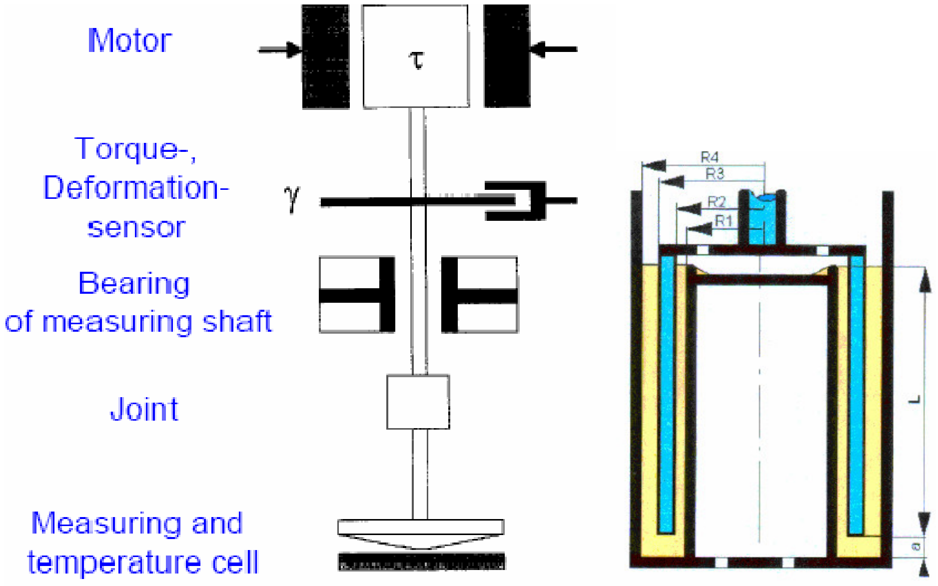

(a) **(b)**

Figure 4.3. Schematic presentation of the a) stress controlled rheometer and b) the double gap geometry used in rheological measurements (Source: WEB_3 2007).

4.2.2.2.4. Sedimentation Tests

For the sedimentation tests suspensions were poured into test tubes (diameter 0.4 cm, length 6 cm) and allowed to settle under the influence of gravity up to one month without disturbing. Suspensions were prepared at 20 vol% as described in the previous section. Digital pictures of the test tubes and the sediment height were recorded at 5 minutes intervals using a Digital Handy Camera, Sony 120X, Mini DV, DCR-TRV11.

4.2.2.2.5. Adsorption Behavior

The adsorption of PAA and PAA/PEO2000 comb polymers on PMN powder in aqueous suspensions was determined by Total Organic Carbon (TOC) analyzer (Shimadzu TOC-V CPH), which provided a quantitative measure of the non-adsorbed fraction of such species in solution. The device uses combustion (at 680 °C) catalytic oxidation method (NDIR method) to detect the organic compounds. The non-dispersive infrared (NDIR) detector consists of: light source, cell, and a detection portion (see Figure 4.4). Light passes through the cell compartment and into the detector. Depending on the concentration of carbon dioxide generated from the sample and consequently the amount of light that passes through the quartz window, the movement of the trapped carbon dioxide within the detector creates electric signals which correspond to the concentration of TOC in the sample (WEB_4 2007). Theoretically the quantity of CO_2 produced is directly proportional to the amount of organic material present in the sample.For the measurements, suspensions with a solids loading of 10 vol% were prepared by adding an appropriate amount of PMN powder to an aqueous stock solutions of PAA and comb polymer with varying concentration. Upon mixing for 24 hours, suspensions were centrifuged (Rotofix 32, Hettich) at 4000 rpm for 60 min. The supernatants were used for TOC analysis. Several aliquots of each sample were measured, and an average value was reported based on standard calibration curves.

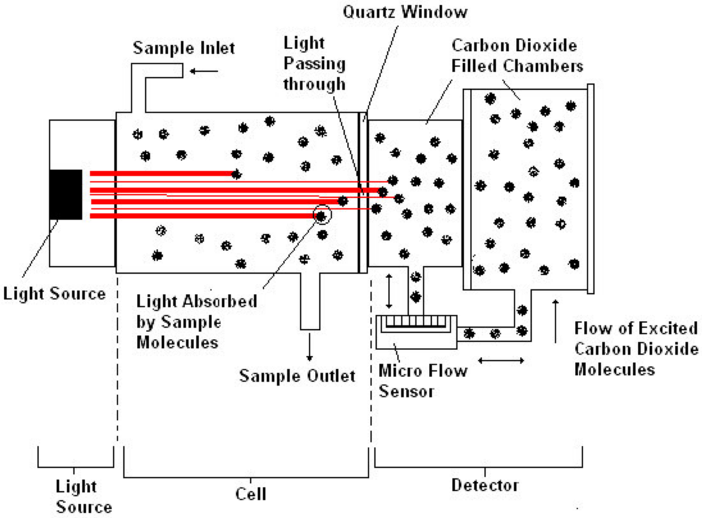

Figure 4.4. Schematic of the TOC analyzer with NDIR detector.
(Source: WEB_4 2007)

4.3. Results and Discussion

4.3.1. Solution Behavior of PAA/PEO Comb Polymers

4.3.1.1. Ionization Behaviour

The carboxylic acid groups on PAA disscociate to produce a negatively charged polymer (Hackley 1997). Dissociation of polyelectrolytes of carboxylic acid type can be expressed as:

$$R-COOH+H_2O \rightarrow R-COO^- + H_3O$$

for each carboxylic group of polyacrylic acid degree of dissociation increases with increasing pH. Figures 4.5 and 4.6 denote the titration curves and the plot of the fraction of ionized carboxylic acid groups, where $\alpha = [COO^-]/([COO^-]+ [COOH])$, as a function of pH. According to the Figure 4.6, complete ionization for both PAA and PAA/PEO occurs at pH 9. On the other hand at pH 3 there are no ionized groups in the structure. Therefore, the ionization behavior of the PAA/PEO comb polymer was nearly identical to pure PAA. The values that have been obtained here are in good agreement with the literature data for acrylic-acid polymers (Kirby et al. 2004, Hackley 1997, Cesarano and Aksay 1988a, Cesarano and Aksay 1988b).

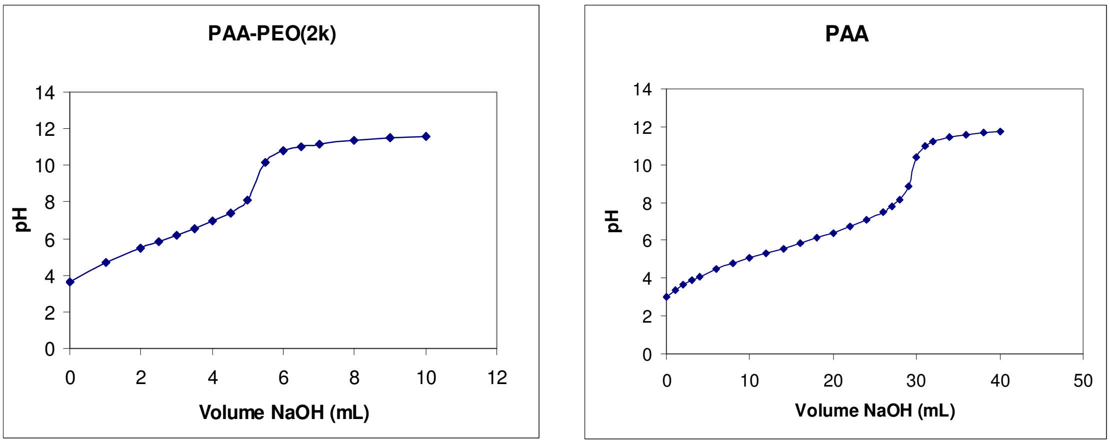

(a) (b)

Figure 4.5. Titration curves of (a) PAA/PEO (2000) comb polymer and (b) PAA.

Hackley previously examined the ionization chemistry of the PAA (having different molecular weights) using potentiometric titration method. He found 4 distinct regions on the titration curves related to the change in the conformational states. According to this study PAA molecules were unstable at the pH<3.5 followed by a coiled state between pH 4-6 and have a stretched conformation at pH>7 (Hackley 1997). Similarly, Kirby investigated the ionization of PAA/PEO comb polymers as a function of molecular weight of PEO group and found that fraction of the ionized carboxylic acid groups are independent of the presence of charge neutral PEO teeth (Kirby 2003).

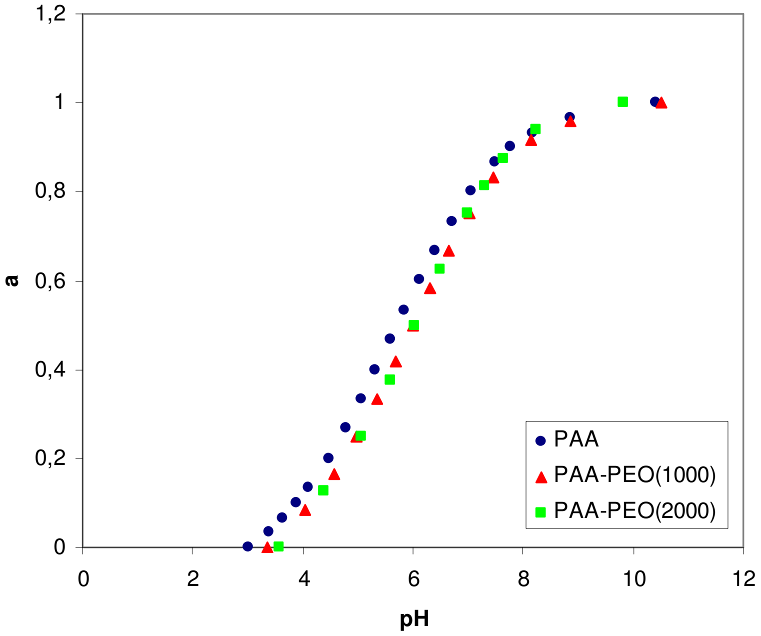

Figure 4.6. Ionization degree of PAA and comb polymers as a function of pH.

The charged groups of poly acids like PAA, are linked together along the chain. Therefore, the dissociation of one acid group is correlated in a complex way to the position and the number of other charged groups of the chain (Houbenov 2005). Thermodynamically, this effect is described in terms of the electrostatic free energy, ΔG_{el} that is required to remove an additional proton at a given degree of ionization: (Hackley 1997)

$$pH = pK_0 + \log\left(\frac{\alpha}{1-\alpha}\right) + \frac{\Delta G_{el}}{2.303kT} \qquad (4.1)$$

where K_o is the intrinsic dissociation constant. If we define an apparent dissociation constant pK_{app} as the sum of the intrinsic and electrostatic free-energy terms then experimental titration data can be represented by the expression:

$$pK_{app} = pH + \log\left(\frac{1-\alpha}{\alpha}\right) \tag{4.2}$$

pK_a of the PAA is around 5 as reported by Hackley 1997.

4.3.1.2. Determination the Critical Micelle Concentrations

4.3.1.2.1. Viscosity Measurements

Figure 4.7 shows the viscosity of PAA and PAA/PEO comb polymers as a function of polymer concentration. Measurements were performed using Bohlin-C14 geometry at pH 9, and 25 ºC. Results show that there is a dilute to semi-dilute transition at 20 mg/ml and 50 mg/ml for PAA/PEO(2000) comb polymer and pure PAA, respectively. The dilute regime is defined by $C_m<C_m^*$, for which C_m denotes the monomer concentration (per unit volume) and C_m^* is the concentration where individual chains start to overlap (Netz and Andelman 2003).

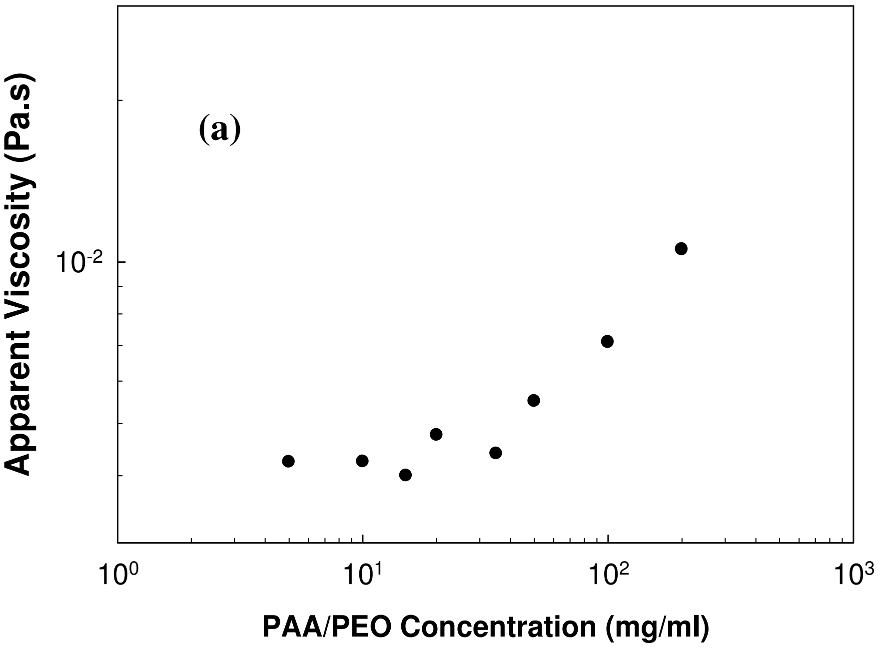

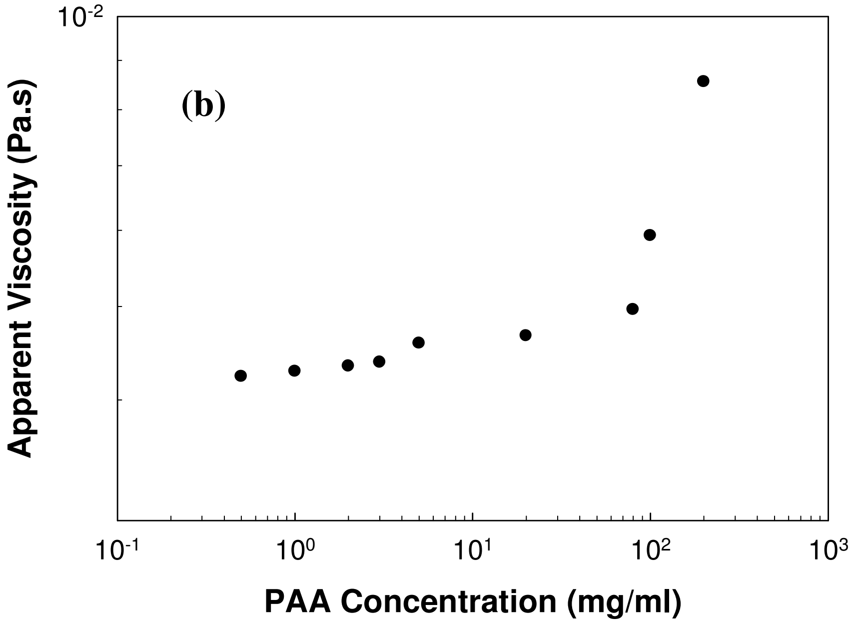

Figure 4.7. Viscosity of (a) PAA/PEO(2000) and (b) PAA as a function of polymer concentration, at pH 9.

4.3.1.2.2. Surface Tension Measurements

Surface tension measurements of PAA and PAA/PEO comb polymers were performed in order to investigate the micelle formation concentration (CMC). Figure 4.8 shows the surface tension versus log PAA concentration. It is clear that the lowest surface tension value in the graph is at 50 mg/ml that may correspond to the CMC of

PAA. In a previous study, Zosel measured the surface tension of PAA solutions (40%) as 69 mN/m. The relatively high surface tension values of PAA and PAA/PEO comb polymers (see Figures 4.8 to 4.10) compared to pure water (γ: 72 mN/m) can be attributed to the low surface activity of the polymers used in this study. Because high surface activity of a polymer requires an ability to reduce the surface tension in water (Zosel 1993, Desai et al. 2001). Similarly Chibowski and Paszkiewicz measured the surface tension of PAA (Mw 2000) as a function of PAA concentration. They found that γ of the PAA solutions is about 68 mN/m and does not change through the concentration range (Chibowski and Paszkiewicz 2006).

On the other hand it has been established now that no single sharp inflexion indicating CMC can be obtained by surface tension-log *C* plots unless the copolymer is fairly hydrophobic, or the measurements are made at a temperature well above room temperature (Desai et al. 2001). In the current study surface tension values were almost constant through the measurements and this may be attributed to the low hyrophobicity of the polymers.

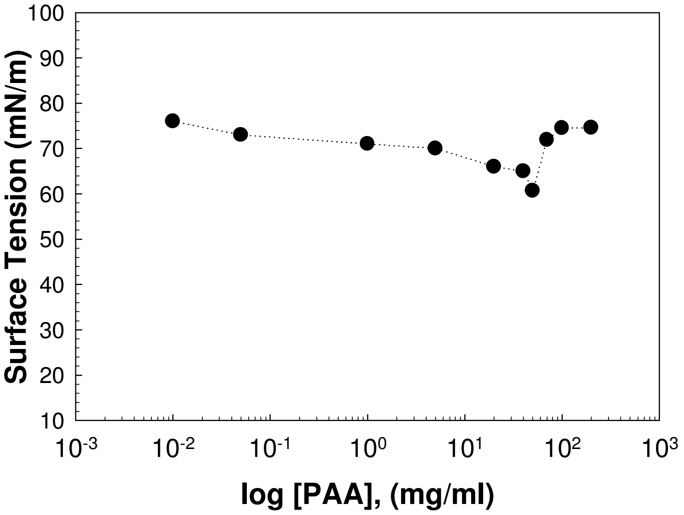

Figure 4.8. Surface tension of PAA as a function of concentration.

Figures 4.9 and 4.10 show the effect of comb polymer molecular architecture on the surface tension values. It is clear that in both figures there is no sharp inflexion point that may be indication of a CMC. However, according to the Figure 4.10 slight transition points were obtained (between 5 to 10 mg/ml) for all comb polymers. The transition point was higher in the case of comb polymer having a PEO group with higher molecular weight that makes it more hydrophilic. As expected more hydrophilic polymers would micelles at high concentrations (Desai et al. 2001).

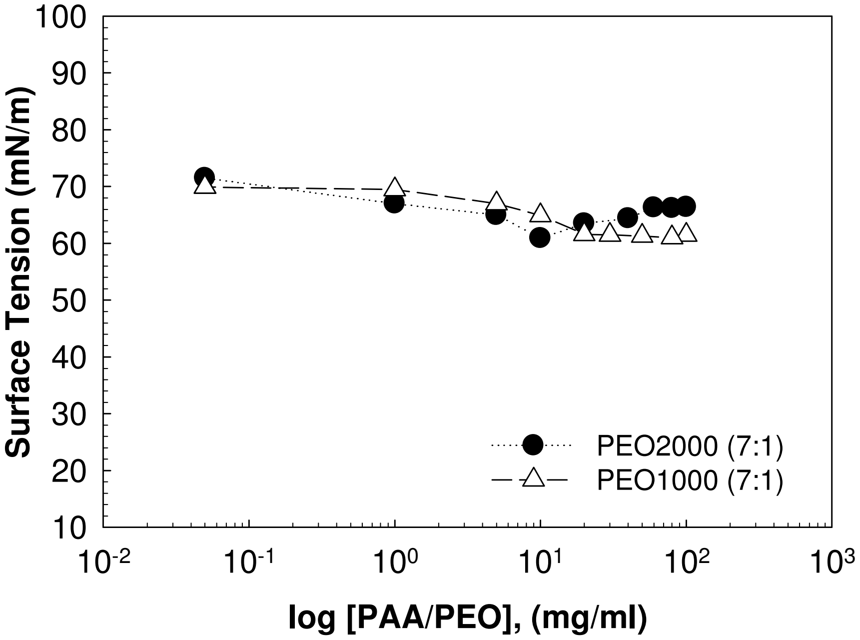

Figure 4.9. Surface tension of comb polymers with acid: ester ratio of (7:1).

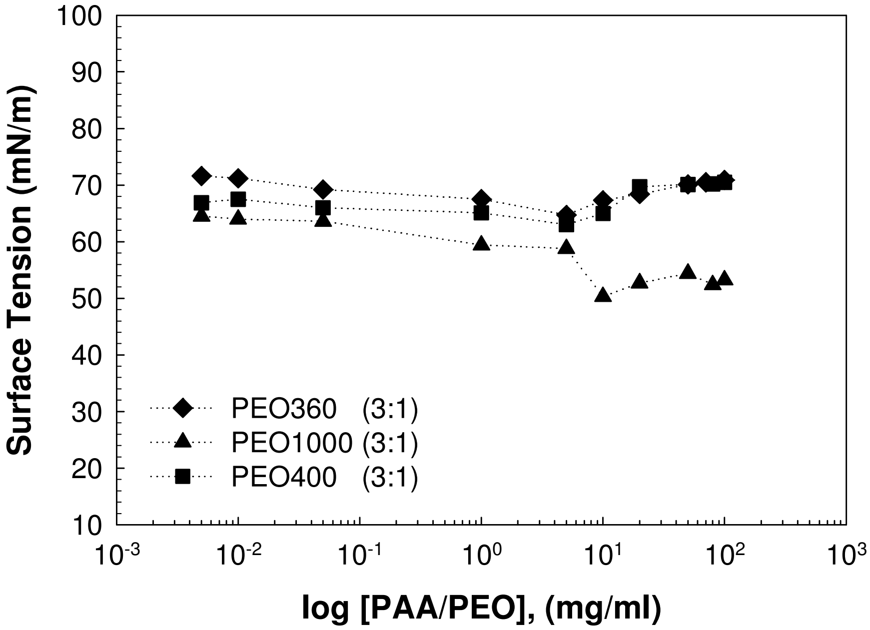

Figure 4.10. Surface tension of comb polymers with acid: ester ratio (3:1).

4.3.1.3. Effect of pH and Ionic Strength on the Solution Stability

4.3.1.3.1. Hydrodynamic Radius

Figure 4.11 shows the hydrodynamic radius values of the PAA/PEO comb polymer and PAA as a function of monovalent and divalent salt addition. This provides a measure of the size of the polyelectrolytes in solution. RH, is the hydro-dynamic radius, which includes both solvent (hydro) and shape (dynamic) effects (WEB_3 2007, Cohen- Stuart et al. 1984).

To make direct comparison between the salt species of varying valency the graph is plotted versus the [I]/[COO$^-$] where the [I] the ionic strength and the [COO$^-$] is the molar concentration of ionized carboxylic acid groups.

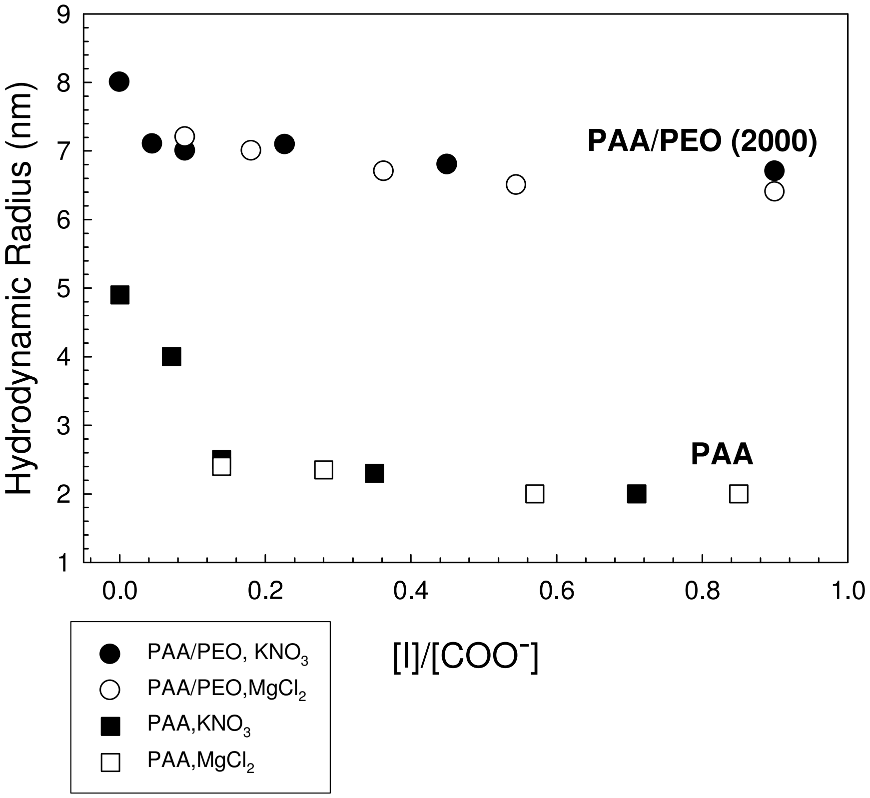

Figure 4.11. Plot of the hydrodynamic radius as a function of salt addition for dilute PAA and PAA/PEO(2000) solutions. Open and closed circle symbols correspond to MgCl$_2$ and KNO$_3$ additions, respectively. Note, [I] $=\frac{1}{2}\sum n_i z_i^2$ due to added salt only, [COO$^-$] = 0.07 *M*, and 0.011 *M* for PAA and PAA/PEO(2000), respectively.

As it is shown in Figure 4.11 R_H values are calculated to be 4.9 and 8.0 nm for PAA and PAA/PEO, respectively under fully ionized conditions. Results suggest that the stability of PAA/PEO comb polymers is not affected by the salt concentration. On the other hand PAA solution stability changes dramatically as the ionic strength increases.

An important characteristic of many ionizable polymers is their ability to undergo expansion from a coiled to a stretched conformation as charge density increases along the chain. This transition is due to electrostatic repulsion between neighboring ionized sites. Dissociation of each carboxyl group along the polymer chain significantly affects the ionization of neighboring groups. As a consequence of electrostatic interactions, dissociation becomes difficult as the fraction of ionized sites, α, increases. The effect is analogous to the well known helix–coil transition that is associated with polypeptides (Hackley 1997, Netz and Andelman 2003).

The behavior of PAA and PAA/PEO comb polymers as a function of pH and ionic strength is represented schematically in Figure 4.12. The differences between two polyelectrolytes were attributed to the presence of the PEO teeth in the comb polymer which prevents large conformational changes in ionized conditions.

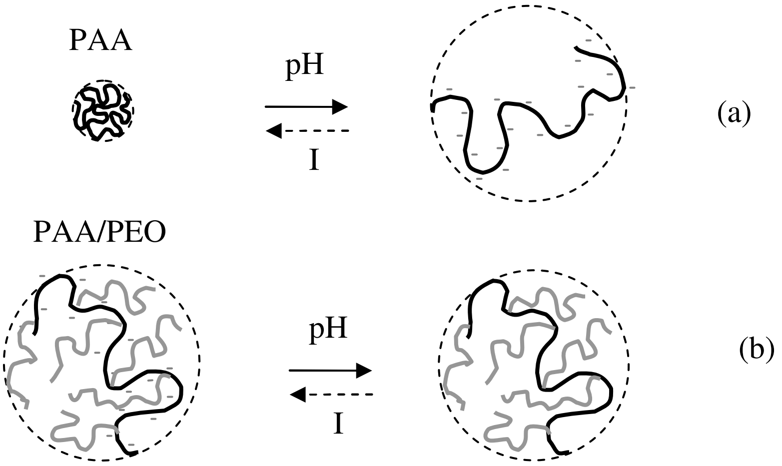

Figure 4.12. Schematic illustrations of (a) pure PAA and (b) PAA/PEO comb polymer molecules undergoing conformational changes in dilute solution, the top arrow (solid line) denotes increasing pH and the bottom arrow (dashed line) denotes increasing ionic strength (Source: Kirby 2003).

4.3.1.3.2. Solution Turbidity

Turbidity measurements were carried out on dilute polymer solutions of varying pH and salt concentration. Figures 4.13 to 4.15 show the turbidity values of polymer solutions as a function of ionic strength and pH. The stable polymer solutions characterized in which the polymeric species remain well solvated and are transparent. Therefore high turbidity values correspond to the solutions having low stability. In other words, as the turbidity increases the solution stability decreases.

According to the Figure 4.13 in the presence of monovalent salt all polymer solutions (both PAA and PAA/PEO) remained stable over a broad range of [I]/[COO$^-$] and in acidic and basic pH values.

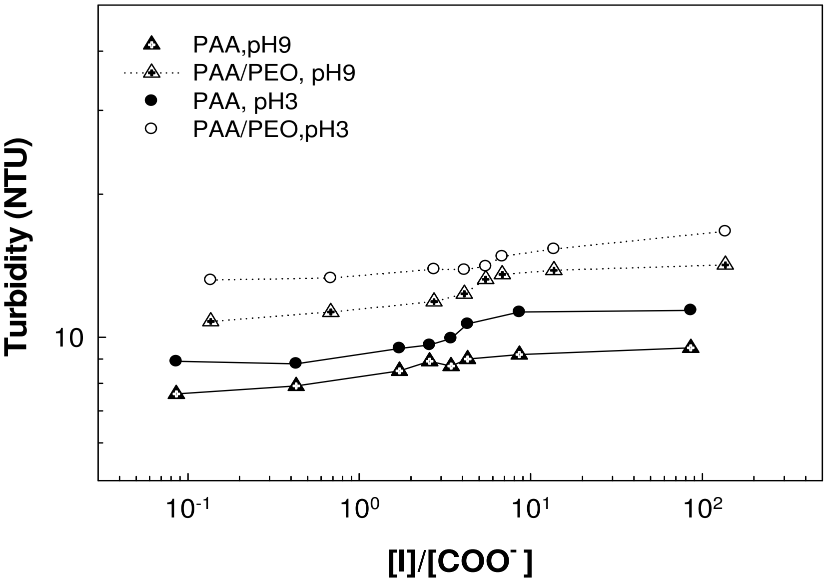

Figure 4.13. Effect of KCl on the turbidity of PAA and PAA/PEO (2000) solutions as a function of ionic strength at pH 3 and pH9. Note, [I] $=\frac{1}{2}\sum n_i z_i^2$ due to added salt only, [COO$^-$] = 0.07 *M*, and 0.011 *M* for PAA and PAA/PEO2000, respectively.

However, as it is shown in Figure 4.14 in the case of divalent salt additions ($MgCl_2$) the stability of PAA solutions were depended on pH and divalent salt concentration. At low pH values where PAA is slightly ionized PAA solutions remained stable over a broad range of [I]/[COO$^-$] values. On the other hand in fully ionized conditions (pH 9) PAA solutions were only stable in the range 0-2x10^{-2} M $MgCl_2$. At higher salt concentrations PAA start to make complexes with Mg^{+2} ions in solution (Figure 4.15).

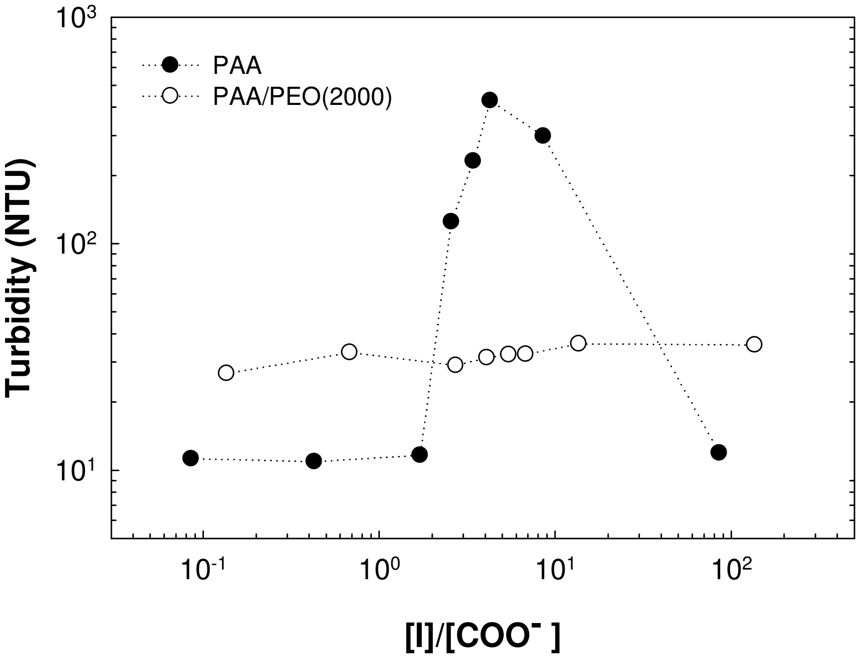

Figure 4.14. Effect of $MgCl_2$ on the turbidity of PAA and PAA/PEO (2000) solutions as a function of ionic strength at pH 9.

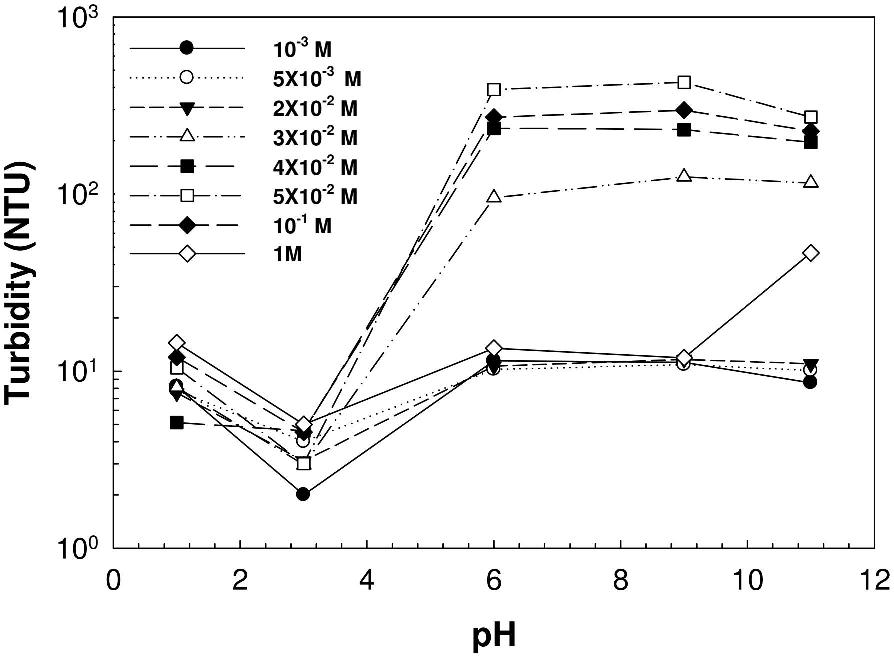

Figure 4.15. Effect of $MgCl_2$ concentrations on the turbidity of PAA (2.5 mg/ml) as a function of pH.

Effect of trivalent cations on the stability of PAA and PAA/PEO comb polymer is shown in Figures 4.16 to 4.21. Kirby reported that dilute polymer solutions with trivalent, $LaCl_3$ additions could not be prepared above pH 7 due to the precipitation of lanthanum hydroxide that would alter the turbidity results (see Figure 4.16) (Kirby 2003). However, this pH value is only slightly below the pH required for full ionization of the PAA-based species (pH 9).

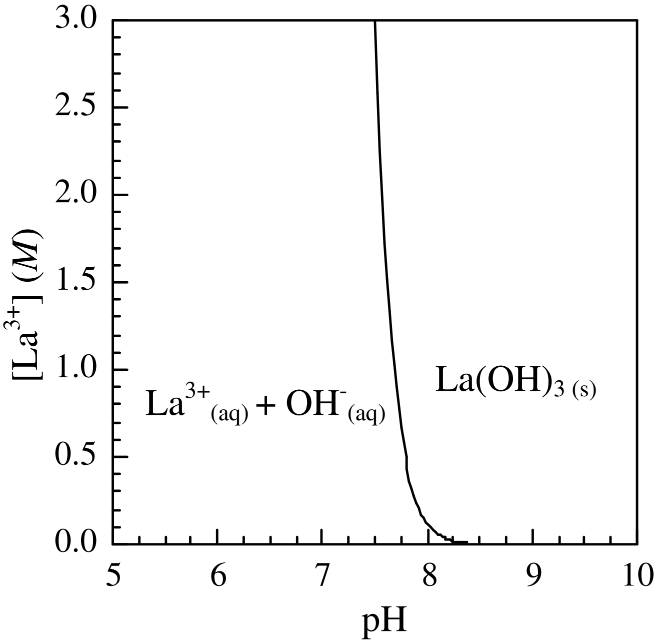

Figure 4.16. Solubility limit of $La(OH)_3$ in aqueous solution.
(Source: Kirby 2003)

Accordingly, the results of the current work showed that at pH 3 presence of $LaCl_3$ did not affect the stability of comb polymers. However, a sharp increase was observed in the turbidity of PAA solutions due to PAA-La^{+3} complexation. The complex formation initiate at $2.5x10^{-3}$ M $LaCl_3$ but the highest turbidity values were obtained at $5x10^{-2}$ M $LaCl_3$. The increase in turbidity values of the PAA/PEO comb polymers at pH 9 in the presence of $LaCl_3$ may be attributed to the precipitation of ions and formation of $La(OH)_3$.

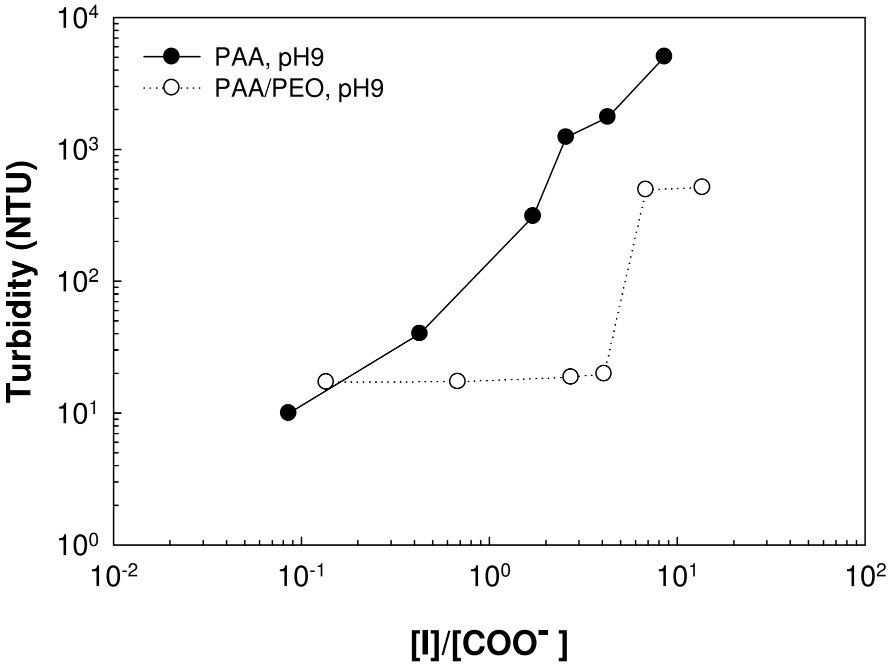

Figure 4.17. Effect of $LaCl_3$ on the turbidity of PAA and PAA/PEO solutions at pH 9.

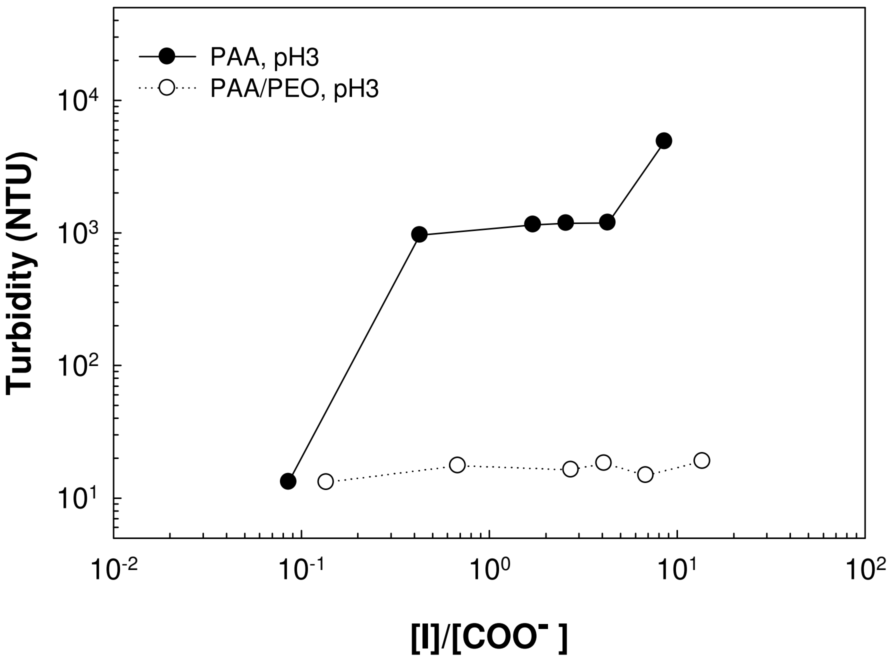

Figure 4.18. Effect of $LaCl_3$ on the turbidity of PAA and PAA/PEO solutions at pH 3.

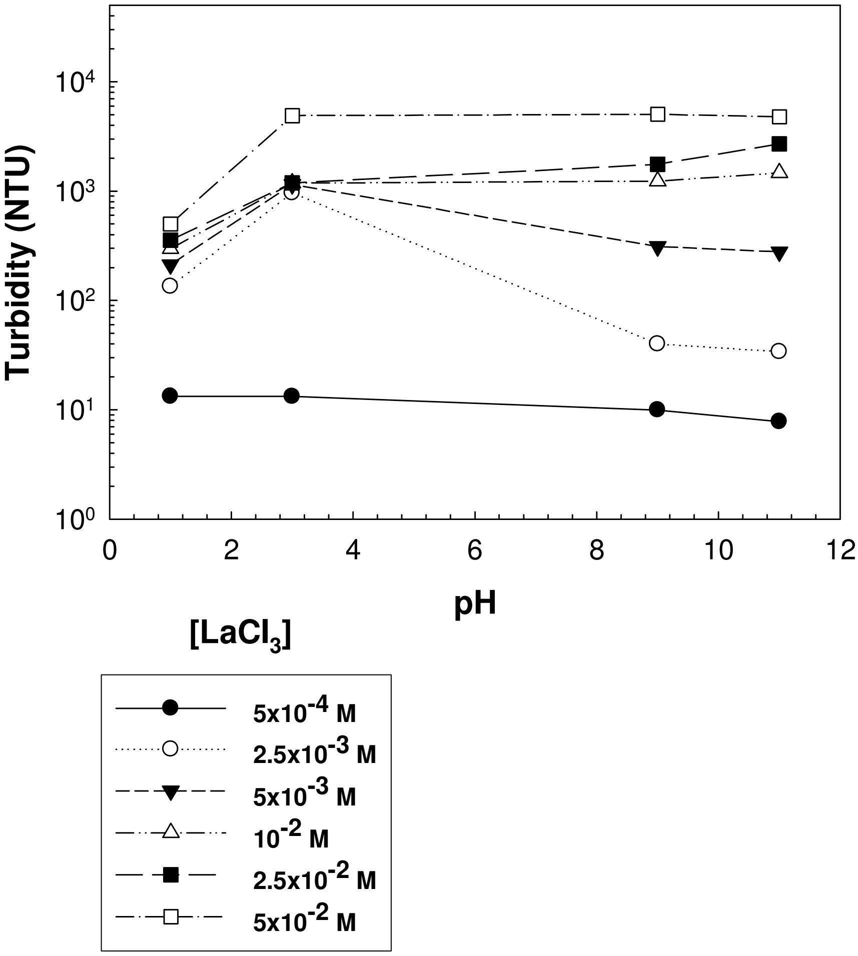

Figure 4.19. Effect of $LaCl_3$ concentration on the turbidity of PAA solutions as a function of pH.

To investigate the interaction of PAA and PAA/PEO comb polymers with the Pb^{+2} ions in solution, turbidity measurements were performed in the presence of lead (II) acetate. First of all, turbidity of pure lead acetate in water was investigated. Results are shown in Fig 4.20. It is known that Pb(II)acetate with water forms $Pb(CH_3COO)_2.3H_2O$ a colorless crystalline substance. Turbidity of Pb(II) acetate solution at $5x10^{-2}$ M started to increase at pH 6 and persist to increase as the pH increases.

Figure 4.21 show the effect of Pb^{+2} ion addition on the stability PAA and comb polymer suspensions. Under very acidic and basic conditions no interaction between comb polymer and Pb^{+2} was observed. On the other hand even at $pH < 6$ an increase was noticed in the turbidity of PAA solutions in the presence of small amount of lead (II) acetate.

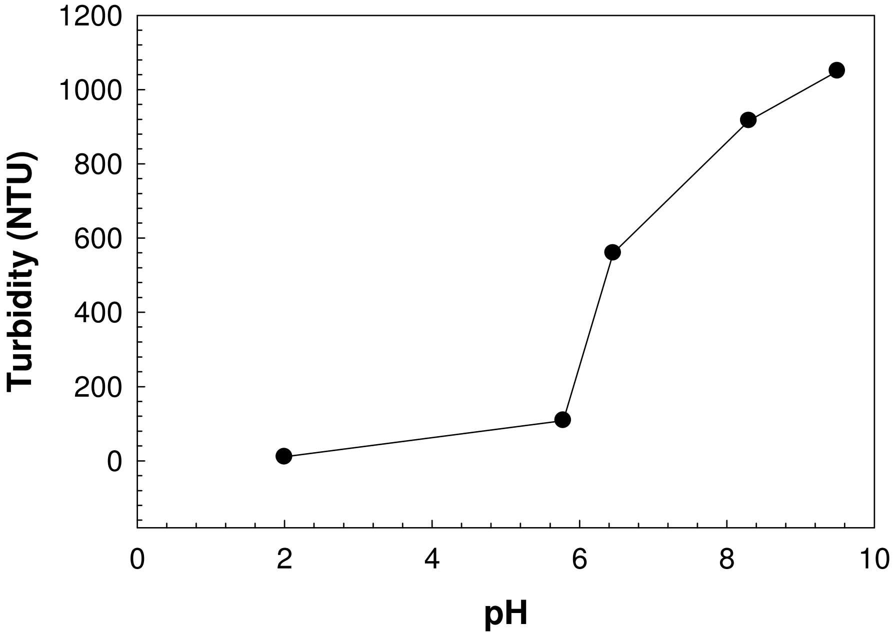

Figure 4.20. Turbidity of Pb(II) acetate/water solutions (5×10^{-2} M) as a function of pH.

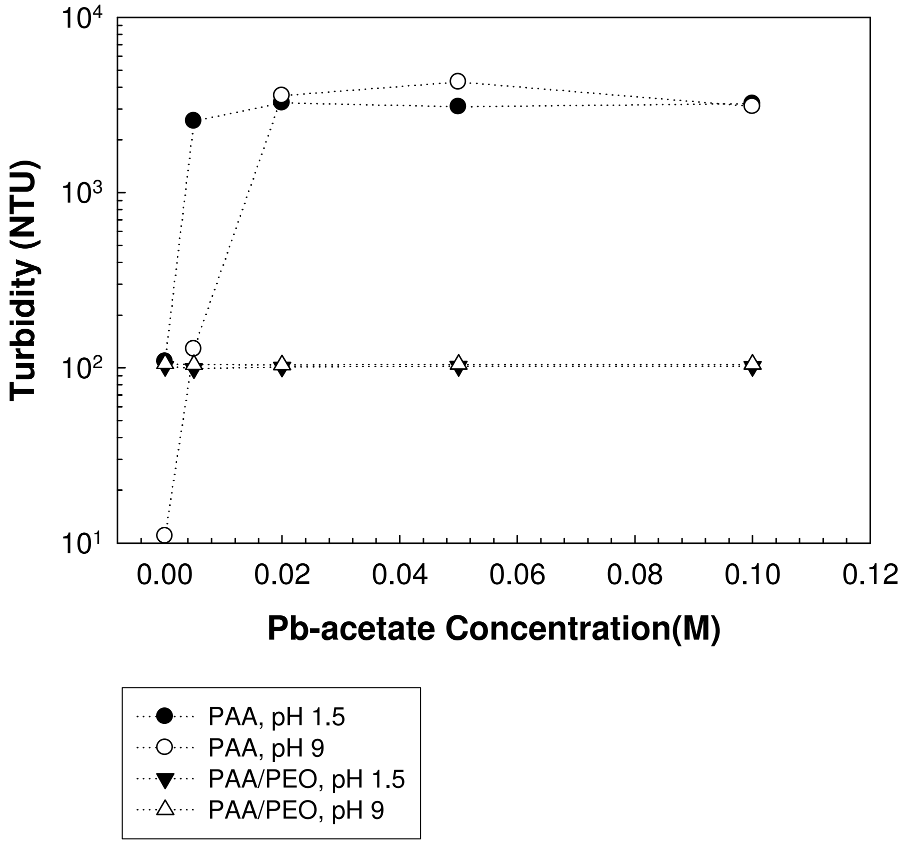

Figure 4.21. Effect of Pb(II) acetate concentration on the turbidity of PAA and PAA/PEO solutions at pH 1.5 and pH 9.

4.3.2. Effect of PAA/PEO on the Stability and Flow Behavior of PMN Suspensions

4.3.2.1. Rheological Measurements

Figures 4.22 and 4.23 show the effect of PAA/PEO and PAA on the flow behavior of PMN suspensions at pH 9, respectively. For each system a critical concentration (c^*) of polyelectrolyte was identified corresponded to the amount required to promote a transition from strongly shear thinning behavior to nearly Newtonian behavior. According to the Figure 4.22, PMN suspensions show a shear thinning behavior at low polymer concentrations however, starting from 5 mg/ml transition to Newtonian behavior was observed. On the other hand, the c^* value corresponding to the lowest suspension viscosity was obtained at 10 mg/ml (1 wt%) polymer concentration (4.35 mg comb polymer /m^2 of PMN). Similarly for the suspensions containing PAA, c^* was found at 2.5 mg/ml (0.25 wt%) polymer concentration (1.1 mg PAA /m^2 of PMN).

The apparent viscosity of PMN suspensions at pH 6 in the presence of PAA/PEO and PAA as a function of shear stress is plotted in Figures 4.24 and 4.25, respectively. Again PMN suspensions were stable over the broad range of PAA/PEO concentration at pH 6. On the other hand, results showed that PAA was not capable to disperse the PMN suspensions under these conditions. Shear thinning behavior was observed in all PMN suspensions containing PAA at pH 6.

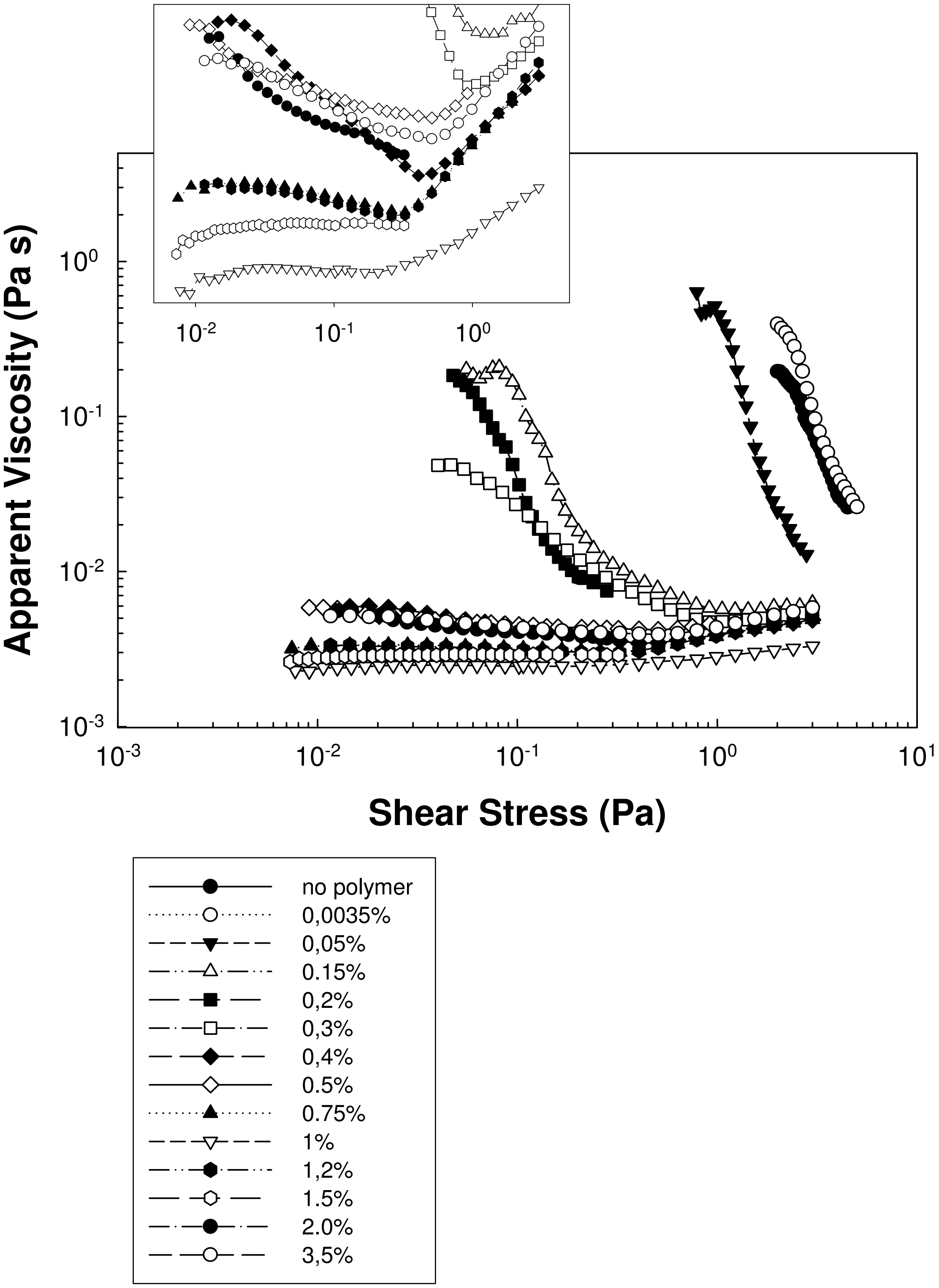

Figure 4.22. Effect of PAA/PEO (2000) concentration on the flow behavior of PMN suspensions, 20 vol%, pH 9, polymer concentration is given as wt% .

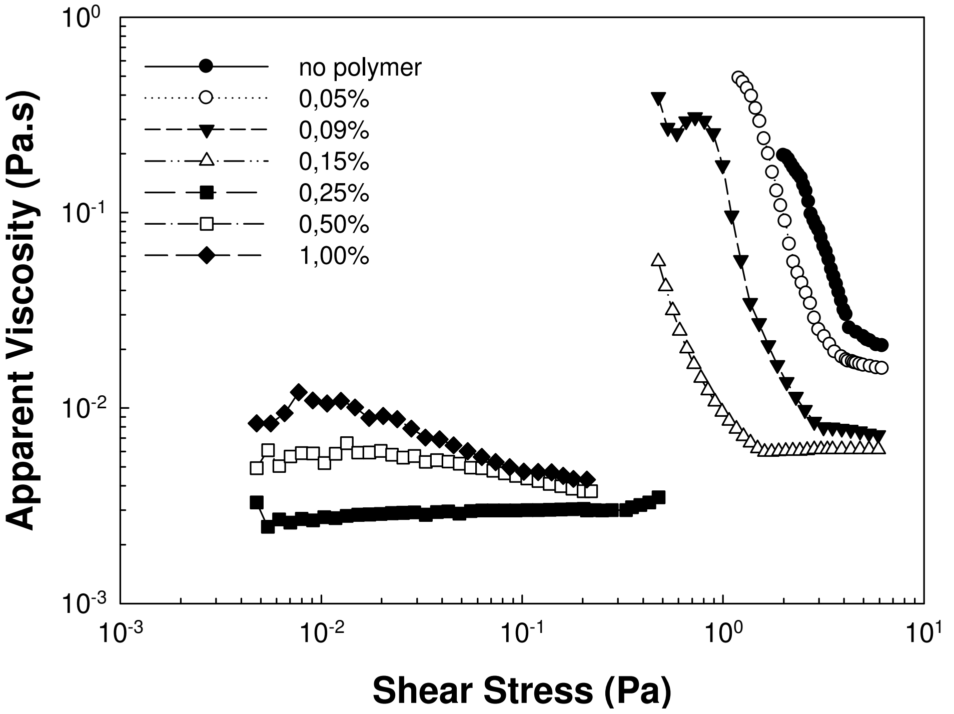

Figure 4.23. Effect of PAA concentration on the flow behavior of PMN suspensions, 20 vol%, pH 9, polymer concentration is given as wt%.

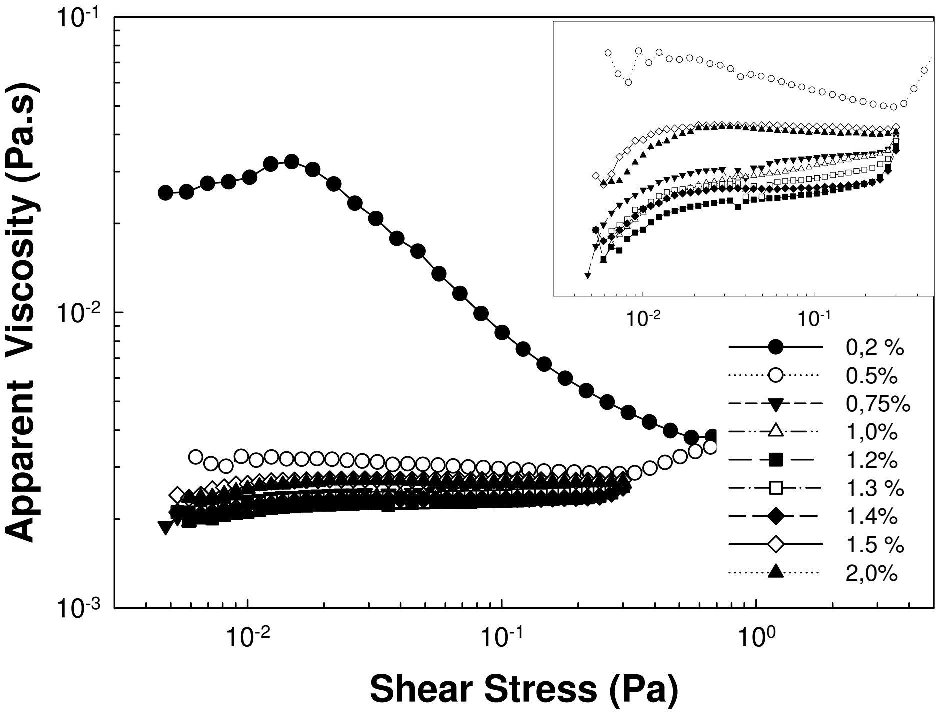

Figure 4.24. Effect of PAA/PEO(2000) concentration on the flow behavior of PMN suspensions, 20 vol%, pH 6, polymer concentration is given as wt%.

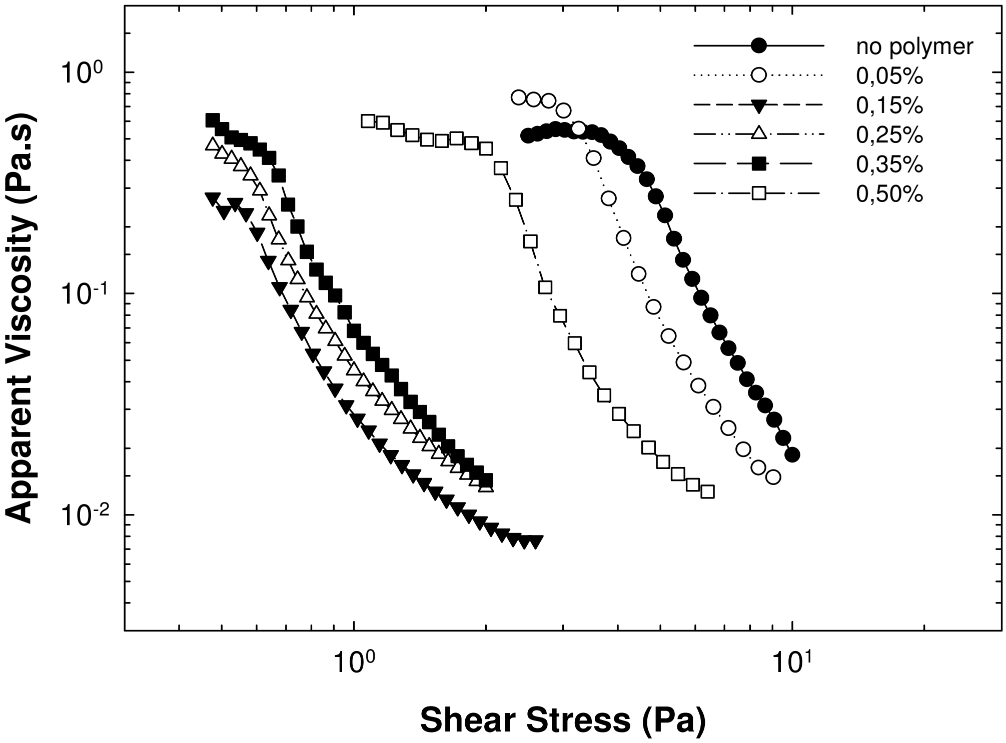

Figure 4.25. Effect of PAA concentration on the stability of PMN suspensions, 20 vol%, pH 6, polymer concentration is given as wt%.

The flow curve of the PMN suspensions in the presence of PAA at pH 6 shows shear thinning behavior and fits to Carreau model. It is an alternative to well known Cross model. The model equation is given below (Barnes et al. 1993):

$$\eta = \eta_\infty + \frac{(\eta_0 - \eta_\infty)}{\left(1 + (k\dot{\gamma})^2\right)n} \tag{4.3}$$

where η_0 and η_∞ are the viscosity at low and high shear rates, k is a time constant and n is a behaviour index (Terrones et al. 1997). Model parameters as a function of PAA concentration is tabulated in Table 4.2. Results showed that zero shear viscosity of the PMN suspensions.

Table 4.2. Carreau model parameters for PMN suspensions in the presence of PAA at pH 6.

PAA	η_0	η_∞	k	n
0%	0.6240	0.01931	0.101	0.5693
0.05%	0.6426	0.008955	0.2519	0.4948
0.15%	0.4018	0.005622	0.6554	0.4619
0.25%	0.6968	0.008678	1.185	0.4543
0.35%	0.8089	0.008836	1.256	0.4504

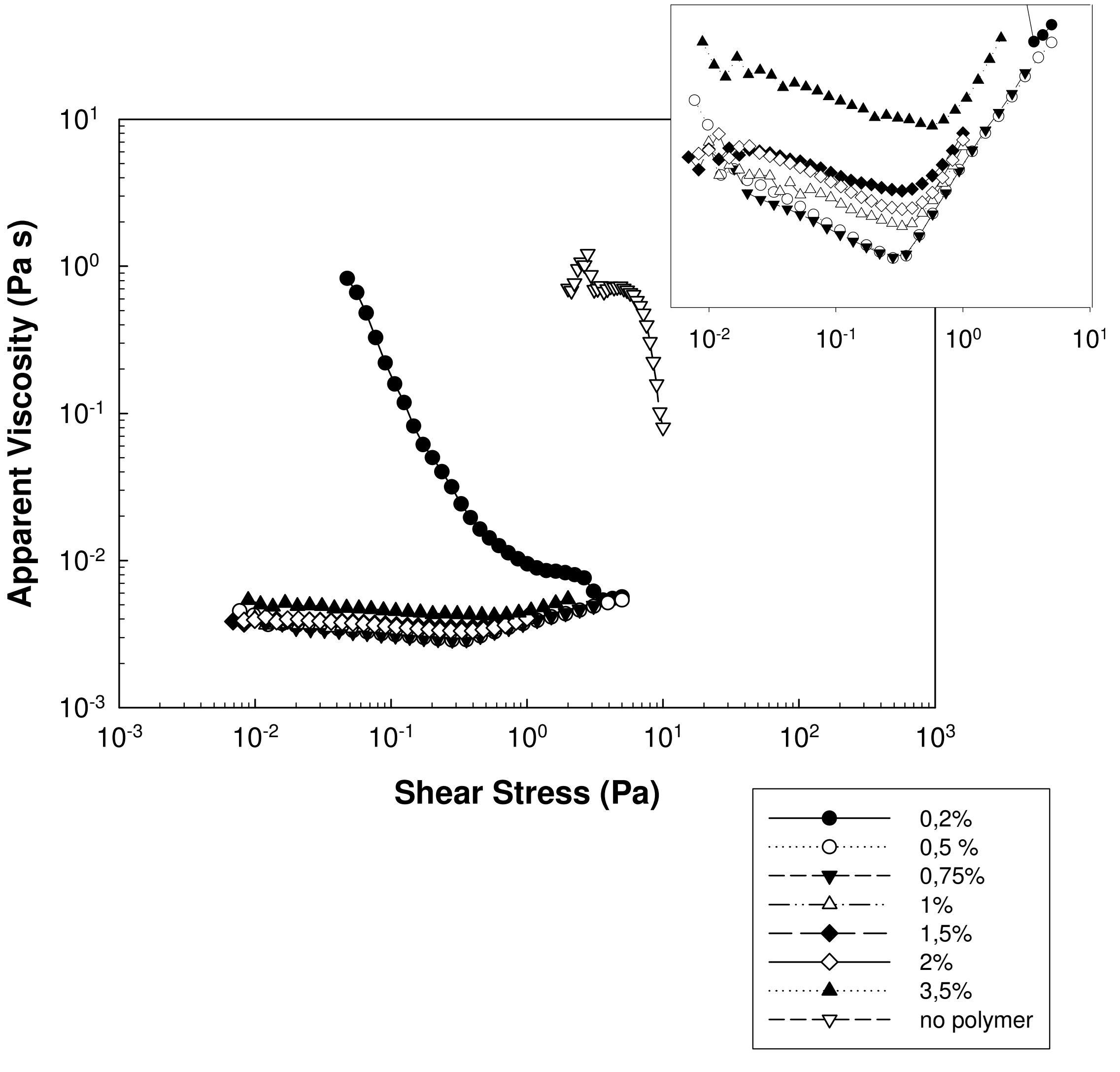

Figure 4.26. Effect of PAA/PEO(2000) concentration on the flow behavior of PMN suspensions, 20 vol%, and pH 3, polymer concentration is given as wt%.

PMN suspensions at pH 3 in the presence of polyelectrolytes showed a similar rheological behavior with suspensions prepared at pH 6. Figures 4.26 and 4.27 display the apparent viscosity of PMN suspensions in the presence of PAA and PAA/PEO as a function of shear stress at pH 3. The suspensions exhibit shear thinning behavior with yield stress (fits with the Carreau model) in the presence of PAA. However, nearly Newtonian behavior was observed in the presence of PAA/PEO comb polymer. In other words on reducing pH, PAA containing suspensions became unstable as reflected by the degree of shear thinning behavior. In contrast, in the presence of comb polymers suspensions were stable over the entire pH range investigated.

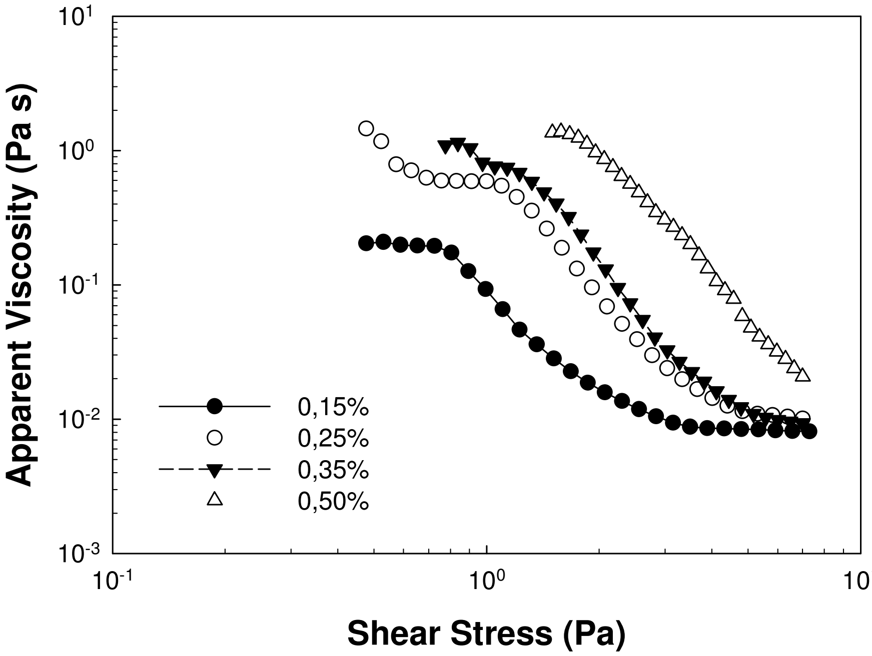

Figure 4.27. Effect of PAA concentration on the flow behavior of PMN suspensions, 20 vol%, and pH 3, polymer concentration is given as wt%.

High stability obtained in the presence of comb polymers may be attributed to the presence of charge neutral PEO teeth. It is grafted at random intervals along the PAA backbone provided stability of PMN suspensions over a broad pH range where pure PAA fails. The stability mechanism of comb polymers was described previously by Kirby and co-workers for barium titanate suspensions (Kirby et al. 2004). In comb polymers the PEO teeth provide two important functions. The effective size (R_H) of PAA/PEO comb polymers on particle surface is not significantly change with variations in pH and ionic strength. Secondly, the PEO teeth shield the PAA backbone from undergoing ion bridging interactions that may cause the rapid aggregation of PAA molecules and PAA stabilized PMN particles. To summarize, viscosity of PMN suspensions at different pH values is given in Figures 4.28 and 4.29 as a function of polyelectrolyte concentration.

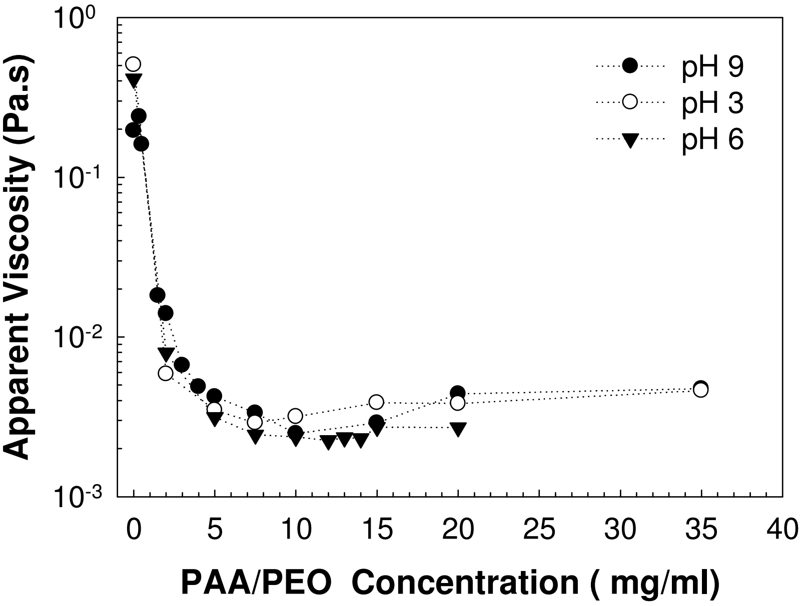

Figure 4.28. Effect of PAA/PEO(2000) concentration on the viscosity of PMN suspensions (20vol%) at pH 3, 6 and 9.

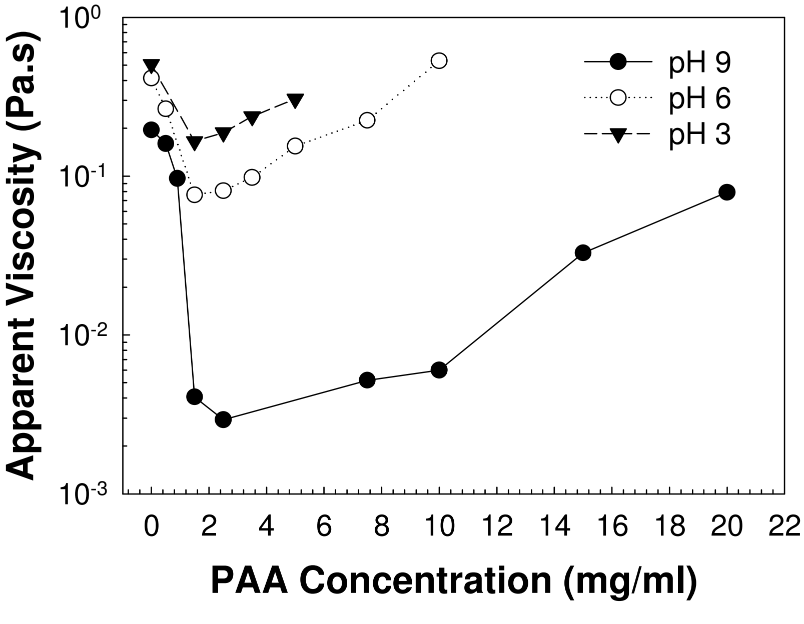

Figure 4.29. Effect of PAA concentration on the viscosity of PMN suspensions (20vol%) at pH 3, 6 and 9.

4.3.2.2. Effect of pH Shift on the Flow Behavior

Effect of pH on the flow behavior of PMN suspensions was discussed in previous section. Results given in previous section describes the behaviour of suspensions prepared separately at different pH values (pH 3, 6 and 9). Results showed that the interaction mechanisms of PAA and PAA/PEO with PMN particles was pH dependent. This is mainly because of the surface charge of PMN, ionization degree of polyelectrolytes, and adsorption behavior of polyelectrolytes. On the other hand, it may be reasonable to investigate the effect of pH on the system after the polyelectrolytes bind to the PMN surface under fully ionized conditions. Therefore in this section stable PMN suspensions (20 vol%) were prepared at pH 9 using the same suspension preparation method discussed in previous section. Then the pH values of the same suspensions were decreased gradually to pH 6 and to pH 3. Results are given in Figure 4.30. According to the Figure 4.30 (a) the flow behavior and the viscosity of PMN suspensions in the presence of PAA/PEO did not change with the decrease in pH. Since the PAA/PEO comb polymers was still in stretched conformation at pH 6 and 3.

On the other hand, the flow behavior of PMN suspensions in the presence of PAA showed important deviation from the initial state as the pH of the medium decreased. This is consistent with the results obtained in the previous section. It is possible to conclude that for stable PMN suspensions prepared at pH 9 containing PAA, a small decrease in pH is enough to destabilize the suspension.

Figure 4.30 (a) also display that suspensions show shear thickening behaviour at high shear stress. Previous study of Brandy and coworkers showed that at low solids concentrations the suspension viscosity is nearly constant, while at high volume fractions (>40 vol%) the viscosity can show shear thinning at low shear stress and can show shear thickening at high stress. It was shown that the Brownian contribution to the shear stress disappear at high shear stress, leaving only hydrodynamic contribution. The disappearance of the Brownian contribution leads to a viscosity reduction of about a factor two for 45 vol% suspensions. Simulations of Visscher and Heyes for 30 vol% suspensions show the formation of lines of particles parallel to the flow direction. These occur at shear rates high enough to be in the shear thinned state, but disappear at very high shear rates where shear thickening occurs (Larson 1999).

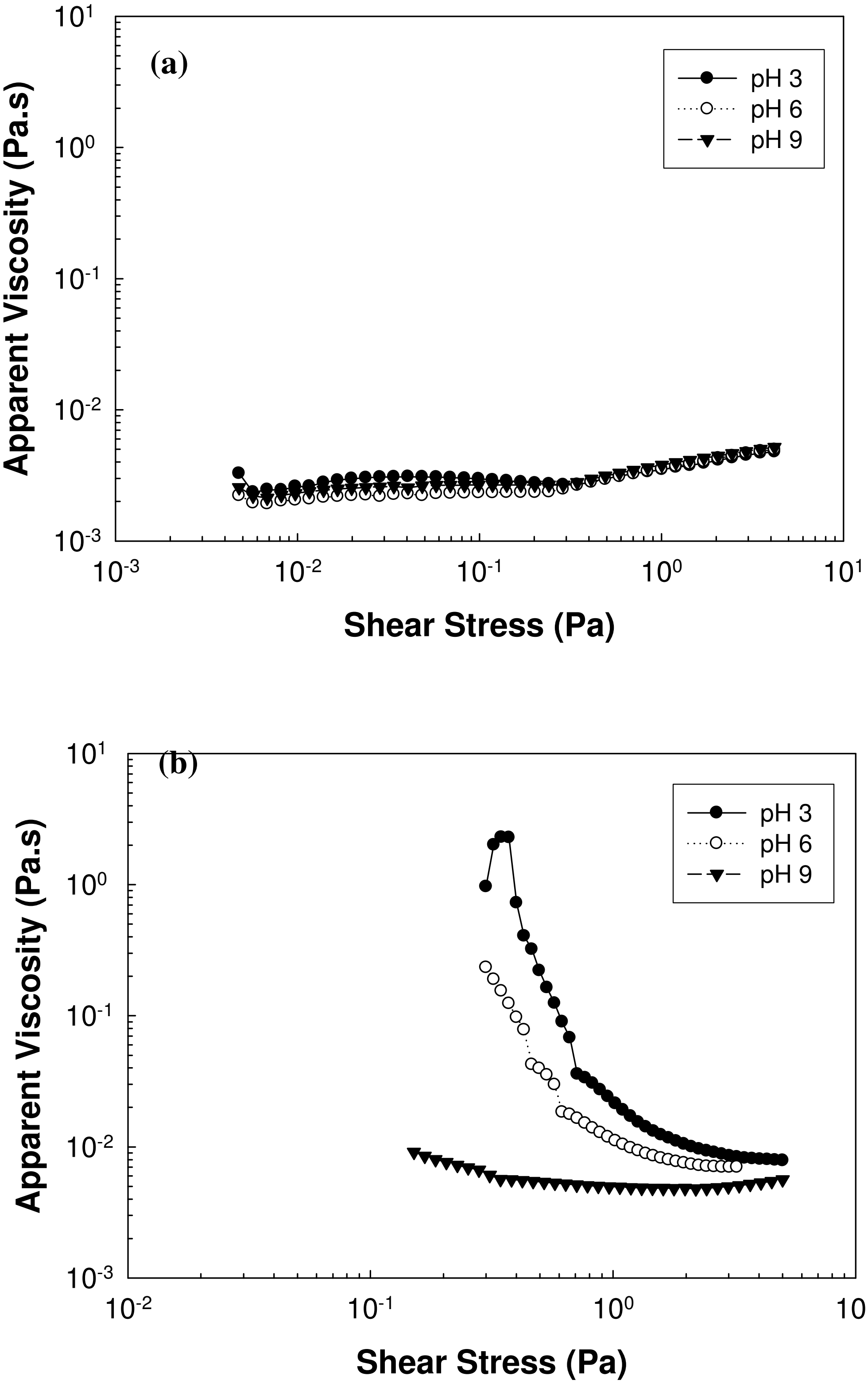

Figure 4.30. Effect of pH variation on the viscosity of PMN suspensions (20 vol%) in the presence of a) PAA/PEO(2000), 1 wt %, b) PAA, 0.25 wt%

4.3.2.3. Effect of Solids Loading on the Flow Behavior

Viscosity of concentrated ceramic suspensions depends on the volume fraction of the solid phase. The influence of solid volume fraction on the viscosity can be analyzed in terms of the relative viscosity and must be referred to one or more reference shear stresses or shear rates because of the non-Newtonian character of the suspensions. (Zupancic et al. 1998). Following equations give the solids concentration dependence of the viscosity:

$$\eta_{rel} = \left(1 - \frac{\phi}{\phi \max}\right)^{-n} \tag{4.4}$$

$$\eta_{rel} = \left(\frac{\eta_{susp}}{\eta_{sol}}\right) \tag{4.5}$$

The dependence of suspension viscosity on the volume fraction of the dispersed phase can be given by Krieger-Dougherty equation:

$$\eta_{rel} = \left(1 - \frac{\phi}{\phi \max}\right)^{-K.\phi \max} \tag{4.6}$$

Where $\phi_{\max}$ is the maximum volume fraction of the suspension, κ is the hydrodynamic shape factor (=2.5). Similarly Quemada equation can be written as:

$$\eta_{rel} = \left(1 - \frac{\phi}{\phi \max}\right)^{-2} \tag{4.7}$$

The exponent n is equal to 2 in the Quemada model and $\kappa\phi_{\max}$ in the Krieger-Dougherty model (Bergstrom et al. 1997). Effect of solids concentration on the viscosity of PMN suspensions were also investigated in this study. Figure 4.31 shows the viscosity of PMN suspensions of different solids concentrations as a function of shear stress.

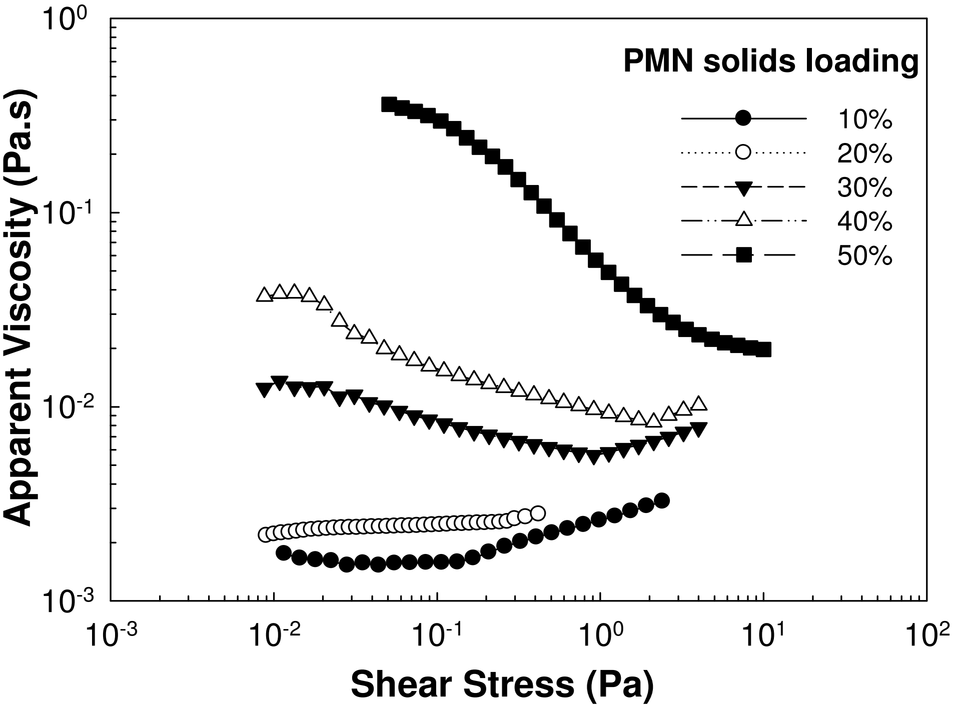

Figure 4.31. Viscosity of PMN suspensions as a function of shear stress, at various solids concentration.

In the current study, Krieger-Dougherty and Quemada models were used to fit the volume fraction dependence of hard sphere PMN suspensions. It is also important to consider that due to adsorbed polymer layer, the actual volume fraction of the suspensions will be higher than one corresponding to the solid phase. Therefore, during the calculations an effective volume fraction should be used to take into account the thickness of the adsorbed polymer layer. The effective volume fraction can be calculated using the following equation:

$$\phi_{eff} = \phi(1 + \delta A_s \rho_s) \tag{4.8}$$

where δ is the thickness of the adsorbed dispersant layer, A_S is the specific surface area of the powder and ρ_S is the powder density. Alternative equation for the calculation of effective volume fraction for spherical particles is given below: (where “a” is the particle radius)

$$\phi_{eff} = \phi(1 + \frac{\delta}{a})^3 \tag{4.9}$$

Thickness of the adsorbed polymer layer (δ) can be estimated as the hydrodynamic radius (R_H) of the polymer in dilute solution (Cohen-Stuart et al. 1984). If we assume the solvent to be good, monomers repel each other. The lateral separation between the polymer coils is fixed by the grafting density, so that the polymers extend away from the grafting surface in order to avoid each other, as depicted in Fig 4.32. (Vincent 1974). The resulting structure is called a polymer 'brush', with a vertical height D which greatly exceeds the unperturbed coil radius.

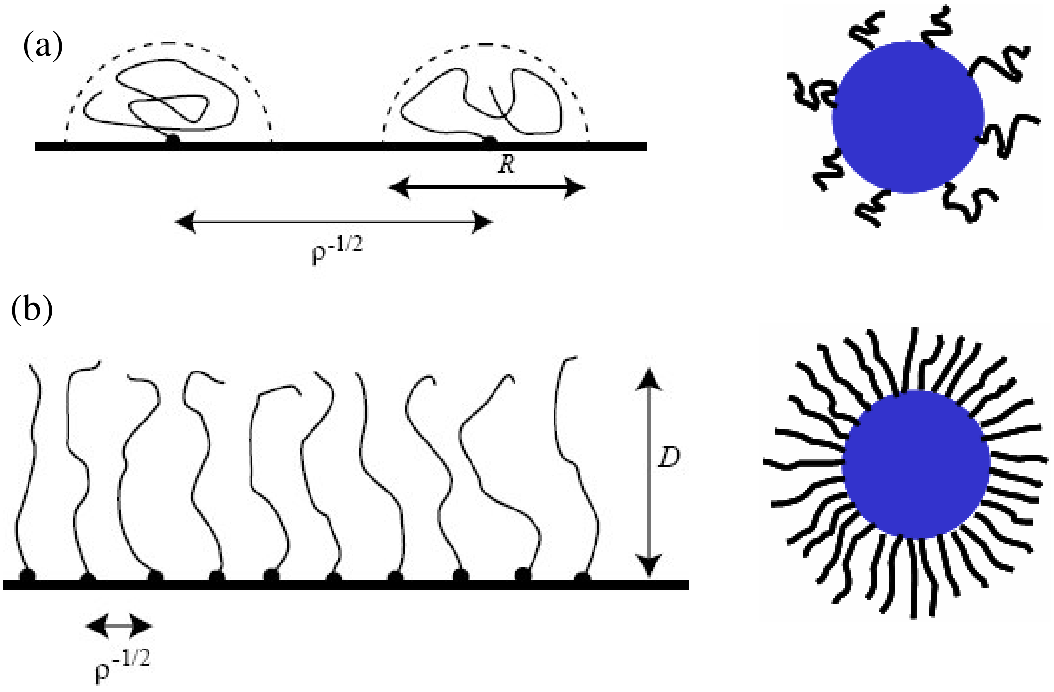

Figure 4.32. Schematic presentation of the adsorbed polymer layer a) the mushroom regime, where the distance between chains $\rho^{-1/2}$ (where ρ is the graft density), is larger than the size of a polymer coil (b) the brush regime, where the distance between chains is smaller than the unperturbed coil size. Here, the chains are stretched away from the surface (Source: Adapted from Netz and Andelman 2003).

For the dilute mushroom regime adlayer thickness of the adsorbed polymer is equal to the polymer size in solution. However, for the brush regime, the scaling behavior of the brush height D can be analyzed using a Flory-like mean-field theory. Then equilibrium height will be equal to the $D_{eq} \sim N^{3/5}$ (Netz and Andelman 2003).

On the other hand, end to end distance of the polymer system can be calculated by equation (4.10) with simplifying assumptions (e.g. each segment of the polymer chain can rotate freely and independently of the neighboring segment). Therefore, the hydrodynamic radius, R_H value of the PAA can be calculated using the following equation derived by Napper and co-workers (Song et al. 2000, Napper 1977):

$$R_H=0.06(M_w)^{0.5} \tag{4.10}$$

where the Mw is the molecular weight of the polymer. This expression was derived for the uncharged polymers under theta solvent conditions. On the other hand R_H value for the PAA/PEO comb polymers can be derived by modifying the above equation:

$$R_H=0.06(M_{wPAA})^{0.5}+0.06(M_{wPEO})^{0.5} \tag{4.11}$$

R_H values of the PAA and PAA/PEO comb polymers were calculated to be 4.2 nm and 6.9 nm, respectively using equations (4.10 and 4.11). Additionally, the hydrodynamic radius of the same polymers were obtained using dynamic light scattering measurements as discussed in the previous section. Table 4.3 shows the calculated (using equation 4.11) effective volume fraction of PMN suspensions in the presence of comb polymers.

Table 4.3. Calculated effective volume fraction of PMN suspensions.

ϕ	ϕ_{eff}	ϕ_{max}
0.1	0.1062	0.63
0.2	0.2124	
0.3	0.3186	
0.4	0.4248	
0.5	0.5310	

Figure 4.33 displays the relative viscosity of PMN suspensions as a function of effective volume fraction. Results fit well with the related theoretical models used to describe effect of volume fraction on the viscosity.

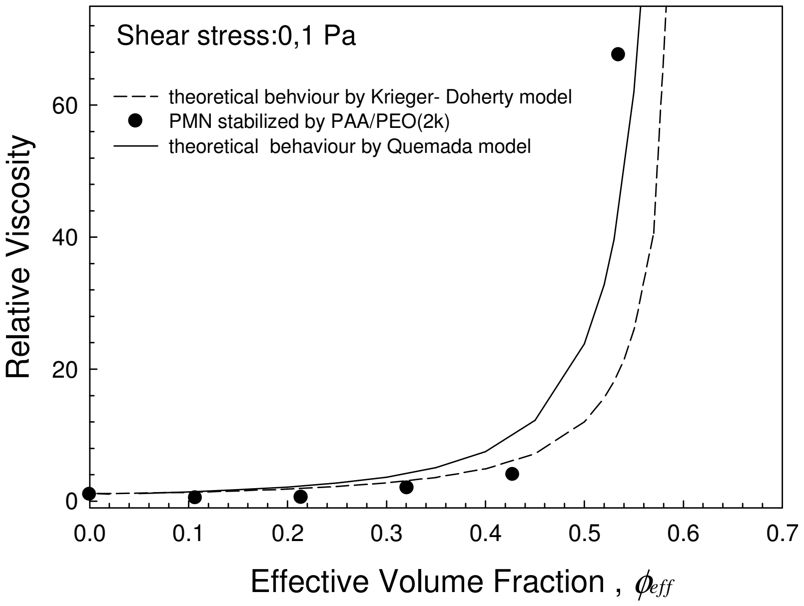

Figure 4.33. Relative viscosity of PMN suspensions as a function of effective volume fraction.

Viscoelastic behavior of PMN suspensions in the presence of PAA/PEO(2000) at various solids loadings are given in Figures 4.34 and 4.35. Very low storage modulus values even for the concentrated suspensions (50 vol%) indicate the liquid like behavior due to the electrosteric stabilization created by the PAA/PEO.

The flow behaviour of the PMN suspensions at 50 vol% in the presence of PAA/PEO fits the Cross model. The model equation is given below:

$$\eta = \frac{\eta_0 - \eta_\infty}{1 + \left(k\dot{\gamma}n\right)} + \eta_\infty \qquad (4.12)$$

Following are the model parameters obtained by the rheometer software (Bohlin,CS-50): $\eta_0 = 0.6426$, $\eta_\infty=0.008955$, k=0.2519, n=0.4948.

As the solids loading decreased to 40 vol% or 30 vol% the viscosity showed power law dependence to applied shear. The model parameters were determined to be $\eta = 0.02587$ and n=0.8082 for the 40 vol%; $\eta=0.01072$ and n=0.8957 for the 30 vol%. In the case of lower solids loadings (20 vol% and 10 vol%) the flow behavior fits to Bingham model.

Oscillation measurements (amplitude sweep at 1 Hz and frequency sweep) showed that the all the suspensions have very low elastic and loss modulus values which indicates very weak internal structure. This also gives information on the degree of flocculation on these systems.

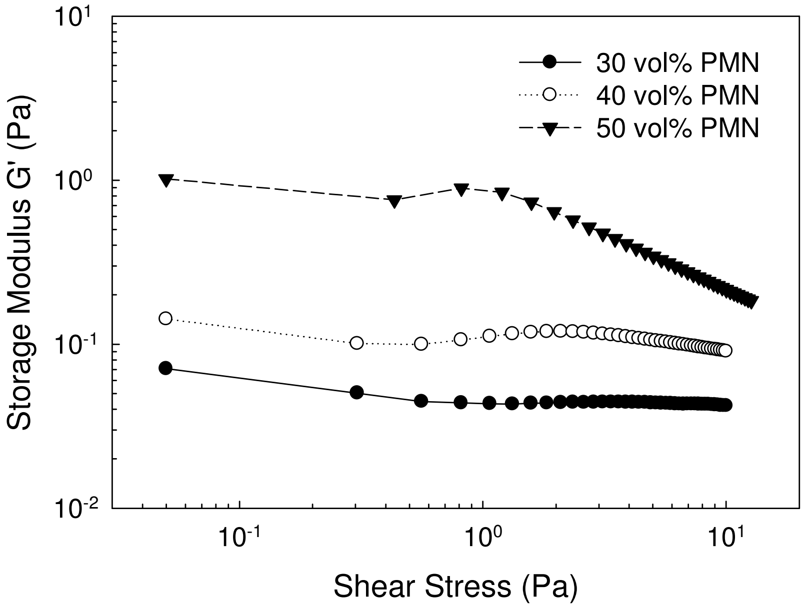

Figure 4.34. Storage modulus versus shear stress of PMN suspensions at different ϕ values in the presence of PAA/PEO(2000), 1wt%, at pH 9.

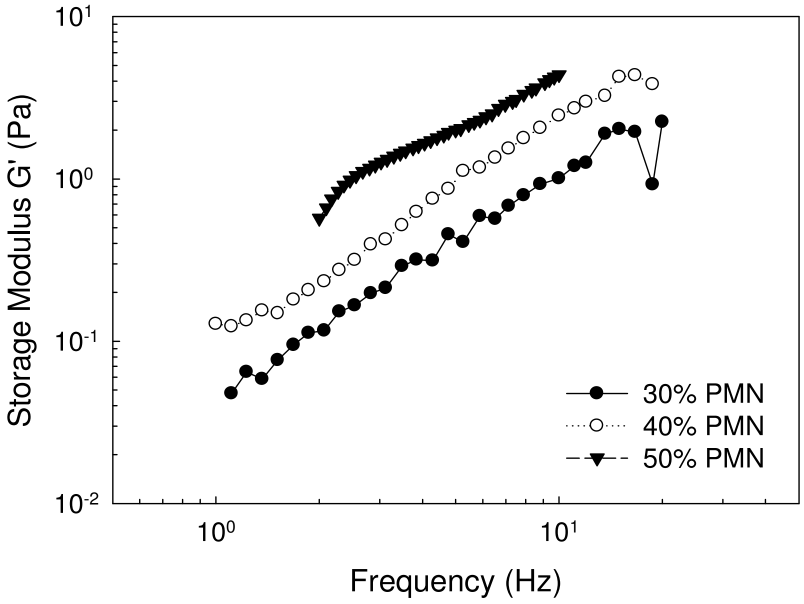

Figure 4.35. Modulus versus frequency graph of PMN suspensions at different ϕ values in the presence of PAA/PEO(2000), 1wt%, at pH 9.

4.3.2.4. Zeta Potential Measurements

The aim of the zeta potential measurements was to observe the influence of dispersants on the surface charge of the PMN particles. Zeta potential of PMN suspensions in the presence of PAA and PAA/PEO were measured as a function of pH and polymer concentration. Figure 4.36 shows the effect of PAA and PAA/PEO on the isoelectric point (IEP) of aqueous PMN suspensions at 20 vol%. As it was reported in the previous section IEP of bare PMN suspension at 20 vol% was around pH 9.8. On the other hand, addition of PAA or PAA/PEO to the system caused a shift in the IEP to lower pH values. The shift is a consequence of the adsorption of negatively charged PAA and PAA/PEO to the positively charged PMN. Therefore, PMN surface becomes negatively charged.

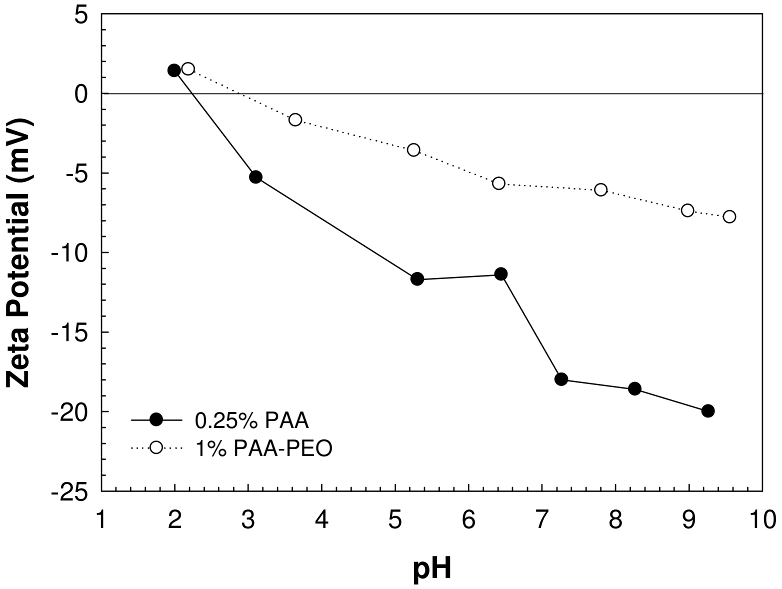

Figure 4.36. Effect of PAA, 0.25 wt% and PAA/PEO(2000), 1 wt% on the isoelectric point of PMN suspensions (20 vol%), 10^{-3} M KNO_3.

Results also showed that zeta potential of PMN suspensions containing comb polymers were lower compared to the zeta potential of suspensions containing PAA (Figure 4.36 to 4.38). In contrast, rheological measurements proved that PAA/PEO comb polymers are much more effective dispersants compared to the pure PAA for the aqueous PMN suspensions. One possible explanation for the low zeta potential values for the suspensions containing PAA/PEO may the charge shielding effect of neutral PEO block.

It is also important to note that the zeta potential of suspensions containing comb polymers at pH 9 and pH 6 were nearly the same at all polymer concentrations. However, suspensions containing PAA showed different behavior at pH 9 and pH 6. It is interesting to observe that PMN particles have a positive surface charge in the presence of polymers at pH 3. This may be related to the high solubility of PMN particles in acidic pH region.

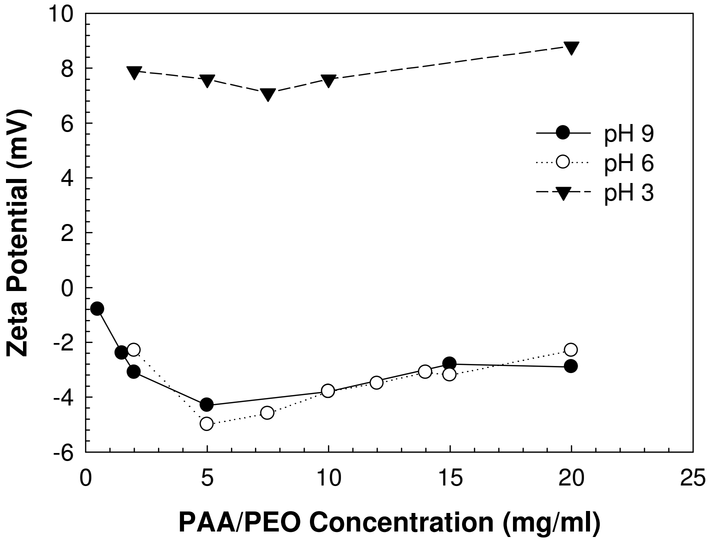

Figure 4.37. Effect of PAA/PEO concentrations on the zeta potential of PMN suspensions (20 vol%) at pH 3, 6 and 9.

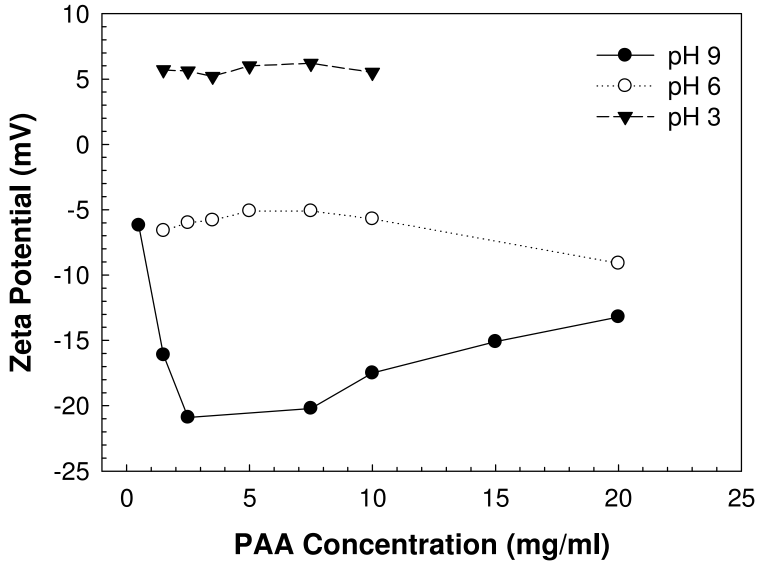

Figure 4.38. Effect of PAA concentrations on the zeta potential of PMN suspensions (20 vol%) at pH 3,6 and 9.

4.3.2.5. Sedimentation

Sedimentation tests were performed to understand the stability of PMN suspensions as a function of time. PMN suspensions (20 vol%) containing dispersants were prepared as discussed in the experimental section. Sediment height was recorded up to 30 days by taking the digital pictures of the samples in every 5 minutes using a video camera. Figure 4.39 shows the sediment heights of PMN suspensions in absence of the dispersant after 1 hour resting period. According to the graph the lowest sediment height was obtained at pH 2 and 3. This may be related to the very high solubility of Pb^{+2} and Mg^{+2} ions from the PMN surface at these pH values. On the other hand, sediment height was high at pH 9 and 10 since this pH is close to the IEP of PMN.

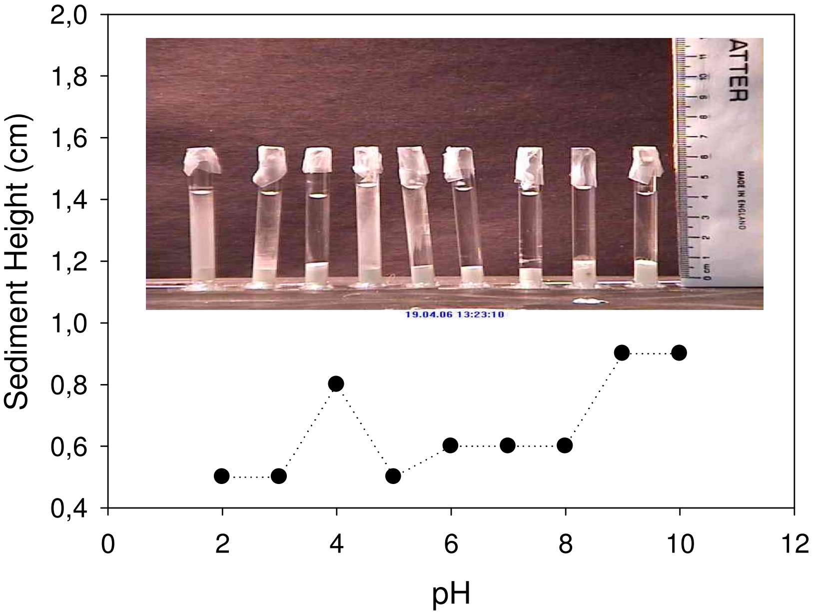

Figure 4.39. Sediment height of PMN/water suspensions (5 vol%) as a function of pH.

Figure 4.40 demonstrate the settling behavior of PMN suspensions in the presence of PAA at pH 9. It is clear from the figure that without dispersant PMN suspensions settles very quickly in 10 minutes. Therefore, the sediment height was high and constant in the absence of PAA through the measurement interval. On the other hand as the PAA concentration increased a decrease was observed in sediment height. The lowest sediment volume was obtained at 1.1 mg/m^2 (0.25 %) PAA concentration. At higher PAA concentrations sediment height started to increase again.

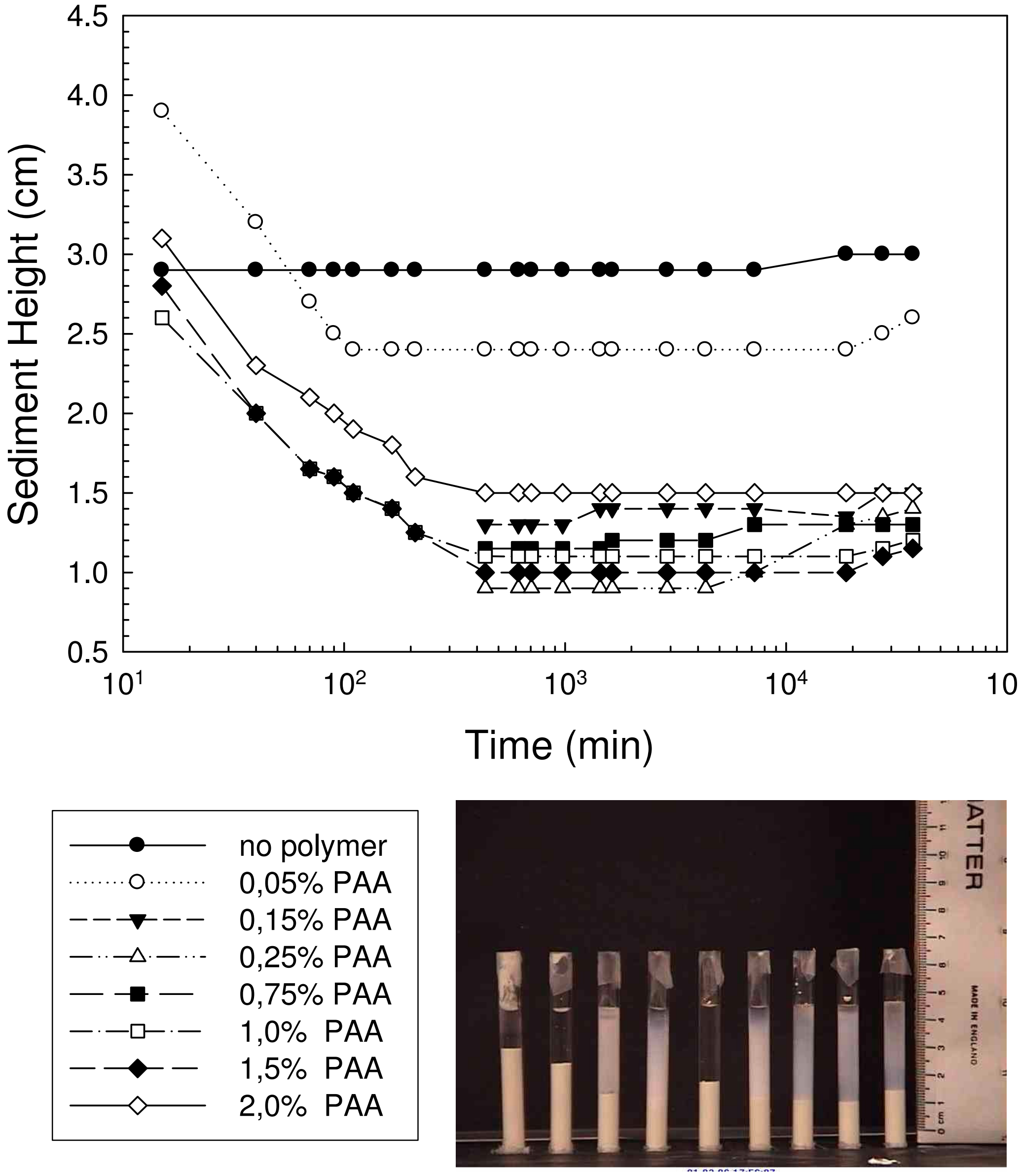

Figure 4.40. Effect of PAA concentration on the sediment height of PMN suspensions as a function of resting time at pH 9 and 20 vol%, polymer concentration in wt%.

Similar behavior was observed for the PMN suspensions prepared at pH 6 in the presence of PAA (Figure 4.41). But in that case the lowest sediment height was obtained for the suspension containing 0.15% PAA. On the other hand at pH 3, PAA caused rapid flocculation almost at all concentrations, as it is seen in Figure 4.42. Only at a concentration of 0.15% PAA the sediment height was slightly lower compared to the no dispersant case.

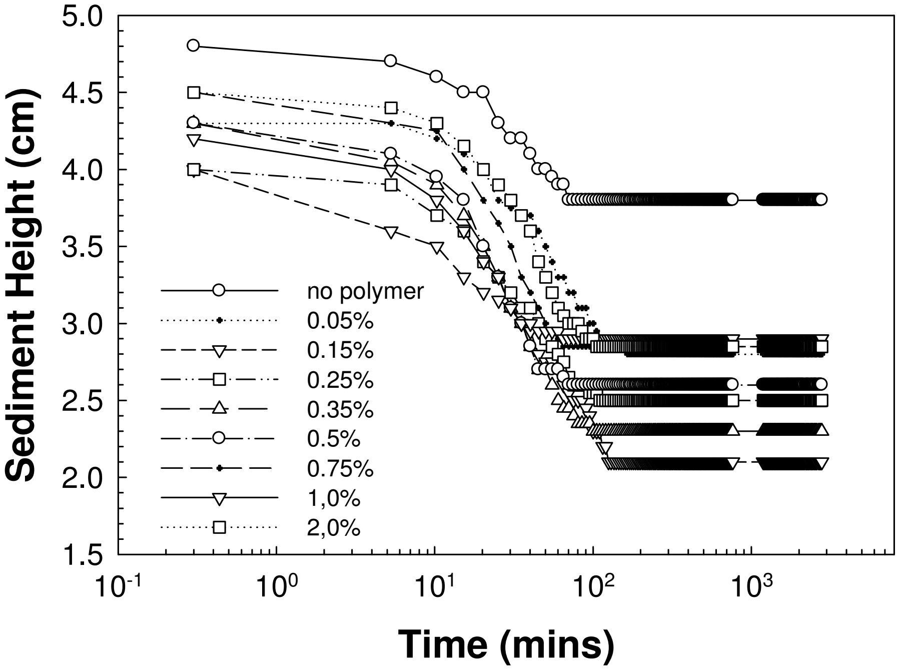

Figure 4.41. Effect of PAA concentration on the sediment height of PMN suspensions as a function of resting time at pH 6 and 20 vol%, polymer concentration in wt%.

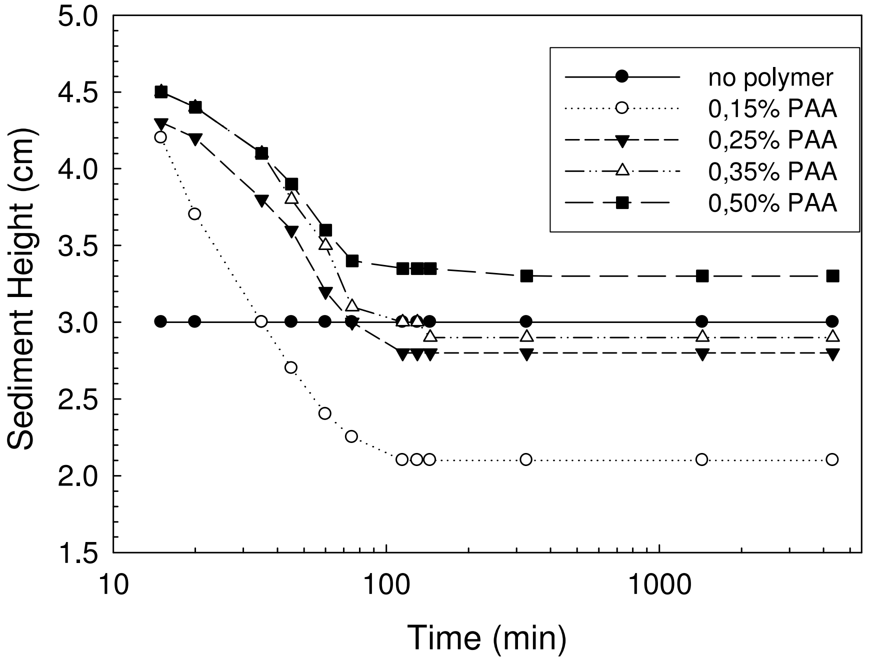

Figure 4.42. Effect of PAA concentration on the sediment height of PMN suspensions as a function of resting time at pH 3 and 20 vol%, polymer concentration in wt%.

Settling behavior of PMN suspensions in the presence of PAA/PEO comb polymer at pH 9, pH 6 and pH 3 are shown in Figures 4.43, 4.44 and 4.45, respectively. For the suspensions prepared at pH 9 the lowest sediment height was obtained at 4.35 mg/m^2 (1%) PAA/PEO. This result was consistent with the result obtained in viscosity measurements.

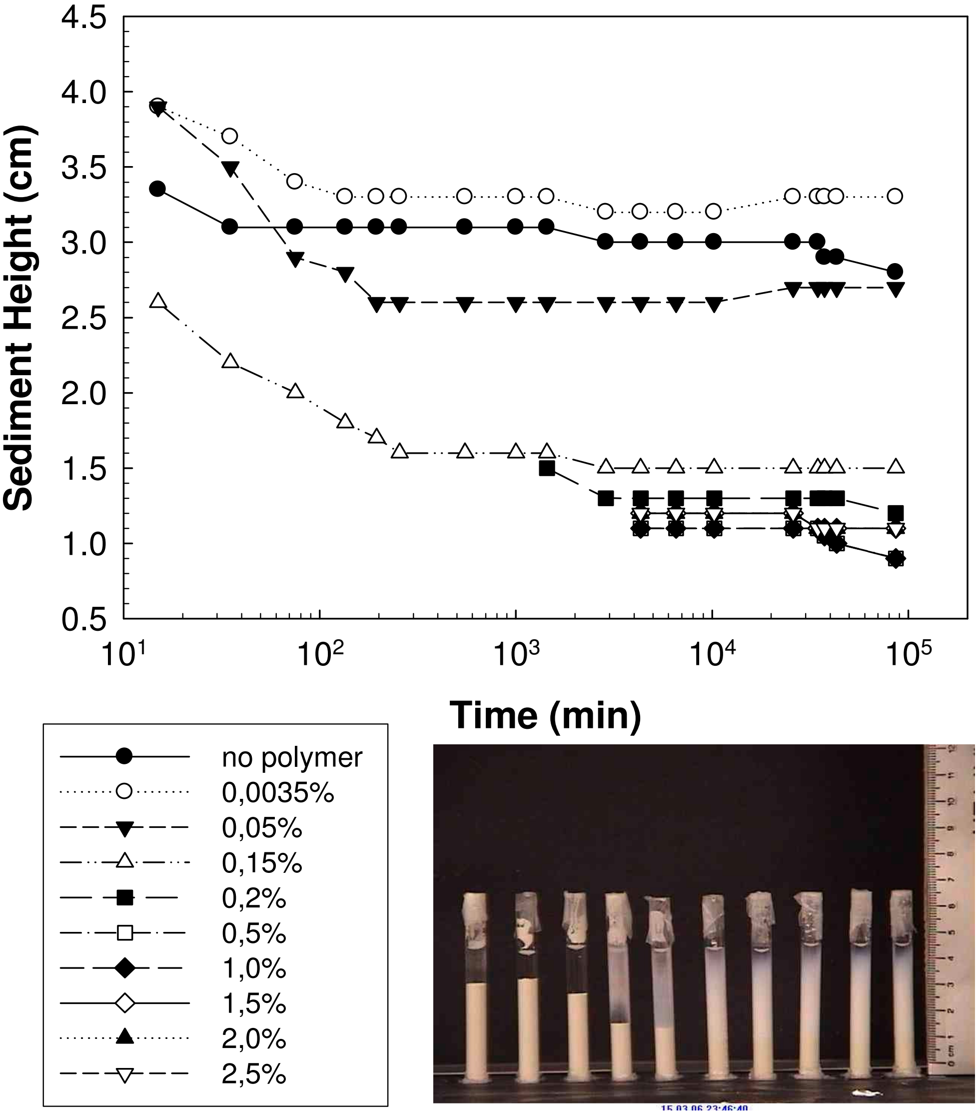

Figure 4.43. Effect of PAA/PEO(2000) concentration on the sediment height of PMN suspensions as a function of resting time at pH 9 and 20 vol%, polymer concentration in wt%.

Settling behavior of PMN suspensions prepared at pH 6 was similar to suspensions prepared at pH 9. On the other hand the settling height of the suspensions was nearly identical at all PAA/PEO concentrations at pH 3. Even at very high polymer concentrations such as 3.5% a flocculation was not observed.

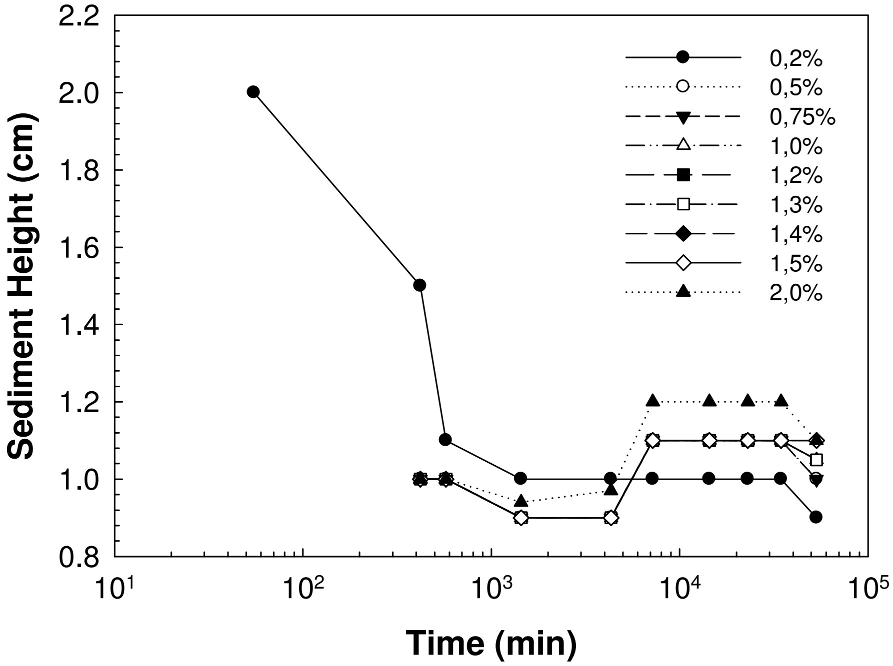

Figure 4.44. Effect of PAA/PEO(2000) concentration on the sediment height of PMN suspensions as a function of resting time at pH 6 and 20 vol%, polymer concentration in wt%.

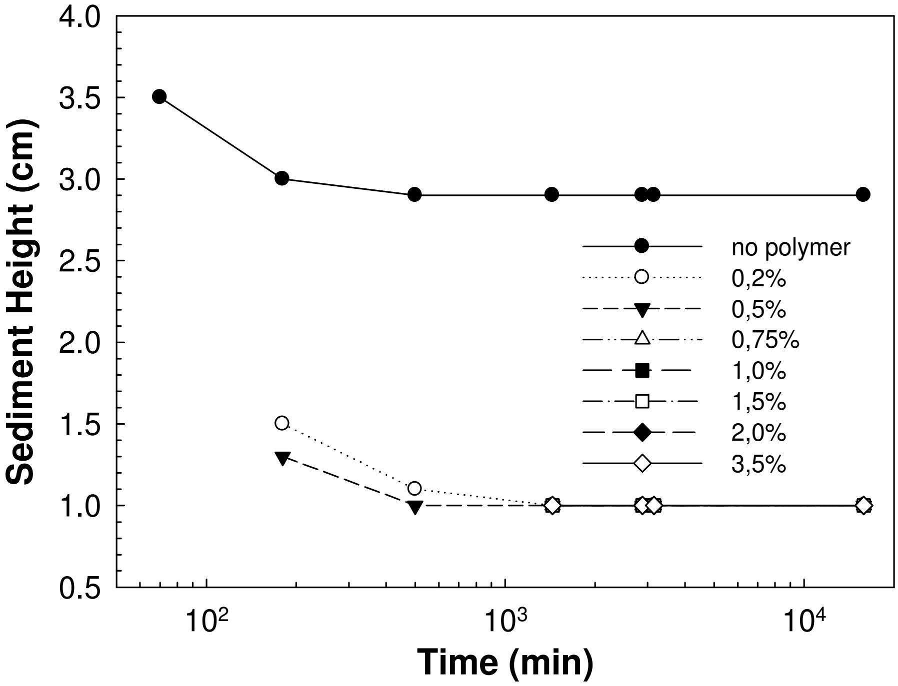

Figure 4.45. Effect of PAA concentration on the sediment height of PMN suspensions as a function of resting time at pH 3 and 20 vol%, polymer concentration in wt%.

4.3.3. Effect of PAA/PEO Molecular Architecture on Dispersion Properties

The influence of PAA/PEO molecular architecture (e.g. backbone molecular weight, teeth molecular weight and density) on the stability of particulate suspensions has been studied in cement/water system by Kirby and Lewis. Comb polymers with PAA backbone molecular weight of 5000 g/mole and a teeth density as defined by an acid: ester ratio of 5:1 have been reported to be the most effective for imparting stability to cement suspensions (Kirby and Lewis 2004). On the other hand, Nawa et al. reported that long teeth (about 3000 g/mole) were required to impart strong steric stabilization (Nawa et al. 2000). Therefore optimal architecture for PAA/PEO comb polymers is a subject of debate and should be investigated for PMN system.

In this work, effect of PAA/PEO comb polymer molecular architecture on the flow behavior PMN suspensions was studied using comb polymers with PEO group having a molecular weight of 2000, 1000, 400 and 360 g/mol and a teeth density (acid to ester ratio) of 3:1 and 7:1. Effect of comb polymer architecture on the stability of PMN suspensions was mainly examined by viscosity measurements, zeta potential measurements and sedimentation tests. Figures 4.46 and 4.47 show the viscosity of PMN suspensions (20 vol%) in the presence of PAA/PEO (1000) with acid: ester ratio of (3:1). Suspensions exhibited nearly Newtonian behavior starting from 1wt% polymer concentration. Below this value all the suspensions showed shear thinning behavior and have high viscosity values. Compared to the viscosity values of the suspensions prepared using PAA/PEO (2000) having an acid: ester ratio of (7:1), higher viscosity values were obtained.

On the other hand, comb polymer with PEO group having a molecular weight of 1000 g/mol with acid: ester ratio of (7:1) showed nearly identical behavior with the one having PEO molecular weight of 2000 and acid: ester ratio of (7:1). Therefore, high viscosity values obtained in the presence of comb polymer with low teeth density can not be attributed to the molecular weight of the PEO group (Figure 4.48 and 4.49). Rather than it may be due to the low acid: ester ratio of the polymer.

In the presence of comb polymers with PEO group having low molecular weights (400 and 360) with low acid: ester ratio of (3:1), suspensions showed similar behavior (Figures 4.50 to 4.53). Especially in the presence of comb polymer PAA/PEO

(400) suspensions exhibited Newtonian behavior starting from 0.5 wt% polymer concentration. The lowest viscosity value was obtained at 0.75 wt%. However, in the presence of PAA/PEO (360) even at the optimum polymer concentration suspensions showed slightly shear thinning behavior (Figure 4.52). Therefore, it is possible to conclude that molecular weight of the PEO group of the comb polymer used to disperse the PMN suspensions should be at least 400 g/mol to create full dispersion.

Zeta potential measurements showed that depending on the comb polymer architecture the magnitude of the zeta potential changes (see Figure 4.54). Comb polymers with PEO group having the same molecular weight showed similar zeta potential values although the acid: ester ratios were different. On the other hand the zeta potential values of the comb polymers having low molecular weight PEO group (360 and 400) were higher compared to the zeta potential of comb polymers with high molecular weight PEO group. The maximum zeta potential value was obtained at 7.5 mg/ml for comb polymers with low molecular weight PEO group.

Effect of polymer architecture on the isoelectric point (IEP) of the PMN suspensions were also investigated in the study. Results are presented in Figure 4.55. According to the graph no significant shift in the IEP was observed depending on the comb polymer molecular architecture. An isoelectric point was obtained between pH 3 and pH 4 at a comb polymer concentration of 10 mg/ml.

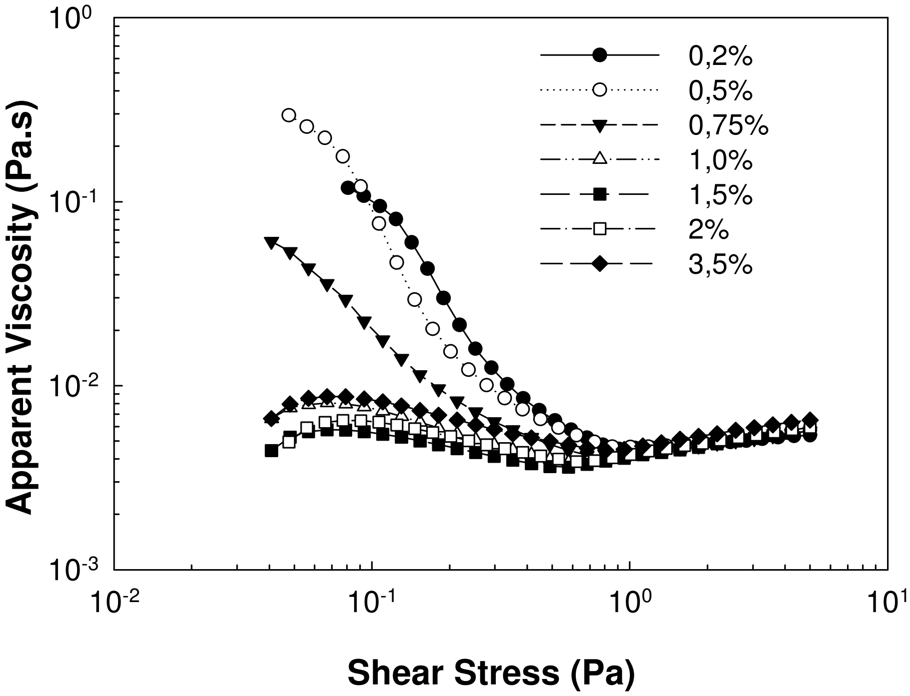

Figure 4.46. Effect of PAA/PEO(1000) acid: ester (3:1) concentration on the flow behavior of PMN suspensions (20 vol%, pH 9).

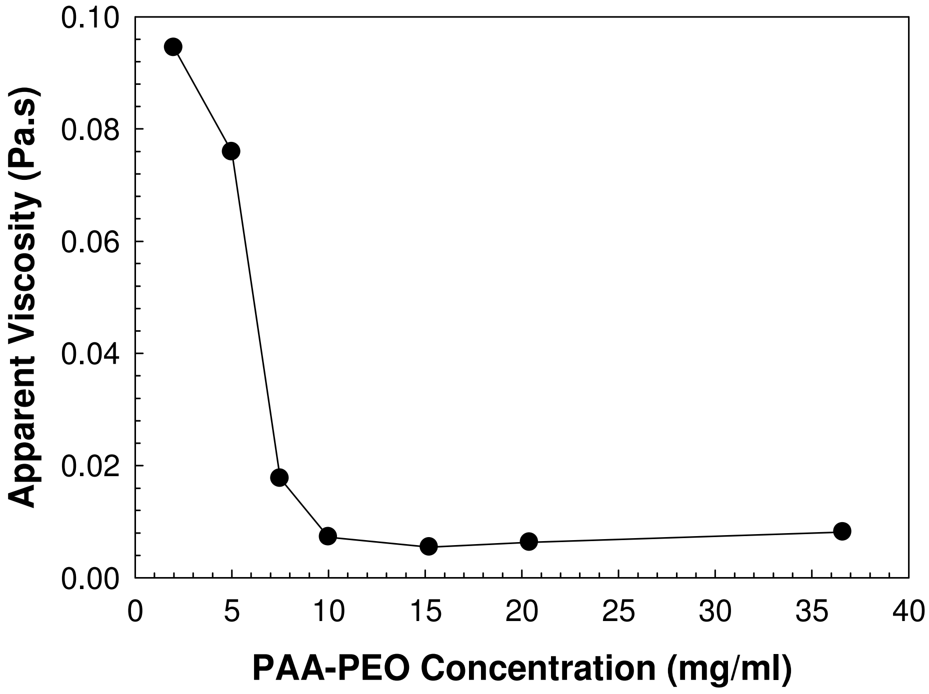

Figure 4.47. Viscosity of PMN suspensions in the presence of PAA/PEO(1000) acid: ester (3:1) at 0.1 Pa.

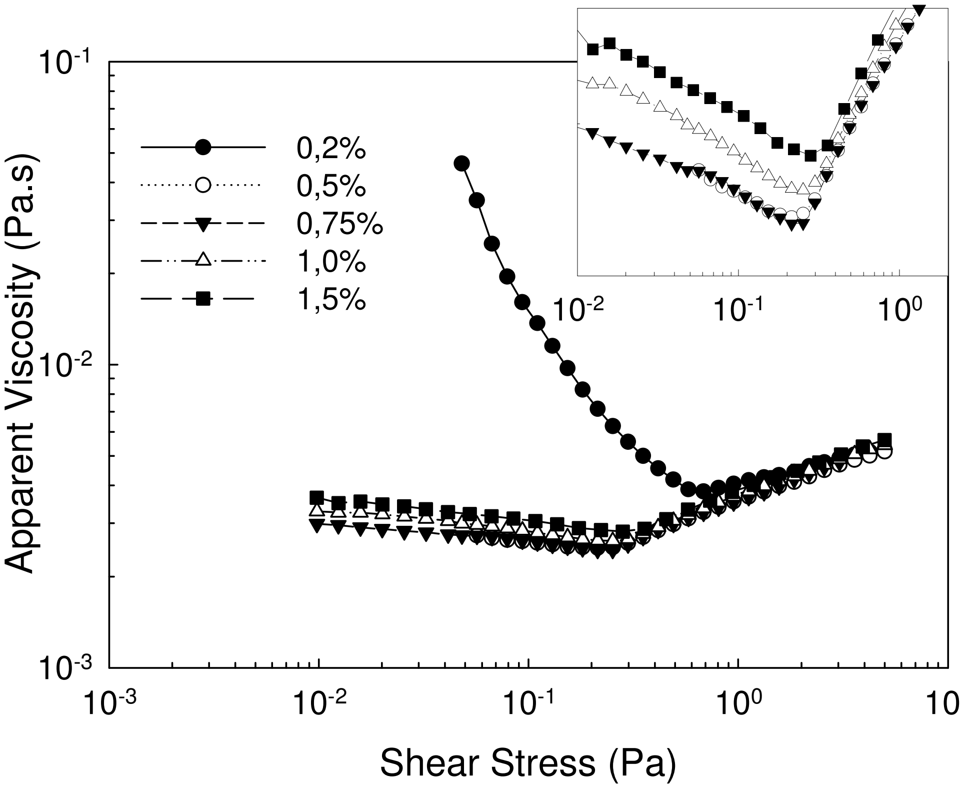

Figure 4.48. Effect of PAA/PEO(1000) acid:ester (7:1) concentration on the flow behavior of PMN suspensions(20 vol%, pH 9).

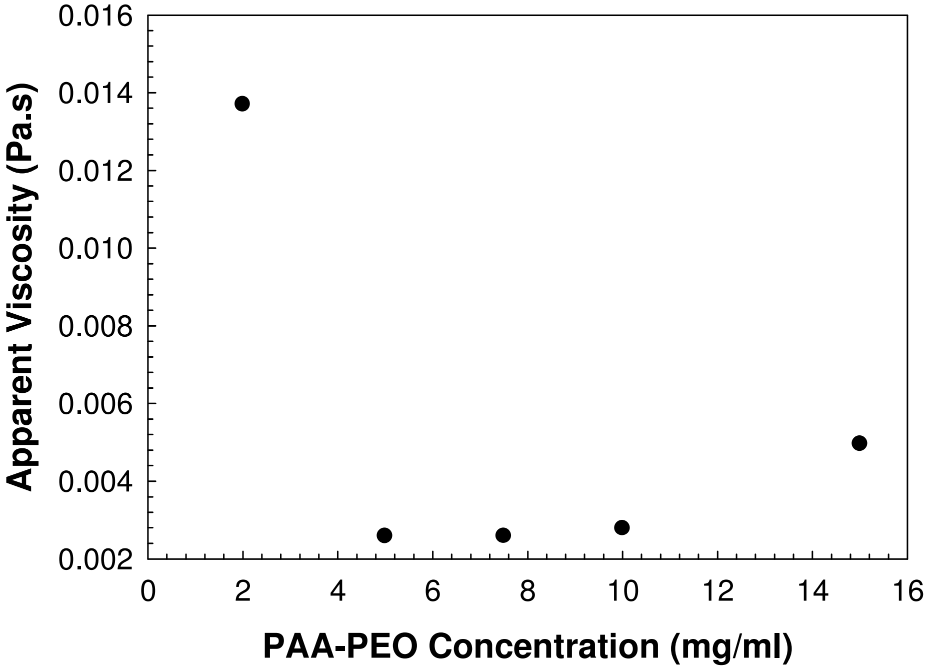

Figure 4.49. Viscosity of PMN suspensions in the presence of PAA/PEO(1000) acid: ester (7:1) at 0.1 Pa.

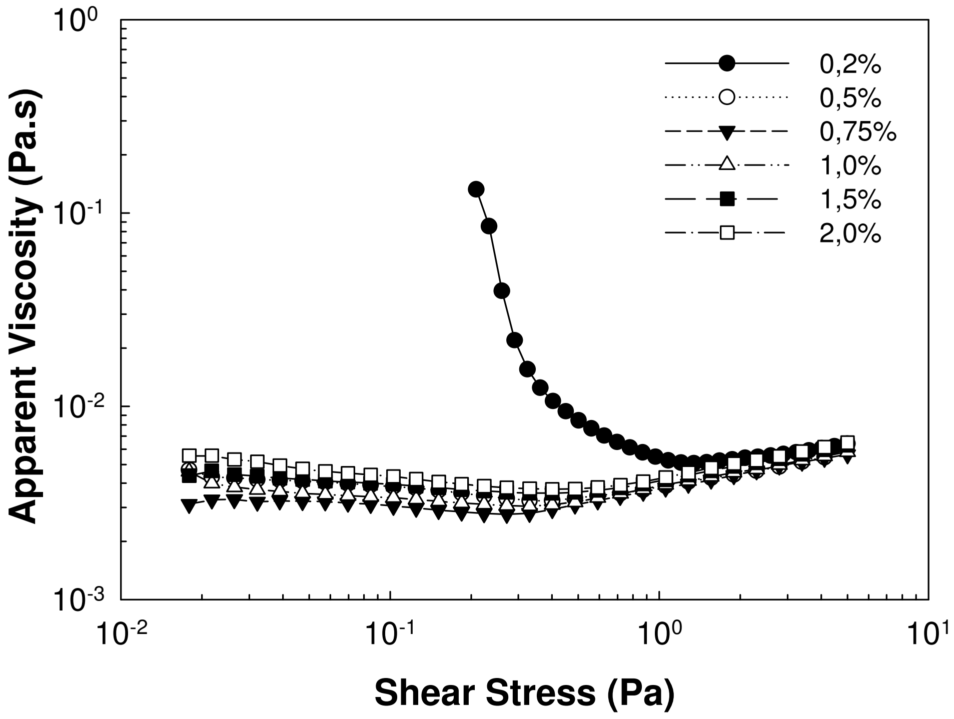

Figure 4.50. Effect of PAA/PEO(400) acid:ester (3:1) concentration on the flow behavior of PMN suspensions (20 vol%, pH 9).

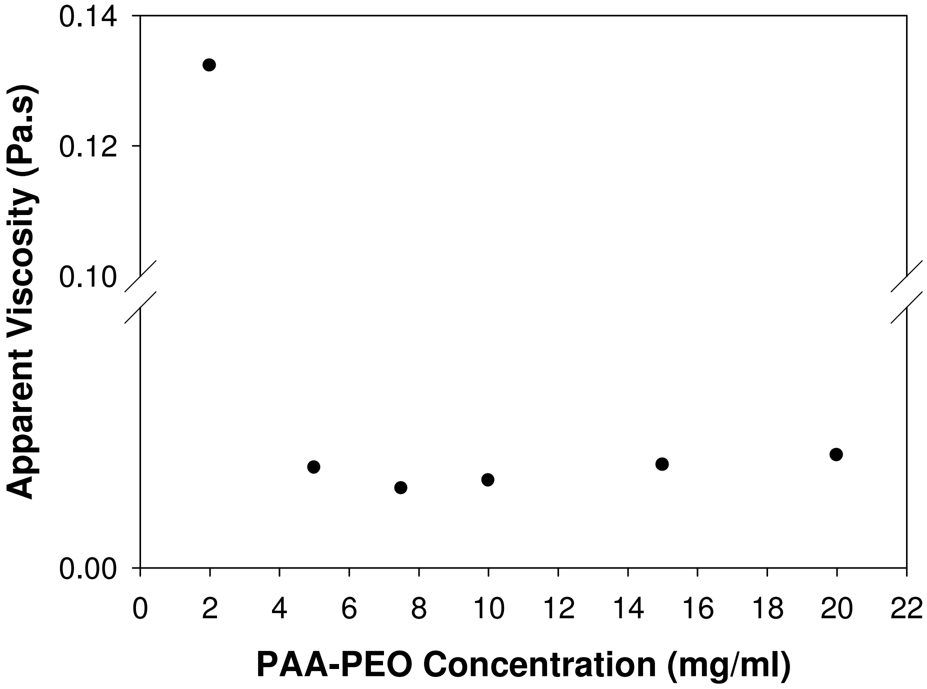

Figure 4.51. Viscosity of PMN suspensions in the presence of PAA/PEO(400) acid:ester (3:1) at 0.1 Pa.

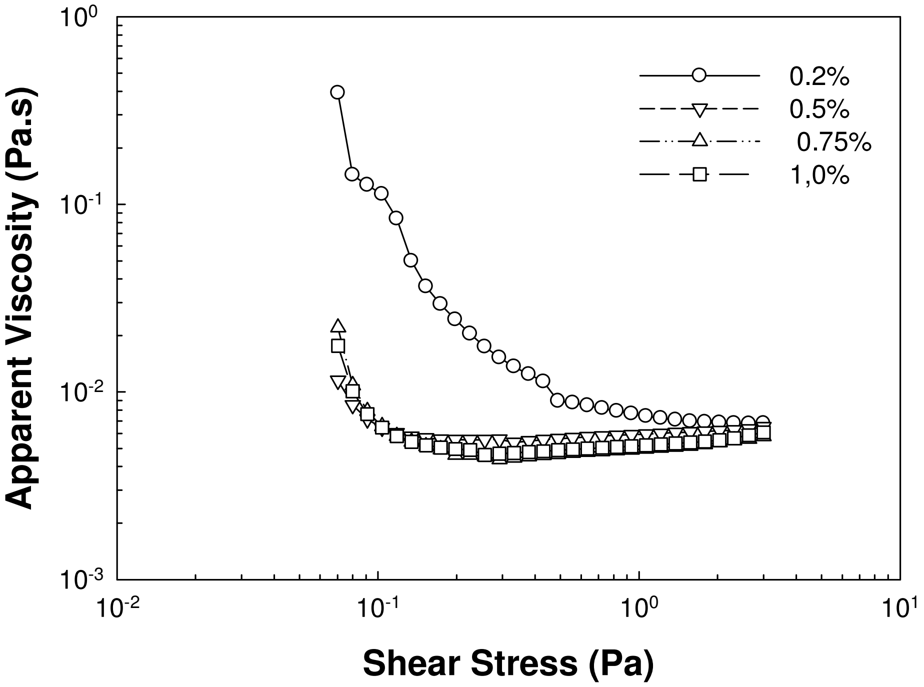

Figure 4.52. Effect of PAA/PEO(360) acid:ester (3:1) on the flow behavior of PMN suspensions (20 vol%, pH 9).

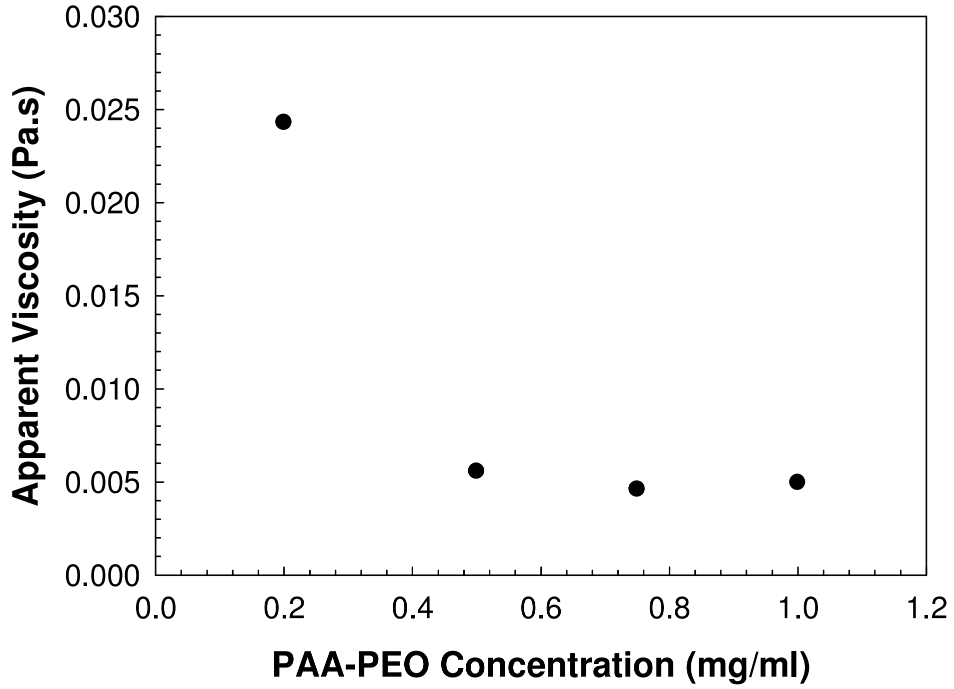

Figure 4.53. Viscosity of PMN suspensions in the presence of PAA/PEO(360) acid: ester (3:1) at 0.1 Pa.

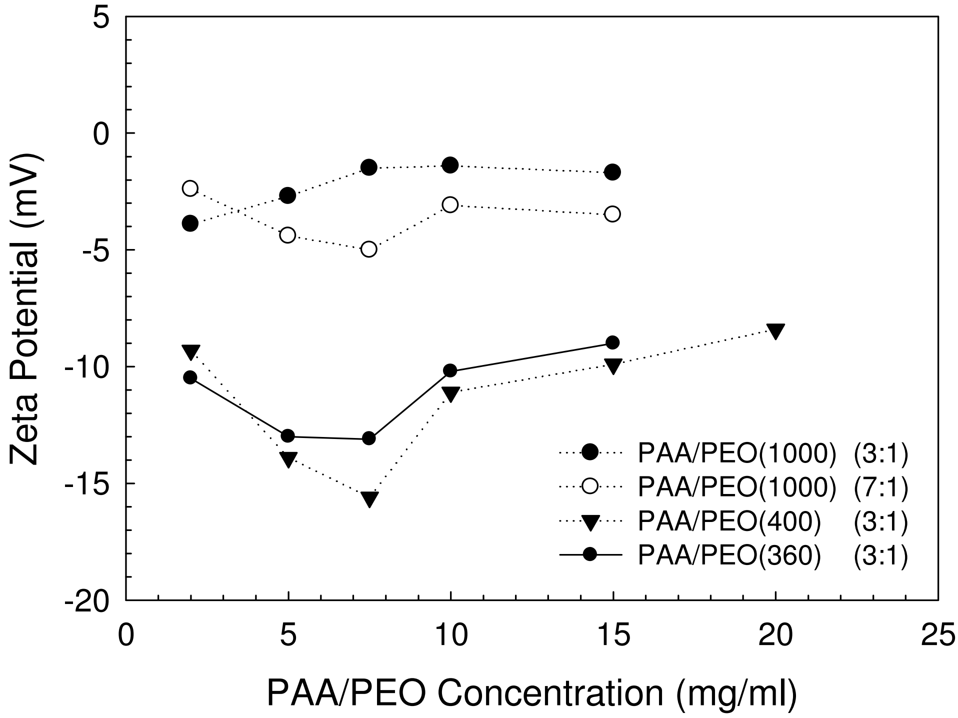

Figure 4.54. Effect of comb polymer architecture on the zeta potential of PMN suspensions at pH 9 and 20 vol%.

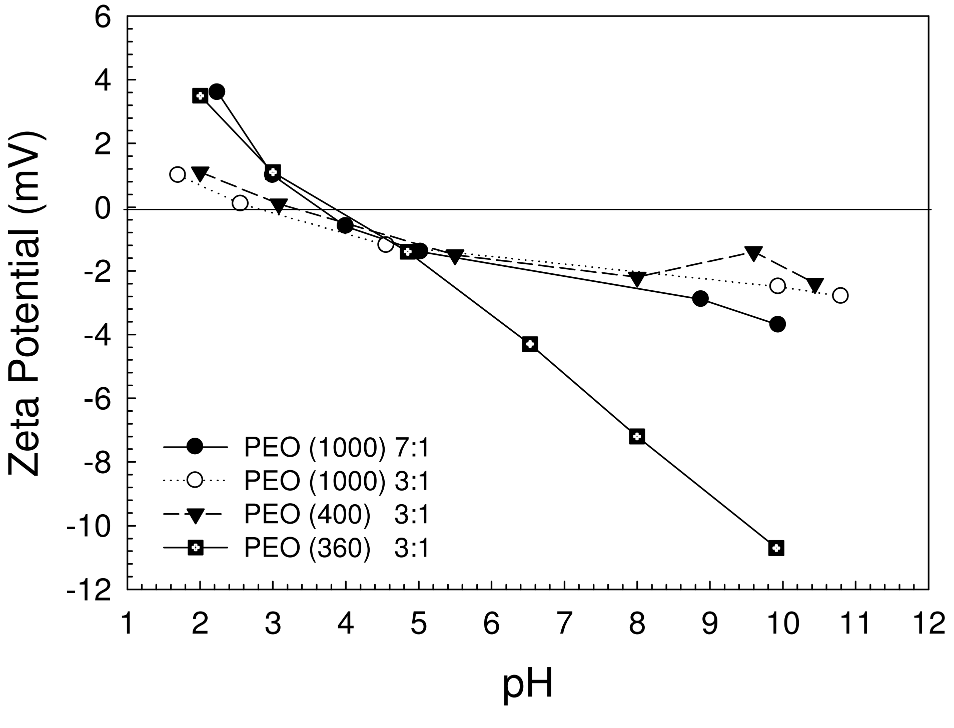

Figure 4.55. Effect of comb polymer architecture on the IEP of PMN suspensions at 20v%, 10^{-2} M KNO_3, PAA/PEO 1 wt%.

Sedimentation tests were performed for PMN suspensions at 20 vol% solids concentration in the presence of comb polymers as a function of time and comb polymer concentration at pH 9. Sediment height was recorded after 24 hours resting time since before this period the suspension turbidity was very high. Figure 4.56 shows the settling behavior of PMN suspensions in the presence of comb polymer with PEO group having a molecular weight of 1000 g/mol and acid: ester ratio of (3:1). According to the figure for polymer concentrations 0.5 wt% and above sediment height was low and constant.

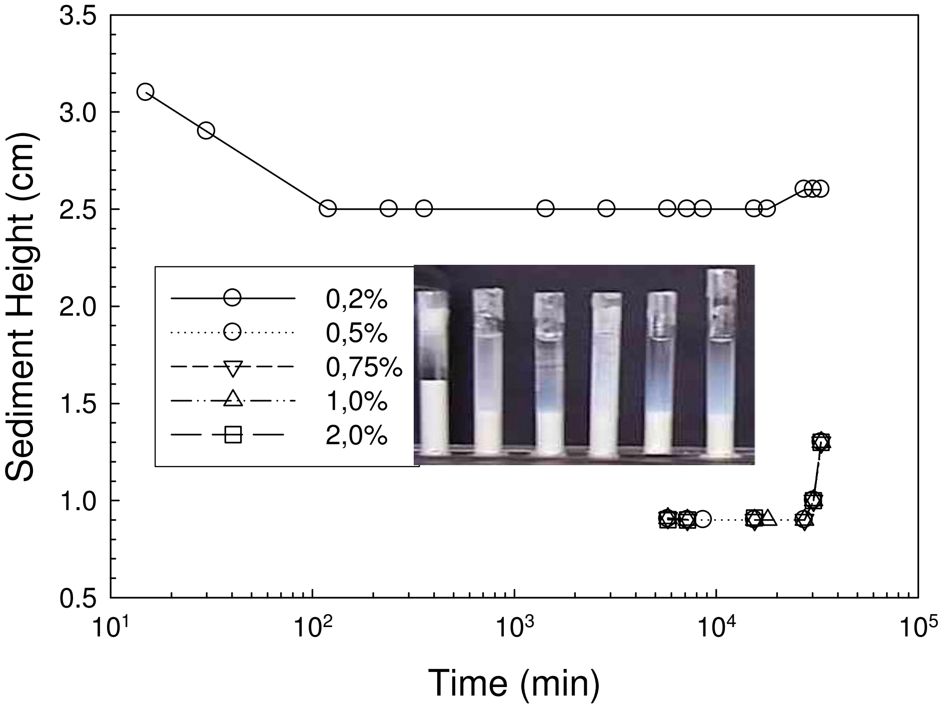

Figure 4.56. Effect of PAA/PEO(1000) acid: ester (3:1) concentration on the sediment height of PMN suspensions as a function of time at pH 9.

Similar results were observed in sedimentation tests of the suspensions containing comb polymers with PEO group molecular weight of 400 g/mole and acid: ester ratio of (3:1) (see Figure 4.58). Again for polymer concentrations 0.5 wt% and above sediment height was low and constant. On the other hand, in the case of comb polymer with PEO molecular weight of 1000 g/mol and acid: ester ratio of (7:1) a slight increase was observed in the sediment height starting from 1.5 wt% polymer concentration (Figure 4.57).

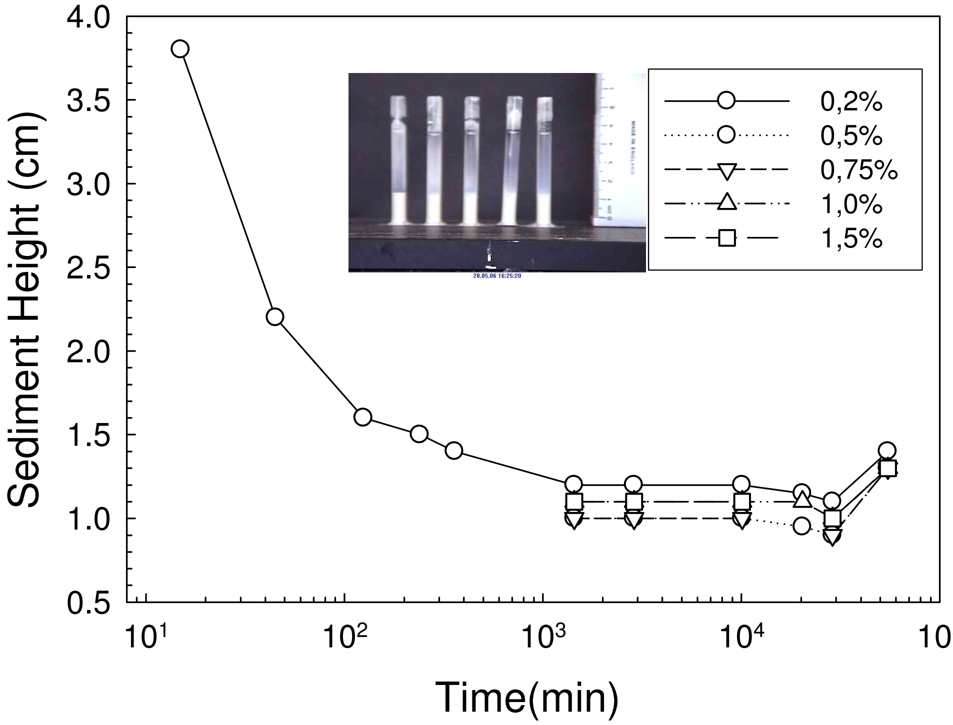

Figure 4.57. Effect of PAA/PEO(1000) acid: ester (7:1) concentration on the sediment height of PMN suspensions as a function of time at pH 9.

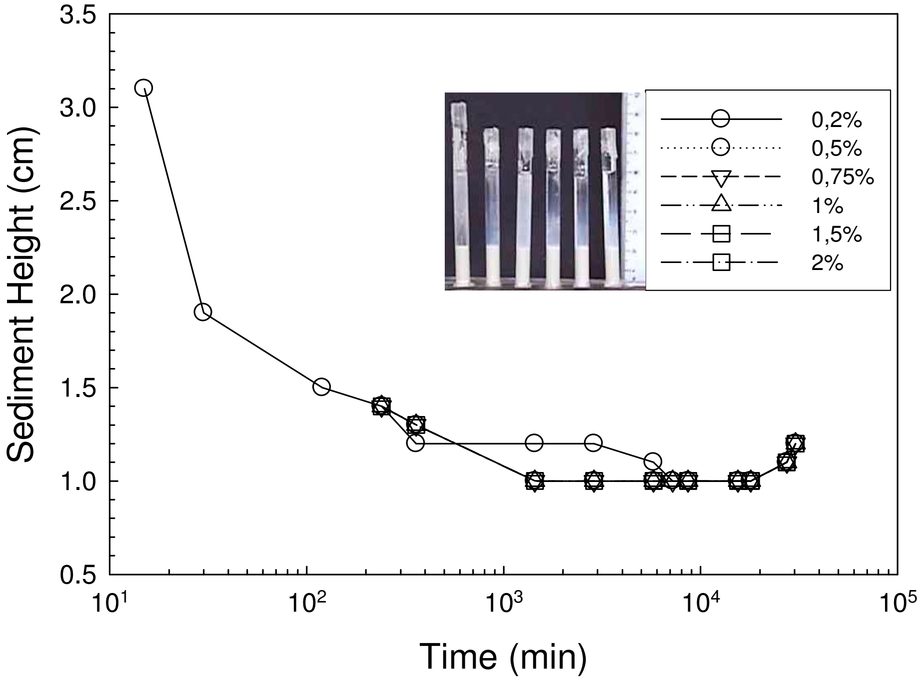

Figure 4.58. Effect of PAA/PEO(400) acid: ester (3:1) concentration on the sediment height of PMN suspensions as a function of time at pH 9.

4.3.4. Adsorption Behavior of Polyelectrolytes onto PMN

Adsorption behavior PAA and PAA/PEO comb polymers onto PMN surface was studied as a function of polyelectrolyte concentration, pH and ionic strength. All experiments were performed at a solids loading of 10 vol%. Figure 4.59 shows the effect of equilibration time on the adsorption behavior of PAA (1.1 mg/m^2) and PAA/PEO (4.35 mg/m^2) at pH 9. According to the graph after 1 hour mixing adsorption of polyelectrolytes onto PMN surface reaches equilibrium.

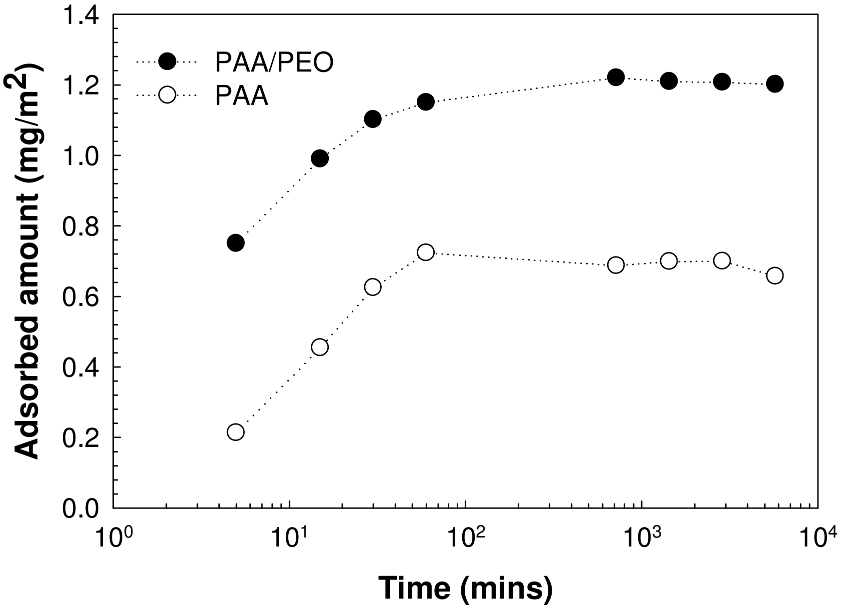

Figure 4.59. Adsorbed amount of PAA and PAA/PEO(2000) onto PMN surface as a function of time.

The pH dependence of adsorption isotherms of PAA and PAA/PEO onto PMN surface are shown in Figures 4.60 and 4.61, respectively. The plots represent the amount of polymer that is adsorbed per unit surface area of the powder versus the total amount of polymer that is added to the suspension. The dash line shows the complete (100%) adsorption.

Results indicate that adsorption increased with decreasing pH for both PAA and PAA/PEO solutions. The adsorption isotherms for PAA at pH 3 can be described as high affinity type and characterized by a strong adsorption. In contrast, isotherms correspond to pH 9 for PAA are non-high affinity type with most of the polymer remaining free in solution. Similarly, PAA/PEO comb polymer showed a low affinity adsorption onto PMN surface at all pH values.

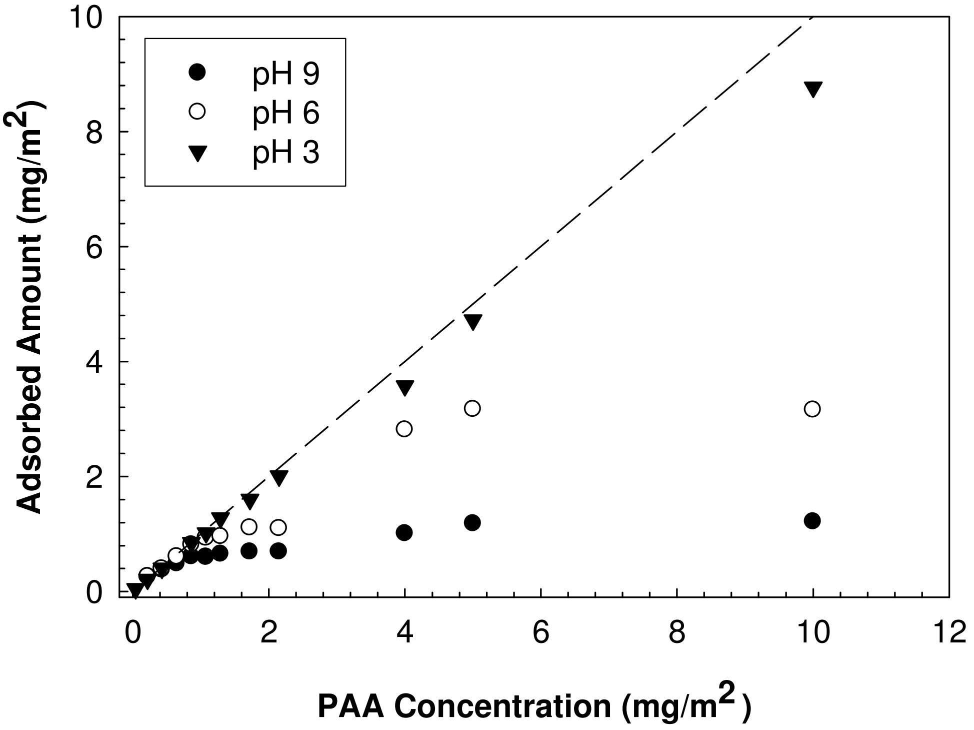

Figure 4.60. Adsorption curves of PAA onto PMN surface at pH 3, 6 and 9.

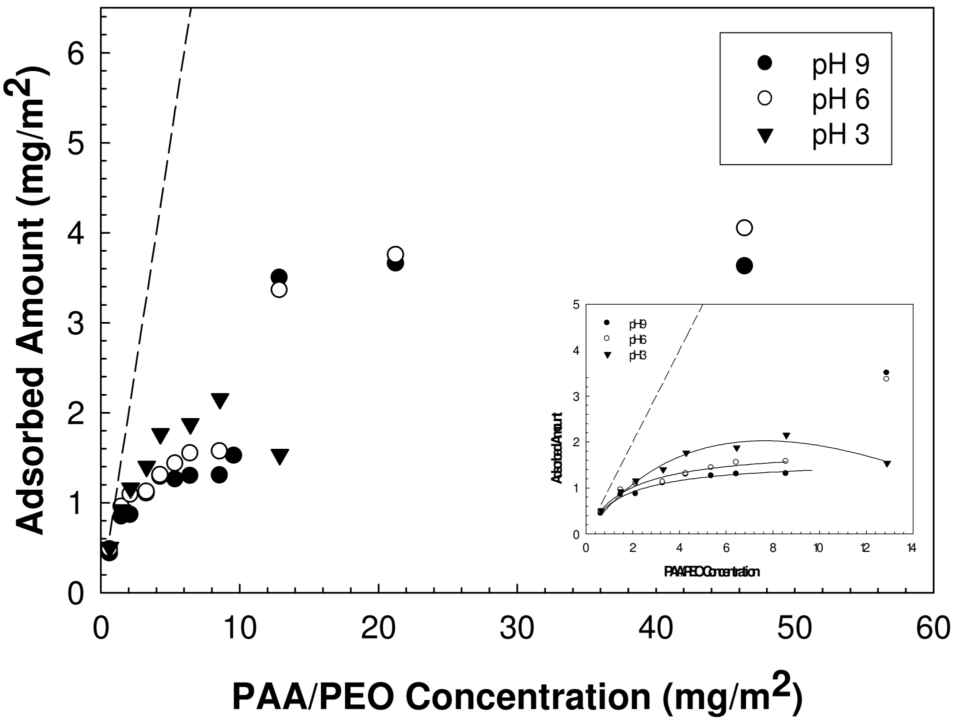

Figure 4.61. Adsorption curves of PAA/PEO(2000) onto PMN surface at pH 3, 6 and 9.

The acidic carboxyl groups in both polyelectrolytes are characterized by a pH dependent ionization behavior and the ability to exchange with surface hydroxyls bonding with the underlying metal ion in PMN. With the binding of multiple carboxyl groups on the surface this may lead to irreversible high affinity adsorption.

As it is known, the free energy of adsorption of polyelectrolyte is a balance between the attractive and repulsive interactions (Joanny 1999). The first term results from the electrostatic attraction between the surface charge group and the opposite charges on the polyelectrolyte, and the contribution of van der Waals interaction between the polyelectrolyte segments and the surface groups. The second term originates from entropy loss or osmotic effect (Bouhamed et al. 2005, Steeg et al. 1992).

Adsorption of PAA may be dominated by electrostatic interactions between the ionized sites on the polymer and surface charged sites on the PMN. Similarly, interaction between polycarboxylates and metal oxide surfaces has been examined by many researchers previously. Results showed that there is a general trend for PAA adsorption on oxide and non-oxide substrates that is adsorption increases with decreasing pH (Pedersen and Bergstrom 2000).

Cesarano and Aksay examined the adsorption of poly (methacrylic) acid onto alpha alumina surface. According their results under fully ionized conditions (pH 9) polyelectrolyte chains adsorb in a relatively flat conformation with each chain covering a large amount of surface area. In this condition polyelectrolyte tails can still extend into the solution even though formation of the loops is inhibited. As the pH decreased and the ionization approaches to zero the polyelectrolyte chains become uncharged and the formation of the loops in the adsorbed configuration is enhanced (Cesarano and Aksay, 1988b). According to the Hackley in the undissociated form, PAA adsorption may be controlled by forces dependent on the polymer chain length such as hydrophobic interactions or hydrogen bonding (Hackley 1997).

Similarly, the strong adsorption of PAA onto metal oxides in acidic region has been attributed to the following effects by Paik and co-workers: i) Ionization is near zero at pH 3 therefore the repulsive interactions between the neighboring carboxyl sites are eliminated. Furthermore the coiled structure permits a denser packing. ii) Solvency will be reduced due to low ionization value and this will force the polymer onto the surface (Paik et al. 2003). Figure 4.62 depicts the adsorption mechanism of PAA onto alumina surface.

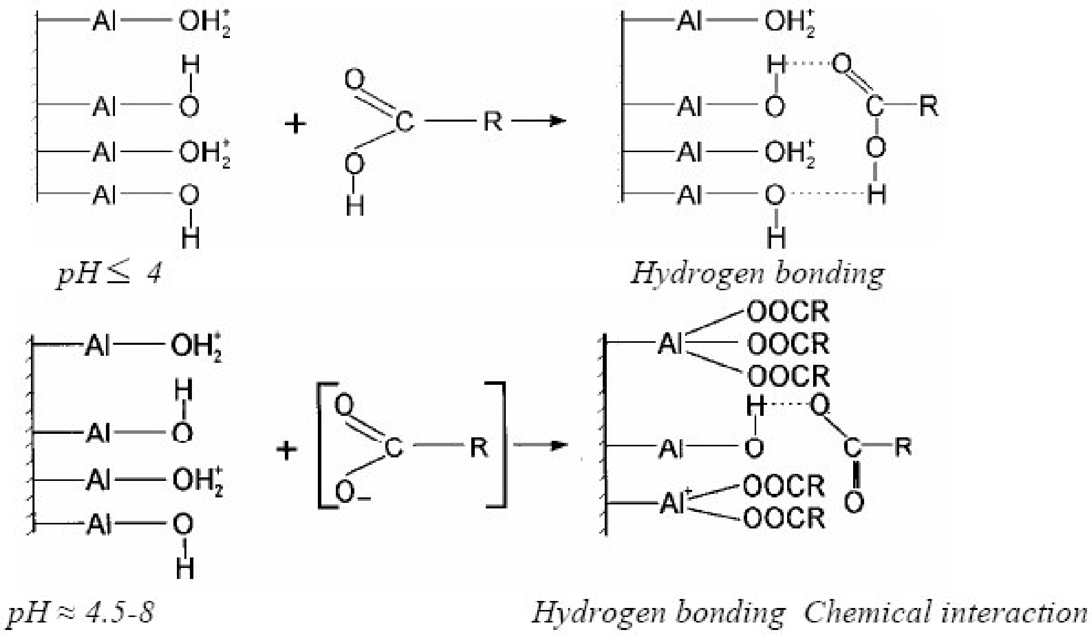

Figure 4.62. Interaction mechanisms between PAA and Al_2O_3 as a function of pH. (Source: Chibowski and Paszkiewicz 2006)

Based on the literature (Pan et al. 2001, Das and Somasundaran 2001, Chibowski and Paszkiewicz 2006, Hoogeveen et al. 1996), and the results of this study a possible explanation for the adsorption mechanism of polycarboxylates onto PMN surface is given in the following paragraph:

Below pHpzc, for adsorption process of the polyelectrolyte with carboxyl groups on positively charged PMN surface the hydrogen bonds and electrostatic interactions are responsible. In pH 4.5-9 range, besides hydrogen bond, chemical interactions between ionized carboxyl groups and Pb^{+2} and Mg^{+2} ions may be present on surface of the oxide can drive the adsorption. Electrostatic interactions also take place in this pH range. Above pHpzc, for adsorption process of polyelectrolytes onto PMN surface only specific interactions are responsible (hydrogen bridge or chemical reactions between $M^{+2}OH$ and $-COO-$ groups). In this pH range there is no electrostatic interactions and therefore adsorption of PAA is low.

Figure 4.63 shows the adsorption isotherms of PAA/PEO comb polymers having different molecular architecture onto PMN surface at pH 9. Accordingly, all comb polymers tested in the study showed low affinity type adsorption onto PMN surface. Adsorption behavior was almost the same for all the comb polymers although their molecular weight and the acid:ester ratios were not identical. Therefore, it was concluded that adsorption of PAA/PEO comb polymers was not very much dependent on the length of the PEO group. Figure 4.63 also shows that comb polymer with low PEO teeth length and acid: ester of 3:1, exhibited poor adsorption characteristics (Γ_p=0.6 mg/m^2 PMN) over the entire range of concentrations studied.

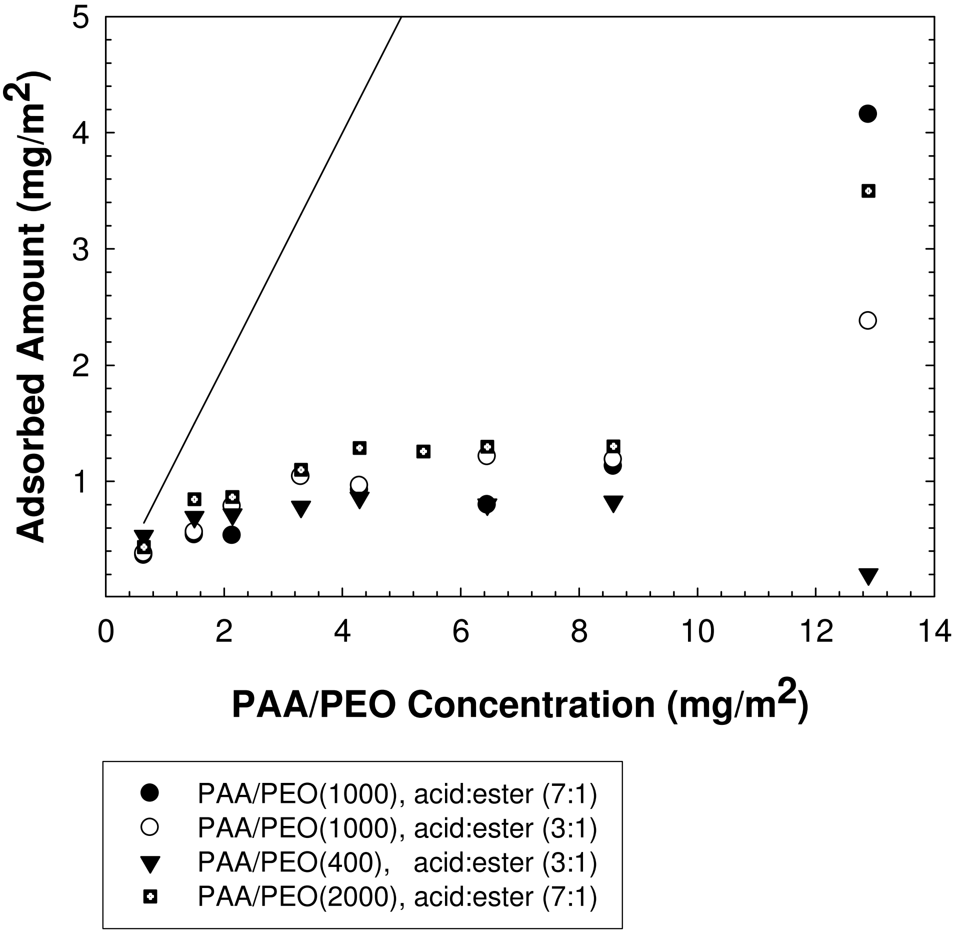

Figure 4.63. Adsorption curves of PAA/PEO comb polymers having different architecture onto PMN surface, pH 9, 10 vol%.

Additionally, a multilayer adsorption was observed in the presence of comb polymers. The reason of the possible multilayer adsorption can be explained by the previous theory of Dobbie and co-workers. Accordingly, they drawn attention to the interaction between the carboxyl groups and the PEO and claimed that there is hydrogen bonding between the –OH groups in the surface carboxyl groups of the polystyrene lattices and the ether oxygen of the PEO group (see Figure 4.64) (Dobbie et al. 1973). Similarly, in our case it may be possible to consider an interaction between the PEO groups of the adsorbed comb polymer and the PAA group of the excess free comb polymer in suspension.

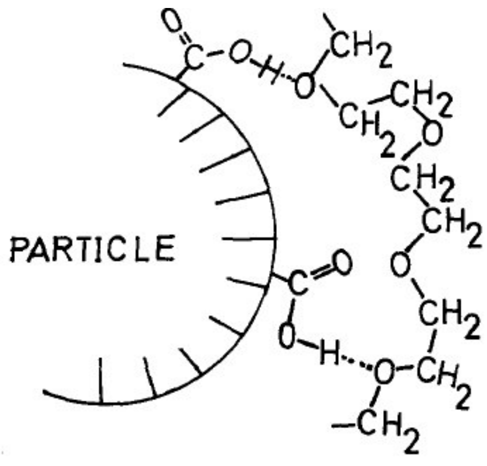

Figure 4.64. Schematic presentation of the interaction between surface carboxyl groups and the PEO (Source: Dobbie et al. 1973).

In the current study, it is also important to know that there is no adsorption between the PEO groups of the comb polymer and the PMN surface because PEO adsorbs only on surfaces with strong Bronsted acid sites, such as MoO_3, V_2O_5 and SiO_2. For materials with IEP greater than SiO_2 adsorption of PEO does not occur (Sindel et al. 1999, Mathur and Moudgil 1997). Therefore, there is no possibility for any interaction between the PMN and PEO groups of the comb polymer.

Other possible explanation for the multilayer adsorption observed at high polymer concentrations can be attributed to the low surface area of PMN in highly concentrated polymer solutions. Pan et al. investigated the effect of solids loading on the adsorption density of PAA on Al_2O_3. Results showed that addition of a few alumina particles to a solution of high polymer concentration may in fact “seed” the precipitation or multilayer adsorption of PAA onto alumina (Pan et al. 2001). Therefore, apparent adsorption density greatly increased at low solids concentrations. As more solids are added however, the surface area for adsorption was no longer limited.

In our study the effect of monovalent and divalent salt additions on the adsorption behavior of PAA and PAA/PEO comb polymers was also studied as a function of polymer concentration. Figures 4.65 and 4.66 depict the effect of background electrolytes on the adsorption of PAA/PEO and PAA, respectively. According to Figure 4.65 in the presence comb polymer both monovalent and divalent salts caused a slight increase in the adsorbed amount. However, the effect was more significant in the in case of PAA. Because the background salt has an electrostatic shielding effect between the negatively charged sites on the PAA thereby causing the chains behave more like uncharged polymers and enhancing the development of the loops (Cesarano and Aksay 1988a).

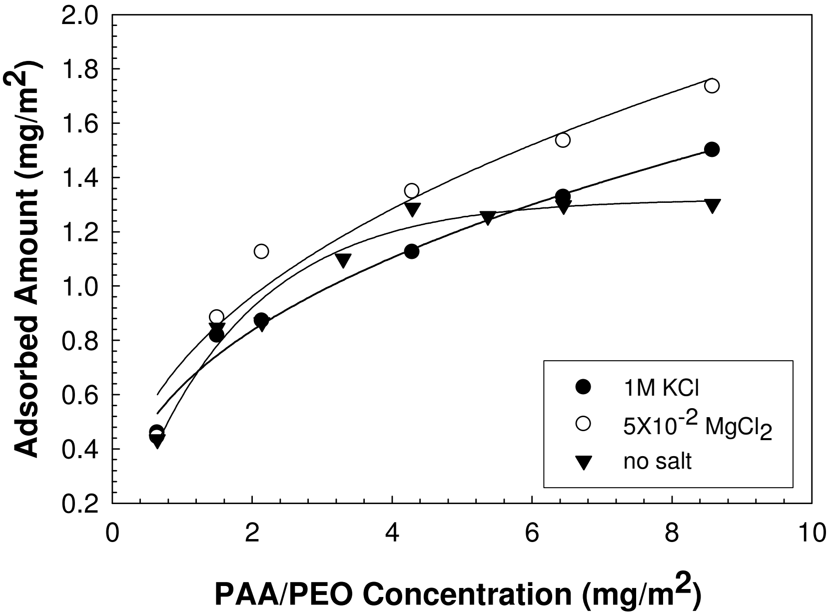

Figure 4.65. Effect of monovalent and divalent salt additions on the adsorption behavior of PAA/PEO(2000) onto PMN surface at pH 9, 10 vol%.

Results showed that for the both polyelectrolytes under investigation the adsorption amount was slightly higher in the case of $MgCl_2$ compared to the KCl. It is a known fact that the adsorption of PAA can be strongly affected by the presence of multivalent ions. Vermohlen et al. investigated the effect of Ca^{+2} on the adsorption of acrylic based polyelectrolytes onto oxide surfaces. It was found that the plateau value of the adsorption isotherms is greatly increased by Ca^{+2} ions (Vermohlen et al. 2000). This is because multivalent cations can bind to the carboxyl functional groups of the polyelectrolyte to form PAA-cation complexes (R- COO— M^{+2}—OOC-R) in solution. This complexation can promote the adsorption by lowering the net charge of the polyelectrolyte or by decreasing the solubility of the complex in solution (Sun et al. 2001).

Similarly, effect of Ca^{+2} ions on the adsorption behaviour of PAA onto alumina surface was examined by Dupont and co-workers. They found that in alkaline media, PAA adsorption strongly depends on the calcium ion concentration however in acidic media only a slight influence of the calcium ions was found. Due to the electrostatic effects, the complexation ratio was slightly higher in the adsorption layer than in the bulk of the solution (Dupont et al.1993). Sun et al. investigated the effects of magnesium ions on the adsorption of PAA onto alumina. They found that the addition of Mg^{+2} ions has a strong effect on the adsorption of PAA and maximum adsorbed amount increases 5 times with increasing $MgCl_2$ concentration (Sun et al. 2001).

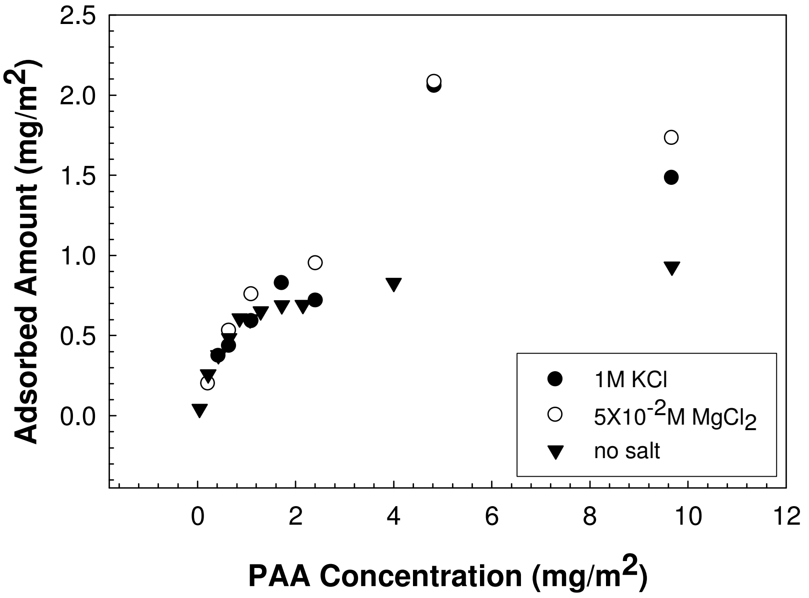

Figure 4.66. Effect of monovalent and divalent salt additions on the adsorption behavior of PAA onto PMN surface at pH 9, 10 vol %.

In the current study we observed that in the presence of PAA, addition of $MgCl_2$ increased the adsorption nearly 2.6 times. It is possible to attribute this increase to the complex formation between PAA and Mg^{+2} ions. On the other hand, the increase in the adsorption of PAA/PEO onto PMN in the presence of monovalent or divalent salt may be attributed to the decrease in the electrostatic forces rather than complex formation with the divalent metal ions in solution.

It is also important to know that complexation promotes adsorption but the effect is very sensitive to the ratio of cation to dissociated carboxylic acid groups in the polyelectrolyte. Therefore increasing the PAA concentration beyond the optimal ratio decreases the adsorbed amount. This is because less complexed PAA has a lower driving force for adsorption (Sun et al. 2001). Similarly, Dupont et al. found a decrease in the adsorption isotherms as PAA increases at constant calcium concentration, and it was due to decrease in the complexation ratio (Dupont et al.1993). Figure 4.67 shows the effect of $MgCl_2$ concentration on the adsorption amount. According to the graph highest adsorption amount were obtained in the presence of 2x10^{-2} M and 5 x10^{-2} $MgCl_2$ for PAA/PEO and PAA, respectively.

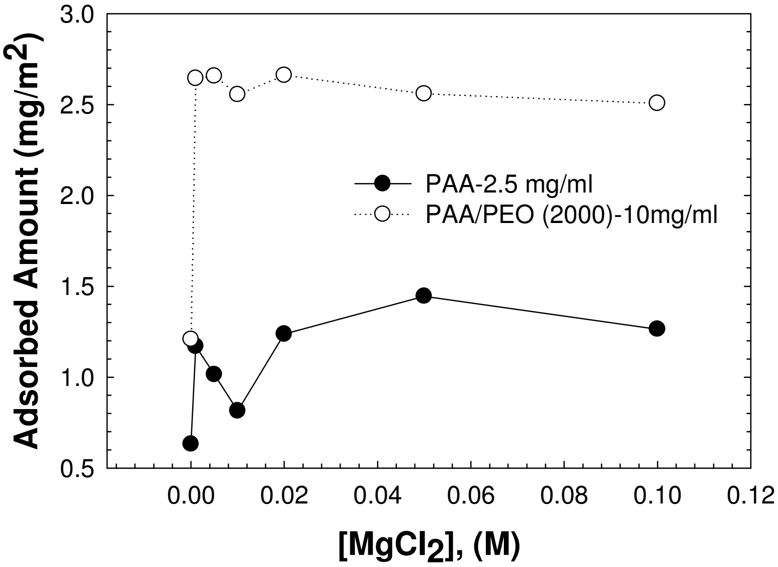

Figure 4.67. Effect of $MgCl_2$ concentrations on the adsorption behaviour of PAA and PAA/PEO(2000) onto PMN surface at pH 9, 10 vol%.

According to the results of the current work following conclusions can be drawn: polycarboxylate adsorption increases with decreasing pH and increasing salt concentration. Furthermore saturation adsorption results in charge reversal and a negative zeta potential as it was reported in the previous sections. Adsorption of high molecular weight comb polymers can be described by the low surface coverage. This may be attributed to the presence of PEO teeth. $MgCl_2$ increased the adsorption of both PAA and PAA/PEO.

To explain the findings of the current study the dominant role of PEO teeth is illustrated schematically in Figure 4.68. PEO teeth provide two important functions to prevent deleterious effects of the dissolved ions on PMN suspension stability. First charge neutral PEO teeth shield the PAA backbone from ion bridging interactions with the multivalent counter ions in solution. Second the charge neutral PEO teeth do not experience large conformational changes with changes in pH or ionic strength. As a result, the conformation of the PAA/PEO layers adsorbed on the PMN surfaces remain nearly constant as the ionic strength increases (see Figure 4.69). However, van der Waals interactions become weak with increasing ionic strength. Therefore, the net result can be weakening of the attractions especially at high ionic strength solutions.

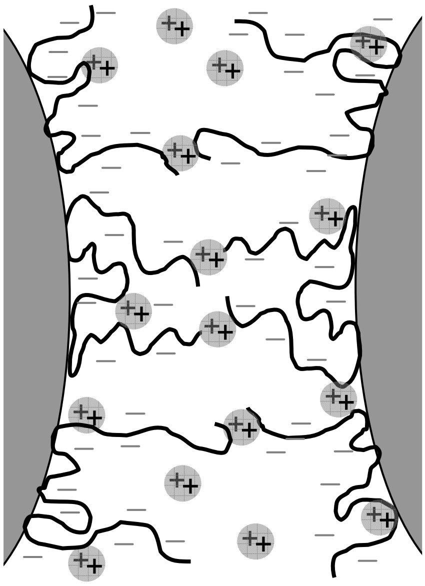

(a)

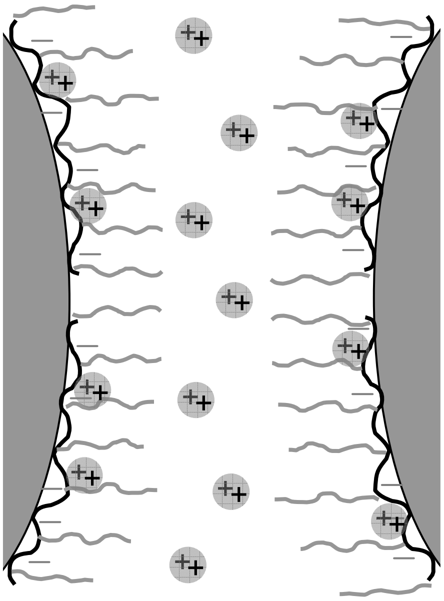

(b)

Figure 4.68. Schematic illustrations of a) flocculation between two PAA coated PMN particles due to multivalent ion bridging and b) shielding from ion bridging interactions provided by the PEO teeth (Source: Adapted from Kirby and Lewis 2004).

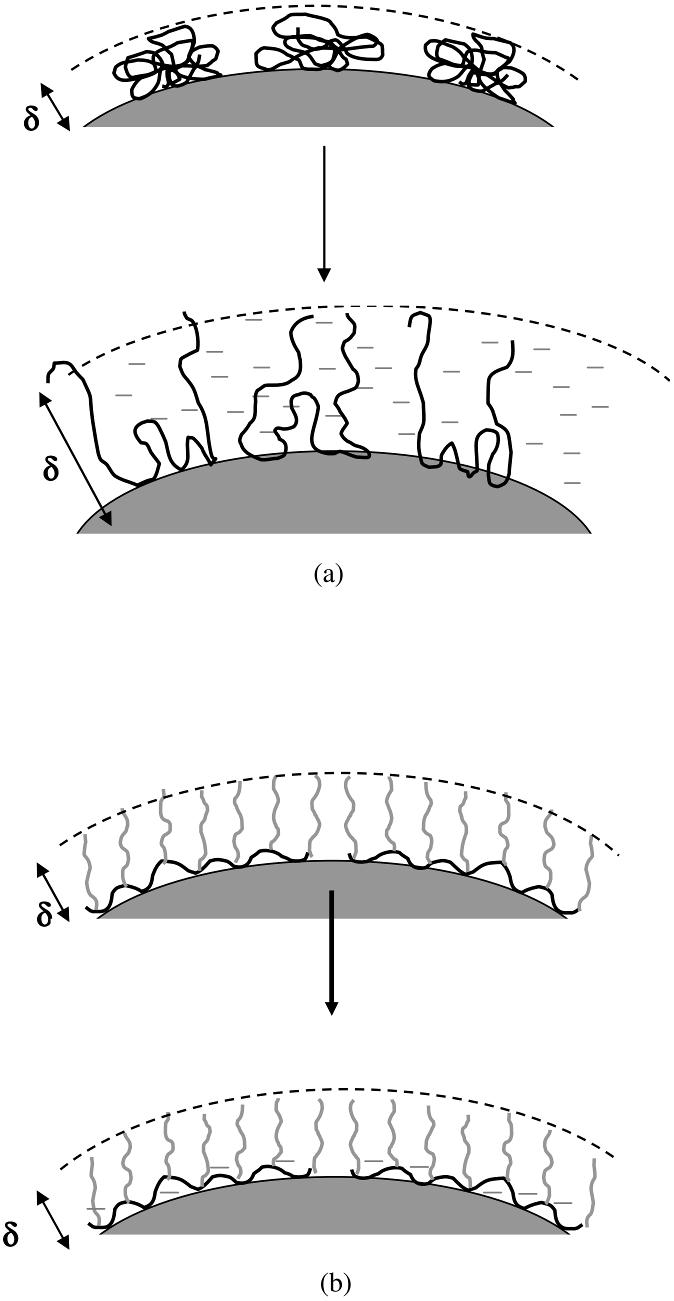

Figure 4.69. Schematic illustrations of adsorbed a) PAA and b) PAA/PEO layers undergoing conformational changes. Arrows indicates increasing pH or decreasing ionic strength (Source: Kirby 2003).

4.3.5. Cation Leaching from PMN in the Presence of Polyelectrolyte

When PAA and PAA/PEO is used in lead magnesium niobate/water system we must also consider their effect on the ion dissolution from PMN surface. As it was discussed in Chapter three, PMN incongruently leach Pb^{+2} and Mg^{+2} ions at the interface below pH 10 and therefore the ionic concentration in suspension increases. In the study, the Pb^{+2} and Mg^{+2} ion leaching from PMN surface as a function of polyelectrolyte concentration was studied. Experiments were performed for 10 vol% PMN suspensions at different pH and ionic strength conditions.

Figures 4.70 and 4.71 display the Pb^{+2} and Mg^{+2} ion concentrations as a function of string time of PMN suspensions in the presence of PAA/PEO. Results show that Pb^{+2} and Mg^{+2} concentration reaches a considerable level immediately after the powder addition and then Pb^{+2} concentration decreases and Mg^{+2} concentration increases with time. In the presence of comb polymer Pb^{+2} concentration in suspension was nearly 10 times higher compared to lead concentration of suspensions in absence of dispersant.

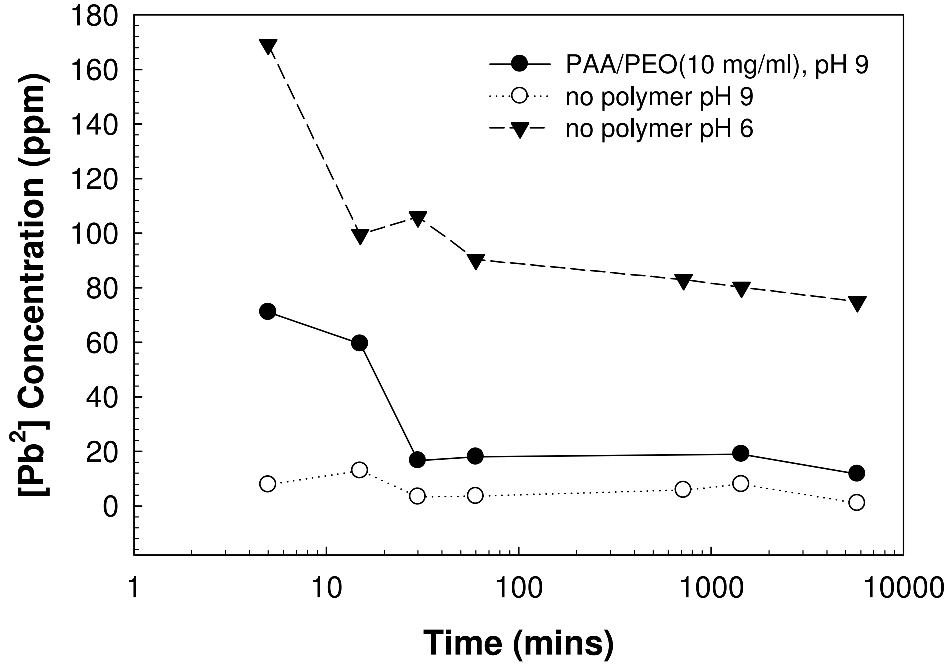

Figure 4.70. Effect of PAA/PEO(2000) on the solubility of Pb^{+2} from PMN (10 vol%) as a function of stirring time.

Neubrand and co-workers observed similar behaviour for Ba^{+2} dissolution from barium titanate surface as a function time (Neubrand et al. 2000). It is possible to explain the decrease in lead concentration by re-adsorption of Pb^{+2} ions to the hydrated PMN surface. Surface charge of the PMN is negative at pH 10. At this negative surface charge Pb^{+2} ions may be readsorbed onto the surface and this may cause a decrease in Pb^{+2} concentrations in solution. Another explanation for the decrease observed in lead amount may due to the complex formation. Further discussion on this subject is given in Chapter three.

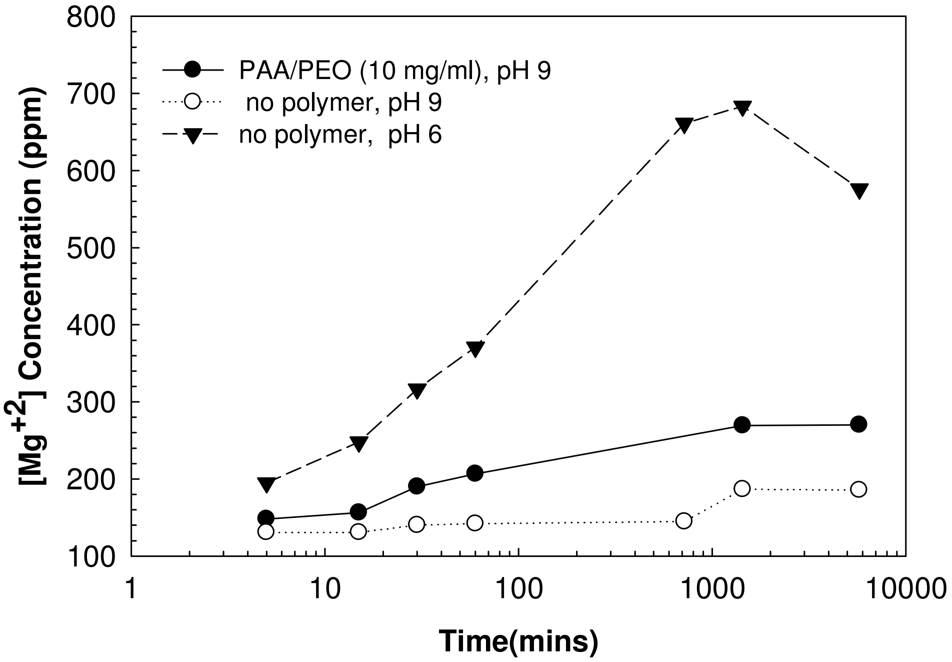

Figure 4.71. Effect of PAA/PEO on the solubility of Pb^{+2} from PMN(10 vol%) as a function of stirring time.

Figures 4.72 to 4.75 show the effect of PAA and PAA/PEO comb polymers on the solubility of PMN as a function of polymer concentration and suspension pH. Both polyelectrolytes enhanced the solubility of PMN and caused an increase in the Pb^{+2} and Mg^{+2} ion concentration in solution at pH 9 and pH 6. Furthermore, an increase was observed in Pb^{+2} and Mg^{+2} concentrations in solution as the polyelectrolyte concentration increase.

Paik and co workers investigated the effect of PAA on the solubility of barium titanate in aqueous medium. Results showed that Ba^{+2} sequestered by PAA in solution at basic pH values. At pH 8 and higher where PAA is well dissociated and the adsorption is low and the polymer enhanced the dissolution of Ba^{+2}. They attributed this result to the complex formation in solution but may involve adsorption of PAA as an initial step (Paik et al. 2003). On the other hand at acidic pH values where PAA adsorption is largely irreversible PAA causes passivation that increases with increasing polymer concentration.

When the adsorption interaction is strong it is irreversible and the polyelectrolytes form a stable passivating layer. In this case surface bound PAA either forms a protecting layer that inhibits the dissolution or complexes with cations in a manner that stabilizes the surface layer and fixes the cations. On the other hand, if adsorption is largely absent due to unfavorable electrostatic interactions then cations will be sequestered only as the ions are released into the solution in accordance with the natural rate of the oxide dissolution (Paik et al. 2003).

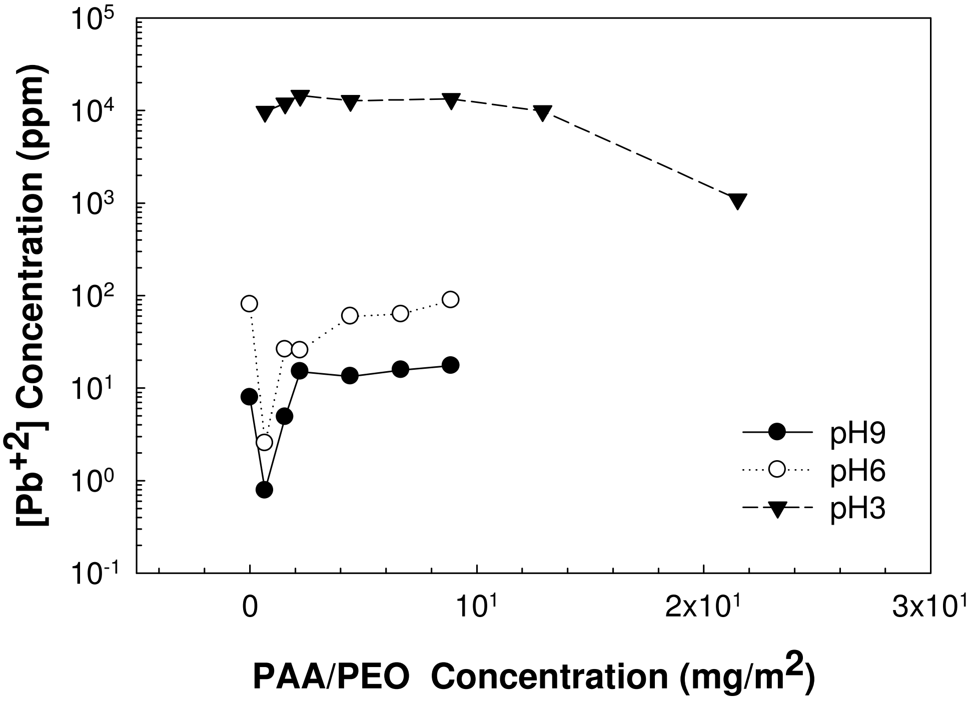

Figure 4.72. Effect of PAA/PEO(2000) concentration on the solubility of Pb^{+2} from PMN at pH 9, 6 and 3.

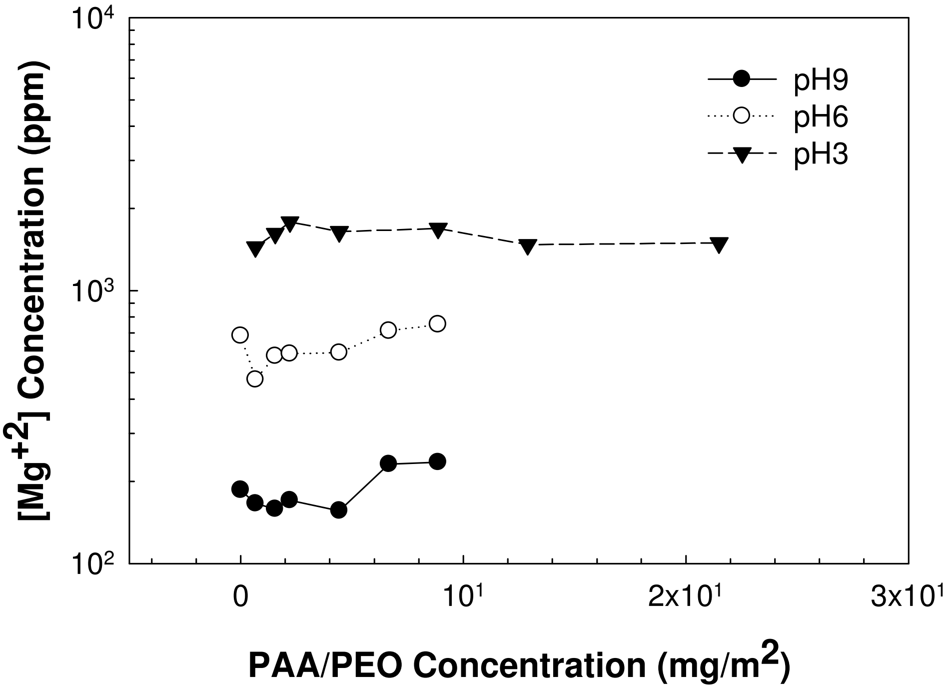

Figure 4.73. Effect of PAA/PEO(2000) concentration on the solubility of Mg^{+2} from PMN at pH 9, 6 and 3.

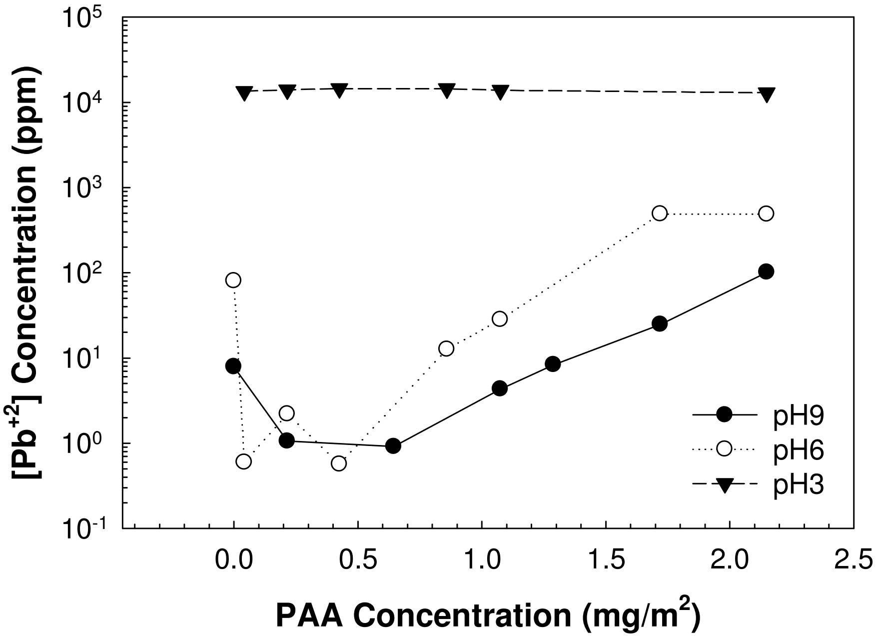

Figure 4.74. Effect of PAA concentration on the solubility of Pb^{+2} from PMN at pH 9, 6 and 3.

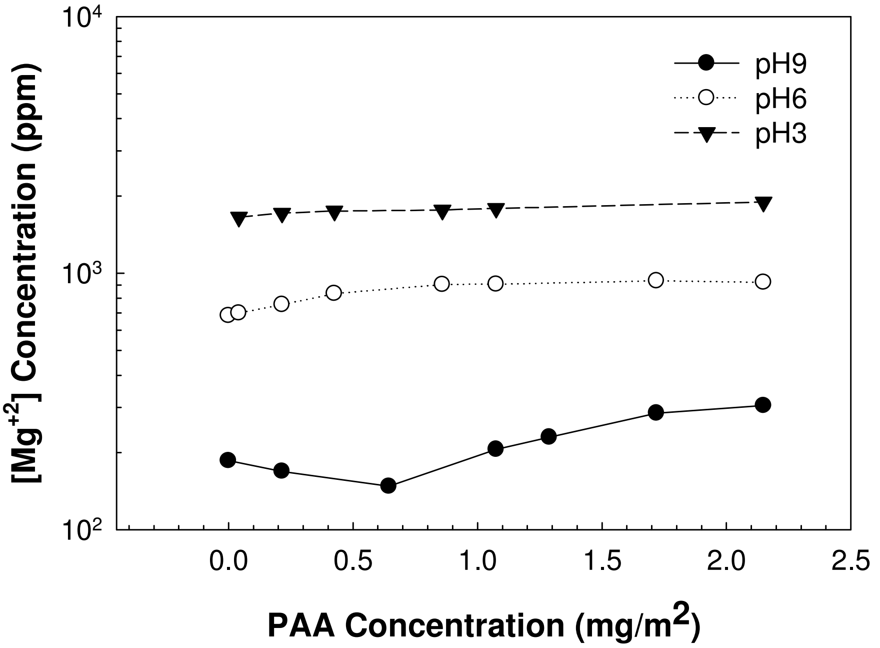

Figure 4.75. Effect of PAA concentration on the solubility of Mg^{+2} from PMN at pH 9, 6 and 3.

As it is discussed previously in Chapter three the cation concentration in PMN suspensions (10 vol%) at pH 3 was about 25000 ppm. However, results obtained in this section showed that Pb^{+2} concentrations were around 12500 ppm in PMN suspensions in the presence of comb polymer under the same conditions. Similarly, Pb^{+2} concentrations were around 13000 ppm in PMN suspensions in the presence of PAA. Therefore, it is possible to conclude that in the presence of polyelectrolytes under acidic conditions cation dissolution from PMN surface is inhibited due to adsorption.

In the current study sequestering of Pb^{+2} and Mg^{+2} from the PMN surface may be attributed to the weak adsorption of anionic PAA and PAA/PEO comb polymer onto fairly unstable Pb^{+2} and Mg^{+2} surface sites. On the other hand, by complexing dissolved cations, PAA enhances the solubility by acting as a Pb^{+2} and Mg^{+2} sink in solution.

CHAPTER 5

PREPARATION OF PMN FILMS BY AQUEOUS TAPE CASTING

5.1. Introduction

Tape casting is a shaping method to produce two-dimensional thin ceramic plates usually have 10–1000 μm thickness (Meier et al. 2004). A paste-like suspension consisting of powder, solvent, dispersant, polymer (binder) and plasticizer is cast onto a substrate by a moving blade in a constant distance to the substrate. The final dried green tape should be flexible, and easy to handle. This processing method as well as the equipment are simple and therefore are interesting for many types of applications, such as dielectrics for capacitors, chip carrier substrates and sensor supports (Tian et al. 2007).With today’s tape casting technology, very thin tapes (down to 5 microns) can be cast, allowing manufacture of capacitors and transducers for high frequency operation in high-resolution medical imaging (Safari et al. 2006).

Lead magnesium niobate (PMN) have important applications in multilayer electronic ceramic industry. Tape casting is a convenient method for manufacturing of thin and thick PMN sheets for various electronic applications such as capacitor and actuators. Thin film deposition is also used to prepare very thin PMN polymer composites (Windlass et al. 2001, Vasanthakumari et al. 2005).

Previously, organic solvents were preferred for the preparation of thin and thick films from ceramic suspensions due to their low latent heat of evaporation and low surface tension (Huei and Dogan 2000). For example, Windlass and co-workers investigated the dispersion of PMN-PT powders in slightly polar solvent, propylene glycol methyl ether acetate (PGMEA) (Windlass et al. 2003). Methyl ethyl ketone, mesitylene and γ-butyrolactone, xylene, toluene, ethanol, isopropanol are other solvents has been used to prepare the stabil PMN-PT suspensions using olecid acid, phosphate ester as dispersants (Agarval et al. 1998, Ogitani et al. 1998, Vasanthakumari 2005).

However, there is now a trend to move away from organic solvents and an expected transition towards water-based systems. The main advantages for switching from organic to a water-based system are reduced health and environmental hazards and lower cost. But, in comparison with organic solvent-based tape casting slurries, aqueous tape casting systems have a smaller tolerance to minor changes in processing parameters, such as composition, and drying conditions (Mistler 1998). Thus, it is very important to understand and control the rheology of water-based tape casting slurries. The viscosity of slurries must be low enough and the slurry should exhibit pseudoplastic behavior. Thixotropy and any other time dependent behavior are undesired (Tian et al. 2007).

The development of slurry formulations for the aqueous tape casting has been studied by many researchers for different ceramic materials (Meier et al. 2004, Acikbas et al. 2006, Jantunen et al. 2004). Water soluble binders such as PVA and cellulose can result in high viscosity slips that are difficult to tape cast. On the other hand, several scientists conducted research by using aqueous based acrylic emulsions as binders for preparing ceramics (Zhang and Binner 2002). Doreau et al. investigated the processing of aqueous tape casting of alumina with acrylic emulsion binders that have different glass transition temperatures (T_g: -40 °C and 10 °C). They did not use any additional organic additives in the system such as plasticizer or defoamer (Doreau et al. 1998). Smay and Lewis developed an aqueous system for the tape casting of lead zirconate titanate. They investigated the effect of acrylic latex suspensions on this system in the presence of hydroxypropyl methylcellulose (Smay and Lewis 2001). Previously, Kristofferson et al. found that latex binders yield high solids loading suspensions with the desired rheological behavior for the alumina suspensions (Kristofferson et al. 1998). Similary, Ushifusa and Cima developed latex based slurry for tape casting of mullite-glass composites suitable for electronic packaging (Ushifusa and Cima 1991).

The aim of the current work is to develop aqueous based PMN slurries to use in tape casting process. In the study, slurries were prepared in the presence of acrylic latex as the binder phase and the hydroxylpropyl methylcellulose as the wetting agent. PMN films were manufactured using doctor blade having a gap height of 30 to 500 µm. Results of the study showed that it is possible to prepare high quality PMN films based on aqueous formulations.

5.2. Experimental

5.2.1. Materials

Lead magnesium niobate powder (average particle size, d_{50}, 1.8 μm and BET surface area of 1.168 m^2/g) was produced by combustion spray pyrolysis provided by the Praxair Inc. USA. PAA/PEO comb polymer (PAA 5000 g/mol, PEO 2000 g/mol) was employed as the dispersant to prepare highly concentrated stable PMN suspensions. The optimum amount of dispersant necessary to disperse the PMN powders was experimentally determined in the study (4.35 mg/m^2 of PMN) and results are reported in Chapter four.

Two different types of acrylic latex emulsion were tested as the binder phase. Anionic binders under investigation were Duramax B1001(Rohm and Haas Co, Philadelphia, PA), and Duramax B1035 (Rohm and Haas Co, Philadelphia, PA) with solids concentration of 55 vol% , average particle size of 0.32 μm and a glass transition of -6 ºC and -40 ºC, respectively. The second type of binder used in the study was an aqueous based nonionic acylic latex emulsion, Rhoplex B-60A (Rohm and Haas Co, Philadelphia, PA) having a glass transition temperature of 6 ºC and a solids loading of 47 wt%.

Rhoplex B-60 is an acrylic polymer containing a small amount of carboxyl groups. When a dispersion of this polymer is dried at a temperature above 9 °C, a continuous film can be formed. Free films prepared from this latex have an initial modulus of 1 to $1.7\text{x}10^7$ dyne/cm^2, ultimate stress of 3.2 to 8.6 x 10^7 dyne/cm^2, and a breaking elongation of 780 to 1060% at 40 to 4000% /min straining rates (Gardon 1963)

In the study hydroxypropyl methycellulose (Methocel F4M, DOW Chemicals Co., Midland MI) with a molecular weight of 3500 g/mol was used as the wetting agent. The unmodified cellulose polymer is insoluble in water. Methocel F4M contains 28% methoxyl with 1.8 degree of substitution and 5% hydroxypropyl with 0.13 molar substitutions.

5.2.2. Suspension Preparation

Suspensions were prepared by a multi-step process at different solids loadings (45, 55 and 60 vol%), with powder/binder ratio of 1 to 3 and, hydroxypropyl methylcellulose (HPMC) content of 3.5 to 15 mg/ml. In the first step of slurry preparation, highly concentrated PMN suspensions were prepared using PAA/PEO comb polymer. Suspensions were ultrasonicated for 2.30 min with on-off intervals (550 Sonic Dismembrator, Fisher Scientific) to break up the agglomerates in the system. Suspensions were ball milled for 24 hours to ensure complete adsorption of PAA/PEO onto powder surface at pH 9. In the next step latex binder and wetting agent were added to the system and the slurry was ball milled 24 hours more. The suspension pH was readjusted to 9.0 using 1 M NH_4OH. The slurry was defoamed for 15 minutes using a planetary centrifugal mixer (Thinky ARE-250) prior to the tape casting. Figure 5.1 shows the slurry preparation procedure for tape casting. The examples of slurry compositions used in tape casting are given in Table 5.1.

Table 5.1. Some of the slurry formulations used for the tape casting.

	R1(7)55	**R1.5 (7)55**	**R2(7)55**	**R3(7)55**
	wt %	**wt %**	**wt %**	**wt %**
PMN	69.60	74.58	77.35	80.33
Binder (B60-A)	9.72	6.94	5.40	3.74
PAA/PEO(2000)	0.12	0.13	0.14	0.14
H_2O	20.46	18.25	17.03	15.71
Methocel F4M	0.10	0.09	0.08	0.08
Total	**100**	**100**	**100**	**100**

Different PMN recipes are identified according to the following formulation: Rx(y)z. Where x: (PMN/binder ratio), y: HPMC (Methocel) content (mg/ml), z: total solids concentration (vol%). In the following sections of this chapter this coding will be used to identify the PMN slurry compositions.

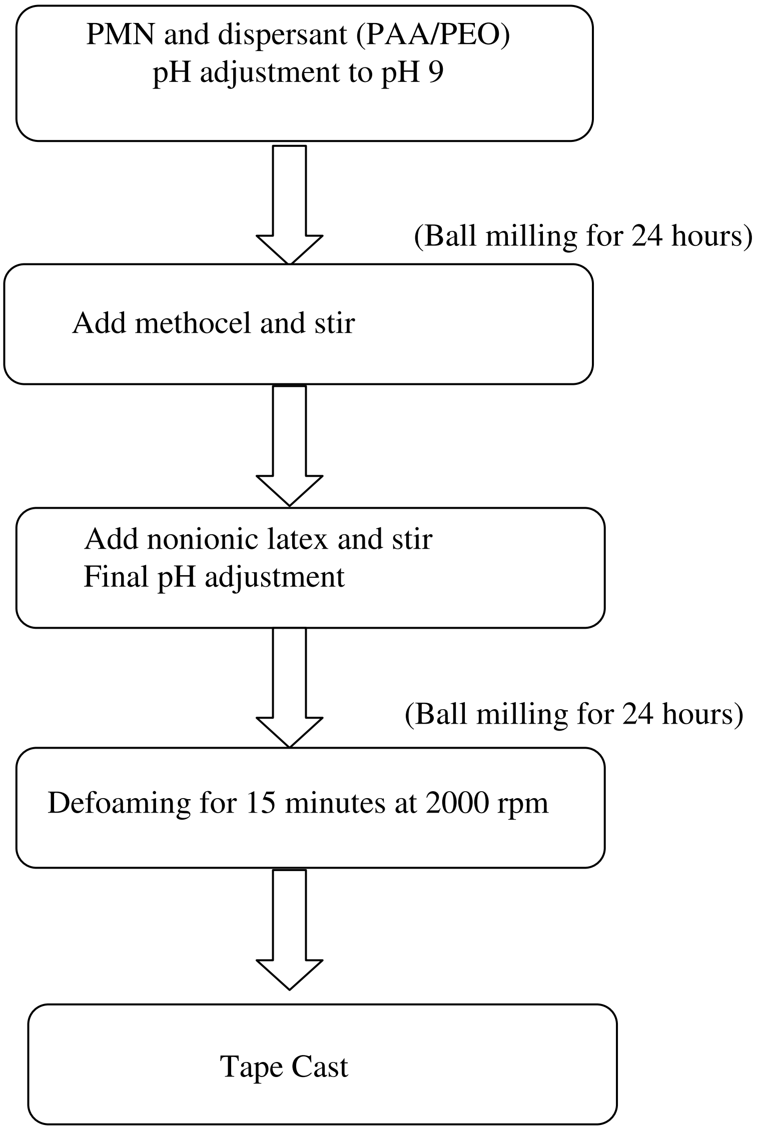

Figure 5.1. Flow diagram showing the slurry preparation procedure for tape casting.

5.2.3. PMN Film Fabrication

PMN films were prepared using laboratory type tape caster (Cladan Inc.Model 133, Serial 181, USA) having dimensions of 240x80 cm (see Figure 5.2). The slurry was cast onto a silicone coated poly(ethylene terephthalate) stationary film (Mylar, PET blend EI-8526, Douglas-Hanson, Hammond, WI). Silicon coating having thickness of 1.27 µm is on one side of the film. Surface energy of the film is 23 mJ/m^2 as reported by the Smay and Lewis in 2001. Similarly, Zosel reported the surface tension of the PET as 42 mN/m (Zosel 1993). The casting rate was 25 mm/s over a length of 1 m. Doctor blade head having width of 100 mm was set at a height of 30 to 500 µm. The tapes were allowed to dry in air at 25 ºC.

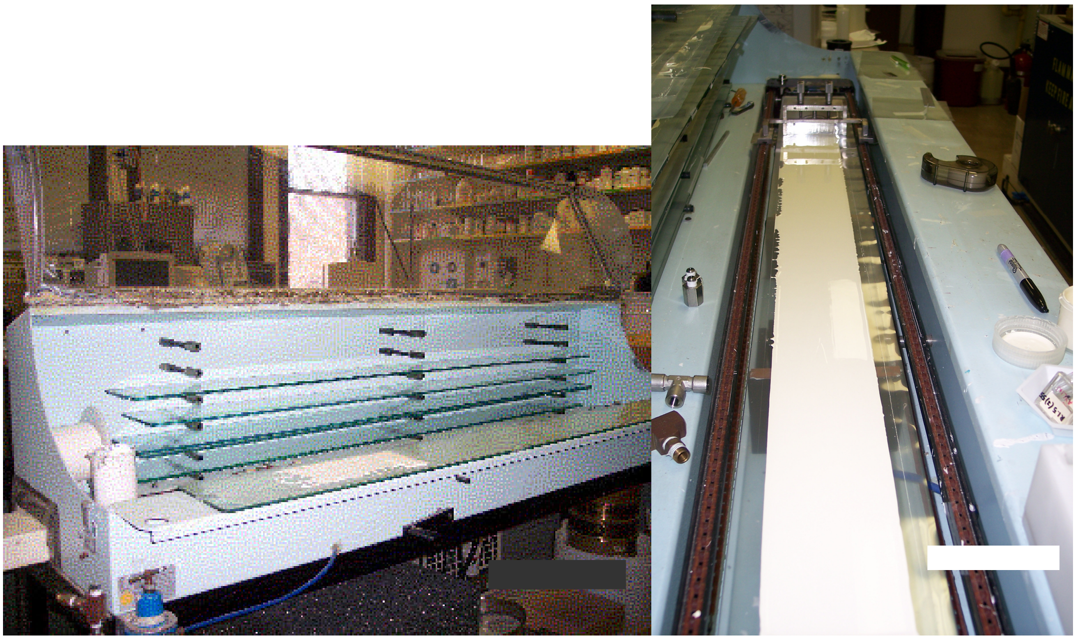

Figure 5.2. Picture of the laboratory type tape caster used in the study and the PMN tape casting process.

5.2.4. Lamination and Sintering

Arrays of samples (22.5 mm x 47 mm) were cut along the length of dried tape. Samples were formed by laminating the 15 layers of green tapes between parallel plates and then heated to 80 ºC and kept at this temperature for 1 hour. After heat treatment 30 MPa pressure applied to the sample for 2 minutes (Figure 5.3).

Figure 5.3. Laminated PMN sample containing 15 layers. Each layer 300 µm.

To investigate the optimum sintering conditions of the films some preliminary experiments were performed. For this purpose, PMN powders containing 3 wt% poly vinyl alcohol were die pressed (diameter 1.5 cm, thickness 0.3 cm) and then sintered at various temperatures ranging from 1000 to 1275 °C. To minimize the lead loss the samples were placed in a $PbZrO_3$ powder bed and covered with double alumina crucible system. The crucible system used during sintering studies is shown schematically in Figure 5.4. The heating regime followed during sintering is given in Figure 5.5.

The lead zirconate powder used during the sintering experiments was produced by mixed oxide method through solid state reactions. For this purpose lead (II) oxide and zirconium oxide powders were mixed in stoichiometric ratios and dry ball milled for 24 hours. Then powder mixture was calcined at 1000 °C for 2 hours to obtain the lead zirconate powder.

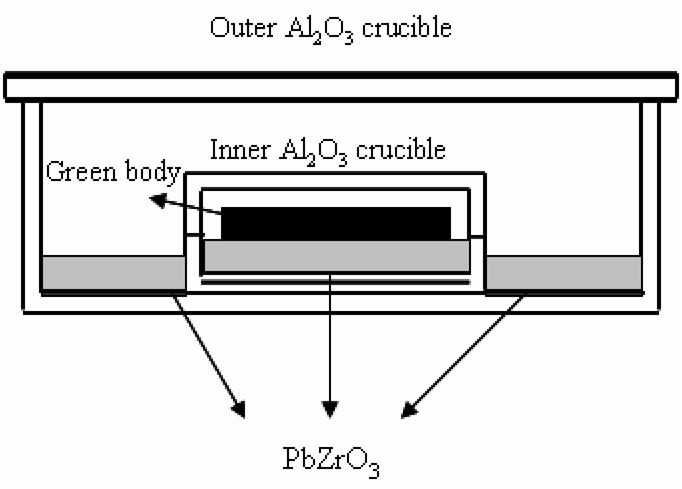

Figure 5.4. Schematic presentation of the crucible system used in sintering studies.

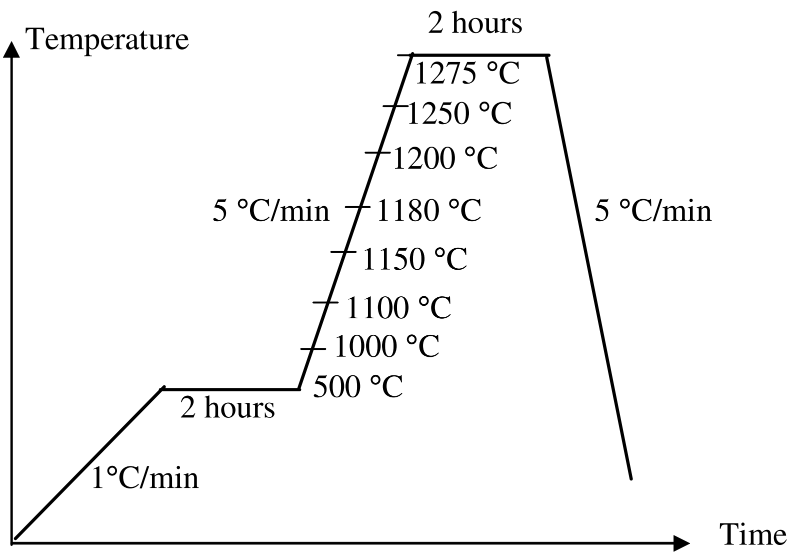

Figure 5.5. Schematic presentation of the heating procedure followed during sintering.

5.2.5. Characterizations

5.2.5.1. Zeta Potential Measurements

Surface charge of anionic and nonionic binders (10 vol%) were characterized by zeta potential measurements (ESA 9800, Matec Applied Science) as a function of pH.

5.2.5.2. Rheological Measurements

Rheological behaviour of PMN suspensions was characterized using a controlled stress rheometer (Bohlin CS-50, NJ). The C14, cup and bob geometry was utilized through the measurements at a constant temperature of 25 ℃. A solvent trap was used to minimize the evaporation during the measurements. The apparent viscosity was measured as a function of shear stress in ascending order. Oscillation measurements were performed to analyze viscoelastic behaviour of the concentrated PMN slurries.

5.2.5.3. Surface Tension and Contact Angle Measurements

The surface tension measurements were performed using a tensiometer (Kruss-Digital K 10ST) employing De Nouy ring method. The measurements were performed at 25 °C and the platinum ring was heated in a flame until it glowed red before each measurement. The surface tension of each sample was measured for three times.

Contact angle measurements were performed using a contact angle measuring instrument (Kruss). Contact angle of the samples were measured on the mylar film (silicon coated side) using sessile drop method. Using an optical microscope, it is possible to observe and measure a finite contact angle as the liquid interface approaches the three-phase-contact perimeter of the drop. Contact angle of each sample is measured for five times and average of these values is reported.

5.2.5.4. Thermal Analysis

Organic content of the green tapes were analyzed using a differential scanning calorimeter (DSC-50, Shimadzu) under nitrogen flow (40 ml/min). To investigate the binder distribution through the entire length of the dried tape, an array of samples were cut from the tapes in parallel and perpendicular to casting direction. DSC analyses were performed up to 600 ºC at a heating rate of 10 ºC/min. Weight loss was analyzed using a thermogravimetric analyzer (TGA, Setaram Labsys) up to 1000 °C at a heating rate of 5 ºC/min under air atmosphere with a flow rate of 2.5 l/h.

5.2.5.5. Microstructural Characterization and Phase Analysis

To investigate the structural evolution of the PMN suspensions during drying concentrated suspensions were diluted to ϕ: 0.001 and observed under an optical microscope (Olympus IX71, UTVO.5XC.3). For this purpose a 4 µl drop of suspension was put on a cover slide and was allowed to dry under ambient conditions (22 ºC and 36% relative humidity). Images of the micro-drop were recorded using a digital camera. Microstructure of the green and sintered tapes were characterized by SEM (Philips, XL-30S FEG). Crystal structures were analyzed using X-Ray diffractometer (Philips, X`pert Pro).

5.2.5.6. Roughness Measurements

Roughness of the green films was analyzed using scanning probe microscope (Digital instruments, MMSPM Nonoscope IV) and a surface profilometer (Mitutoya Surftest SJ-201 P/M). Through the measurements, profilometer sampling length and cut off length was adjusted at 5 mm and 0.8 mm, respectively. Measurements were performed on PMN films at 5 cm arrays through the entire film length.

5.2.5.7. Drying Stress Measurements

A cantilever deflection based device was used with a controlled temperature and humidity test chamber for measuring the drying stress in tape-cast films (see Figure 5.6). The device uses cantilever deflection method for measuring stress. When the applied coating dries, a bending moment on the cantilever is created due to the stress transferred from the stress in the coating to the substrate at the interface (Lewis 2000, Smay 2002).

The stress evolution of PMN tape cast layers was monitored as a function of drying time. The cantilever deflection was determined as a function of drying time using an optical lever consisting of a 3 mW HeNe laser, position sensitive photodiode and appropriate optics. The deflection data were recorded by a data acquisition computer. A steel substrate was mounted onto a movable sample holder fixed at one end. Then suspensions were deposited onto the substrate with a syringe. This assembly was then moved towards the doctor blade at a constant speed of 1 cm/s to create a film with a thickness of 300 µm. Figure 5.7 shows the mechanism of the stress development on the cantilever substrate. Stress in coating causes cantilever to bend. It is related to the deflection by the following equation:

$$\sigma = \frac{dEt^3}{3cl^2(t+c)(1-\nu)} \tag{5.1}$$

where c is the final coating thickness, d is the cantilever deflection, E is the elastic modulus, ν is the Poison`s ratio, t and l are the thickness and the length of the cantilever, respectively.

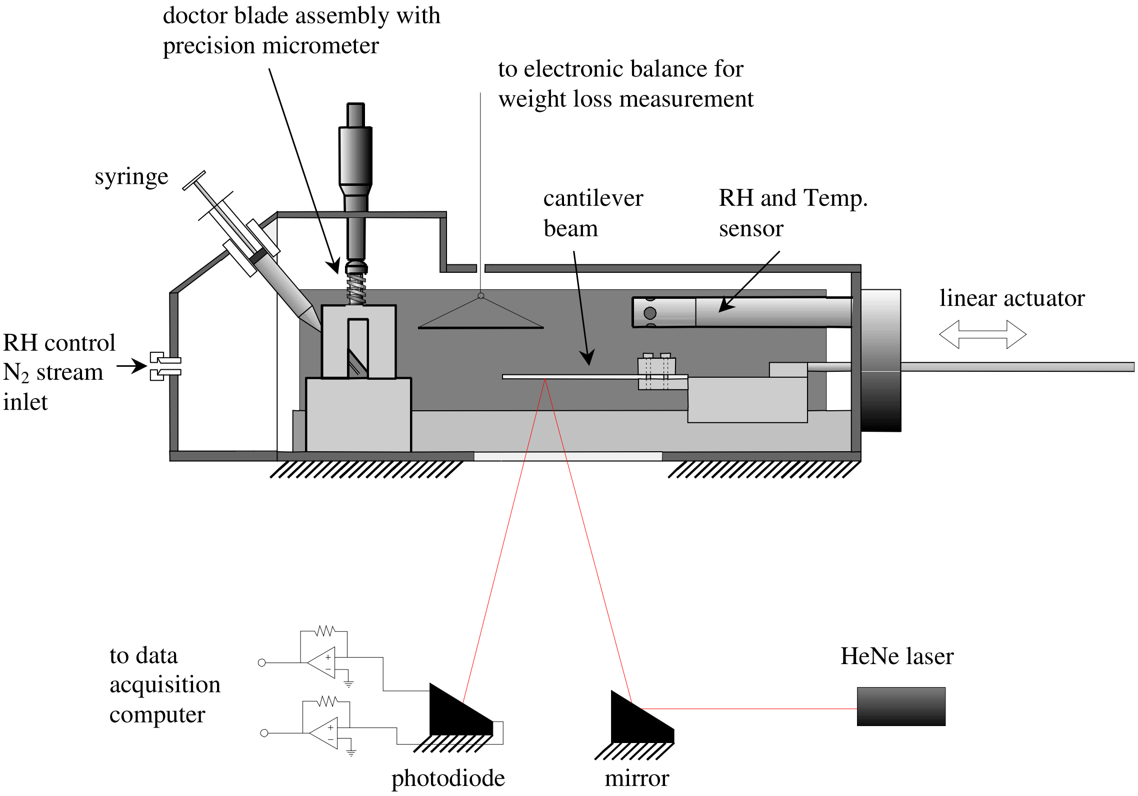

Figure 5.6. Schematic illustration of the drying stress measurement device. (Source: Smay 2002)

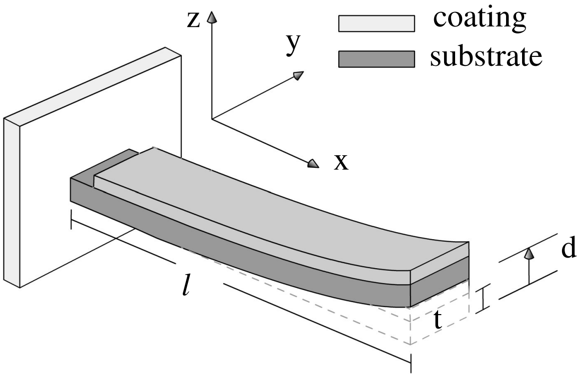

Figure 5.7. Illustration of cantilever bending from influence of stress in coating.

5.2.5.8. Electrical Characterization

Dielectric constant of PMN samples were measured using a high resolution dielectric analyzer (Novo Control, Alpha-N). The principle of the measurement is to apply an AC voltage with a certain frequency to the sample, then measure the current through the sample. The applied and the measured signals are compared, to obtain the complex impedance of the sample. From complex impedances at several frequencies, the complex dielectricity and conductivity spectra are extracted (Kofod 2001). Figure 5.8 shows schematically the impedance analyzer and the measurement cell used in the study.

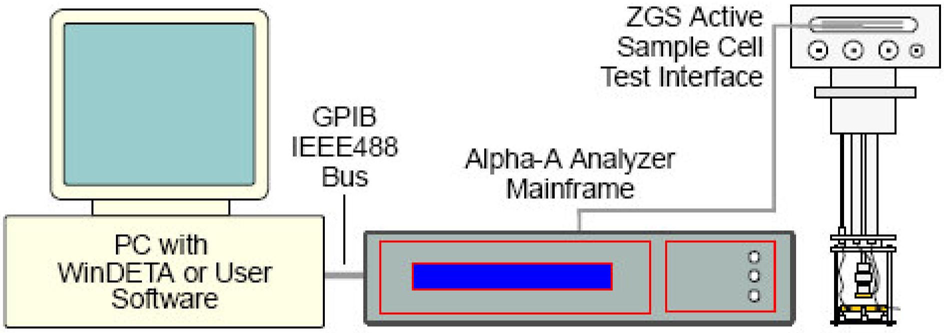

(a)

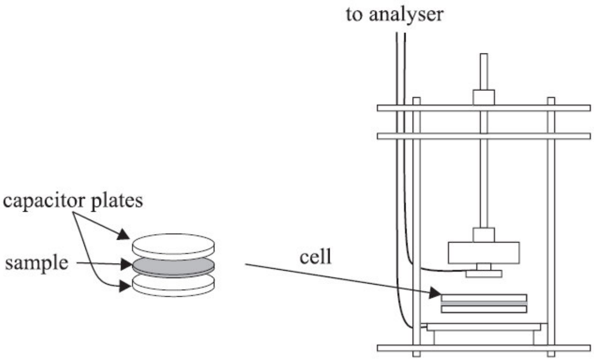

(b)

Figure 5.8. Schematic presentation of the a) impedance analyzer b) measurement cell. (Source: WEB_5 2007)

For the measurements the silver paint were applied to the both sides of the sintered pellets and PMN films to improve the contact with the analyzer plates. A heat treatment at 600 °C was applied to the silver (Ag) paste coated samples for 30 minutes. Then they were placed between two capacitor plates as shown in Figure 5.8 (b). The samples were inserted to the sample holder, and clamped tightly in place, in order to ensure perfect connection between plates and sample. Permittivity of the PMN pellets and the laminated films were measured at room temperature as a function of frequency in the range 10^{-2} to 10^{5} Hz. AC volts (3 Vrms) were applied to the samples during the measurements.

5.3. Results and Discussion

5.3.1. Surface Charge and Viscosity of Binders

Figure 5.9 shows the zeta potential of anionic binder (B-1001) as a function of pH. Isoelectric point of B-1001 is determined to be pH~2. Similarly, the zeta potential of nonionic acrylic emulsion of B-60A is given in Figure 5.10. Although it is as a nonionic latex emulsion, results showed that IEP of B-60 A was lower than pH 2. Additionally, the magnitude of the zeta potentials was lower compared to the zeta potential values of B-1001. According to the Brown and Garrett B-60 A is an emulsion containing acrylic copolymer and nonionic emulsifier (Brown and Garrett 1959). Nahass et al. reported that based on the infrared spectroscopy and glass transition analysis, Rhoplex B-60A is likely a copolymer between methyl methacylate and another acrylic monomer such as ethyl acrylate. The average molecular weight of Rhoplex chains was measured to be 298,000 g/mol by gel permeation chromatography (Nahass et al. 1992). Ushifusa and Cima measured the zeta potential of B-60A using the ESA analyzer. They obtained an IEP value near to pH 2 in absence of any electrolytes (Ushifusa and Cima 1991). Therefore, results obtained regarding the surface charge of the binder B-60 A are consistent with the literature values.

The apparent and relative viscosity as a function of shear stress of pure latex suspensions of varying solids loading are shown in Figures 5.11 - 5.15. As it is clearly indicated in Figures B-1001 and B-1035 emulsions exhibited Newtonian behaviour at low solids content $\phi < 0.3$. However, above ϕ: 0.3 a transition to shear thinning was observed and the degree of shear thinning increased with increasing solids concentration (ϕ). In the case of Rhoplex B-60A a shear thinning behavior was dominant at 47 wt% (See Figure 5.14). Such a behavior is in good agreement with the requirements for the tape casting process. Because the relatively high shear stress enables the slurry to have a low viscosity under the blade during casting, facilitating the tape casting. After deposition, the slurry recovers a high viscosity level, avoiding the settling of particles along the tape thickness (Doreau et al. 1998).

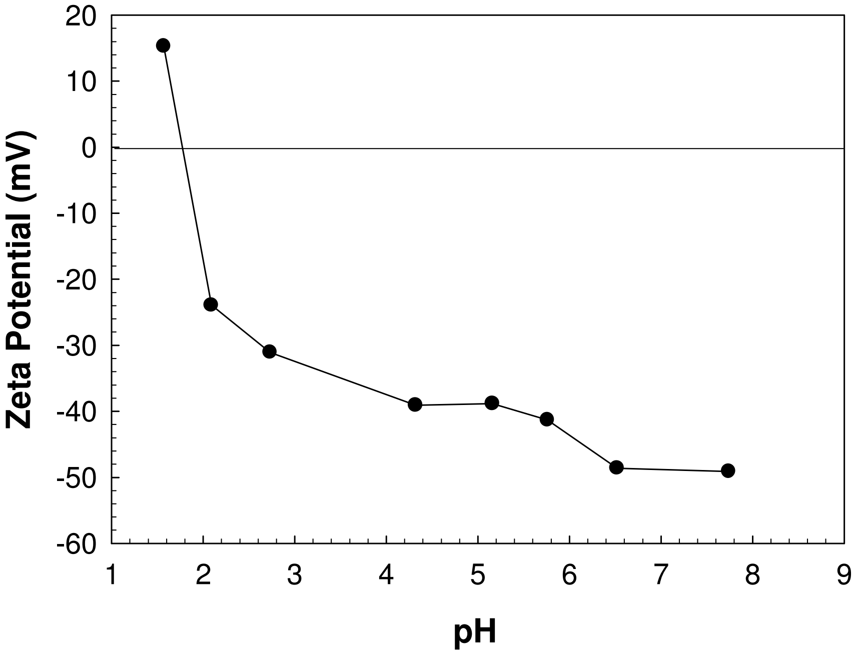

Figure 5.9. Zeta potential versus pH of anionic latex B-1001 solution (10 vol %).

It is known that particle size does affect emulsion viscosity, with large particle size generally being associated with low viscosity. Small latex particle size (<200 nm) gives best binding and adhesion. It requires the use of associative thickeners to obtain required rheological properties. Large particle size (>500 nm) gives interesting rheological properties but less efficient binding and low gloss. It is prone to sedimentation. The moderate size of the latex particles used in this study, give optimum binding and rheological properties. Since the latex size of the emulsions used was nearly identical, the difference between the viscosity values of the latex emulsions may be attributed to the different nature of chemical additives used to modify Tg and other properties.

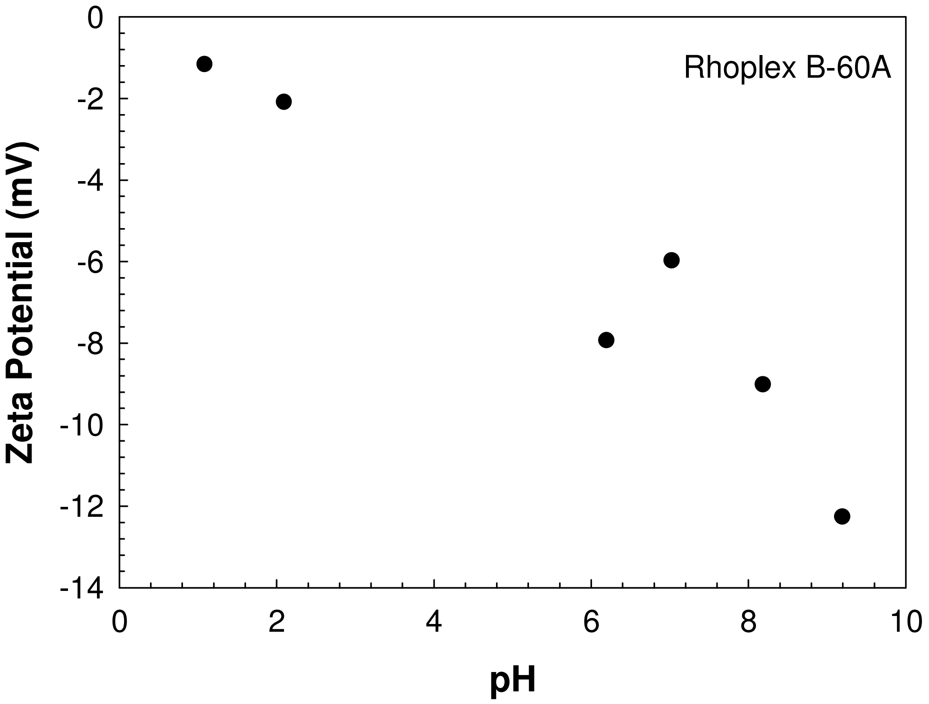

Figure 5.10. Zeta potential versus pH of latex B-60A solution (10 vol%).

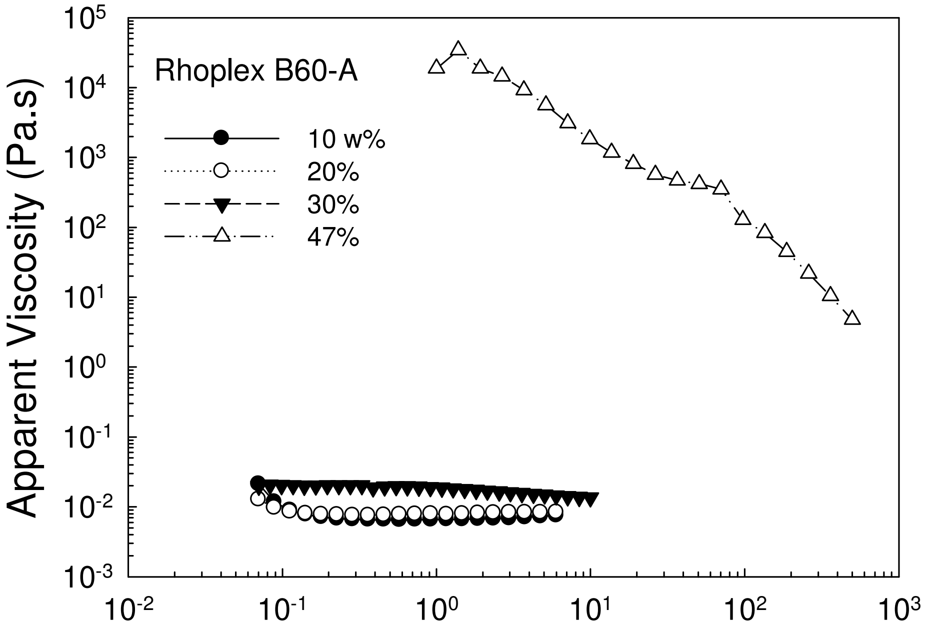

Figure 5.11.Log-log plot of apparent viscosity as a function of shear stress for pure latex suspension (B-60 A) of varying concentrations.

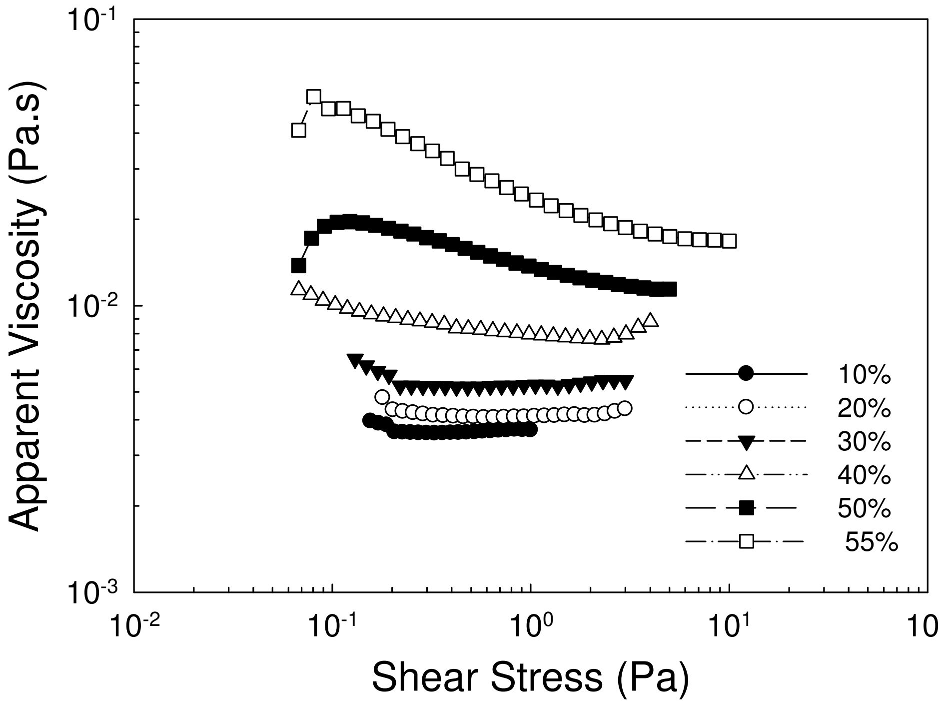

Figure 5.12.Log-log plot of apparent viscosity as a function of shear stress for pure latex suspension (B-1001) of varying volume percent.

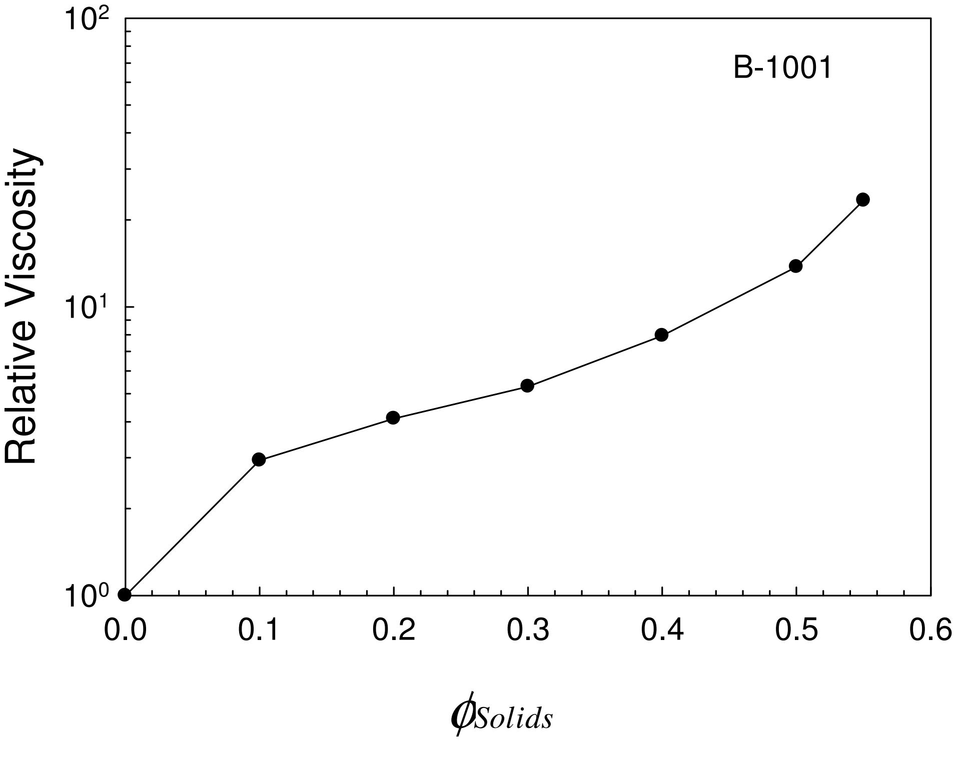

Figure 5.13.Relative viscosity of B-1001 as a function of solids volume fraction where apparent viscosity at 10 s^{-1}.

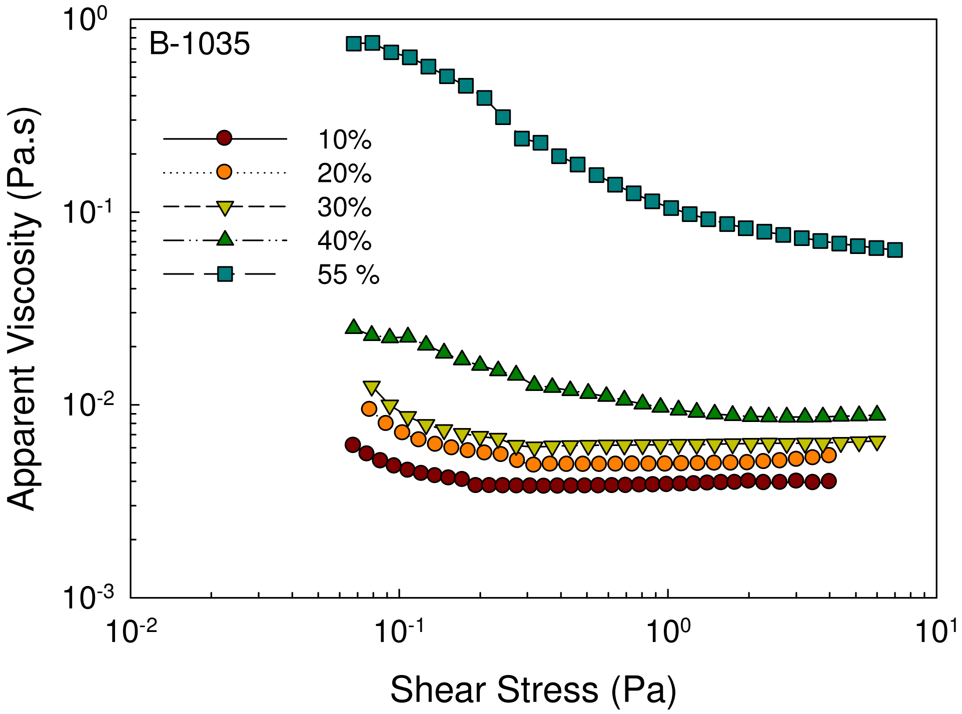

Figure 5.14.Log-log plot of apparent viscosity as a function of shear stress for pure latex suspension (B-1035) of varying volume percent.

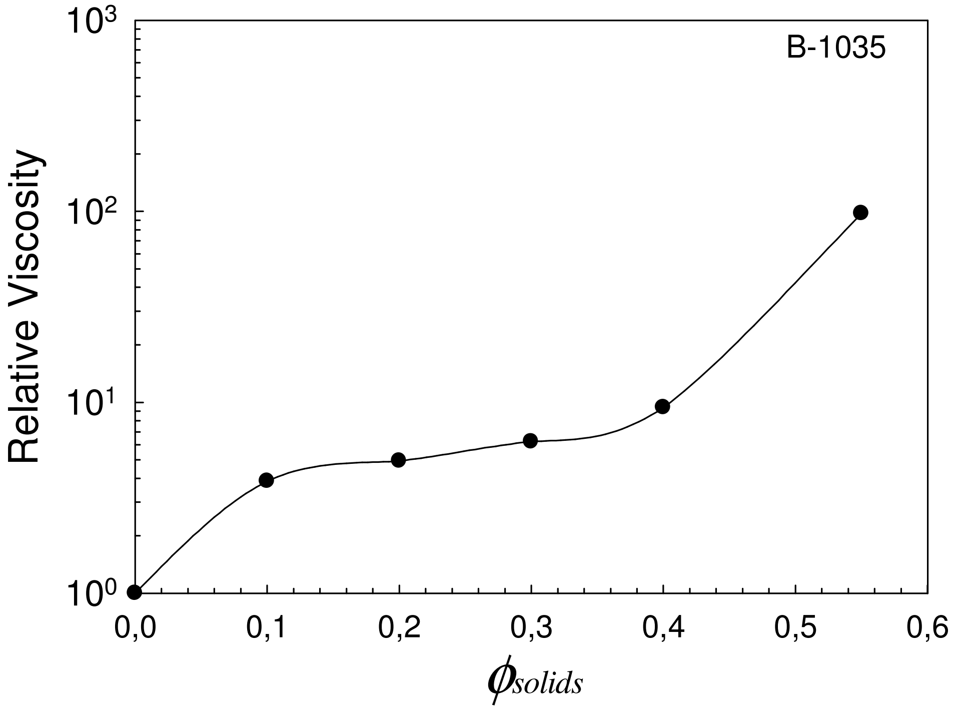

Figure 5.15. Relative viscosity of B-1035 as a function of solids volume fraction where apparent viscosity at 10 s^{-1}.

5.3.2. Solution Properties of Hyroxypropyl Methylcellulose

Figure 5.16 shows the viscosity of the hydroxypropyl methylcellulose (HPMC) solution as a function of concentration. It is clear that starting from 5 mg/ml the viscosity of the solution increases dramatically. This increase may also affect the viscosity of the PMN slurry to be used in tape casting. Similarly the viscoelastic properties of the HPMC solution are represented in Figure 5.17. At a concentration of 10 mg/ml the solution exhibited slightly gel like behavior. Results showed that HPMC can be also used as a thickening agent to modify the viscosity of the PMN suspensions.

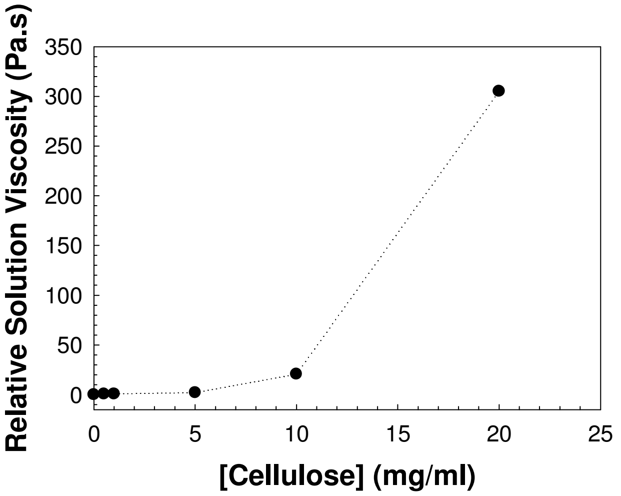

Figure 5.16. Relative viscosity of HPMC as a function of concentration.

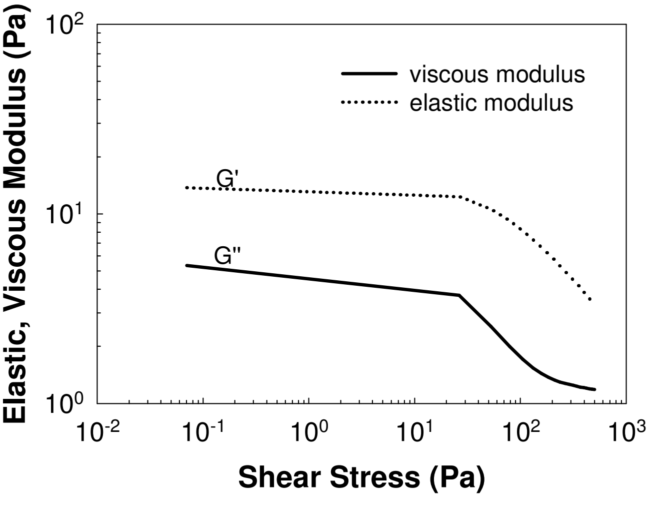

Figure 5.17. Storage and loss modulus of HPMC (10 mg/ml) as a function of stress.

5.3.3. Rheology of PMN Suspensions

In this study, to prepare the PMN slurries preliminary experiments were performed using anionic latex emulsions (B-1001 and B-1035). Concentrated PMN suspensions were prepared using PAA-PEO(2000) comb polymer as described in experimental section of this chapter. The pH of the suspensions was adjusted to 9. It is known from the zeta potential measurements discussed in Chapter four that PMN particles carry a net negative charge after PAA-PEO adsorption because of the negative surface charge of PAA backbone.

Therefore, in the study, the general expectation was to obtain a stable dispersion with the addition of anionic latex to the comb polymer coated PMN particle suspensions due to negative surface charge of PMN. This is because the repulsive forces should arise between anionic latex and the negatively charged comb polymer molecules. However, addition of anionic latex emulsion to comb polymer coated PMN suspension caused a strong agglomeration in the system (see Figure 5.18). The reason of the agglomeration can be partially attributed to the possible electrostatic interactions between the PAA/PEO and the other constituents in acrylic emulsion system other than the acrylix latex particles.

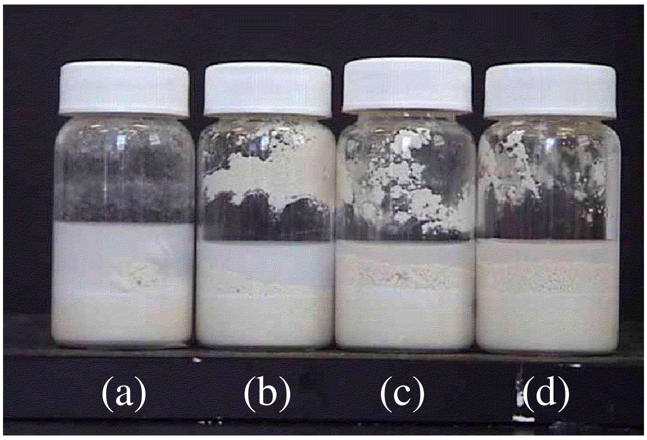

Figure 5.18. Picture of PAA-PEO comb polymer coated PMN suspensions in the presence of (a) B-1035 (b)B-1001 , PMN:latex (3:1) (c) B-1001 PMN:latex (2:1) (d) B-1001 PMN:latex (1:1).

On the other hand, agglomeration was not observed in PMN slurries prepared by nonionic latex binder, B60-A. This may be due to the non-ionic surfactant exist in B60-

A composition. Therefore, in PMN slurry preparation nonionic latex emulsion was used as the binder in the rest of the experiments.

Rheological behaviour of PMN slurries was investigated as a function of total solids loading, PMN:binder ratio and the cellulose content. Figure 5.19 shows the effect of PMN /nonionic latex binder ratio on the apparent viscosity of the tape casting suspension (ϕ_{tot}: 0.45). According to the figure there is a gradual increase in the viscosity as the binder content increase.

In the study the viscoelastic properties were examined by dynamic tests. Such experiments must be carried out at small amplitude of oscillation, so that the test conditions can be considered nondestructive. Under these conditions dynamic functions belong to the linear viscoelastic regime. In the case of concentrated suspensions like tape casting slurries the linear viscoelastic region is often limited in the very low strain amplitudes (Zupancic et al. 1998).

Complex modulus of the PMN suspensions as function of shear stress and frequency (Figures 5.20 to 5.21) states that especially as the binder content of the slurry increases a gel like behavior was observed that is indicated by a high yield stress. The complex modulus of the suspensions having PMN:binder ratio of (1:1) is about 5 times higher than the modulus of the suspension having PMN:binder ratio of (2:1). Complex modulus versus frequency graph describes a liquid like response for the low binder content (PMN:binder ratio (3:1)), whereas a gel like response at higher binder content. Similarly, the effects of cellulose content on the viscosity of the PMN slurries at 45 vol% is presented in Figure 5.22. As expected the vicsocity of the PMN slurry increases slightly as the HPMC content increases from 5 to 7 mg/ml.

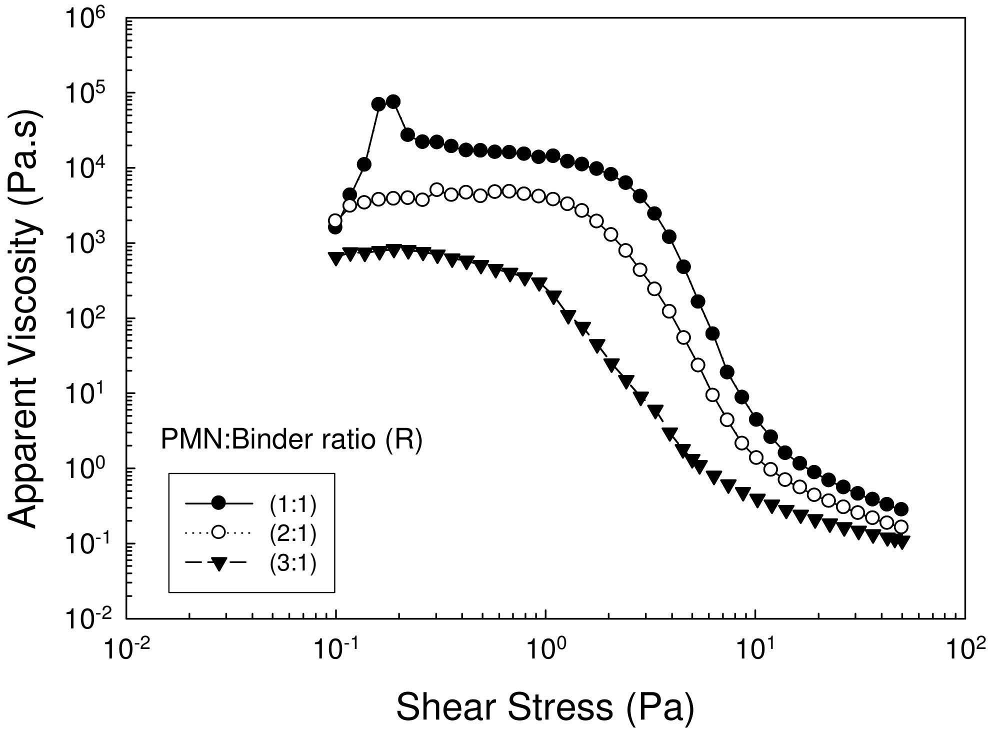

Figure 5.19. Viscosity of slurries having different PMN:latex ratio as a function of shear stress, ϕ_{tot} :0.45, HPMC content (5 mg/ml).

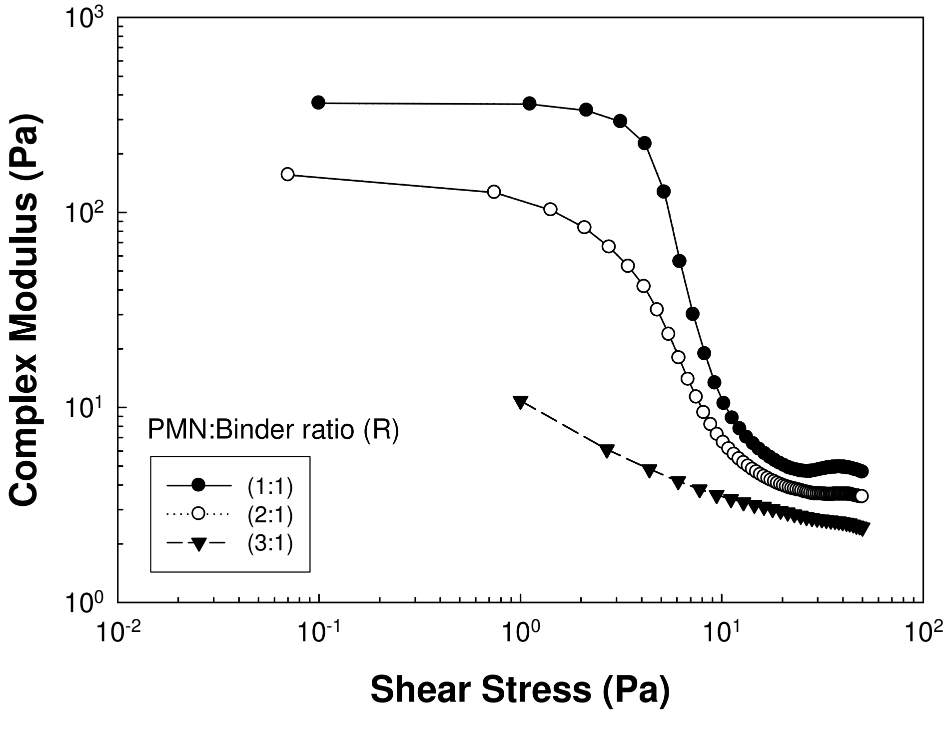

Figure 5.20. Complex modulus of slurries having different PMN:latex ratio as a function of shear stress, ϕ_{tot} :0.45, HPMC content (5 mg/ml).

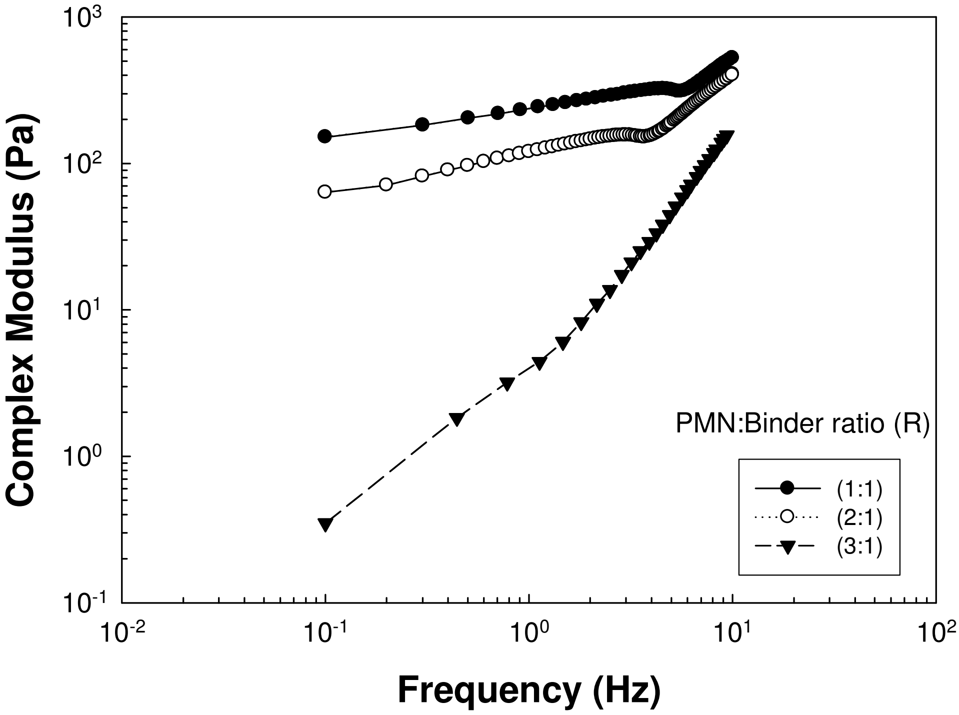

Figure 5.21. Complex modulus of slurries having different PMN:latex ratio as a function of frequency, ϕ_{tot} :0.45, HPMC content (5 mg/ml).

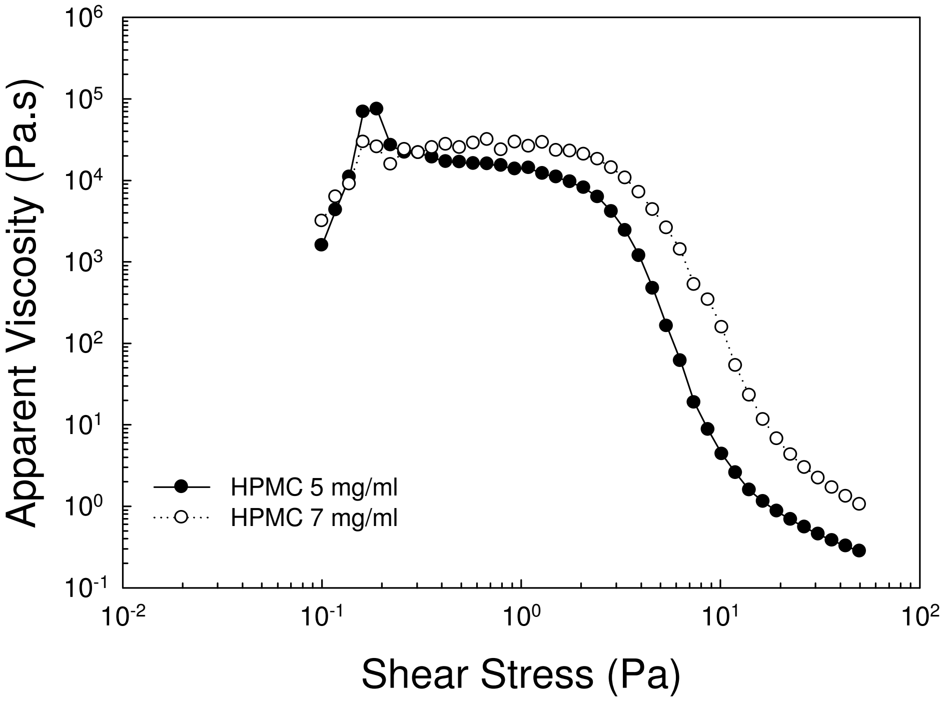

Figure 5.22. Viscosity of slurries having different cellulose concentration as a function of shear stress, ϕ_{tot} :0.45, PMN:binder ratio (2:1).

Figure 5.23 show the elastic and loss modulus (G` and G``) of the PMN slurry in dependency on the shear stress amplitude. The storage module G` of the slurry ($\phi$: 0.45) reached a maximum value of 500 Pa. This is caused by the high solid content which increases the elastic properties of the slurry. At low shear stresses the modulus remained nearly constant and G` was larger than G``, which means that the slurry behaves more elastic than viscous. The storage module G` exhibited a sudden decrease at a critical shear stress, τ_c.

Above τ_c weak attractive forces between the powder and/or binder particles are broken up by the external shear stress, which destroys the internal network. The elastic properties of the slurry become very low and the storage modulus decreases. The loss modulus G`` reaches a maximum at this point. This is also due to the breaking up of the weak connections between the particles in the slurry at these shear rates. The energy is used to break these networks and it is now transferred into the system cannot be stored as elastic deformation. The tendency for viscous deformation increases and both moduli decreases (Rueb and Zukoski 1997, Larson 1999).

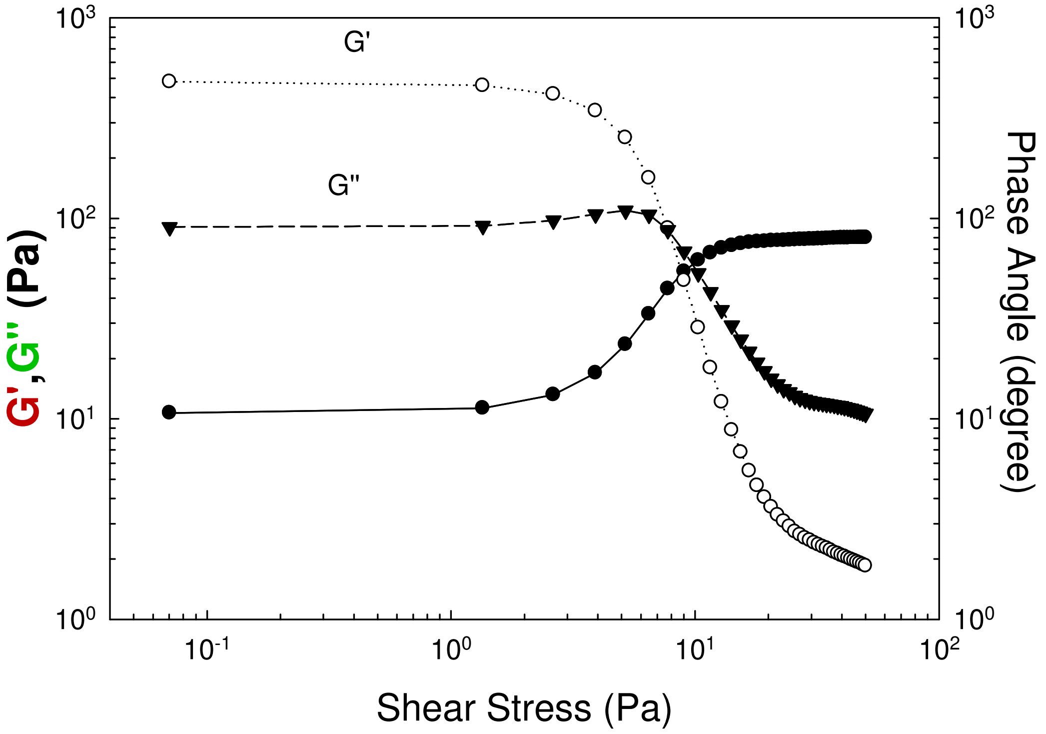

Figure 5.23. Viscoelastic properties of slurry having PMN: latex ratio (2:1), HPMC (7 mg/ml) and ϕ_{tot} : 0.45 as a function of shear stress.

The slurry must spread the carrier film during tape casting process. This means a shear stress greater than τ_c must be applied to the slurry. For tape casting the critical shear stress should be high enough, thus the gravitational forces on the powder are too weak to cause viscous deformation in the slurry, which could result in sedimentation of the particles. On the other hand, τc must not be too high because the slurry must flow under the shear conditions which occur during passing the doctor blades (Bitterlich et al. 2002).

To investigate the thixotropic behavior of the slurry the viscosity was measured as a function of shear rate in the range of 0.1 to 700 s^{-1} in an up and down sweep. Figure 5.24 show the flow behavior of the PMN slurry at 55 vol%, PMN:binder ratio of (1:1) and HPMC content of 7mg/ml. A good superposition of up and down curves was observed in the whole range of shear rate. Therefore, it is possible to conclude that suspensions exhibit a high degree of particle stabilization.

Viscosity of the PMN slurries at 55 vol% with PMN: binder ratio of (1:1) and (2:1) are presented as a function of HPMC content in Figures 5.25 and 5.26, respectively. Both suspensions showed a similar flow behavior at specified shear stress range. The increase in cellulose concentration caused a gradual increase in apparent viscosity. Viscoelastic behavior (G` and G``) of the PMN slurries at 55 vol% with PMN: Binder ratio of (1:1) is shown in Figures 5.27 and 5.28. According to the graphs the increase in HPMC content did not cause a significant rise in the elastic and loss modulus of the slurries at this solids loading.

Time dependent behavior of the PMN slurry at 55vol% was also examined by oscillation measurements (see Figure 5.29). During the time of oscillation (15 minutes) almost no changes in the internal structure of the slurries occurred. The storage and loss modulus remained nearly constant during this period. This means that slurry build up the internal structure very fast and do not change it afterwards. This time independent behavior is crucial in tape casting, because slurries should not change their properties during processing.

Viscosity and the elastic modulus of the PMN slurries prepared at 60 vol% were also investigated in a similar manner. Results are given as function of shear stress in Figures 5.30 to 5.32. The effect of HPMC concentration on the flow behavior and modulus are given in the same figures. Suspensions exhibit similar flow behavior with the PMN suspensions prepared at 45 and 55 vol%. At low HPMC content a linear increase was observed in elastic modulus with increasing frequency. However, as the HPMC concentration was increased the effect of frequency on the storage modulus became less significant. Because at high HPMC concentration suspension shows more solid like response (see Figure 5.32).

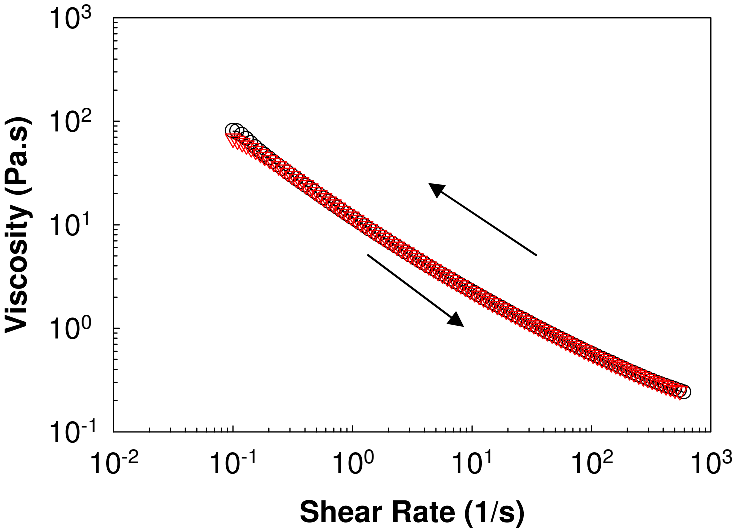

Figure 5.24. Viscosity of slurry having PMN: binder ratio of (1:1), HPMC (7 mg/ml) and ϕ_{tot}: 0.55 as a function of shear rate. Arrows indicate the increasing and decreasing rate sweeps.

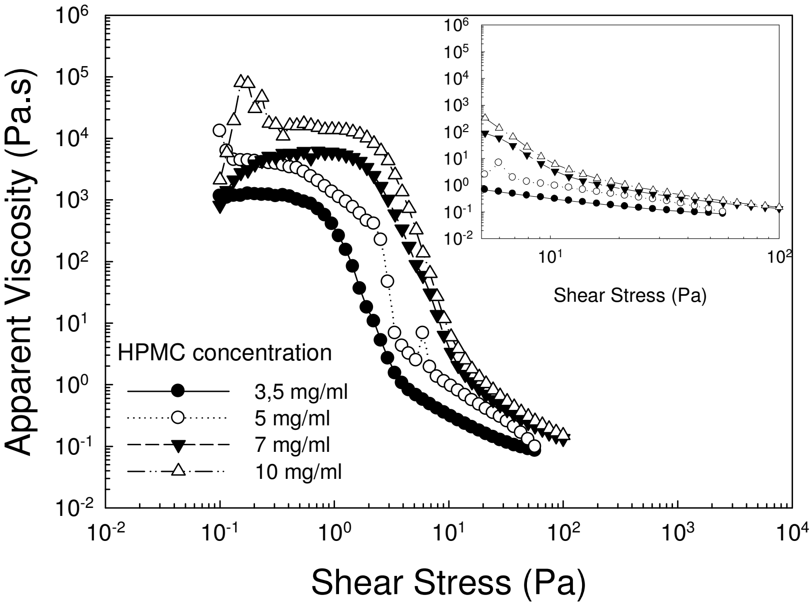

Figure 5.25. Effect of HPMC concentration on the viscosity of slurries having PMN: binder ratio (1:1), ϕ_{tot}: 0.55 as a function of shear stress.

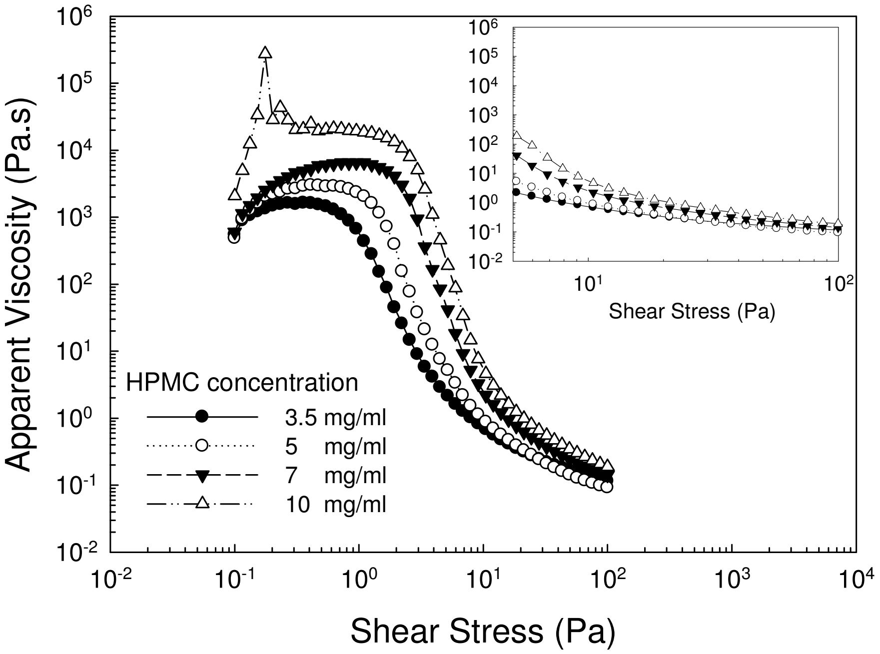

Figure 5.26. Effect of HPMC concentration on the viscosity of slurries having PMN: binder ratio (2:1), ϕ_{tot}: 0.55 as a function of shear stress.

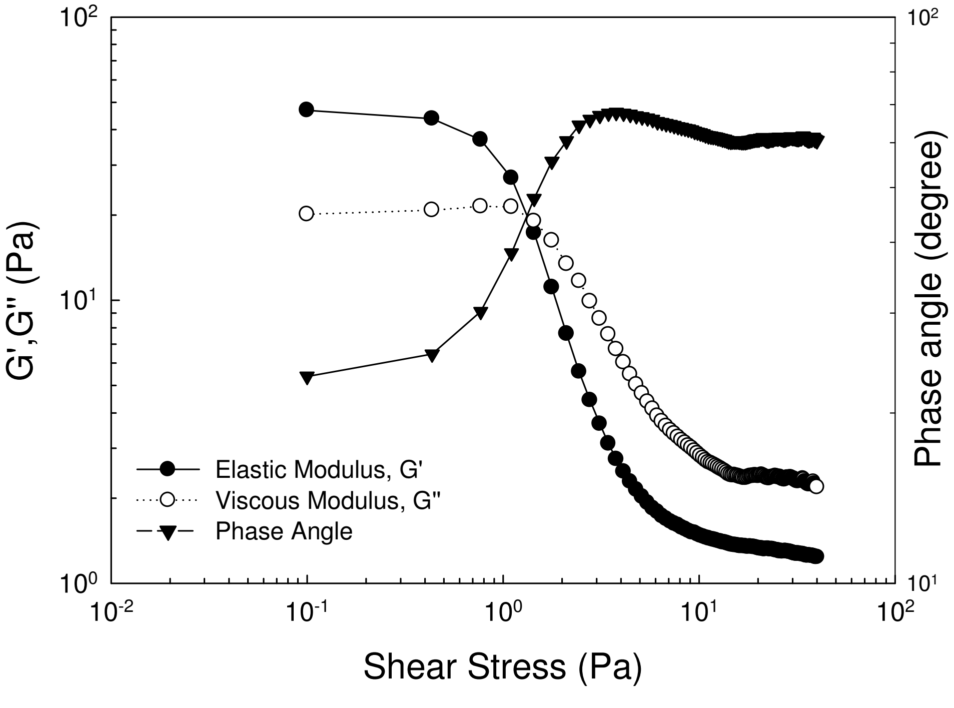

Figure 5.27. Viscoelastic properties of slurry having PMN: binder ratio (1:1), HPMC (3.5 mg/ml) and ϕ_{tot}: 0.55 as a function of shear stress.

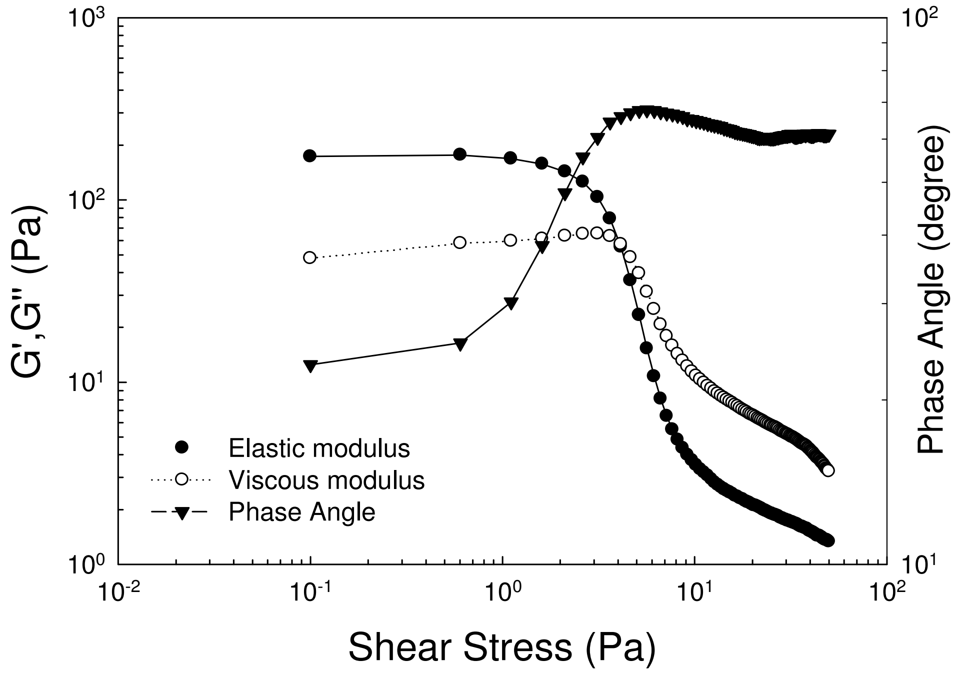

Figure 5.28. Viscoelastic properties of slurry having PMN: binder ratio (1:1), HPMC (5 mg/ml) and ϕ_{tot}: 0.55 as a function of shear stress.

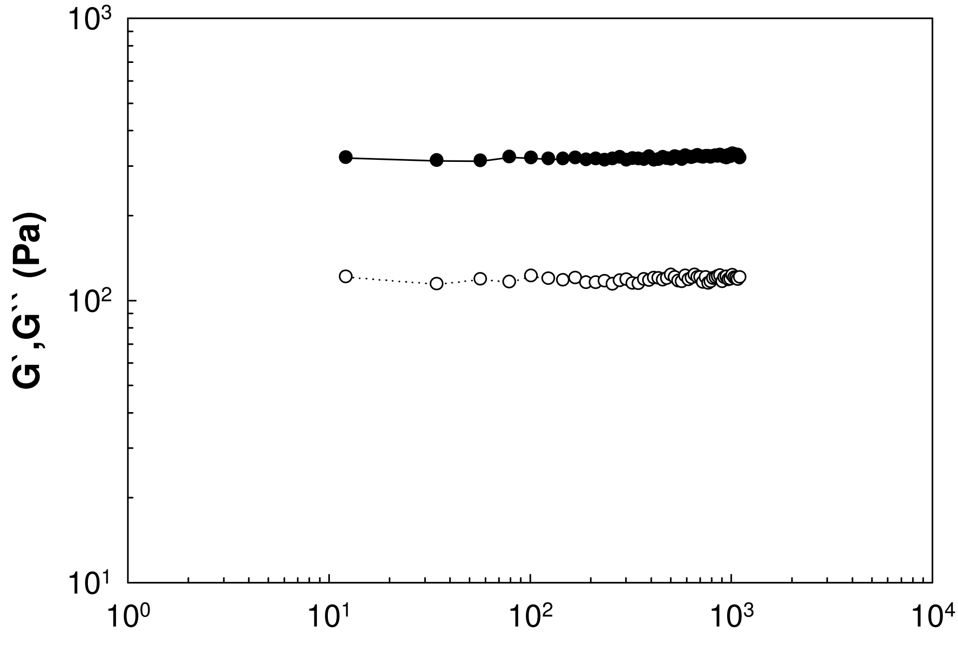

Figure 5.29. Time dependent response of modulus for PMN slurry having a PMN:latex ratio (1:1), HPMC content (7 mg/ml) and ϕ_{tot} :0.55.

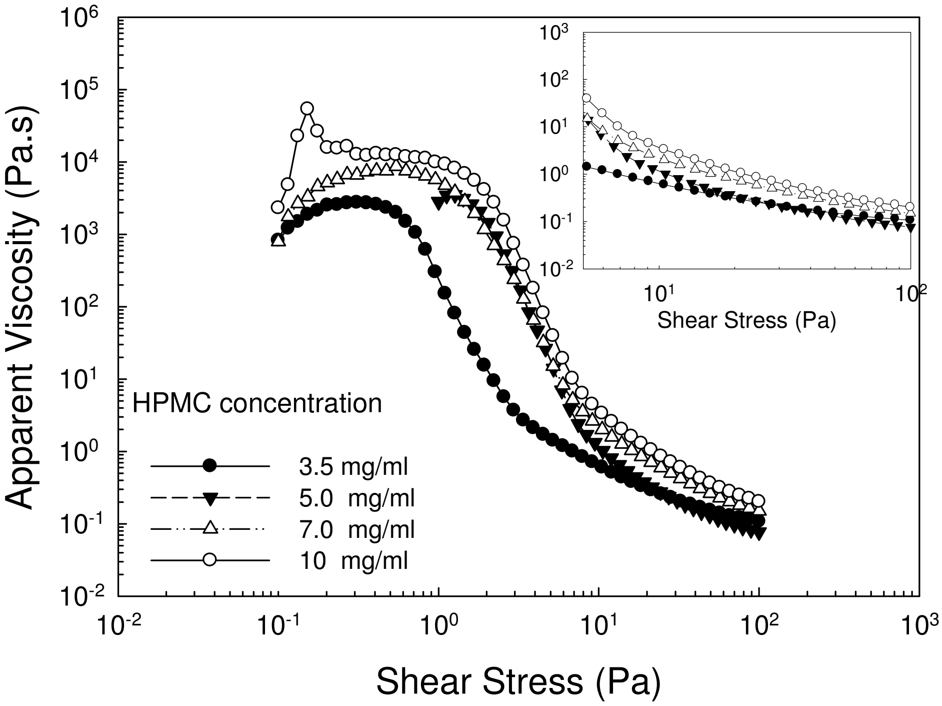

Figure 5.30. Effect of HPMC concentration on the viscosity of slurries having PMN: latex ratio (1:1), ϕ_{tot}: 0.60 as a function of shear stress.

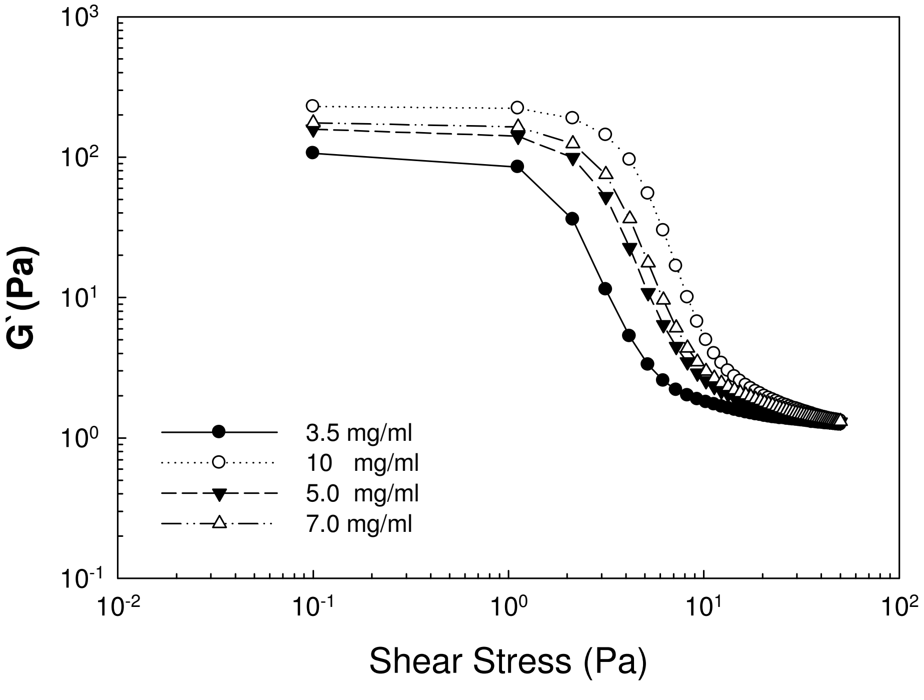

Figure 5.31. Effect of HPMC concentration on the elastic modulus of slurries having PMN: latex ratio of (1:1), ϕ_{tot}: 0.60 as a function of shear stress.

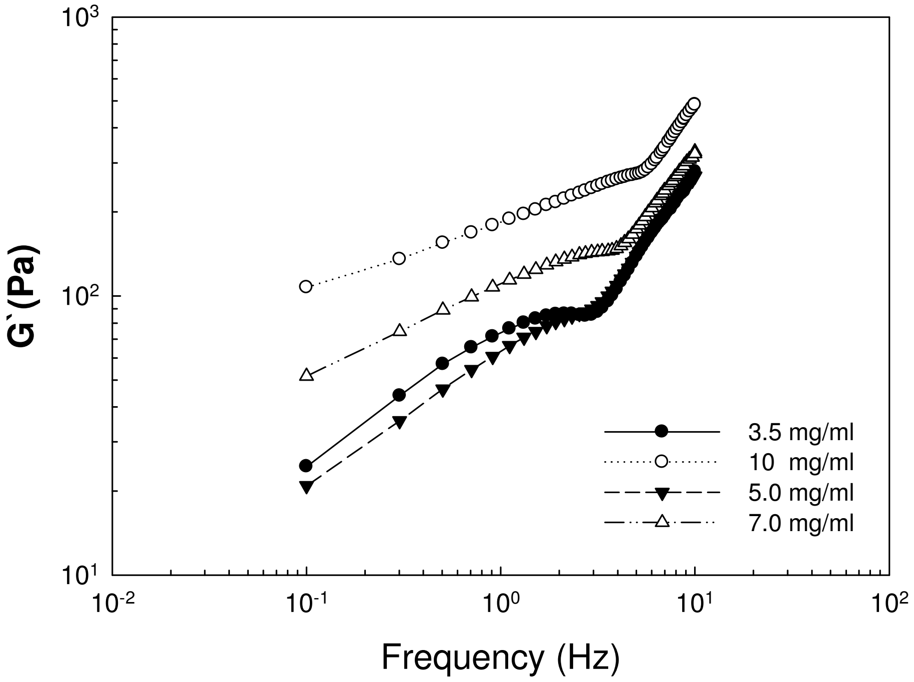

Figure 5.32. Effect of HPMC concentration on the elastic modulus of slurries having PMN: latex ratio (1:1), ϕ_{tot}: 0.60 as a function of frequency.

Rheological behavior of PMN slurries having PMN:binder ratio of (1.5:1) were studied by steady shear and dynamic (oscillation) measurements. Results are shown in Figures 5.33 and 5.34. The viscosity of PMN slurries (60 vol%) at a PMN: binder ratio of (1.5:1) is presented in Figure 5.32. Viscosity and modulus values of some other compositions were also figured out for comparison purposes. Viscosity and modulus of the PMN slurry with this specified composition did not show significant difference compared to the values of slurry having PMN:binder ratio of (1:1).

To summarize the effects of the solids concentration on viscoelasticity, Figure 5.35 is plotted at all concentrations tested in the study. Structural information was obtained by conducting the frequency (ω) sweeps at a given strain. A gel like response was observed since G` and G`` vary as $\omega^j$, where j: 0.3-0.7 at high solids concentrations (Lewis 2000). According to the graph the elastic contribution exceeds the viscous one (G`> G``) over the entire ω range. With increasing solid volume fraction the traces of G`(ω) and G``($\omega$) are getting more and more close and become parallel to each other. A further increase in particle concentration may reduce the influence of frequency on G` and G`` (solid response).

Among the various rheological models existing in literature, the Hershel Bulkley model gave the best fitting results for describing the plastic flow behavior of examined suspensions. The model combines the Powder law model with a yield stress variable. The Herschel Bulkley model is:

$$\sigma = \sigma_0 + K.\ \dot{\gamma}^n \qquad (5.2)$$

where σ_0 is the yield stress, K is the consistency index and n is the shear thinning constant. The model parameters for tape casting slurries were calculated using rheometer software (Bohlin) and results are reported in Tables 5.2 and 5.3.

Table 5.2. Herschel Bulkley model parameters of tape casting slurries.

Slurry composition	**r**	**σ_0**	**K**	**n**
R1(7)55	0.9973	1.796	5.734	0.4694
R1(7)60	0.9971	2.309	7.962	0.4302
R1.5(7)60	0.9966	1.954	6.379	0.4694
R1.5(7)55	0.9975	1.665	9.829	0.4064

Table 5.3. Herschel Bulkley model parameters as a function of HPMC content (R1-x-55).

HPMC, x (%)	**r**	**σ_0**	**K**	**n**
3.5	0.9990	0.8772	1.099	0.5993
5.0	0.9986	1.6090	3.817	0.4278
7.0	0.9977	1,741	3.486	0.4995
10.0	0.9977	1.912	4.741	0.4601

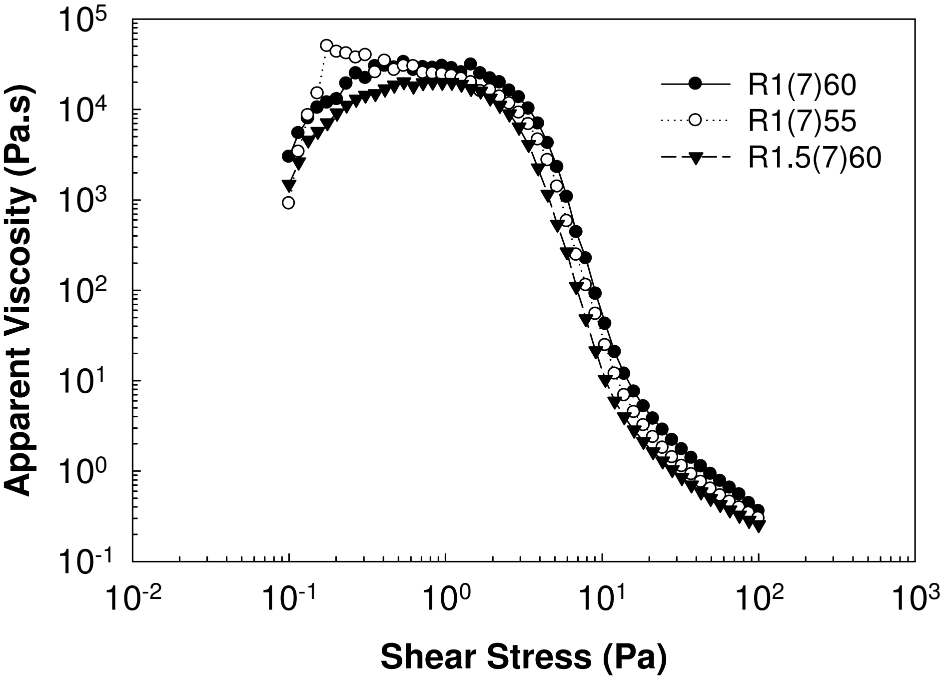

Figure 5.33. Effect of slurry solids loading and PMN: latex ratio on the viscosity as a function of shear stress.

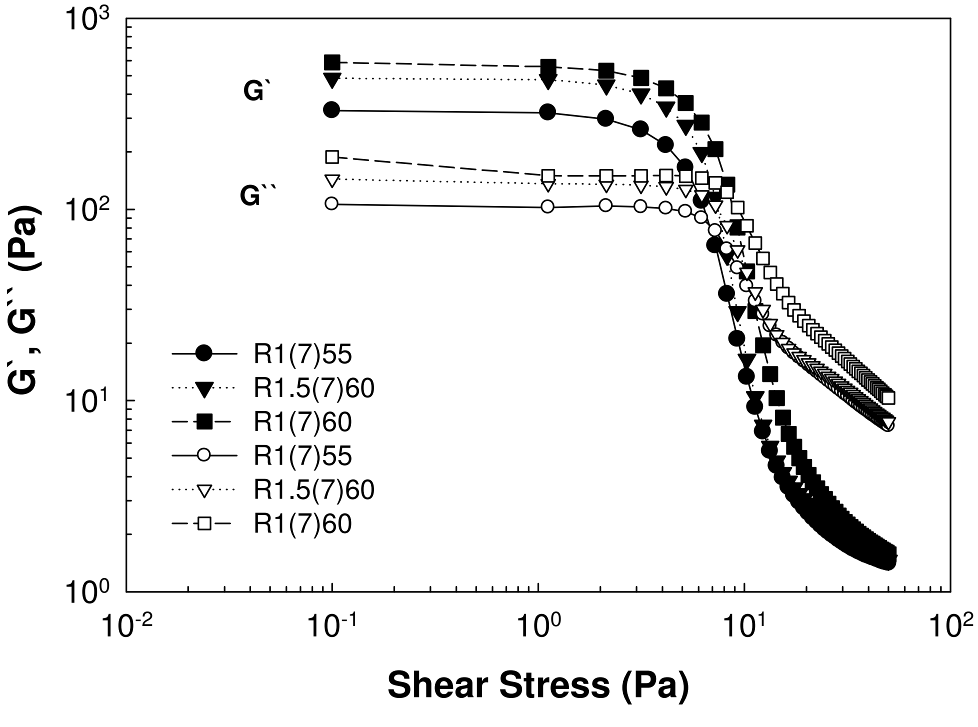

Figure 5.34. Effect of slurry solids loading and PMN:latex ratio on the molulus as a function of shear stress, closed symbols G`, open symbols G``.

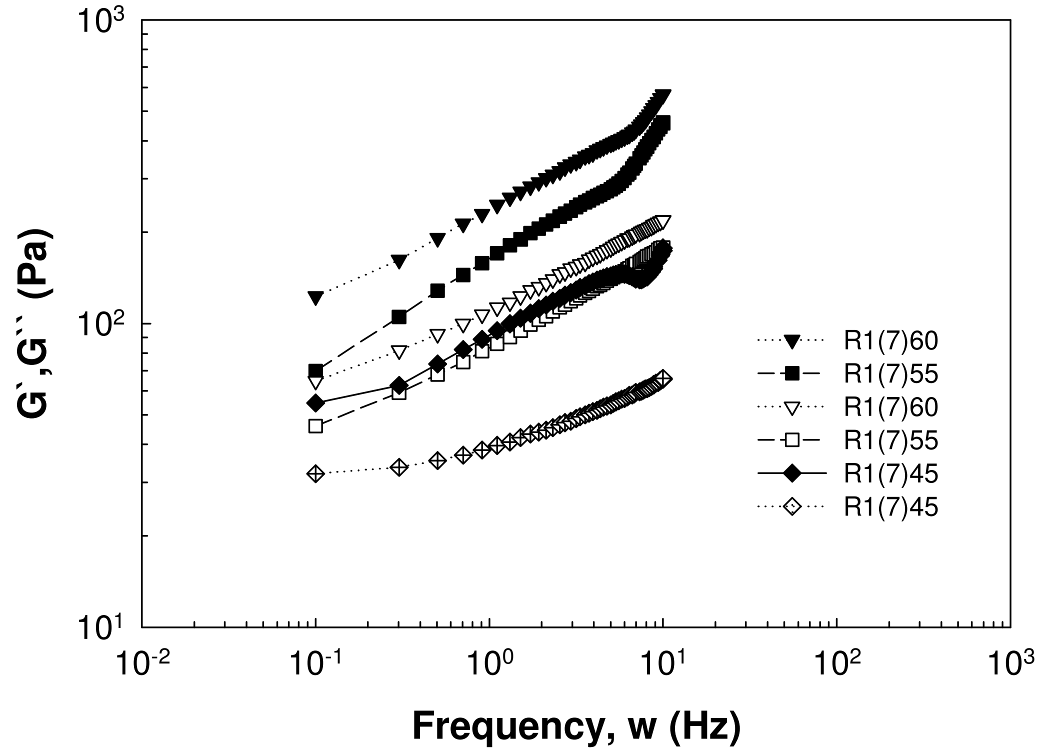

Figure 5.35. Effect of slurry solids loading on the modulus as a function of frequency, closed symbols G`, open symbols G``.

In this study, the slurries under investigation showed some differences between their rheological properties but most of them match the demands for tape casting: no thixotropy, time stability, and a critical stress in ranges practicable for tape casting. On the other hand, suspensions showed plastic behaviour with yield stress. This rheological behaviour may be partially attributed to the contribution of the binder phase. It was shown that the binder emulsion is pseudoplastic, at high concentration ~47% and Newtonian at lower concentrations. Therefore, as the binder concentration in PMN suspensions is increased higher viscosity values were obtained. Similarly, addition of HPMC increased the viscosity of the slurries although it is used in small amount as a wetting agent. It is also known that, HPMC is used as the thickening agent in ceramic suspensions, and especially in acrylic latex emulsions (Brown and Garrett 1959).

5.3.4. Wetting Behavior

In the study, a silicone-coated mylar film was used for slurry deposition. The main purpose of the silicone coating was to facilitate the easy release of the dried tape. However, suspensions experienced strong dewetting forces during casting onto these films. Dewetting phenemona is influenced by both surface energy and viscosity. The other parameter that influence wetting is the contact angle between solid and liquid. The velocity of a receding solid-liquid interface is proportional to $\gamma_{lv}(1-\cos\theta)/(\eta)$, where θ is the contact angle between the solid and liquid, γ_{lv} is the liquid-vapor interfacial energy, and η is the liquid viscosity (Smay and Lewis 2001, Hunter 1995, Zosel 1993). Therefore, to improve shape retention of as-cast layers, the effects of reducing the surface tension and enhancing the low shear viscosity of this system should be investigated. Figure 5.36 show the surface tension and contact angle of HPMC as a function of concentration.

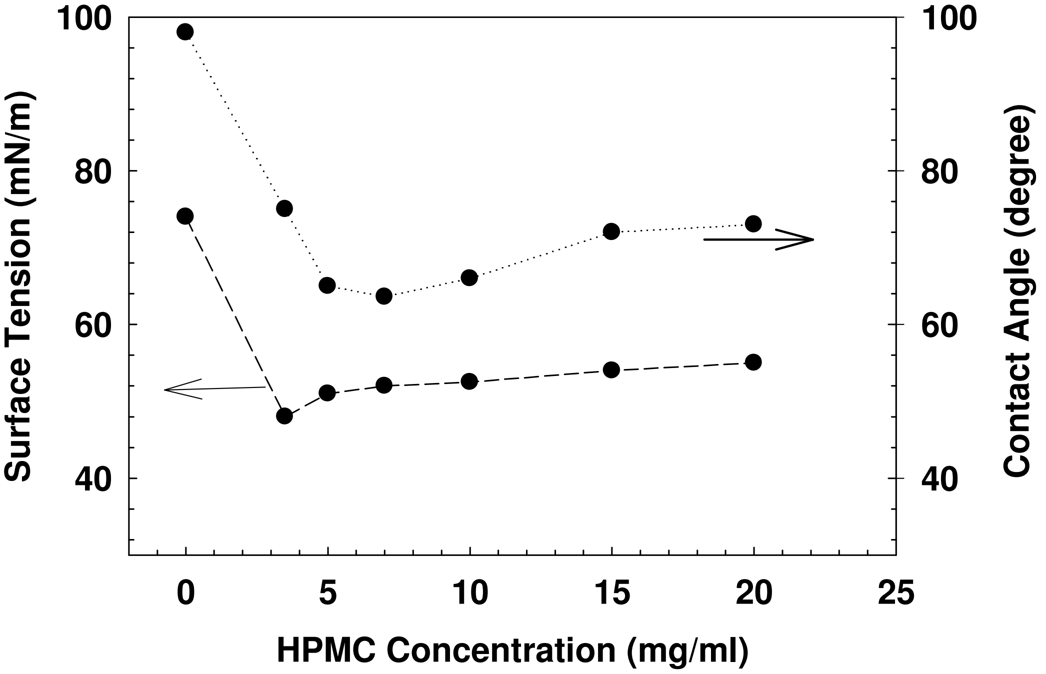

Figure 5.36. Surface tension and contact angle of HPMC as a function of concentration.

Contact angle measurements were carried out on the mylar film (silicon coated side) using sessile drop method. According to the Figure 5.36, surface tension and contact angle of HPMC is much lower compared to the corresponding values of water. With increasing polymer concentration thereby increasing viscosity, slight increased was observed in the measured contact angle values. Consequently, spreading of the solutions on the mylar surface decreased. Riedl and co-workers investigated the surface tension and contact angle of HPMC in the absence and presence of plasticizer. Surface tension value of HPMC 2 wt% was reported to be 52.88 (±1.4) mN/m (Riedl et al.

2000). Therefore, there is an agreement between the surface tension values obtained in this study and the literature values.

Contact angle of the PMN slurries having different compositions with the mylar film are tabulated in Table 5.4. Contact angle of pure binder and distilled water is also given in the same table. Results showed that contact angle of PMN slurries with the mylar film was dependent on the HPMC content as well as the suspension viscosity.

Table 5.4. Contact angle values of PMN suspensions having different compositions.

Sample	Contact Angle(°)
Water- mylar film	94
Water-glass	19
B60A	63
R1(3.5)55	64
R1(5)55	64
R1(6)55	54
R1(7)55	52.5
R1(8)55	52.5
R1(10)55	66
R1.5(7)55	52.5
R2(5)55	64

Figure 5.37 depicts the deposition characteristics of the PMN films having different slurry compositions. Pictures were taken just after tape casting process. Results reveals that samples having low and very high HPMC content exhibit strong wetting problems. On the other hand according to the Figure 5.37 (d), PMN: binder ratio has some effects on the wetting behavior. Observed wetting characteristics can be explained well with the related contact angle values given in Table 5.4. For the composition of R1 (15) 55 a similar wetting behavior was observed as shown in Figure 5.37 (c). The increase in contact angle of PMN slurries in the presence of high HPMC may be attributed to the increase in viscosity.

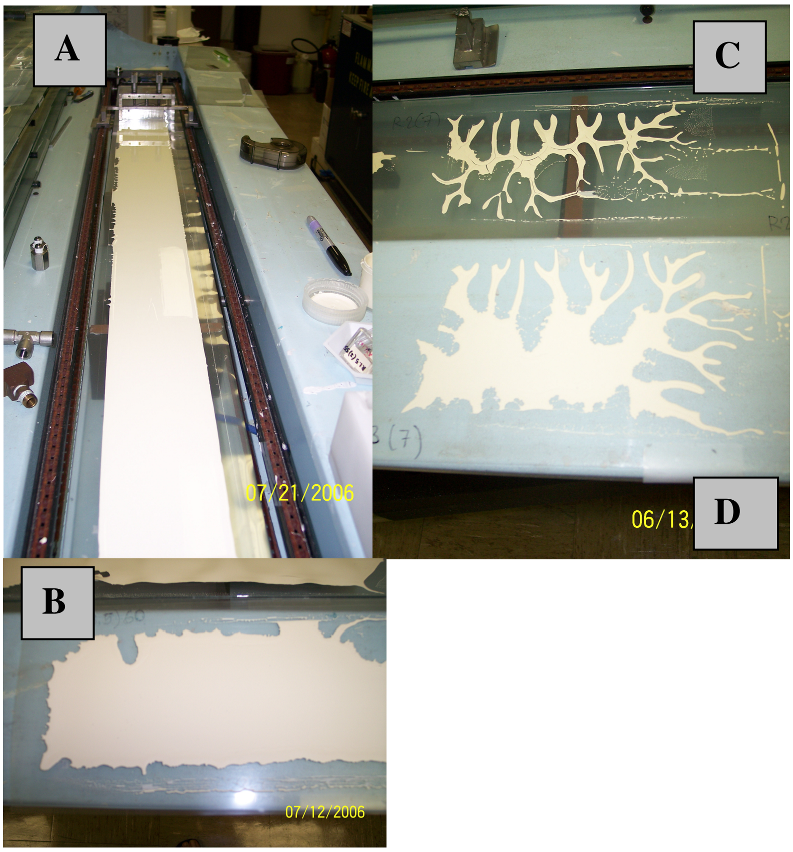

Figure 5.37. Deposition characteristics of PMN slurries onto mylar film a) R1(7)55, b) R1(3.5) 55, c) R2(7)55, d) R3(7)45.

5.3.5. Drying of PMN Films

During drying biaxial stresses may develop in ceramic films. As the solvent evaporates the film shrinks freely in the z-axis while shrinkage in the x-y plane is constrained due to strong adhesion to the casting substrate. This result in a residual stress on the film (Lewis 2000, Scherer 1990). These stresses cause formation of cracks unless relatively large amounts of organic binders added. On the other hand, presence of organic additives in large quantities may cause other defects such as carbon contamination, large pore volumes or delamination during heat treatment (Chiu et al. 1993). Therefore it is crucial to adjust the binder content in tape casting slurries and observe its effect on the drying step.

Figure 5.38 show the pictures of PMN green films having different powder: binder ratio after drying. Figure 5.38 (b) depicts the cracks formed in the film (powder: binder) ratio of (2:1) during drying period. At higher binder content, such as PMN: binder ratio of (1.5:1), perpendicular cracks were observed on the surface of the film with respect to casting direction. Pictures also reveal the effect of film thickness on the crack formation. For the slurry composition having PMN:binder ratio of 2:1, drying cracks were observed in 300 µm and 500 µm films . However, in the case of PMN:binder ratio of 1.5:1 less cracks and more buckling were observed in 500 µm films compared to the 300 µm films (see Figure 5.38 (a)). In the study, the slurry having a composition of R1(7)55 did not showed any significant defects during drying. PMN films having thickness of 300 and 500 µm were prepared successfully using this composition.

On the other hand, it is known that such kind of films crack if applied too thickly. Previous studies have shown that, above a critical thickness, the film will crack spontaneously, and independently of the drying rate. Chiu et al. showed that there is a critical cracking thickness (CCT) above which films would crack during drying. CCT occurs because cracking will not occur unless the energy required to form a crack is less than the energy gained in relieving the strain in the film. The CCT is a function of magnitude of the biaxial stress and the fracture resistance of the material that construct the film. Hence biaxial stress that develops in the film can cause cracking even if a moisture gradient does not exist across the thickness of the film (Grau et al. 1999, Chiu et al. 1993).

In this study, the stress development during drying can be attributed to the moisture gradient in green bodies. Differential shrinkage between the top and bottom of the film can produce stress that results in cracks. A biaxial tensile stress can also develop due to the capillary tension in the pore liquid. The capillary pressure may cause shrinkage in the film if it was not constrained by the substrate. Particle rearrangement may bring some stress in the thickness direction. But the substrate creates a dimensional constraint that prevents the complete relaxation of the stress. In this case drying stress must be as high as the capillary pressure of the liquid. The capillary stress is proportional to surface tension and inversely proportional to the pore size. Therefore, the film stress decreases as the liquid surface tension decreases and the particle size increases (Chiu and Cima 1993, Scherer 1990, White 1992). On the other hand, there has been evidence of drying zones (saturated, super-saturated, and dry) in aqueous based tape cast films. Suspension instabilities at the super-saturated and saturated interface can lead to microstructural inhomogeneities such as large pores and clusters (Chiu and Cima 1993, Martinez 2002).

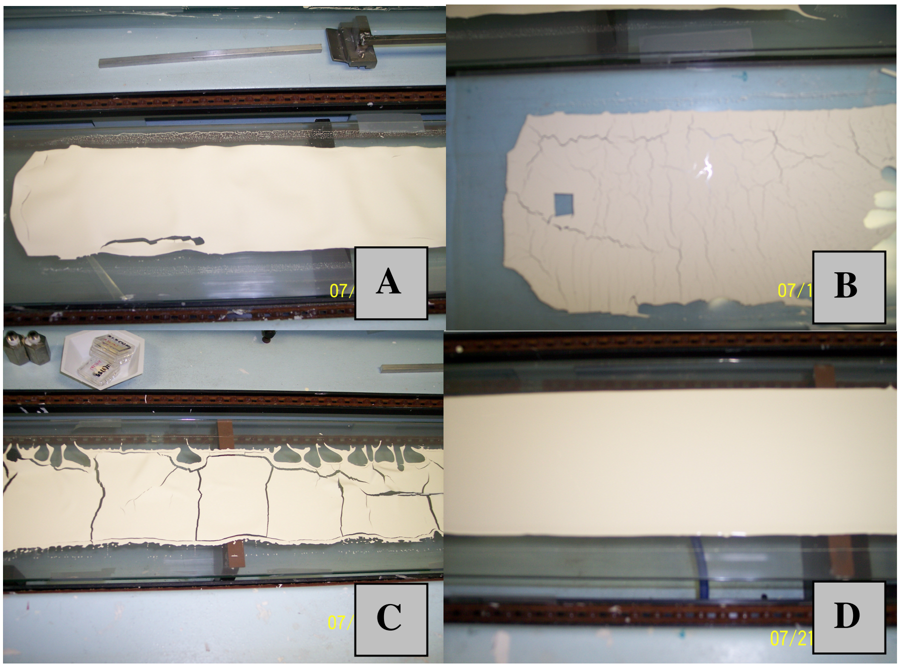

Figure 5.38. Digital pictures of PMN green films having different compositions. Total solids concentration 55 vol%, HPMC content 7 mg/ml a) PMN:latex (1.5:1), 500 µm b) PMN:latex (2:1), 300 µm c) PMN:latex (1.5:1), 300 µm, d) PMN:latex (1:1), 300 µm.

Defects observed during drying in PMN films prepared from various slurry compositions were listed in Table 5.5. Accordingly, slurries prepared at 45 vol% generally exhibited strong wetting problems at all compositions. For the total solids concentration of 55 vol%, again wetting problems were observed at low HPMC content and at high powder: binder ratio. PMN compositions having powder: binder ratio of (1:1) and HPMC content in the range of 6 to 8 mg/ml did not experienced any problem during deposition and during drying period. Similar result was obtained for the slurries having total solid concentration of 60 vol%.

Table 5.5. Defects observed in PMN films (300 µm) having different compositions.

	Total Solids Loading (vol%)	**PMN: Binder**	**Cellulose Content (mg/ml)**	**Viscosity (Pa.s) high shear**	**Defects**
1	45	1:1	5	0.38	moderate wetting problem
2	45	1:1	7	0.92	moderate wetting problem
3	45	2:1	5	0.19	drying cracks
4	45	2:1	7	0.67	drying cracks
5	45	2:1	15	2.12	strong wetting problem
6	45	3:1	5	0.26	strong wetting problem
7	45	3:1	7	0.39	strong wetting problem
9	55	1:1	3.5	0.30	moderate wetting problem
10	55	1:1	5	0.94	moderate wetting problem
11	55	1.1	6	0.98	no problem
12	55	1:1	7	1.60	no problem
13	55	1:1	8	1.65	no problem
14	55	1:1	10	2.56	strong wetting problem
15	55	1.5:1	7	1.73	buckling
16	55	2:1	3.5	0.28	drying cracks
17	55	2:1	5	0.85	drying cracks
18	55	2:1	7	1.42	drying cracks
19	55	2:1	10	2.48	drying cracks, moderate wetting problem
20	60	1:1	3.5	0.60	moderate wetting problem
21	60	1:1	5	1.02	no problem
22	60	1:1	7	2.00	no problem
23	60	1:1	10	3.34	moderate wetting problem
24	60	1.5:1	7	1.98	drying cracks, buckling

5.3.5.1. Drying Stresses

Drying stress in PMN films were investigated using cantilever deflection method as a function of drying time and the HPMC content. Figure 5.39 show the effect of HPMC concentration on the stress formation of the PMN films. All layers exhibited a rapid period of rise in tensile stress followed by a maximum stress and subsequent stress decay to a final residual stress. A decrease was observed in stress formation as the

HPMC concentration increase. This may be attributed to the decrease in surface tension in the presence of HPMC.

In all films, the drying stress evolution displayed three distinct regions: (1) stress rise (σ_{rise}), (2) stress maximum (σ_{max}) followed by relaxation, and (3) secondary stress rise ($\sigma_{secondary}$) followed by the presence of a residual stress ($\sigma_{residual}$). During the stress rise period evaporation leads an increase in solids concentration (Smay et al. 2001). Chiu and Cima found that stress maximum occurs when the network does not shrink further in other words when the 100% saturation is reached. Further evaporation causes $\sigma_{secondary}$ as the water evaporates from within the pore network. Residual stress occurs due to strength of the particle network that consist binder and polyelectrolyte (Chiu and Cima 1993).

Stress rise period is directly proportional to the surface tension of the liquid phase and inversely proportional to the particle size. σ_{max} can be related to the capillary pressure (P_{cap}) at 100% saturation. It is given by the Laplace equation: (Scherer 1990, White 1992)

$$P_{cap} = \frac{2\gamma}{r_p} \qquad (5.3)$$

where γ is the liquid/vapor surface tension and r_p is is the pore radius. The pore radius can be approximated by the following equation:

$$r_h = \frac{2(1-\varphi)}{\phi \rho_s S} \qquad (5.4)$$

where ϕ is the colloid volume fraction, ρ_s is the density of the colloid phase and S is the specific surface area. Chiu and Cima also showed that the maximum drying stress, σ_{max}, is proportional to the surface tension of the liquid phase and inversely proportional to the particle size. Therefore, in this study the observed reduction in the σ_{max} may be attributed the reduction in the surface tension in the presence of HPMC (Chiu and Cima 1993).

The secondary stress rise observed for the PMN/latex films, was attributed to latex coalescence. Latex coalescence involves the particle consolidation caused by evaporation, deformation of the lattices and rupture of the emulsifying layer by capillary pressure, and permanent deformation driven by capillary pressure and polymer interfacial tension. The transition from distinct lattices to a continuous organic film results in contraction of the binder phase and increased compressive force on the PMN network, resulting in a secondary stress rise in the dry film (Smay and Lewis 2001, Martinez and Lewis 2002).

The behavior observed in PMN/latex films during secondary stress period is a general characteristic of the films that contain powder and organic phase. It was reported that in binder free films (contain only the powder) the stress relaxas after the maximum stress period. Martinez showed that initially during drying both latex and rigid particles behave similarly. But the main difference is the slope of the stress rise. The degree of stress relaxation at this stage depends on how fast the particles can deform under a given capillary pressure. For polymers with small relaxation times (low Tg) deformation occurs congruently with capillary pressure. Polymers with large relaxation times (high Tg) will resist deformation so the strain in the film should be larger or equal to the evaporation time (Martinez 2002).

To summarize, during drying of the gels solvent is transported from the interior of the film to the surface trying to limit the exposure of the energetically unfavorable solid/gas interface. This behavior induces compression in the particle network. The drying body would like to shrink in three dimensions but since it is constrained by the substrate it can only shrink in the z-direction. But it is kept in tension in the x-y plane (Martinez 2002, Scherer 1988, Rahaman 1995, Kiennemann et al. 2005). This solvent induced tension in the particle network is what drives the drying stress measured in our studies. A reduction by half from the normal surface tension of water can result in a proportional reduction in capillary pressure (Scherer 1990).

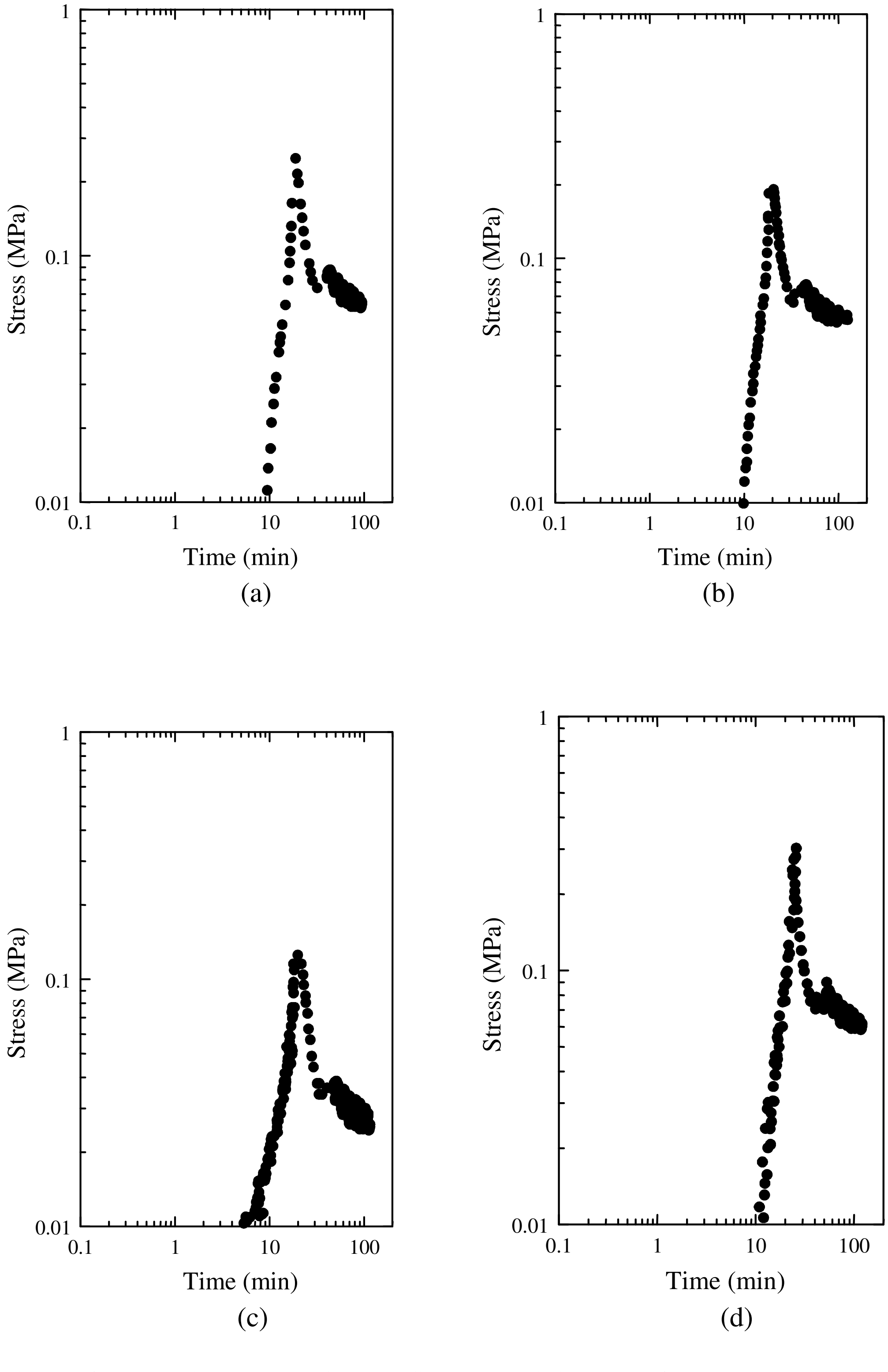

(a)

(b)

(c)

(d)

Figure 5.39. Drying stress of PMN films containing a) 3.5 mg/ml cellulose, b) 5 mg/ml cellulose c) 7 mg/ml cellulose d) no cellulose. PMN: latex (1:1), ϕ: 0.55.

5.3.5.2. Structural Evolution of Droplets during Drying

Structural evolution of the concentrated tape casting suspensions is difficult to observe whereas one can analyze the structural evolution of the dilute droplets. This investigation can give some information about the powder-binder interaction during drying period. Upon drying a droplet of liquid typically leaves a ring of solute on the substrate on which it rested (Hu and Larson 2005). To investigate the structural evolution of PMN suspensions during drying, samples were diluted to ϕ=0.001 and observed under an inverted optical microscope. For this purpose, a 4 μL slurry drop on a glass slide was imaged using an optical microscope during drying (Figure 5.40). Images were recorded using a digital camera. Results are given in Figures 5.41 to 5.45.

The images reveal that the formation of a dense particle layer at the μ-drop perimeter, as drying proceeds (see Figure 5.41). Figure 5.42 shows the images of the tape casting suspensions having PMN:latex ratio of (1:1). In the later stage of the drying process, particle clusters were observed in the supersaturated region. Particles also migrated to the edge of the droplet. Furthermore, some flocculation behavior was observed between the particles in the center of the droplet. Similar behavior was noticed in the suspension having PMN:latex ratio of (2:1) (Figure 5.44). On the other hand, cluster formation was not observed in the droplets deposited from the pure PMN suspensions (Figure 5.43) or pure latex emulsions or suspensions having PMN:latex ratio of (3:1) (Figure 5.45).

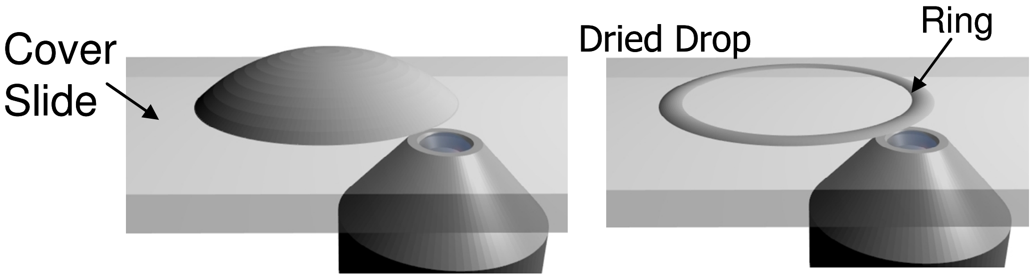

Figure 5.40. Schematic presentation of the method followed in the droplet drying experiments.

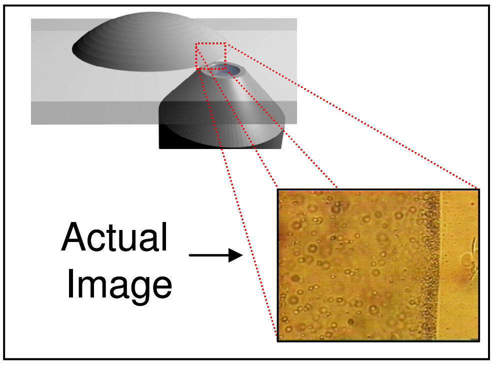

Figure 5.41. Schematic illustration that identifies the regions in optical microscope images (Source: Martinez 2002).

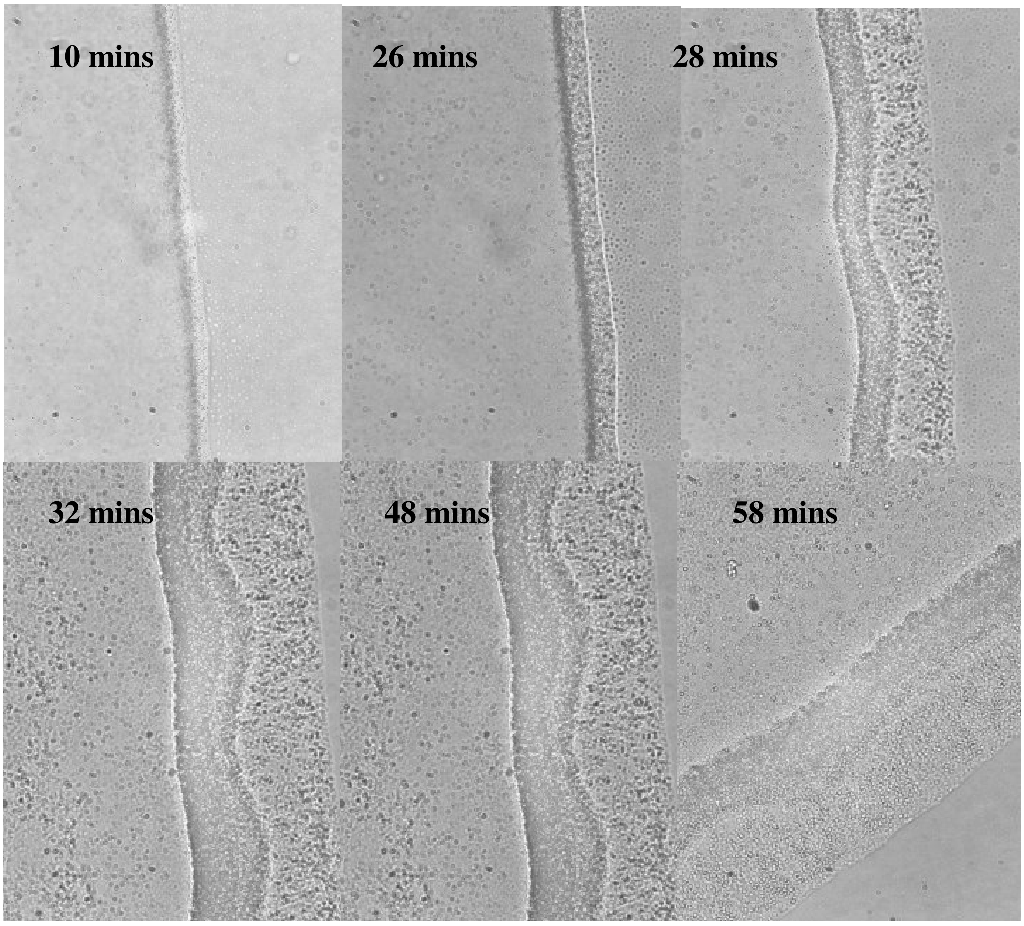

Figure 5.42. Optical microscope images that show the drying of a droplet having a composition of R1(7)55.

Ring formation due to drying of droplet is caused by evaporation driven flow (Hu and Larson 2005). The streaming of the particles from the center of the drop to the edge is due to the constrained geometry of the drop. Since the contact line of the drop is pinned the fluid has to flow the interface in order to prevent the shrinkage of the drop. The resulting capillary flow drives the particles from the center to the edge of the drop. As a result particle network forms on the contact line. Therefore, when drying is completed the most of the solid phase is deposited at the edge. It is also important to know that the streaming of particles during drying is not limited to dilute suspensions (Deegan et al. 1997).

On the other hand, a possible explanation for the flocculation behavior observed in the droplet can be the PMN-binder interactions. Previously, Martinez and Lewis investigated the structural evolution of the alumina: latex system with the same method and they obtained similar results for the alumina: anionic latex system. However, they did not explain the reason that drives the flocculation (Martinez and Lewis 2002).

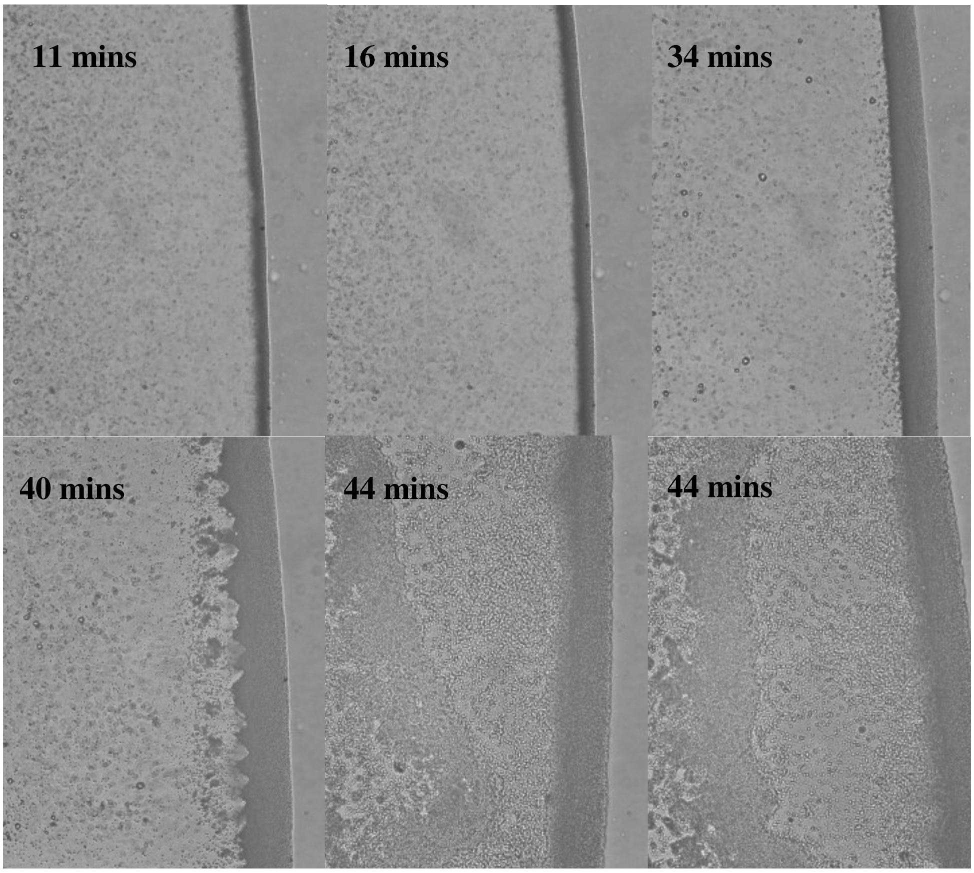

Figure 5.43. Optical microscope images that show the drying of a droplet contains only PMN particles as a function of drying time.

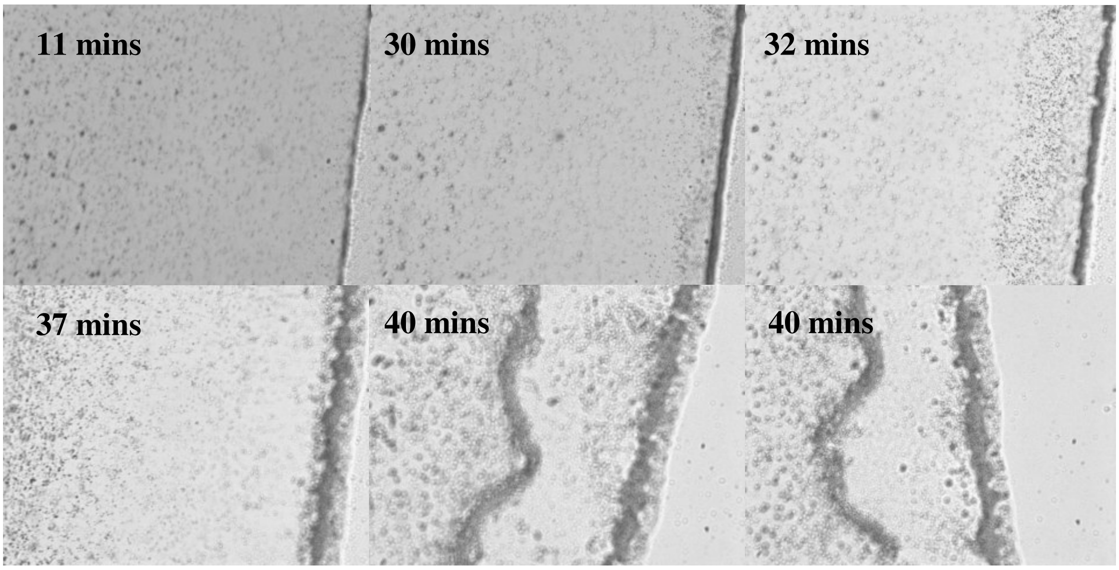

Figure 5.44. Optical microscope images of a droplet having composition of R2(7)55 as a function of drying time.

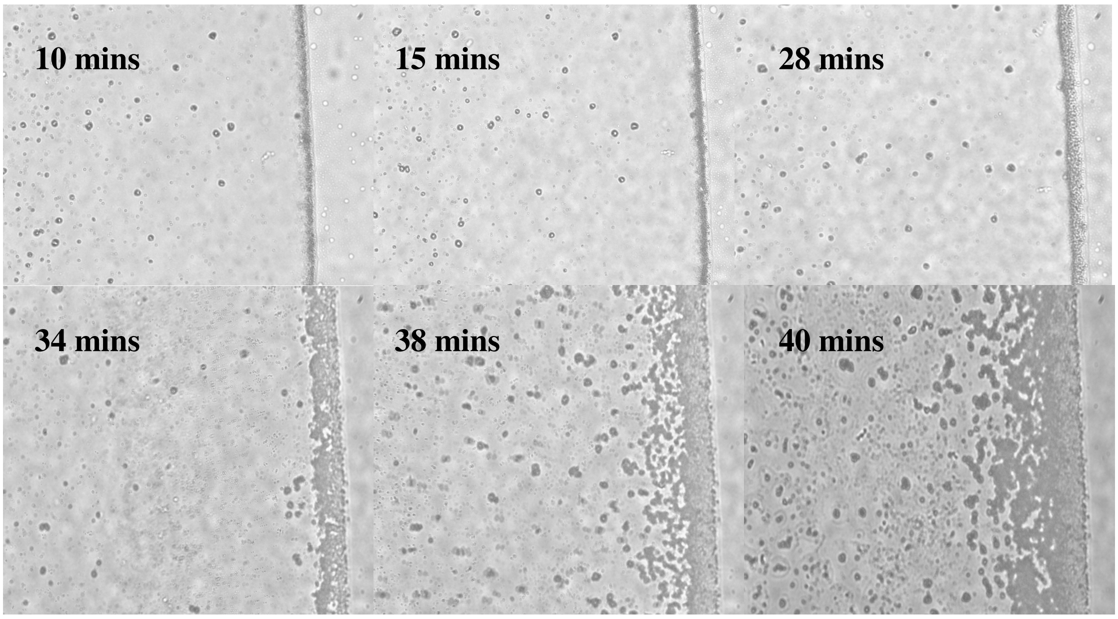

Figure 5.45. Optical microscope images of the droplet having composition of R3(7)55 as a function of drying time.

To summarize, Figure 5.46 shows schematically the structural evolution of the liquid droplets during drying. Hu and Larson analyzed the evaporation of a sessile droplet. Accordingly, droplet evaporation occurs in two stages. In the first stage, contact line is pinned and the contact angle decreases during drying. As drying progresses particles move to the drop edge under the influence of capillary flow, resulting in the formation of a ring of particles. If evaporation of liquid from the pores is exposing to the solid phase, a solid/liquid interface would be replaced by a more energetic solid/vapor interface. To prevent such an increase in the energy the liquid tends to spread from the interior. Since the volume of the liquid has been reduced by evaporation the meniscus becomes curved. When contact angle reaches a critical value the contact line starts to recede, and this is the second stage. Finally, when the solvent has evaporated the resulting structure is a particulate ring with an outer diameter similar to the initial diameter of the drop (Hu and Larson 2005, Martinez and Lewis 2002, Deegan et al. 1997).

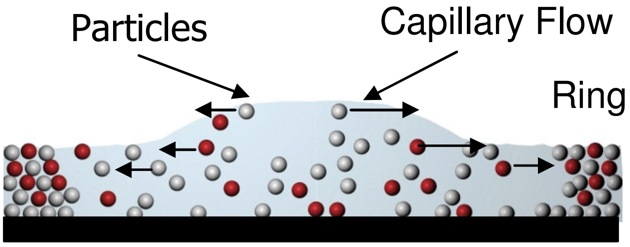

Figure 5.46. Schematic presentation of the ring formation during drying of a droplet. (Source: Martinez 2002)

5.3.6. Characterization of the Green Tapes

Microstructure of the PMN green tapes were analyzed using scanning electron microscope. Figure 5.47 show the structure of the top and the bottom surface of the PMN green film. Results reveal that there is no significant difference between the top and the bottom surface of the green PMN film (casting thickness 300 µm) which means that there is no particle segregation. Similarly, cross section of the PMN films having different thicknesses is shown in Figure 5.48. Accordingly, the lowest film thickness was ~10 µm in green state (casting thickness 30 µm). On the other hand, highest film thickness obtained in the study was 265 µm corresponded to the sample having a casting thickness of 500 µm.

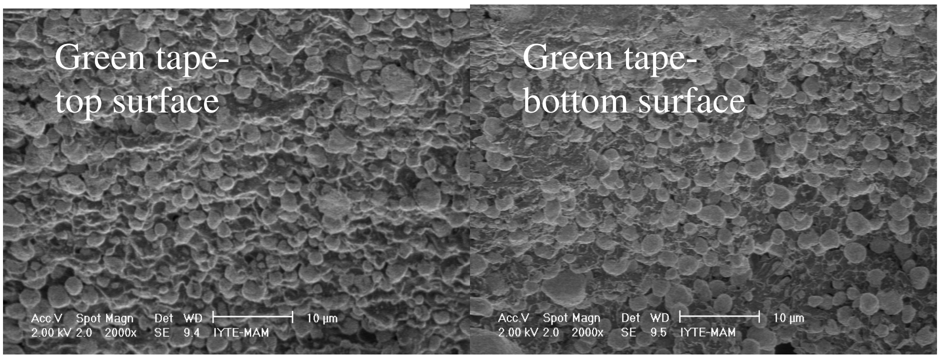

Figure 5.47. Top and bottom view of the green tape prepared from R1(7)55, 300 µm.

Densities of the green tapes were measured using geometric method. The theoretical density of the dry films were calculated to be 61-64% and 58-60 % prepared from the compositions of R1(7)60 and R1(7)55, respectively.

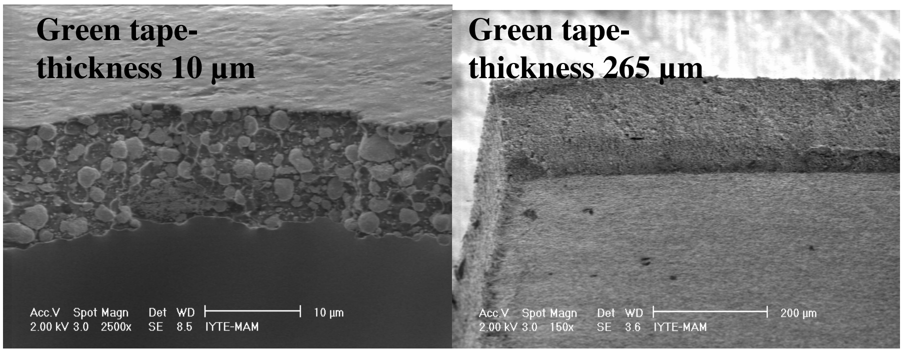

Figure 5.48. Microstructures of the PMN layers in green state, cross sectional view.

5.3.7. Roughness of the PMN Green Tapes

5.3.7.1. Atomic Force Microscopy Analysis

Surface morphology of the PMN green tapes (casting thickness of 300 µm) were analyzed using atomic force microscope with contact mode. Figure 5.49 show the effect of HPMC concentration on the roughness of the PMN films. Roughness values are also tabulated in Table 5.6. Results showed that there is no significant difference between the roughnesses of the films as a function of HPMC content. On the other hand, the scanning area was very small (100 µm) during the AFM analysis therefore, some small local heterogeneities may effect the results in a great extend.

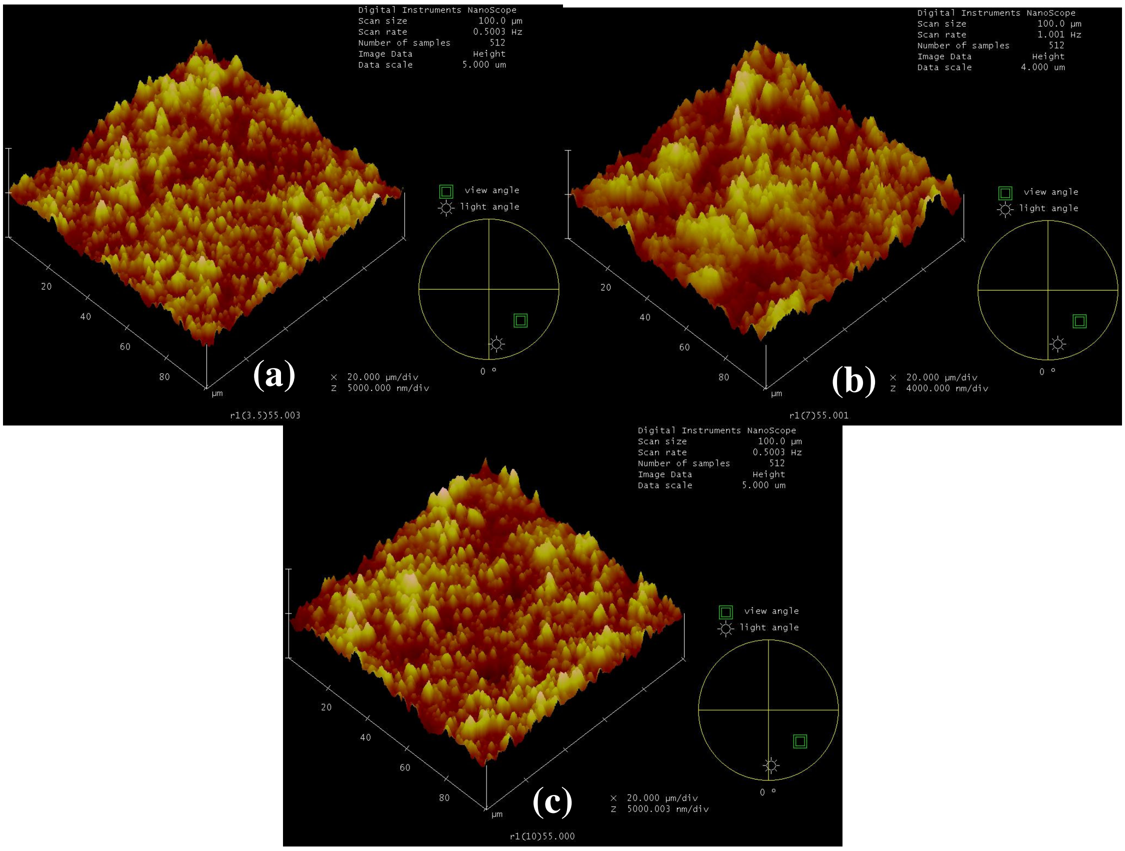

Figure 5.49. AFM images of the PMN films having different HPMC concentration a) 3.5mg/ml b) 7 mg/ml, c) 10 mg/ml.

Table 5.6. Roughness values PMN films as a function of HPMC concentration.

PMN film composition	Average Roughness (nm)
R1 (3.5) 55	488.96
R1 (7.0) 55	650.35
R1 (10) 55	542.33
R1 (7.0) 60	520.826

Figure 5.50 presents the effects of PMN:binder ratio on the roughness of the green tapes. AFM pictures reveal that roughness of the films decreases as the binder content decreases. This may be an indication of the possible PMN powder and latex particle interactions. Roughness values are also tabulated in Table 5.7.

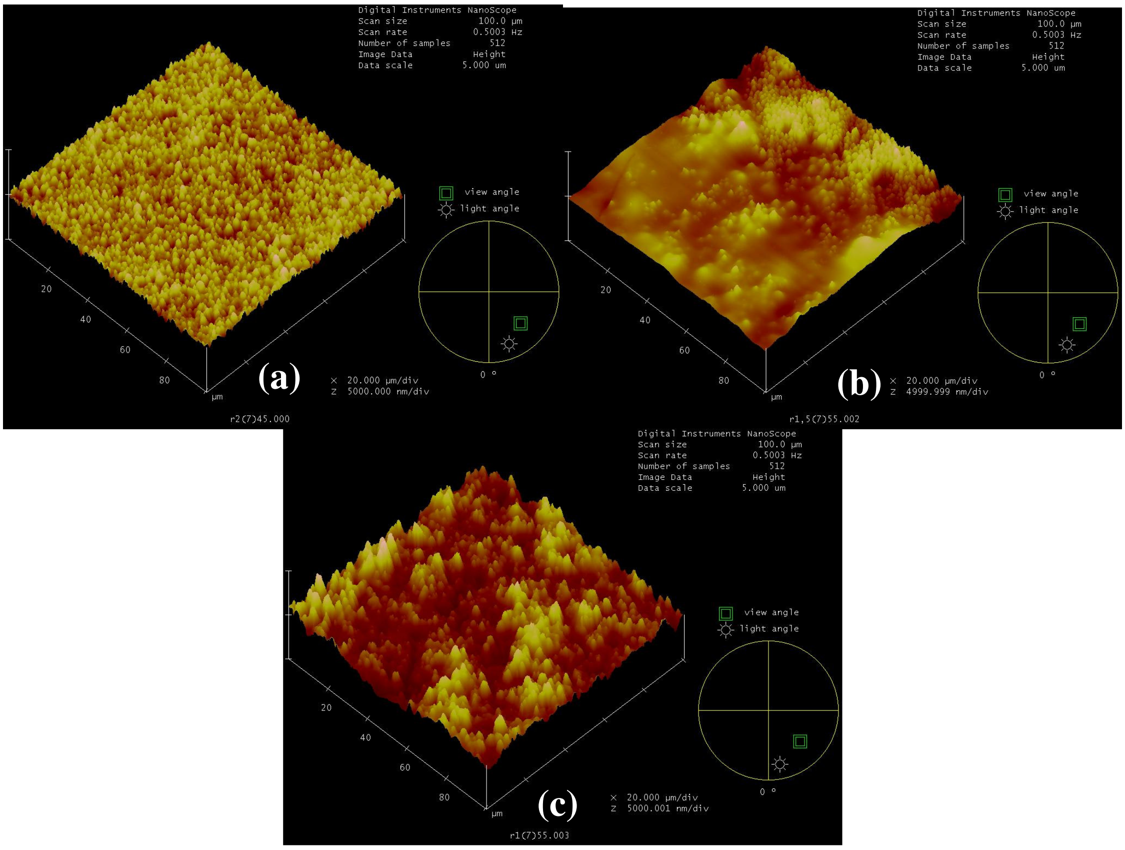

Figure 5.50. AFM images of the PMN films having different PMN: binder ratios(R) a) R2 b) R1.5 c) R1.

Table 5.7. Effect of PMN:binder ratio on the roughness of the PMN films.

PMN film composition	Avg.Roughness (nm)
R1.0 (7.0) 55	650.35
R1.5 (7.0) 55	313.16
R2.0 (7.0) 55	266.39

5.3.7.2. Profilometry Analysis

Surface profilometry analysis was performed in order to investigate the roughness of the PMN films through the entire film length. Figures 5.51 and 5.52 depict the effect of film thickness and the casting rate on the roughness of the PMN green sheets, respectively. Results showed that roughness of the films prepared from slurry composition of R1(7)55, was dependent on the film thickness. As the thickness of the film was decreased an increase was observed on the roughness of these films.

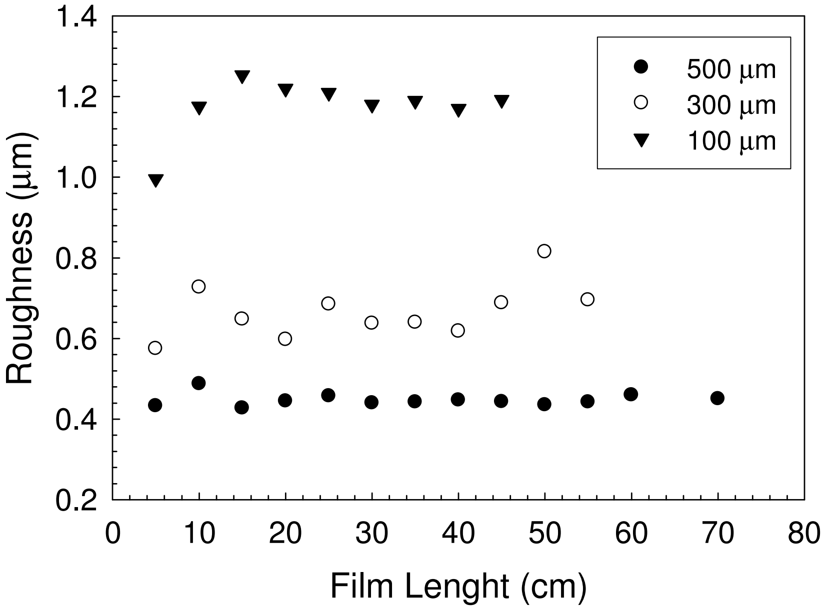

Figure 5.51. Roughness of the PMN films prepared from slurry composition of R1(7)55.

Similarly, effect of casting rate on the roughness of the PMN films was also examined in the study. Figure 5.52 shows the roughness values of the PMN films deposited at different rates. Accordingly, there is no significant difference between the roughnesses of the films depending on the casting rate. However, the film deposited at 25 mm/s showed more homogeneous distribution.

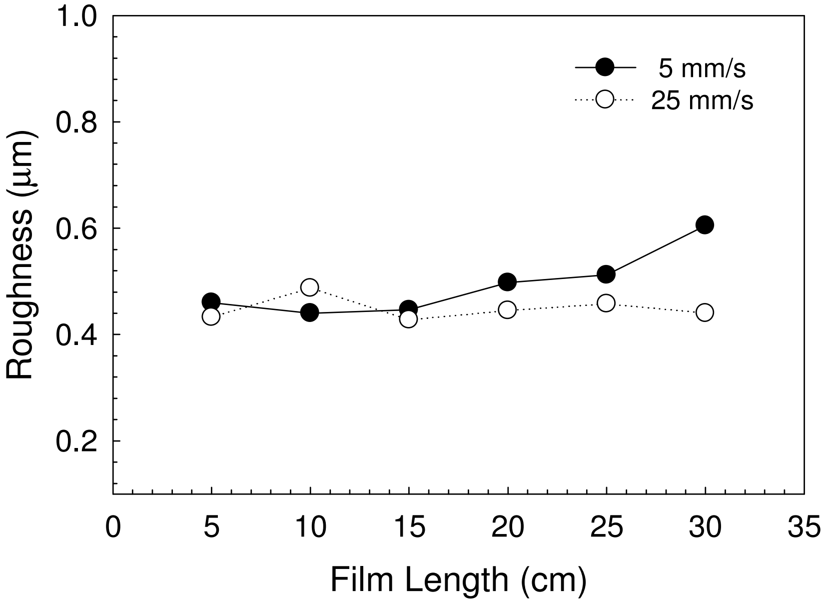

Figure 5.52. Effect of slurry deposition (casting) rate on the roughness of the PMN green sheets.

5.3.8. Thermal Analysis of the Green Tapes

Binder distribution and the weight loss of the green tapes prepared using different slurry compositions were analyzed using differential scanning calorimeter (DSC) and thermogravimetric analyzer (TGA). Figure 5.53 shows the TGA analysis result of the samples having different powder: binder ratios. Results showed that weight loss occurs mainly between 300 to 400 ºC due to removal of the organic phases. Above 400 ºC the weight of the samples remains nearly constant. As expected, weight loss of the samples showed a strong dependence on the binder content of the films. Weight loss was about 10% for the film prepared from a slurry composition of R1(7)55.

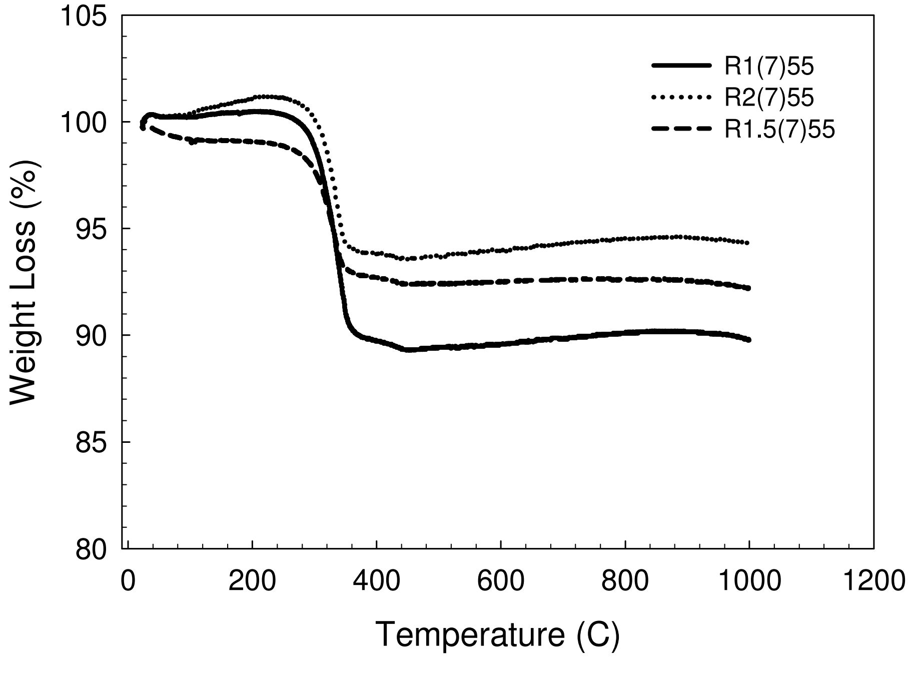

Figure 5.53. TGA analysis of the PMN films having different PMN: binder ratio.

Figure 5.54 and 5.55 show the binder distribution through the length of the film in parallel and perpendicular to the casting direction. For these measurements array of samples were cut in 10 cm intervals (for y direction) and in 1 cm intervals (for x direction) and analyzed by DSC to investigate the distribution of organics through the film. Results indicate that the binder distribution across the length of the film is generally homogeneous in both directions. On the other hand, small differences observed may be attributed to the non-uniform film thickness through the film length. As it was discussed before the distribution of the all the contents of the ceramics (especially the binders) has very important effects on the final properties of the ceramics. Therefore, a uniform binder distribution must be assured during tape casting. Non-uniform distribution of binders may cause important defects during sintering step.

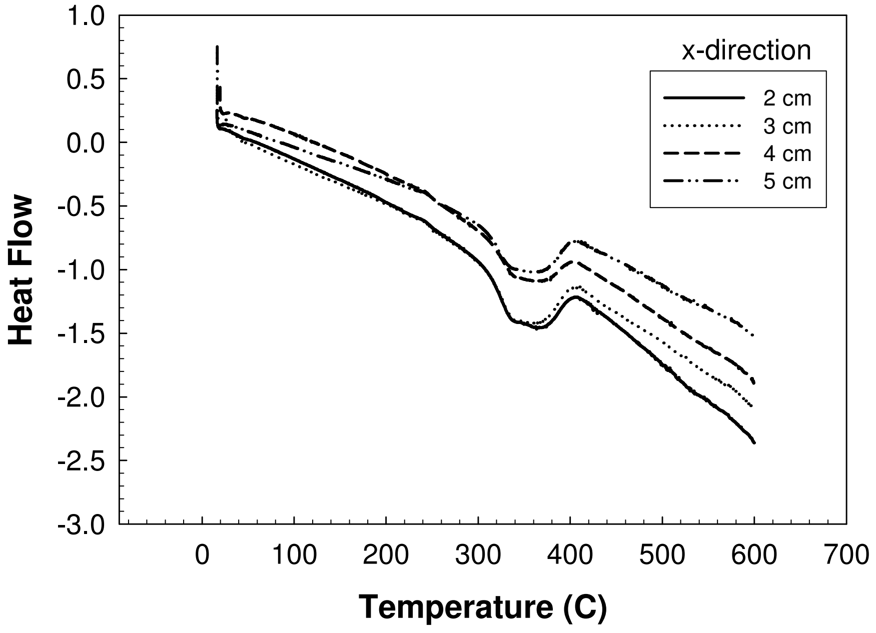

Figure 5.54. DSC analysis of the PMN film, samples from perpendicular to casting direction, composition R1(7)55, 300 μm.

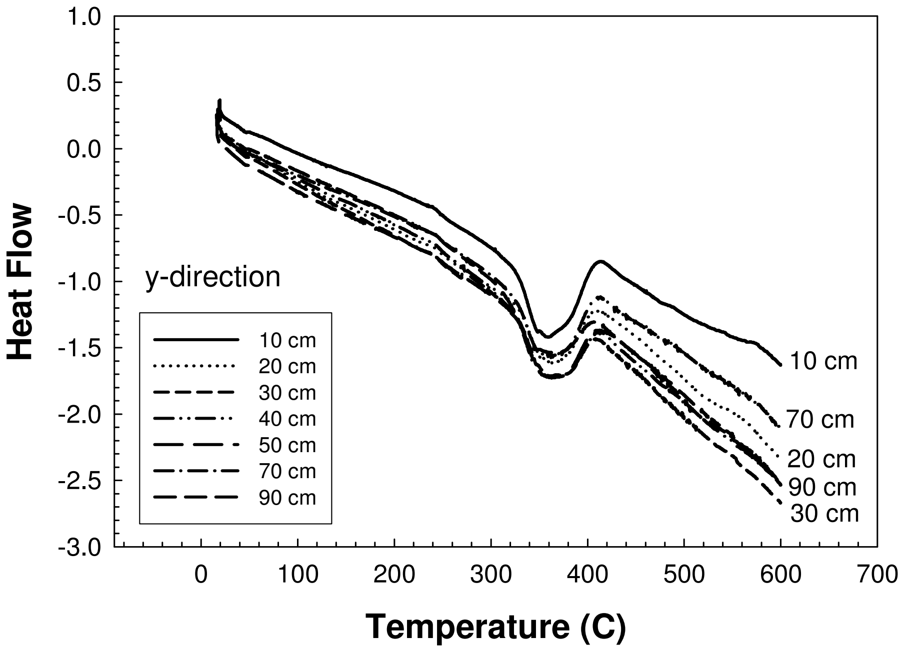

Figure 5.55. DSC analysis of the PMN film, samples from parallel to casting direction, composition R1(7)55, 300 μm.

5.3.9. Sintering

High density products are generally desired in ceramic processing and it is a requirement in the production of electronic ceramic components. Because the final density of the ceramic layers strongly affects the mechanical and electrical properties of the related products (Rahaman 1995). Therefore, sintering of the green tapes has a significant importance in tape casting process. Figure 5.56 show the theoretical density of PMN pellets as a function of sintering temperature. In the study all the samples were held at the specified temperatures for 2 hours and the heating rate was 5 °C/min. Densities were determined by measuring the weight and dimensions of the samples. Results showed that the theoretical density of the PMN pellets reached to 99% after sintering at 1180 °C for 2 hours. Above that temperature, the density of the samples showed a slight decrease. Additionally, at 1275 °C a sharp decrease was observed in the sample density. The reason of this decline was attributed to the significant lead loss occurred from the samples that cause formation of a pyrochlore phase.

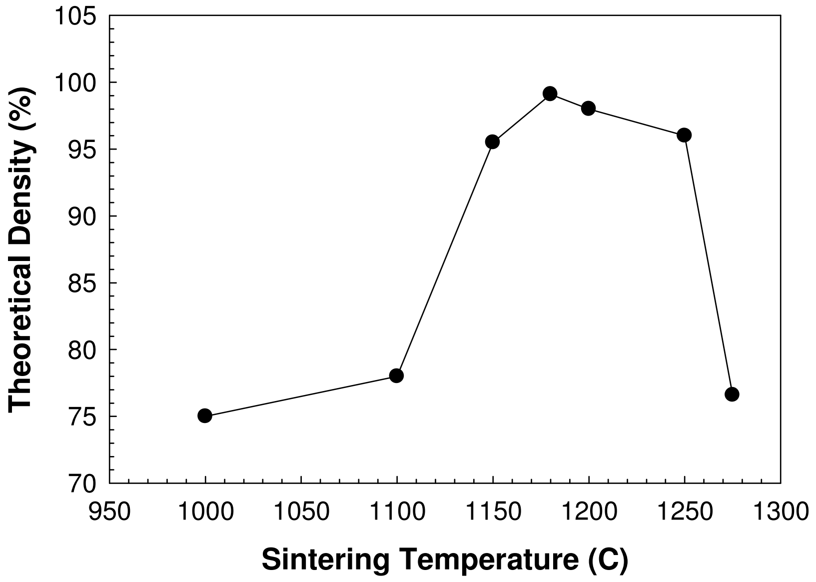

Figure 5.56. Density of the PMN pellets as a function of sintering temperature.

Figure 5.57 presents the effect of heating rate on the density of PMN pellets sintered at 1180 °C for 2 hours. Results showed that highest density was obtained at a heating rate of 3 °C/min and above this value a gradual decrease was observed in the density.

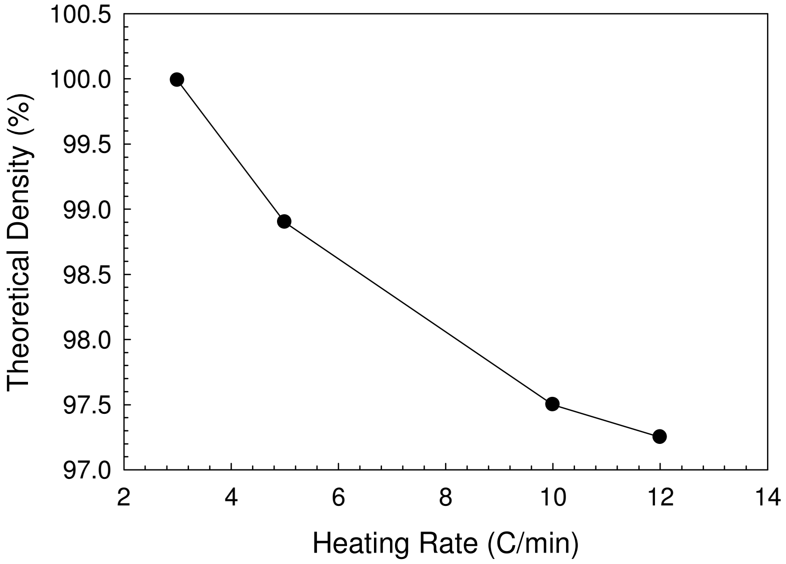

Figure 5.57. Effect of heating rate on the theoretical density of PMN pellets, sintering at 1180 °C for 2 hours.

For the sintering of the PMN tape cast layers following procedure were followed: The binder was burned out by heating the samples at 1 ºC/min to 350 °C, 1 h dwell at 350 °C and 3°C/min to various temperatures ranging from 1000 to 1250 °C. Density of PMN films were obtained by measuring the weight and dimensions of the films after sintering. Accordingly, the sintered theoretical density of the PMN films (casting thickness 500 μm) prepared from slurry having a composition of R1(7)55 was measured to be 90-95%.

Figure 5.58 show the microstructure of the PMN films after a heat treatment at 1000 ºC. SEM micrographs reveal the influence of the binder content on the final microstructure of the PMN films. Accordingly, samples sintered at 1000 ºC for 2 hours has low densities with a porous structure. As expected a decrease was observed in the porosity as the PMN: binder ratio increased. Therefore, it is always necessary to use low amount of organic phase in tape casting since binder removal step strongly affect the final microstructure of the films.

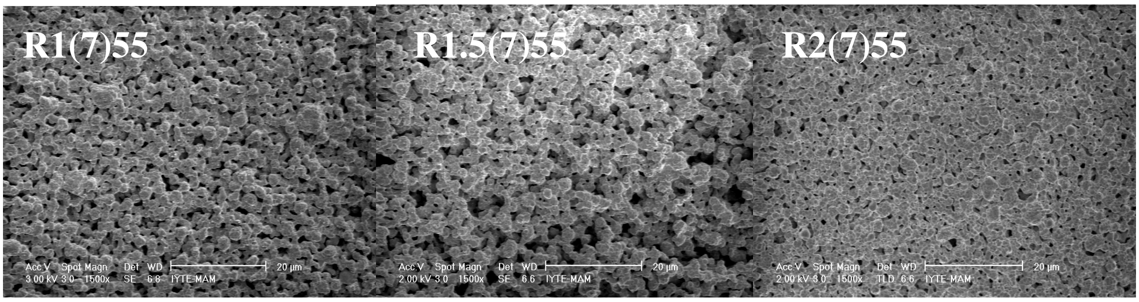

Figure 5.58. SEM micrographs of the PMN films prepared from slurries having different PMN:latex ratio a) R1(7)55 , b) R1.7(7)55, c) R2(7)55.

Figure 5.59 demonstrates the effect of sintering temperature on the crystal structure of PMN films. According to the XRD diagram the film has a perovskite structure after sintering at 1180 °C for 2 hours. On the other hand, few low intensity pyrochlore peaks were detected in the sample that is sintered at 1250 °C for 2 hours.

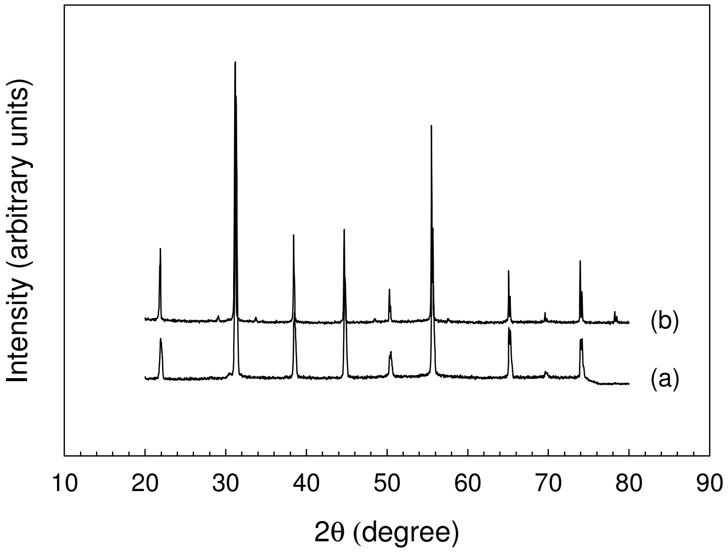

Figure 5.59. X-Ray diffraction patterns of the PMN films sintered at (a) 1180 °C (b) 1250 °C.

Microstructures of the PMN films sintered at different temperatures are given in Figure 5.60. PMN films sintered at a temperature up to 1150 °C are highly porous and therefore their densities are low. Figure 5.60 (e) shows that starting from 1180 °C, defect free, high density PMN films are obtained. At higher sintering temperatures abnormal grain growth starts with the formation of a second phase such as pyrochlore (Figure 5.60 e).

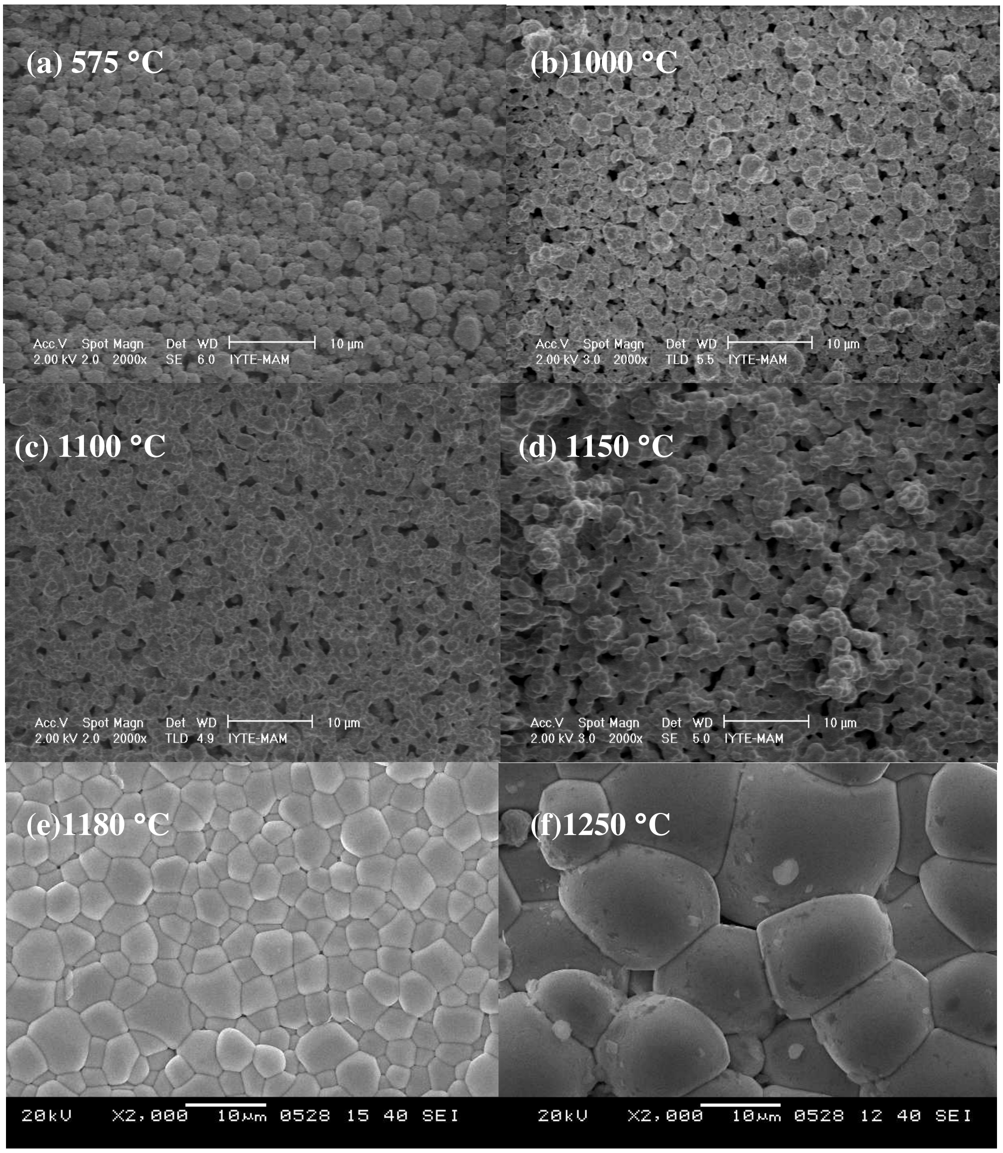

Figure 5.60. SEM micrographs of the PMN films sintered at different temperatures (a) 575 °C (b) 1000 °C (c) 1100 °C (d) 1150 °C (e) 1180 °C (f)1250 °C.

The cross sectional view of the PMN films sintered at 1180 °C for 2 hours is given in Figure 5.61. SEM micrographs demonstrate the final thickness of the PMN films after heat treatment. PMN films cast at 30 µm have a thickness of 5 µm after the heat treatment at 1180 °C for 2 hours.

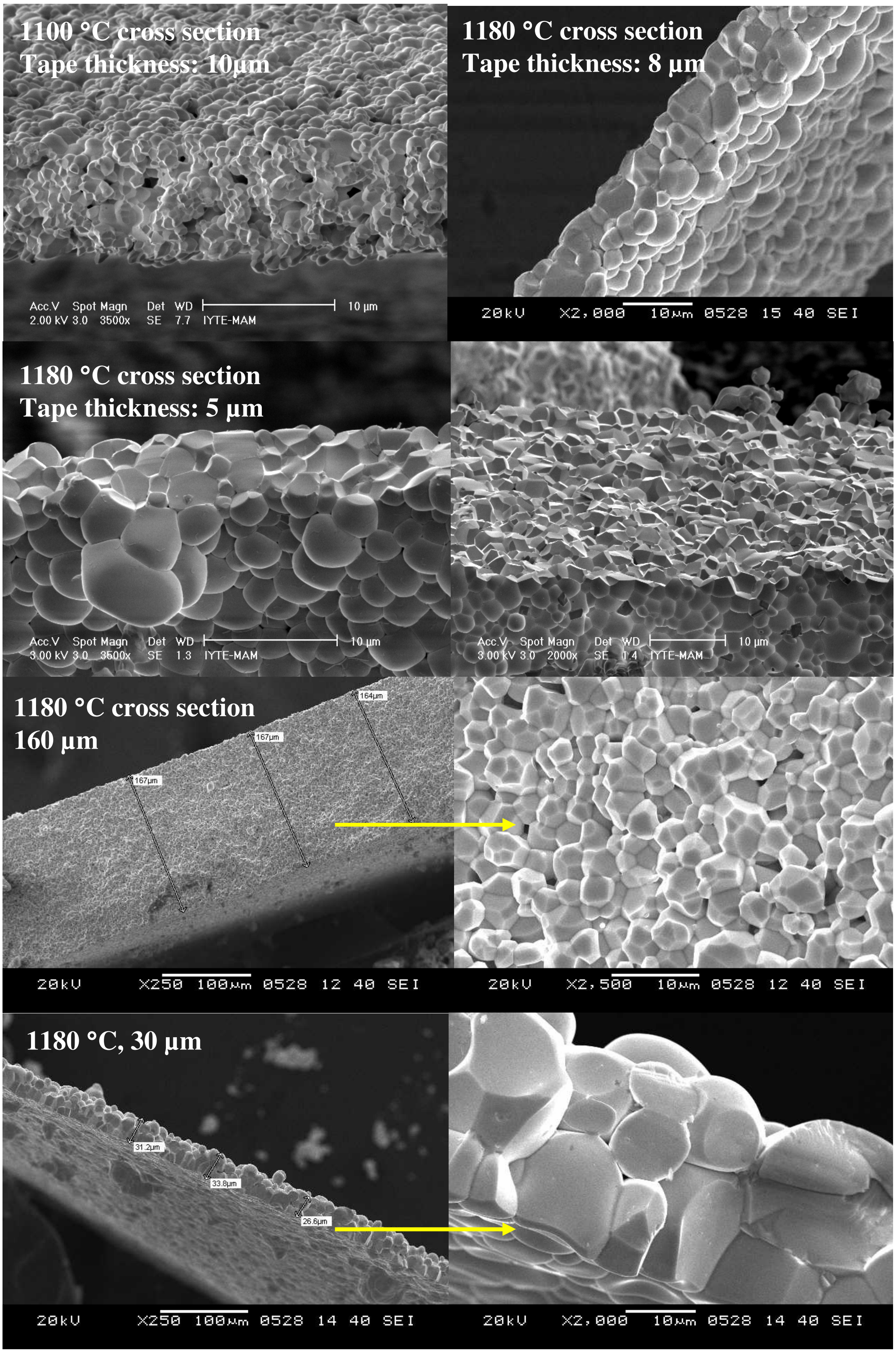

Figure 5.61. SEM micrographs showing the final thickness and the microstructure of the PMN films sintered at different temperatures.

5.3.10. Electrical Properties

In the study relative permittivity of the PMN bulk samples and films were measured as a function of frequency and the sintering temperature. It is known that, dielectric constant of this material has maximum at about -10 °C (Gentil et al. 2004) and above this temperature dielectric constant decreases with increasing temperature. In this work, measurements were performed at room temperature (25 °C ± 2) therefore; permittivity values do not refer the maximum values. Accordingly, Figure 5.62 and Figure 5.63 describe the relative permittivity, ε_r, (dielectric constant) and the tangent loss of the PMN bulk samples as a function of frequency, respectively. It is obvious from the Figure 5.62 that ε_r of the PMN bulk samples was dependent on the frequency. Relative permittivity of the PMN sample was measured to be 11000 at 0.01Hz.

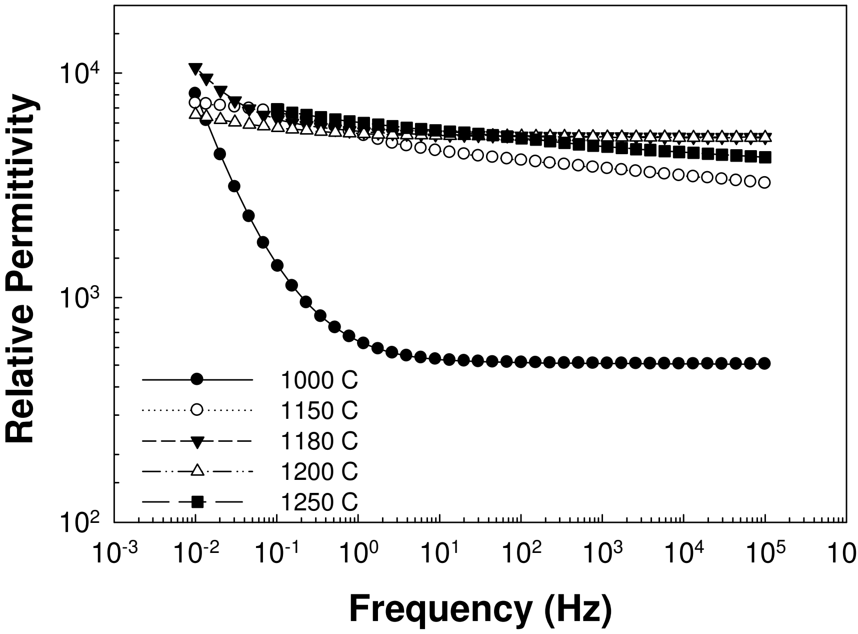

Figure 5.62. Relative permittivity of the PMN disks as a function of frequency and the sintering temperature.

Results also showed that permittivity of the samples were dependent on the sintering temperature. At low sintering temperatures such as 1000 °C, dielectric constant of the samples were also low. This is mainly attributed to the high porosity in samples sintered at low temperatures. It is also known that dielectric constant of the ferroelectric materials is dependent on the grain size. With increasing sintering temperature an increase was observed in grain size and this may cause an increase in the dielectric constant of PMN ceramics. It is also important to note that during heat treatment at high temperatures pyrochlore formation, which degrades the electrical properties of PMN should be restricted.

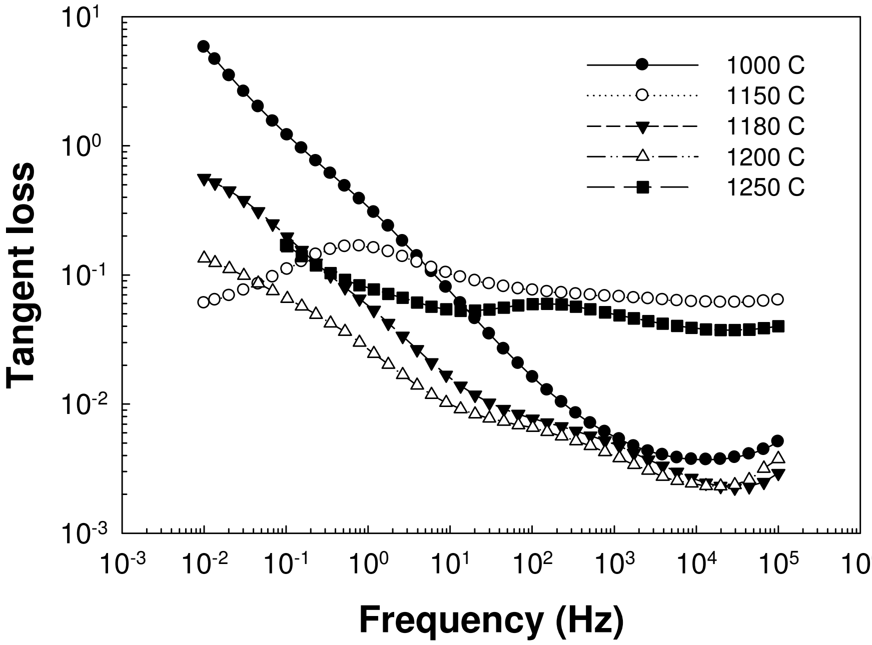

Figure 5.63. Tangent loss of the PMN disks as a function of frequency and the sintering temperature.

As it is shown in Figure 5.63 tangent loss of the PMN bulk samples were low except the sample sintered at 1000 °C. Since the tangent loss is a measure of the electric loss in the material low values are desirable.

Dielectric constant of the PMN films produced via tape casting method were also measured in the study. Results are given in Figure 5.64. Measurements were performed on the samples laminated (15 layers, but no silver paste between the layers) and sintered at different temperatures. Relative permittivity of the PMN film sintered at 1180 °C was measured to be 8000 at 0.01 Hz. Under the same conditions dielectric constant of the PMN bulk sample was higher. Previous studies related to the electrical characterization of PMN thick films showed that films may have a lower relative permittivity compared to the bulk ceramics (Dorey and Whatmore 2004). For example, Gentil and co-workers 2004 measured the relative permittivity for PMN film as 10,000 (at 0.1 kHz) which is lower that in bulk ceramics (17,800 at 0.1 kHz) under the same conditions. They also found that a decrease of film thickness lead to a decrease of dielectric properties (Gentil et al. 2004).

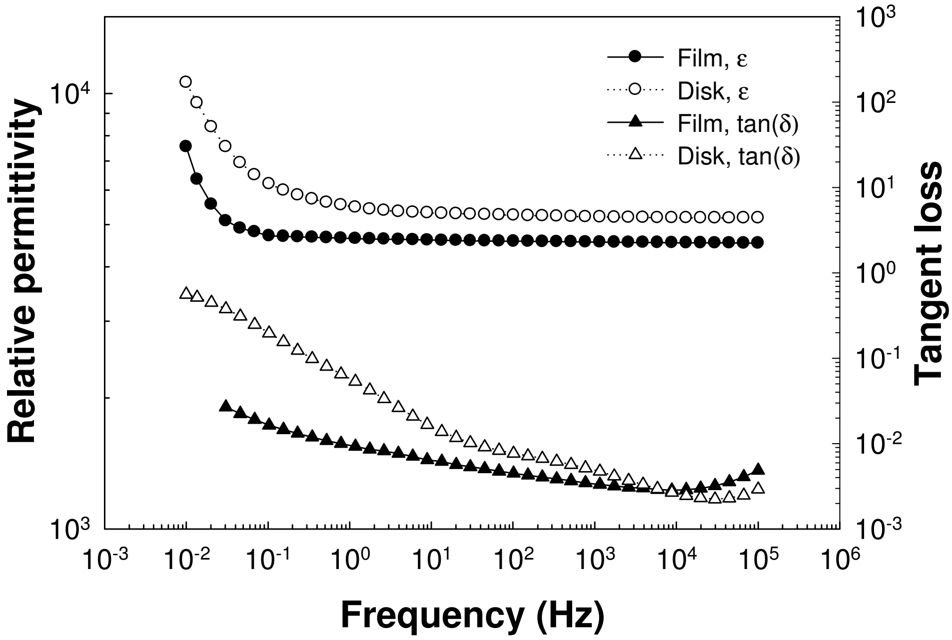

Figure 5.64. Relative permittivity and the tangent loss of the PMN disks and films as a function of frequency.

Therefore, the lower permittivity in PMN thick films may result from several effects, including a higher porosity (sintered theoretical density of the PMN films were lower 90-95% compared to the density of the bulk samples 99%), roughness, presence of a second phase or some void formation between the layers.

CHAPTER 6

PMN INKS FOR DIRECTED ASSEMBLY OF 2-D ARRAYS AND 3-D PERIODIC STRUCTURES

6.1. Introduction

The manufacturing of three dimensional micro-periodic structures from polymeric, colloidal, or semiconductor materials is critical for several technologies. These structures may find potential application as tissue engineering scaffolds (Cohen et al. 2006, Das and Hollister 2002, Chu et al. 2001), drug-delivery devices (Wu et al. 1996), microfluidic networks, actuators, sensors, photonic band gap materials, and electronic ceramic applications (Gratson 2005, Geissler and Xia 2004, Safari et al. 2006). Some of these applications require use of functional materials such as ferroelectric ceramics.

Lead magnesium niobate is a relaxor ferroelectric material and especially used in the manufacturing of electrostrictive actuators and transducers. Electrostrictive actuator is a category of smart material transducers. An electrostrictive actuator transforms electrical signals into mechanical forces. Their physical properties include high response speed, large electrostrictive strains and low hysteresis behavior. Therefore, electrostrictive actuators have potential for applications in adaptive optics, hard disk drives and ultra-precision machining, which require high resolution, high stiffness and fast frequency response motion control (Hu et al. 2004, Jing and Luo 2005, Uchino 1986). Lau and co-workers developed ceramic fibre with an active element as small as 0.25 mm in diameter. Lead magnesium niobate-lead titanate (PMN-PT) ceramic fibre with a nominal composition of $0.65Pb(Mg_{1/3}Nb_{2/3})O_3$-$0.35PbTiO_3$ was fabricated by an extrusion method to use in hydrophone applications (Lau et al. 2005).

In actuators it is desirable to enhance the displacement while maintaining the load bearing capability. This can be achieved by manipulating the geometry of simple shape actuators into more complex geometries. These actuators include spiral, telescoping, dome, tube, curved and multilayer tubes, oval and monomorph benders (Jadidian et al. 2002). Especially spiral actuators with compact geometry show large field induced strains. The application of an electric field across the spiral width induces both tangential and radial displacements. Similarly piezoelectric tubes are utilized for actuator and sensor applications. They have been used to shift mirror of laser resonators in scanning tunnel microscopy and atomic force microscopy (Safari et al. 2006).

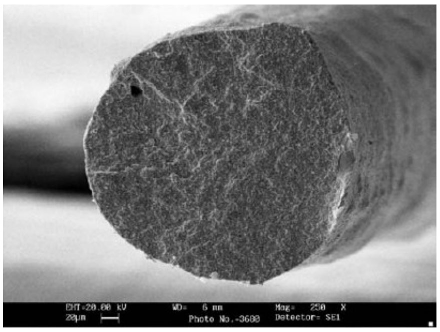

Figure 6.1. SEM micrograph of the cross-sectional area of a PMN-PT fiber.
(Source: Lau et al. 2005)

Direct write technologies are able to produce 2-D or 3-D periodic structures to use in these application areas. Methods such as dip-pen nanolithography, focused ion beam lithography, and laser direct write micromachining are used in direct write technologies (Clendenning et al. 2004, Calvert and Crockett 1997, Xiaogong et al. 2002) but often restricted to making components with sub millimeter overall dimensions. Structures with a larger feature size and overall dimensions have been fabricated using techniques such as robocasting, ink jet printing, and micropen writing (Nadkarni and Smay 2006, Calvert 2001, Dimos et al. 1999). All these methods is a part of growing field known as solid free form (SFF) fabrication that provides forming materials without use of expensive tooling, molds, and dies (Lewis 2002, Safari et al. 2006).

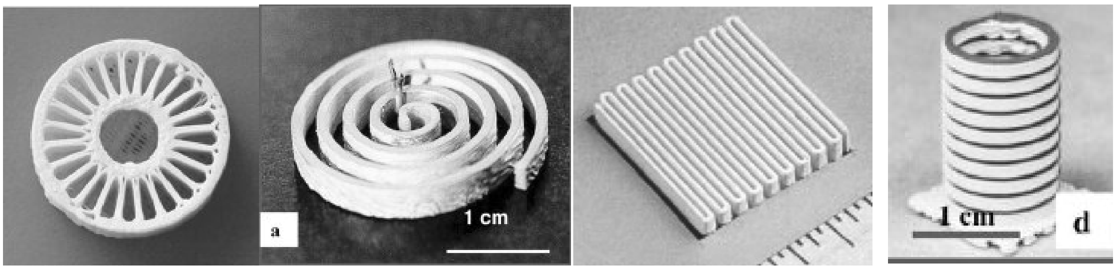

Figure 6.2. Spiral piezoelectric and multilayer tubular actuators.
(Source: Safari et al. 2006)

Robocasting is an extrusion-based, direct write technique. It is the only SFF technique developed to date that utilizes colloidal systems of low organic content to directly write three dimensional bodies (Lewis et al. 2006a, Lewis 2000, Cesarano et al. 1998). In robocasting, the processing steps include formulation of the colloidal ink, the printing, and finishing processes. The ink formulations consist of preparation of uniform, highly concentrated and low viscosity slurry. High solids loading are necessary because it increases the green body density, and also minimizes drying shrinkage. Next, a fluid-to-gel transition is created which is suitable for the printing operation. The printing operation utilizes a motion and flow rate controlled deposition system. This concept is similar to a three-axis computer numerical control (CNC) mill. But in that case cutting tool is replaced by the deposition nozzle. Colloidal inks are feed to syringes that are connected to the deposition nozzle. A 3-D structure to be assembled is virtually sliced into layers, and deposition tool paths are calculated using a computer-aided design (CAD) program. The layers of the 3-D structure are deposited sequentially, starting from the bottom layer. After the printing operation, the structure is dried and sintered to obtain a dense product (Smay 2002). Previously, Lewis co-workers conducted research on the robocasting of alumina (Morisette et al. 2002), silica, barium titanate (Li and Lewis 2003) and lead zirconate titanate (Smay et al. 2002b, Smay and Lewis 2001, Morissette and Lewis 2001) powders and produce different geometries to be used in different applications (Lewis et al. 2006a).

In this work, three dimensional PMN lattices were produced using robotic deposition. Structures produced may be considered as the basic building blocks for the novel design actuators. On the other hand, current technology includes the manufacturing of stack type PMN actuators using slip casting, tape casting or more commonly dry pressing.

In the study, concentrated aqueous colloidal PMN gels have been designed to use in the robocasting process. Concentrated PMN suspensions were stabilized by polyacrylic acid and then gelation induced by changing the pH or ionic strength of the suspension or by addition of a cationic electrolyte to the system. Through this procedure it was essential to understand the solid-liquid transition under shear to explore the feasibility of forming without excessive use of polymers. Therefore, rheological response of the samples having a gel network was investigated. Results showed that complex PMN shapes can be successfully produced by robocasting process to be used in microelectronic applications such as spiral actuators.

6.2. Experimental

6.2.1. Materials

Lead magnesium niobate powder (average particle size, d_{50}, 1.8 μm and BET surface area of 1.168 m^2/g) was produced, using combustion spray pyrolysis provided by the Praxair Inc.,USA. Polyacrylic acid (Polyscience Inc., USA) supplied as a 40 wt% aqueous solution served as the dispersant for the PMN particulate suspensions. Hydroxypropyl methylcellulose, HPMC (Methocel F4M, Dow Chemical Co., Midland, MI) was incorporated into the ink as a viscosifier and binder. Cationic polyelectrolyte poly(ethylene imine) PEI (M_W ~ 600) was supplied (Polysciences, Inc.USA) as a concentrated liquid (99%), which was diluted with deionized water to form a concentrated aqueous solution (40 wt%) for ink formulation. Figure 6.3 shows the chemical structure of poly (ethylene imine) used in the study. During the experiments all pH adjustments were made using certified 1.0 M solutions of KOH and HNO_3 (Fisher Scientific). Stock solutions of 1.0 M Magnesium chloride (Fisher Scientific, USA), 1.0 M Zinc Acetate (Fisher Scientific,USA) and 3.0 M potassium chloride (Fisher Scientific,USA) were prepared with deionized water and these solutions were used through the experiments . Nano pure water having conductivity 16.4 $(\Omega.cm)^{-1}$ obtained from Millipore, Direct Q was used for all experiments.

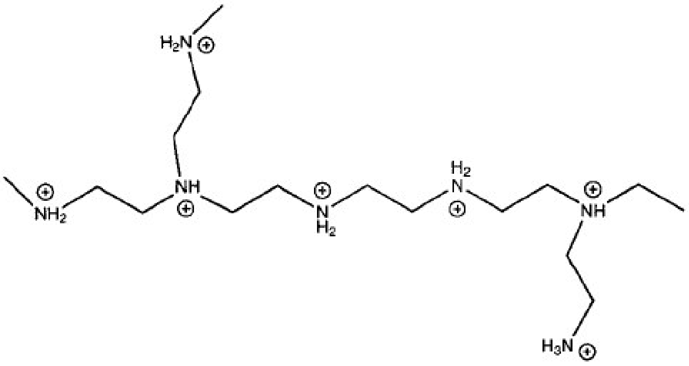

Figure 6.3. Schematic picture of a PEI molecule.
(Source: Anderson and Bergstrom 2000)

6.2.2. Ink Preparation

Stable colloidal suspensions (55 vol%) were prepared by adding 1 wt% PAA in terms of the dry weight basis of the PMN powder. Suspensions were ultrasonicated for 1.30 min with on-off intervals (550 Sonic Dismembrator, Fisher Scientific). Then suspensions were stirred for 24 hour to ensure the complete adsorption of PAA onto powder surface. An aliquot of HPMC stock solution was added to yield a final cellulose concentration of 5 mg/ml, which acted as a thickening agent thereby increase the solution viscosity and reduce flocculation kinetics. This allowed the rigid core-fluid shell architecture of the deposited filaments to persist facilitating rod-rod adhesion during assembly. Suspensions were homogenized using planetary centrifugal mixer (Thinky ARE-250, Japan) for 3 minutes.

Gelation was induced using three different methods. In the first method, coagulated inks were prepared by adding poly (ethylene imine) (PEI) to the system. PEI is a highly branched polyamine that contains primary, secondary, and tertiary amine groups in a ~1:2:1 ratio. Over the pH range of interest, PEI is positively charged with approximately 50% of these groups protonated at pH~6 (Gratson 2005). In the second approach, the pH of the system was reduced below pH 9 to obtain a strong gel network. In the last method, monovalent and divalent salts were introduced to the system and their ability to construct a gel network was evaluated. Before the direct writing process coagulated inks were homogenized again using planetary centrifugal mixer for 3 minutes.

6.2.3. Method

6.2.3.1. Direct-Write Assembly

Periodic lattices were assembled using a robotic deposition apparatus (JL2000, Robocasting Enterprises, Inc., Albuquerque, NM) (see Figure 6.4). The 3-axis motion of the *x-y* and *z*-stages was independently controlled by a custom-designed, computer-aided program (RoboCAD 2.0) that allowed for the construction of complex, 3-D architectures in a layer wise deposition scheme. Figure 6.4 and Figure 6.5 show the pictures of the robocaster that is used in the study and the deposition nozzles having different geometries.

Each layer in the structures had a finite thickness (Δz) defined by the height change of the deposition nozzle from layer to layer. The cross-sectional area of the deposited rods is determined by the nozzle diameter (D), however, their shape can be varied by changing Δz. The assembly of rods in a layer is described using a planar filling fraction (Γ_p), defined as the ratio of D/L where, L is the rod spacing within a layer. When $\Delta z \approx D$, $\Gamma_p = 1$ describes a layer in which the rods begin to overlap and $\Gamma_p < 1$, indicates that gaps exist between adjacent rods. To form a completely space filling layer, it is necessary to use $\Gamma_p > 1$ such that $\pi D^2 = 4L\Delta z$ (Smay 2002, Gratson 2005, Lewis 2006).

For the deposition the ink was housed in a 1ml syringe (barrel diameter = 4.6 mm, EFD Inc., East Providence, RI) and deposited through a tapered stainless steel nozzle length of 14 mm held in a plastic housing (EFD Inc, RI diameter, D = 100 μm, 200 μm and 500 μm) at a volumetric flow rate ($=0.25\pi D^2 v$) required to maintain a constant x-y table speed (v) of 7.5 mm/s (see Figure 6.5 b). A constant pressure was applied to induce the ink flow through the nozzle. The applied pressure (between 10 – 100 psia) varied according to the nozzle diameter and ink viscosity to achieve the desired constant deposition speed. The deposition process was carried out under a non-wetting oil to prevent drying during assembly. All test structures were allowed to rest undisturbed in this bath for 30 min after deposition was completed. This procedure was adopted to eliminate the effects of non-uniform drying during the deposition process.

Aging period of 30 min was sufficient for the structures to reach their equilibrium shape. After aging, the oil was slowly drained and the test structure was dried under ambient conditions for 24 hours and then in a low temperature furnace at 80 ºC for over night. Dried pieces were sintered in an electric furnace at various temperatures for the densification of green samples.

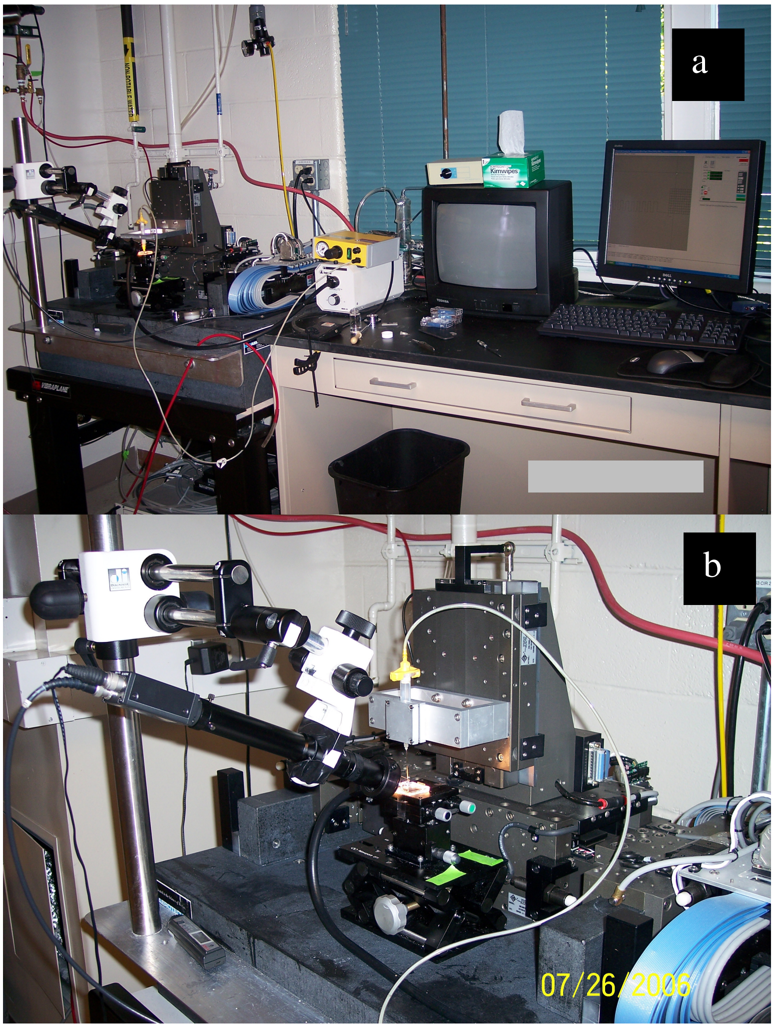

Figure 6.4. Pictures of the robacasting assembly a) general view b) deposition modul with camera.

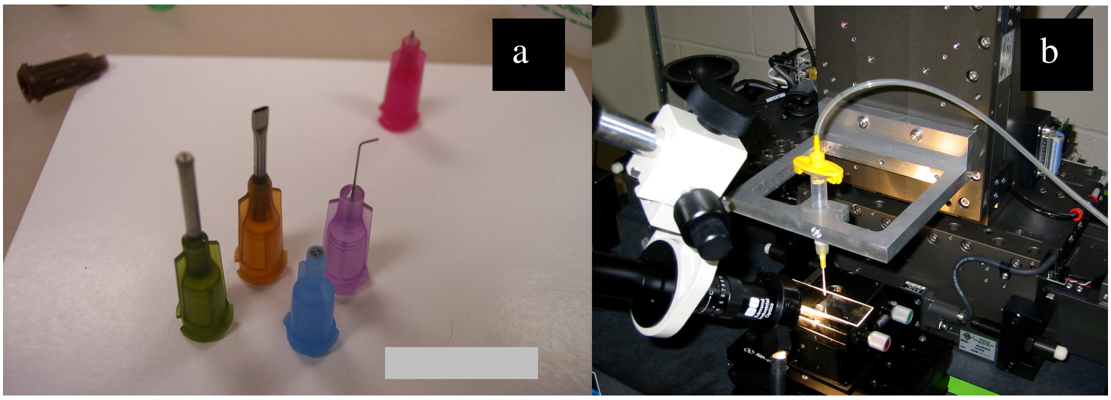

Figure 6.5. Pictures of a) deposition syringe tips having different geometries b) printing process in air onto the glass substrate.

6.2.3.2. Rheological Measurements

Rheological measurements were performed using a stress controlled rheometer (Bohlin CS-50) with “C14” geometry (cup inner diameter: 16 mm and bob outer diameter: 14 mm). To prevent wall slip serrated walls was used during the measurements. Additionally, to prevent sample evaporation a custom-made solvent trap was utilized. Each measurement required a sample size of 3.0 ml, which was loaded into the cell using an automatic pipette. Slurry temperature was kept constant at 25 ºC during the measurements using a temperature bath.

For the steady shear and dynamic (oscillation) measurements, a pre-shear of 10 s^{-1} was applied for a period of 60 s to the loaded sample to induce the same shear history for all samples. Then the samples were left undisturbed for 10 minutes to attain the equilibrium.

Oscillatory measurements were performed in order to understand the strength and yield information of the gels. Amplitude sweep measurements were conducted between 0.1 to 100 Pa. 50 measuring points were selected for each measurement.

The ink rheology was investigated as a function of pH, PEI concentration and salt concentration and correlated to the electrostatic interactions of the polyelectrolyte-coated particles. By adjusting the pH of this system or by PEI or salt addition, a fluid-to-gel transition was induced that resulted in a concentrated, viscoelastic ink for direct-write assembly.

6.2.3.3. Characterizations with Optical Microscope and SEM

Digital images of the 3-D structures were taken by a Digital Camera (Kodak Easy Share Z650). Optical images of the samples in the wet, green and sintered state were obtained using a Stereo Microscope (Nikon, SMZ 2T, Light 2) with a camera. Microstructures of the samples were observed using a scanning electron microscope, (Philips, XL-30S FEG).

6.3. Results and Discussion

6.3.1. Gelation with Cationic Polyelectrolyte

A cationic polyelectrolyte, polyethylene imine was used to create flocculation in PAA coated PMN suspensions. The primary amine groups in PEI molecule can ionize at pH < 11, resulting in a positive surface charge. It is important to note that for the ink design, PEI concentration should be below the concentration needed to form monolayer coverage around the PMN particle. Because only at a critical concentration PEI acts as a bridging flocculant otherwise it may serve as a dispersant in the case of full surface coverage.

Experiments were performed at pH 9 since at this pH surface charge of the PMN particles are positive and anionic polyelectrolyte PAA is fully and PEI is partially ionized. Titration experiments showed that PEI is fully charged at about pH 2 (Figures 6.6 and 6.7). At pH 6 it is positively charged with approximately 50% of the amine groups are protonated. However, results of the current study showed that at this pH the slurries are over gelled which were not suitable to use in robocasting process. Therefore, printing inks were prepared at pH 9 to reduce the yield strength of the gel network and having appropriate flow properties for deposition.

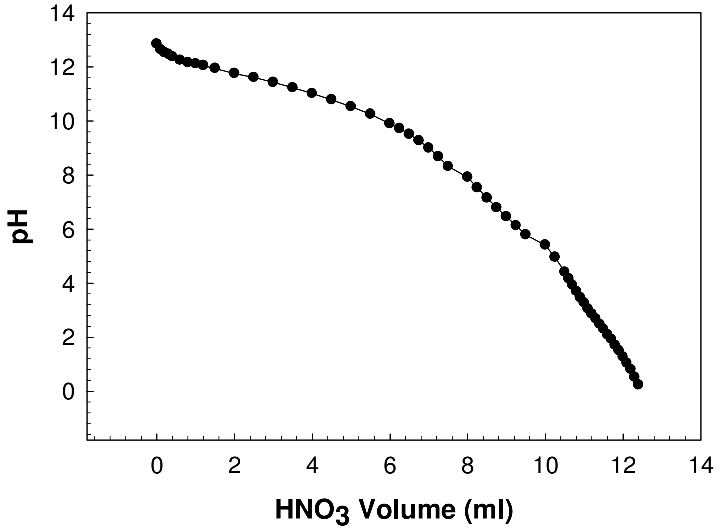

Figure 6.6. The change in the pH of the PEI solution as a function of titrant volume.

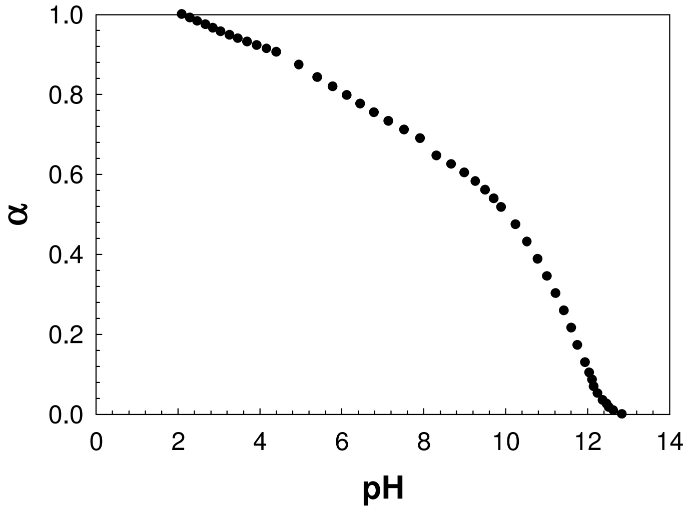

Figure 6.7. The ionization degree of PEI solution as a function of pH.

The effect of PEI concentration on the viscosity of concentrated PMN suspensions in the presence of HPMC (Methocel) is shown in Figure 6.8. As it is clearly indicated in the figure, gelation starts at a PEI concentration of 0.04 mg/m^2 (5 μl PEI 40 w% for 20 ml of PAA coated PMN suspension). As the PEI concentration increases to 0.06 mg/m^2 viscosity of the gel network also increases. Although it is not demonstrated in Figure 6.8 at very high PEI concentration a decrease in viscosity was observed.

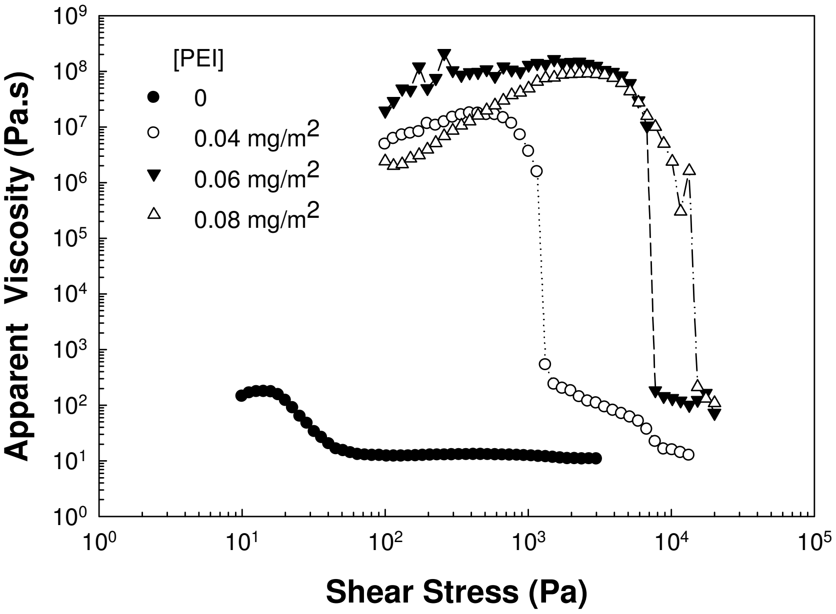

Figure 6.8. Viscosity versus shear stress graph of PMN slurries as a function of PEI concentration, 55 vol% PMN, pH 9, in the presence of 3 mg/ml HPMC.

Possible flocculation mechanism induced by the PEI addition can be explained as follows: PEI molecule approaches the negatively charged polyacrylic acid on the surface of the particles. Complexation reactions allowed for PEI adsorption can be as a second layer on the top of the PAA layer or by incorporation into the PAA layer. But even if incorporated into the PAA layer PEI may protrude sufficiently from the particle surface to enable bridging between the neighboring particles (Netz and Andelman 2003, Smay 2006, Napper 1977).

According to Sato and Ruch flocculation by bridging mechanism may occur in different ways. One of these mechanisms are due to the low surface coverage by polymer adsorption as it is shown schematically in Figure 6.9. By this way there are more chances for adsorption of polymer extending from one particle to another particle. This bridging flocculation occurs only at low polymer concentrations where the surfaces of the particles have less than half of their saturation value of the adsorbed flocculant (Sato and Ruch 1980).

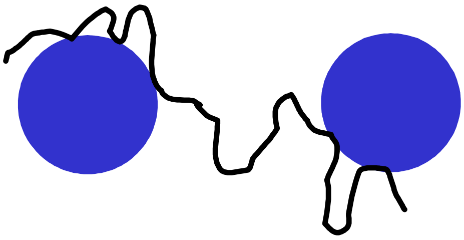

Figure 6.9. Schematic presentation of the bridging flocculation induced by the PEI molecule.

Similary, Figure 6.10 shows the effect of PEI concentration on the elastic modulus of the concentrated PMN gels (55 vol%). Again the high elastic modulus value at a PEI concentration of 0.04 mg/m^2 indicates the gelation. On the other hand, at a PEI concentration of 0.31 mg/m^2 a dramatic decrease was observed in viscoelastic properties. It was hypothesized that at this concentration PEI concentration exceeds the critical concentration and electrostatic stabilization starts since all particles covered by PEI molecules.

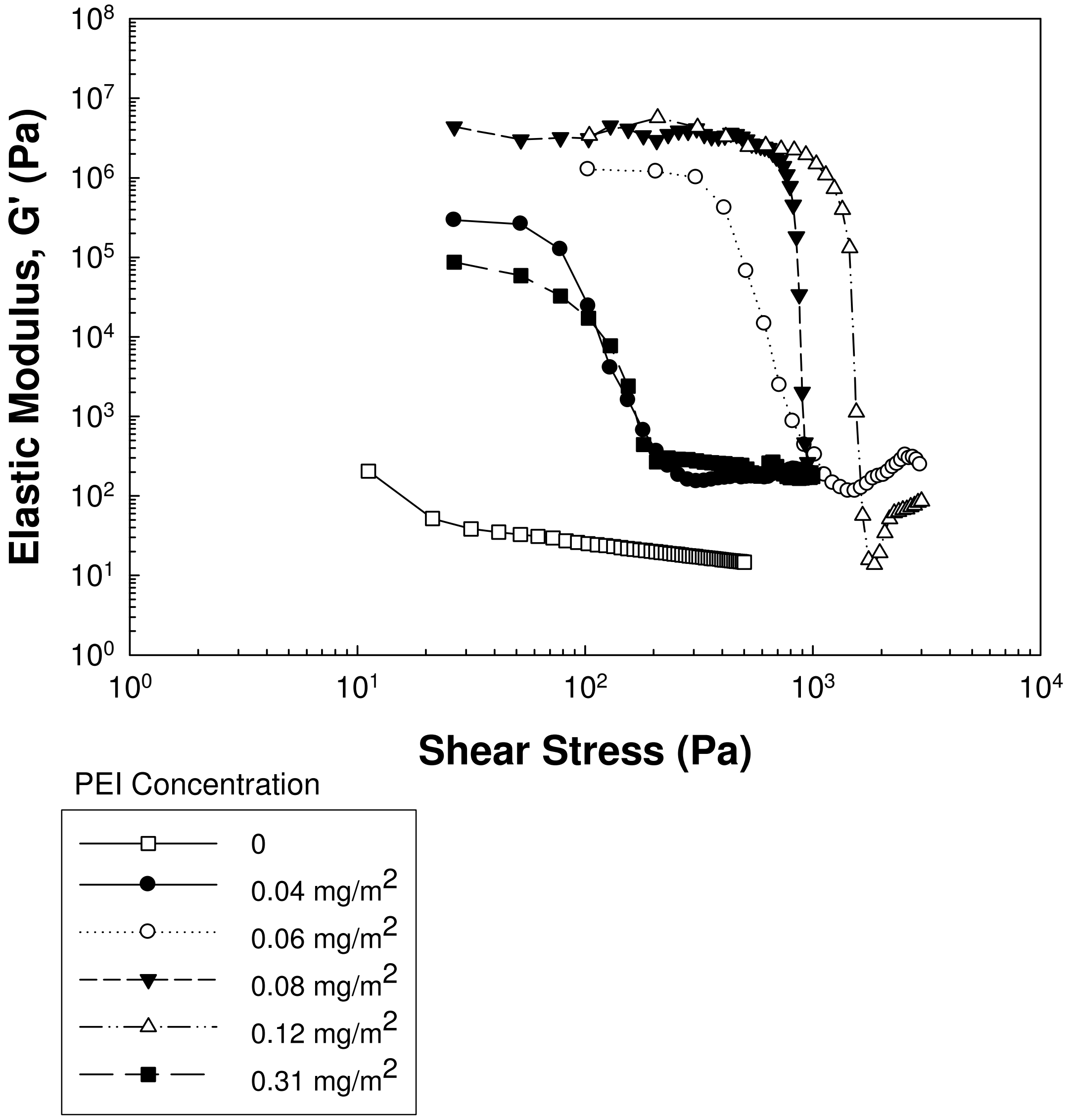

Figure 6.10. Effect of PEI concentration on the elastic modulus of PMN suspensions in the presence of PAA, 55 vol% PMN, pH 9, 3 mg/ml HPMC.

6.3.2. Gelation with pH Modification

Figures 6.11 and 6.12 show the effect of pH modification on the apparent viscosity and elastic modulus of the PAA coated PMN suspensions. At pH values lower than the IEP of PMN, suspensions exhibited nearly Newtonian behavior. Starting from the pH ~ 8.7 a dramatic increase in apparent viscosity was observed. As the pH decreased to 5.5, viscosity reached to 10^8 Pa.s. Elastic modulus of the gels at this pH was also very high. However, the gels prepared under these conditions were not suitable to use in direct writing process because of the poor flow properties.

The reason of the strong coagulation observed at low pH values in PAA coated PMN suspensions was attributed to decrease in ionizable groups in PAA molecules. As it is discussed in Chapter three, PAA molecule consists ionizable carboxylic acid groups and it is fully negatively charged at pH 9. Therefore, as the pH decreases below 9, PAA caused a strong destabilization in concentrated PMN suspensions.

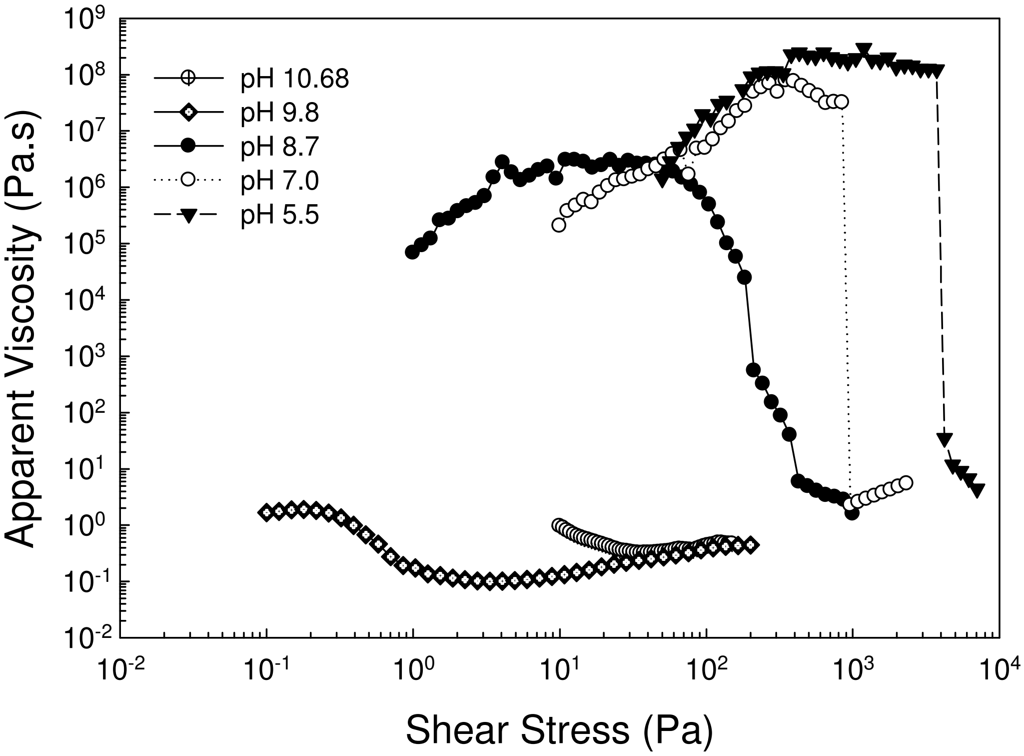

Figure 6.11. Effect of pH shift on the viscosity of PMN suspensions (55 vol%) in the presence of PAA.

Results of the study also showed that gelation of PMN suspensions using pH modification method may be challenging due to leaching of lead and magnesium ions from the particle surface especially at acidic pH values. Furthermore, during acid titration the reactivity of PMN particles may lead to a time dependent pH rise and this cause partial restabilization of the PMN suspensions. The reason of the pH rise may be due to capture of the Pb^{+2} ions by the carboxylic acid groups on the adsorbed PAA which drive equilibrium towards the alkaline region. Further discussion regarding the time depended pH rise in PMN suspensions was made in Chapter three.

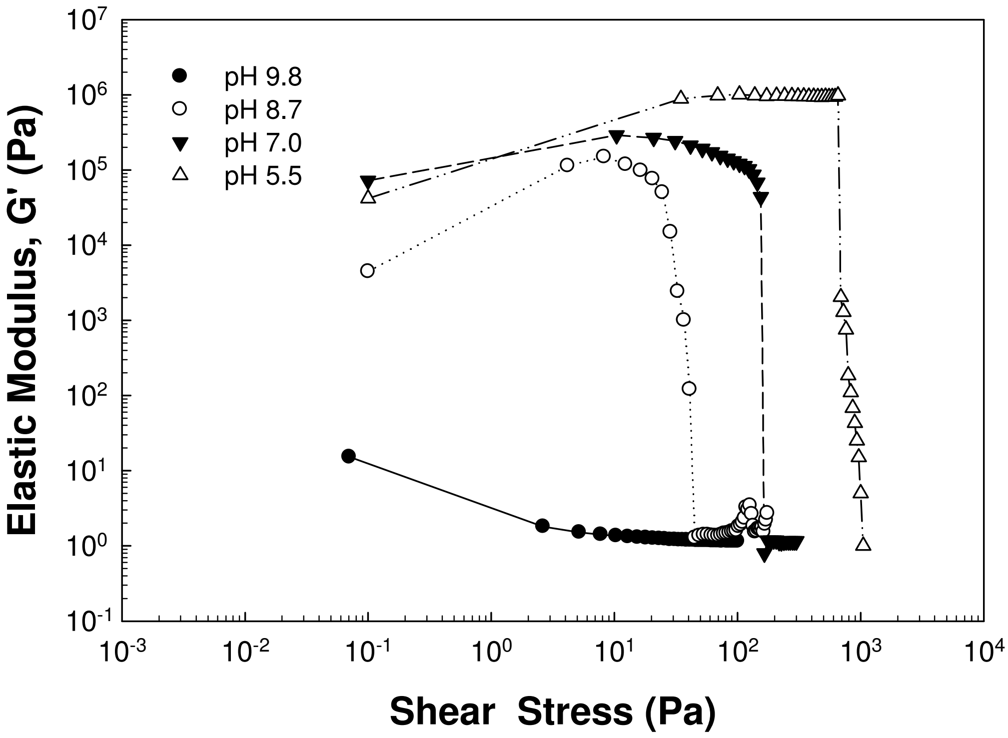

Figure 6.12. Effect of pH shift on the viscoelastic properties of PMN suspensions (55 vol%) in the presence of PAA.

6.3.3. Gelation with Salt Addition

6.3.3.1. Effect of Divalent Salts

In the study, magnesium chloride and zinc acetate were tested to investigate the effect of divalent salt additions on the gelation behavior of PAA coated PMN suspensions. Figures 6.13 and 6.14 show the effect of Mg^{+2} ion concentrations on the viscosity and elastic modulus of the colloidal PMN inks. The PAA-PMN suspensions exhibited a strong rise in both their low shear apparent viscosity and degree of shear thinning flow behavior with increasing Mg^{+2} ion concentration.

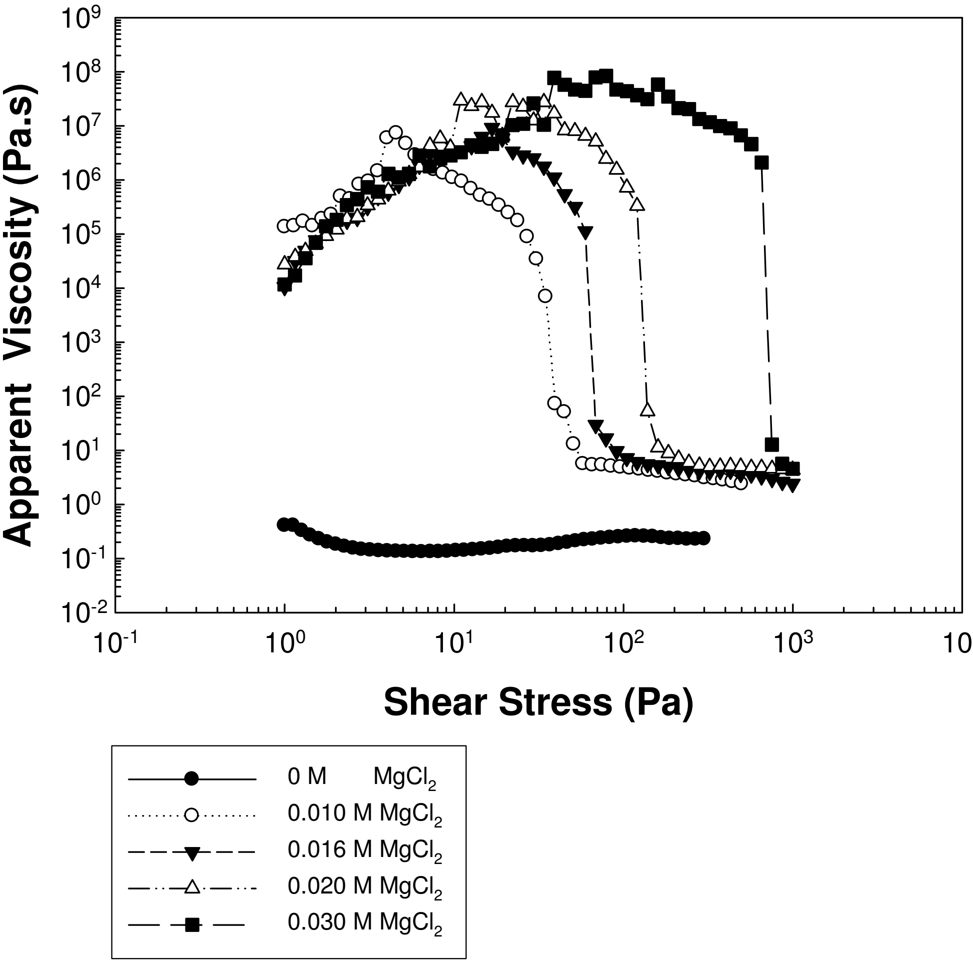

Figure 6.13. Effect of $MgCl_2$ on the viscosity of the PMN suspensions (55 vol%) in the presence of PAA, pH 9.

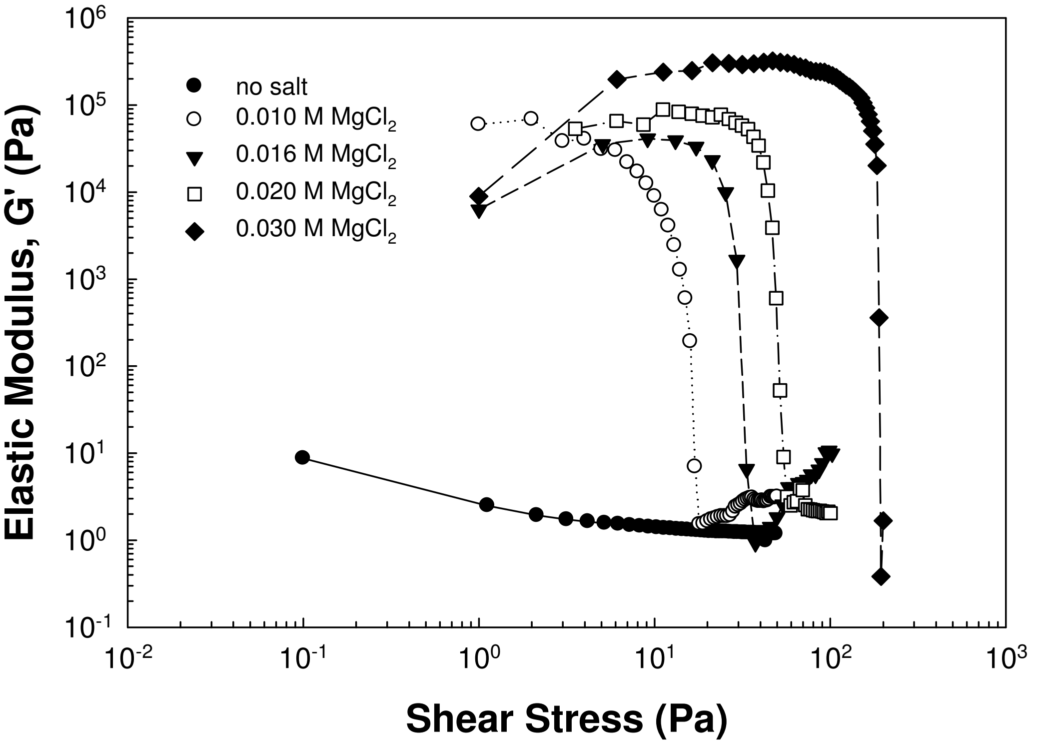

Figure 6.14. Effect of $MgCl_2$ on the elastic modulus of PMN suspensions (55 vol%) in the presence of PAA, pH 9.

Similar results were obtained for PAA coated PMN suspensions containing zinc acetate. As it is shown in Figures 6.15 and 6.16 there is a dramatic rise in apparent viscosity and elastic modulus of the PMN suspensions as the zinc acetate concentration increase. On the other hand, as the applied shear stress was increased a linear viscoelastic region (low shear stress, G_{eq}` plateau) preceded a decrease in G` at the shear yield stress, τ_y. For $\tau > \tau_y$ the particle network was ruptured and the suspension became fluid.

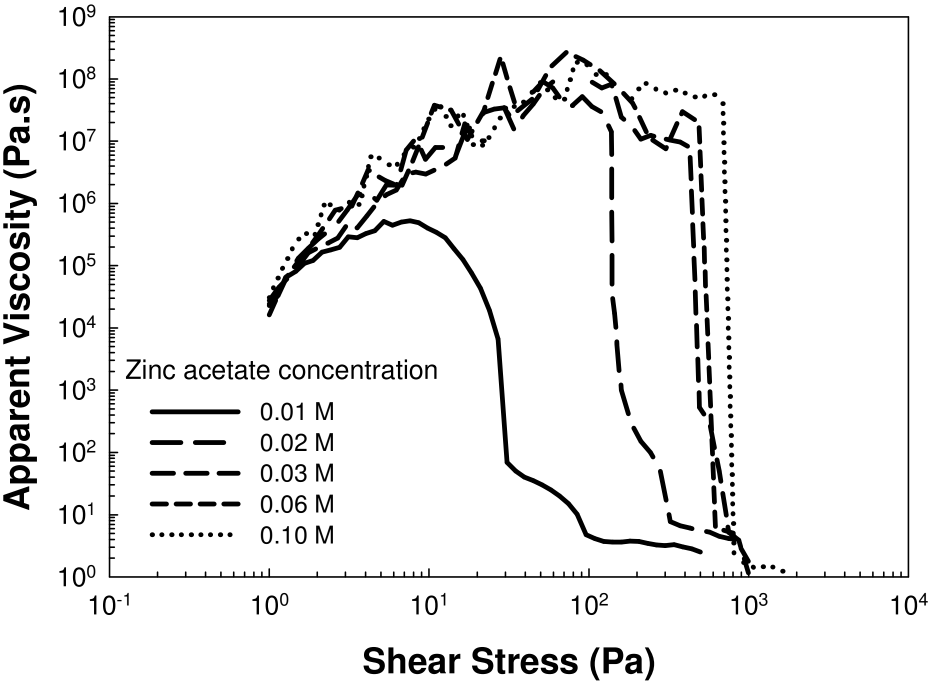

Figure 6.15. Effect of zinc acetate on the viscosity of the PMN-PAA suspensions, pH 9.

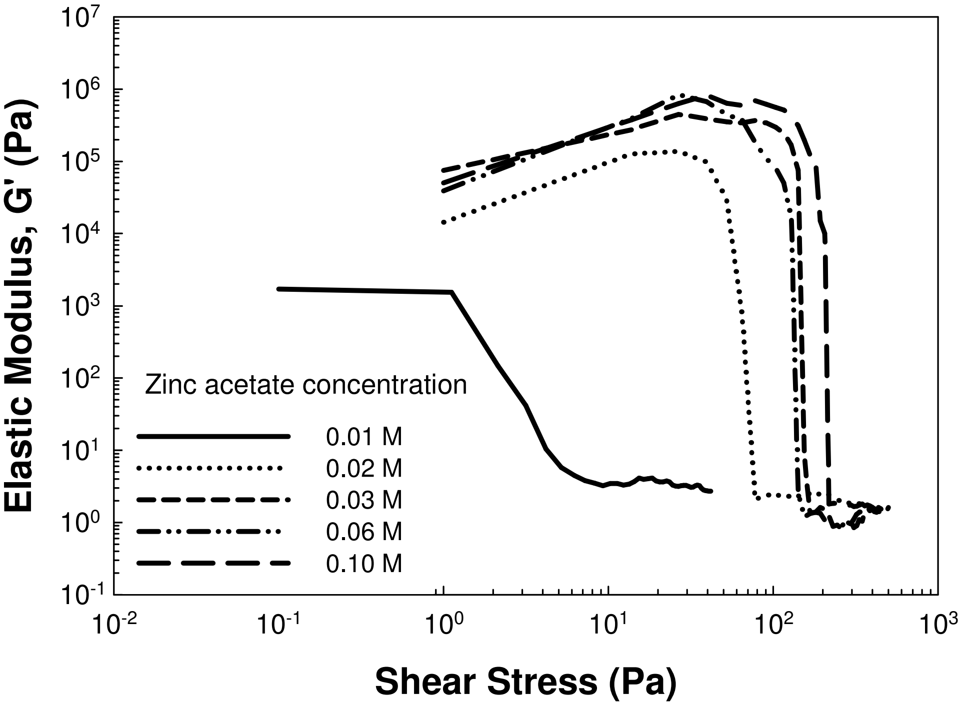

Figure 6.16. Effect of zinc acetate on the elastic modulus of PMN suspensions (55 vol%) in the presence of PAA, pH 9.

As it was discussed in Chapter four the PAA adlayer thickness decreases with increasing ionic strength. The negatively charged PAA coated particles are stable under low ionic strength but rapidly aggregate at high ionic strength conditions. This behavior is also closely related with the valence of the ions introduced to the system.

In this study to investigate the effect of monovalent and divalent salt species on the gelation behavior of PMN suspensions, the viscosity and elastic modulus was examined as a function of ionic strength. The ionic strength was calculated according to following equation:

$$[I]=\frac{1}{2}\sum_{i} n_i z_i^2 \tag{6.1}$$

where n_i is the molar concentration of ionic species and z_i the valency of the ion.

Results showed that the addition of divalent salt species led to the destabilization of the PAA coated PMN suspensions. According to the Manning counterion condensation theory, a fraction of the charged groups along the polyelectrolyte backbone of both PAA and PAA/PEO dispersants will be neutralized when counterions are present in solution. Counterion condensation occurs due to electrostatic interactions between oppositely charged side groups and counterion species, which inhibit counterion diffusion away from the polyelectrolyte chains. Condensed counterions screen the negative charges associated with the carboxylic acid groups therefore decrease the repulsive electrostatic interactions between like-charged, adsorbed PAA-based dispersants on different particles. Polyelectrolye species can undergo additional attractive interactions by sharing counterions. This is commonly referred to as ion bridging (Netz and Andelman 2003, Napper 1977). Because both screening efficiency and bridging interactions intensify with increasing counterion valency, divalent counterions are more effective at promoting attractions between polyelectrolyte species than monovalent ones.

6.3.3.2. Effect of Monovalent Salts

Figure 6.17 demonstrates the effect of monovalent salt (KCl) on the coagulation behavior of the concentrated PMN suspensions. At very high salt concentrations such as

0.2 M KCl any flocculation was not observed in the system. Experiments were also performed at lower salt concentrations such as 0.03 M KCl. Although it is not demonstrated in Figure 6.17, at low salt concentrations again KCl did not cause destabilization.

For monovalent salt additions such as KCl the only available mechanism for reducing the electrosteric stabilization between the PMN particles is screening the charge between the particles and the adsorbed PAA layer. This screening causes a reduction in the repulsive electrostatic interactions between the particles and possibly a small contraction of the adsorbed PAA layer because of the conformational changes.

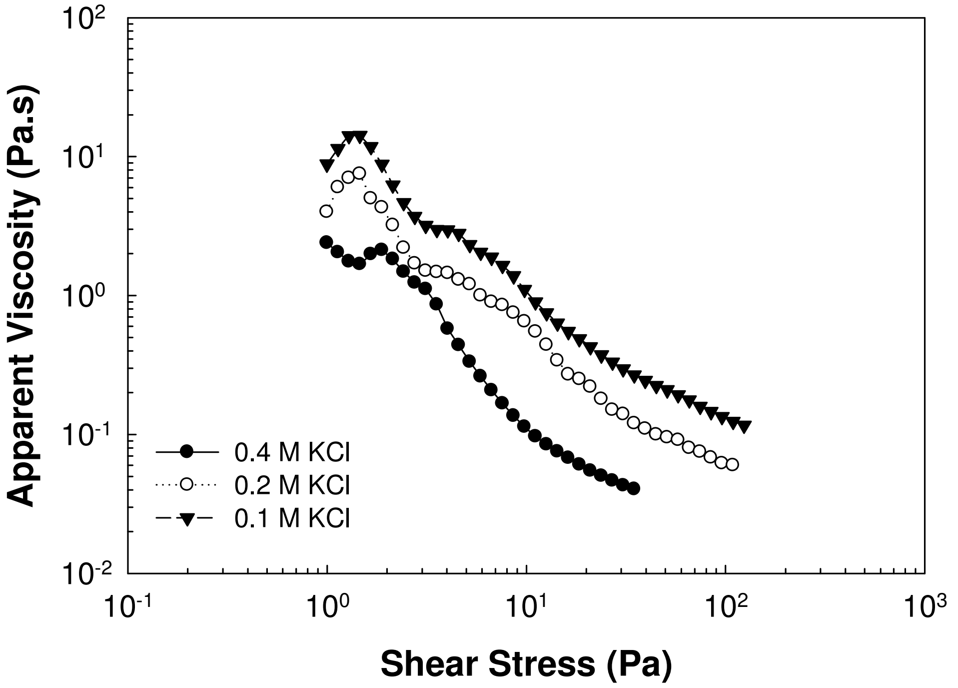

Figure 6.17. Effect of monovalent salt on the apparent viscosity PMN suspensions (55 vol%) in the presence of PAA, pH 9.

It is possible to conclude that monovalent counterions such as K^+ only screens the negatively charged COO^- groups, on the other hand divalent counterions such as Zn^{+2} and Mg^{+2} can promote the aggregation through the ion bridging effects between PAA adsorbed on the particle surface. Figure 6.18 describes well the effect of both monovalent and divalent salt species on the equilibrium shear modulus of PMN suspensions.

It is well known that the negatively charged PAA coated particles are stable under low ionic strength but rapidly aggregate under high ionic strength conditions.

Results of this study showed, nearly an order of magnitude increase in the low shear apparent viscosity of the PAA-stabilized suspensions containing Mg^{2+} or Zn^{+2} ions relative to those with K^+ ions at the same ionic strength. This observation indicates that increased ionic strength is not solely responsible for destabilizing the pure PAA-PMN suspensions.

On the other hand, there is always possibility for a complex formation between $MgCl_2$ and PMN particle surface as it was discussed in Chapter three of this thesis. Electrophoretic mobility measurements of the PMN suspensions showed that in the presence of $MgCl_2$,as background electrolyte, isoelectric point of PMN was depended on the salt concentration which means that there is Mg adsorption on the surface (see Chapter 3).

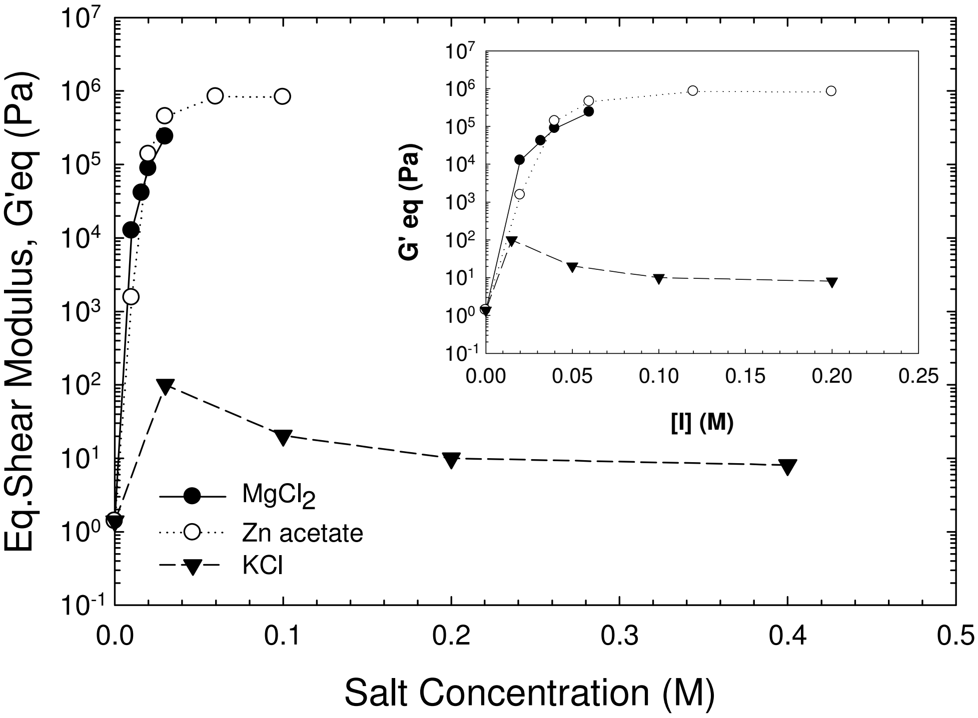

Figure 6.18. Effect of monovalent and divalent salts on the viscoelastic response of PAA coated PMN suspensions as function of salt concentration and ionic strength.

6.3.4. The Flow through the Deposition Nozzle

In robotic deposition process it is necessary to calculate the pressure required to initiate the flow of the viscous and highly concentrated fluid from the deposition nozzle or printing tip. The laminar flow of viscous inks through a cylindrical tube can be described by the Hagen-Poiseuille equation (Larson 1999, Barnes et al. 1993):

$$Q = \pi R^4 \Delta p / 8 \eta L \tag{6.2}$$

where Q = volumetric flow rate, R = tube radius, Δp = pressure drop, η = ink viscosity, and L = length of the tube. The deposition nozzles consist of long tapered capillaries whose radius gradually decreases to the final nozzle size. Because the capillary radius far exceeds the nozzle radius, the pressure drop can be estimated using the following relationship for flow through a slowly-varying channel (Gratson 2005):

$$\Delta p = \frac{8\eta Q}{\pi} \int_{x_1}^{a} R^{-4} dx \tag{6.3}$$

where a = nozzle radius and x_1 = capillary radius. In this case R varies with x:

$$R = x\tan(\alpha) \tag{6.4}$$

where α = the angle of taper. Solving the integral yields:

$$\Delta p = \frac{8\eta Q}{3\pi(\tan\alpha)a^3} \tag{6.5}$$

where the pressure drop at x_1 can also be neglected because x_1 is much greater than a. This relation assumes a sufficiently small α and also neglects inertial forces, which is valid for the ink and deposition parameters used in this study since (Gratson 2005):

$$\alpha \frac{2\rho Q}{\pi a \eta} < 1 \tag{6.6}$$

Using the above expressions (Gratson 2005), the pressure required to maintain the desired volumetric flow rate ($Q = \nu\pi R^2$) at a constant deposition speed (ν) of 0.75 μm/sec was estimated. For comparison, the actual applied pressures utilized for each set of deposition conditions studied are also reported in Table 6.1. As expected, the pressure required to maintain a given flow rate increased with increasing ink viscosity or decreasing nozzle diameter.

Table 6.1. Calculated and applied pressures values for robotic deposition.

Ink Composition	Nozzle Diameter (μm)	Applied Pressure (psia)	Calculated Pressure (psia)
PEI (0.06mg/m^2)	100	90	108.82
PEI (0.06mg/m^2)	200	40	33.60
PEI (0.06mg/m^2)	500	20	1.16
I (Zn-acetate)	200	30	12.366
I ($MgCl_2$)	200	20	6.183
I ($MgCl_2$)	100	40	49.46
pH 7.5	200	30	12.36
pH 8.7	200	20	8.6
pH 7.5	500	20	1.056

As it is tabulated in Table 6.1 some differences were observed between the applied and theoretically calculated pressure values. Previously, Smay reported that a Hershel-Bulkley material flowing through a capillary may consist of a three zone velocity profile: 1) an un-yielded core of radius r_c moving at constant velocity surrounded by 2) a yielded shell experiencing laminar flow and, possibly, 3) slip at the nozzle wall. The term slip refers to the development of a thin fluid layer, whose thickness (δ) << R, between the nozzle wall and the bulk ink (Smay 2002, Smay et al. 2002a). The geometry of a section of the capillary tube is shown in schematically in Figure 6.19.

The volumetric flow rate (Q) as a function of applied pressure is found then by summing the contributions from slip at the nozzle wall and the integrated velocity profile in the core-shell region:

$$Q = \pi R^2 \left(v_s + f(\tau_s)\right) \tag{6.7}$$

where v_s is the slip velocity and $f(\tau_r)$ is the integrated velocity profile of the core and shell region. The slip velocity is determined by:

$$v_s = \frac{\left(\tau_R^4 - \tau_s^4\right)}{4\tau_R^3 \eta_c} \tag{6.8}$$

where τ_R is the shear stress at the nozzle wall, τ_s is the shear stress at the slip layer-gel interface. The function $f(\tau_s)$ is given by

$$f(\tau_s) = \frac{R\alpha^{m+1}}{m+1}\left(\frac{\tau_s}{K}\right)^m \left(\frac{\tau_s}{\tau_R}\right)\left[1 - \frac{2\alpha}{m+2} + \frac{\alpha^2}{(m+2)(m+3)}\right] \tag{6.9}$$

where $m = 1/n$, n is the Hershel-Bulkley shear thinning exponent, K is the viscosity parameter, $\alpha = (1-\tau_y/\tau_s)$, and τ_y is the gel yield stress. Under the no slip boundary condition ($\delta = 0$), last equation reduces to the Hagen-Poiseuille relationship for a Newtonian fluid as described in the first equation (Smay 2002). Therefore, in the current study the difference between the applied and the calculated pressure values may be attributed to the slip formation inside the nozzle. Under these conditions pressure required to achieve deposition should be calculated using equation (6.9).

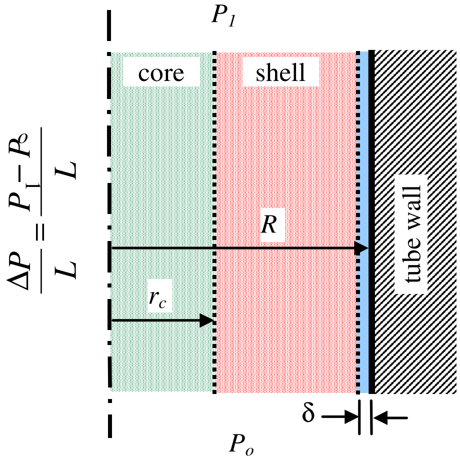

Figure 6.19. Schematic cross section (half-space) of ink in a capillary tube with assumed core-shell architecture (Source: Smay and Lewis 2001).

6.3.5. Robocasting

In the study the PMN inks was robotically deposited onto a moving *x-y* stage yielding a 2-D pattern (Figure 6.20). After a given layer was generated, the stage was incremented in the z-direction (Δz) and another layer was deposited. This process was repeated until the desired 3-D structure was created. In other words, 3-D periodic lattices were assembled by patterning an array of parallel rod-like filaments in the x-y plane. The build time varied with the size of the structure, the road width, and the deposition speed. For the simple lattices, the rod spacing (L) was varied depending on the rod size and spacing (or lattice constant) desired ($L = 200 - 250$ μm for nozzle sizes 200 μm). Radial arrays were assembled by the sequential deposition of layers with alternating patterns of concentric rings and a circular array of radially oriented rods.

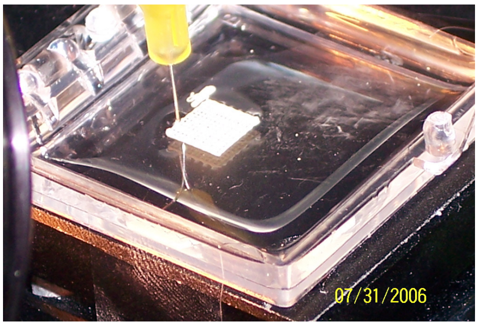

Figure 6.20. Picture showing the printing process using 100 μm tip. Feature size 5mm.

The ink flowed through the nozzle at a volumetric flow rate required to maintain a constant deposition speed (v) of 7.5 mm/s. Depositions down to D: 100 μm were successfully performed, but below D: 100 μm (such as 30 μm) deposition led to clogging and this may be attributed to the ratio of the particle size to nozzle diameter. The tip sizes between $100 < D < 30$ μm could not be tested since it is not commercially available. As the ink exits the nozzle, it forms a continuous, rod-like filament with a rigid (gel) core-fluid shell architecture that simultaneously promotes shape retention while allowing the rods to fuse together at their contact points. This filamentary architecture arises because the percolating network of attractive particles within the gelled ink is capable of transmitting stress above ϕ_{gel} (Lewis 2006). To maintain constant ink composition (ϕ) and, thereby, prevent changes in ink rheology due to water evaporation during assembly, the deposition process was carried out in an oil reservoir. Figures 6.21 and 6.22 show the 3D lattices produced by robocasting method. The pictures were taken just after deposition step therefore the structures are still in oil reservior.

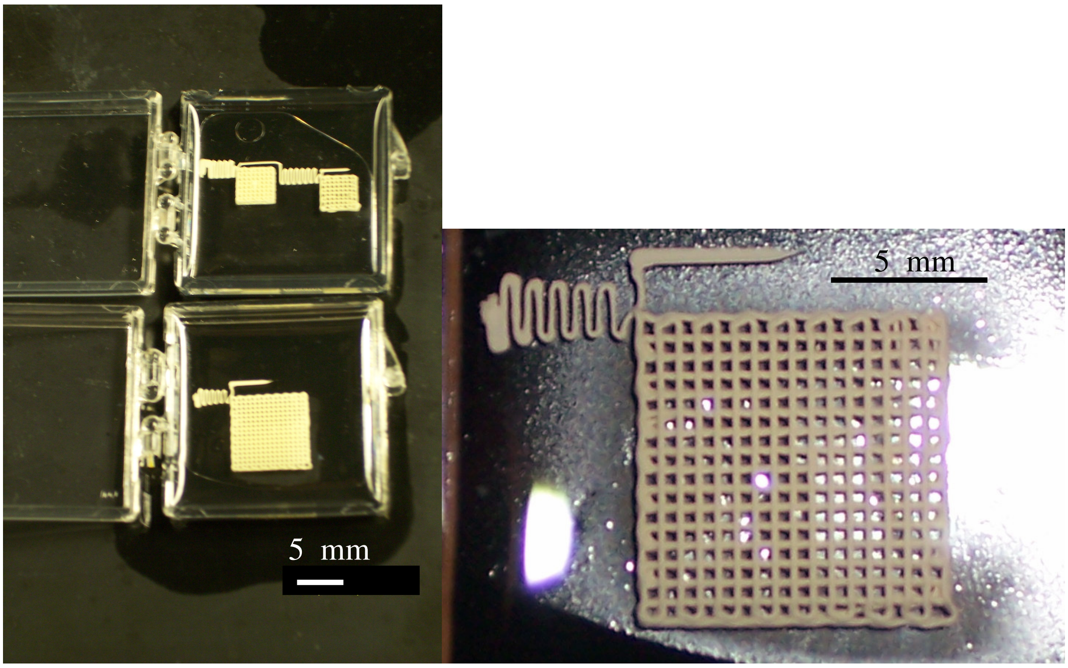

Figure 6.21. Images of the robocast structures produced from PMN inks prepared by ΔpH method (pH 7), 10x10 mm, and 6 layers.

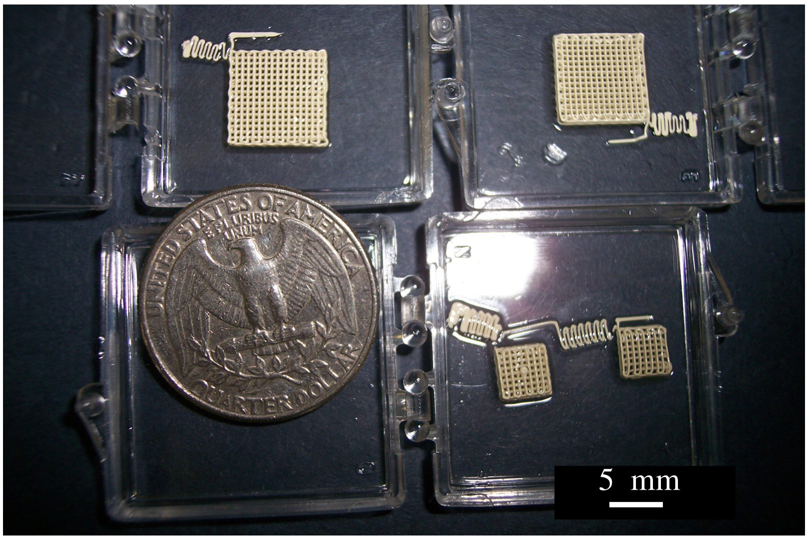

Figure 6.22. Images of the robocast structures produced from PMN inks prepared by PEI (0.06 mg/m^2) addition method, 5x5 mm and 10 x10mm, 6 layers.

The radial lattice in Figure 6.23 (a) has a cylindrical symmetry where Γ_p in the radially oriented layer is 0.83. Here, the top layer is an array of radial lines and the underlying layer is a series of concentric rings. The rings maintained their circular shape during deposition despite the changing arc length between supports provided by the radial lines in the previous layer. The rings appeared to maintain the arc shape during deposition.

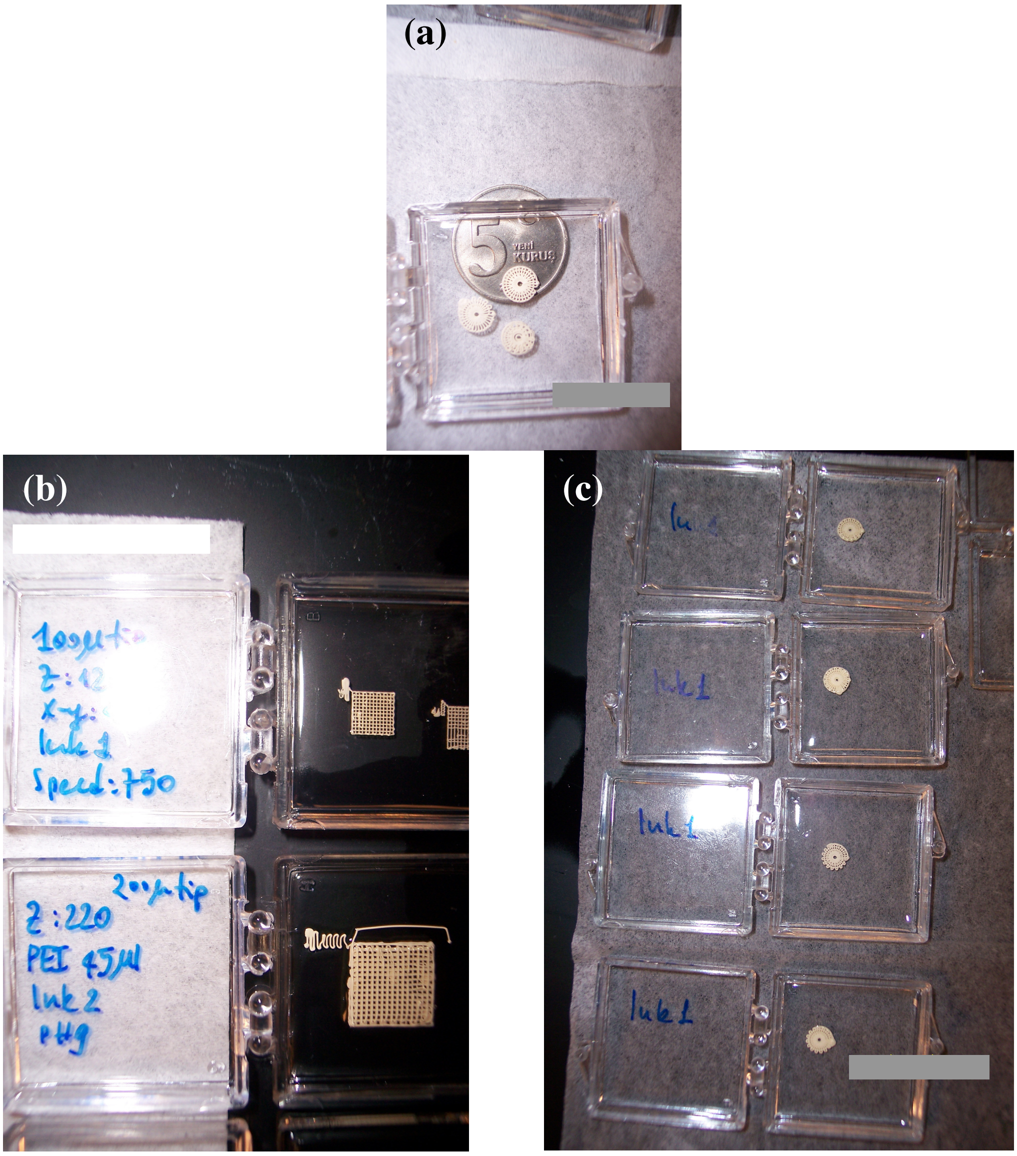

Figure 6.23. Pictures of radial and square lattices produced by a) PEI addition method b) ΔI method ($MgCl_2$), first sample c) ΔI method ($MgCl_2$), diameter 5 mm, 2 layers.

6.3.5.1. Optical Microscope Images

Two dimensional arrays consisting of a continuous spiral pattern and a parallel array of rods were produced by robotic deposition using 100 µm tips, as shown in Figure 6.24.

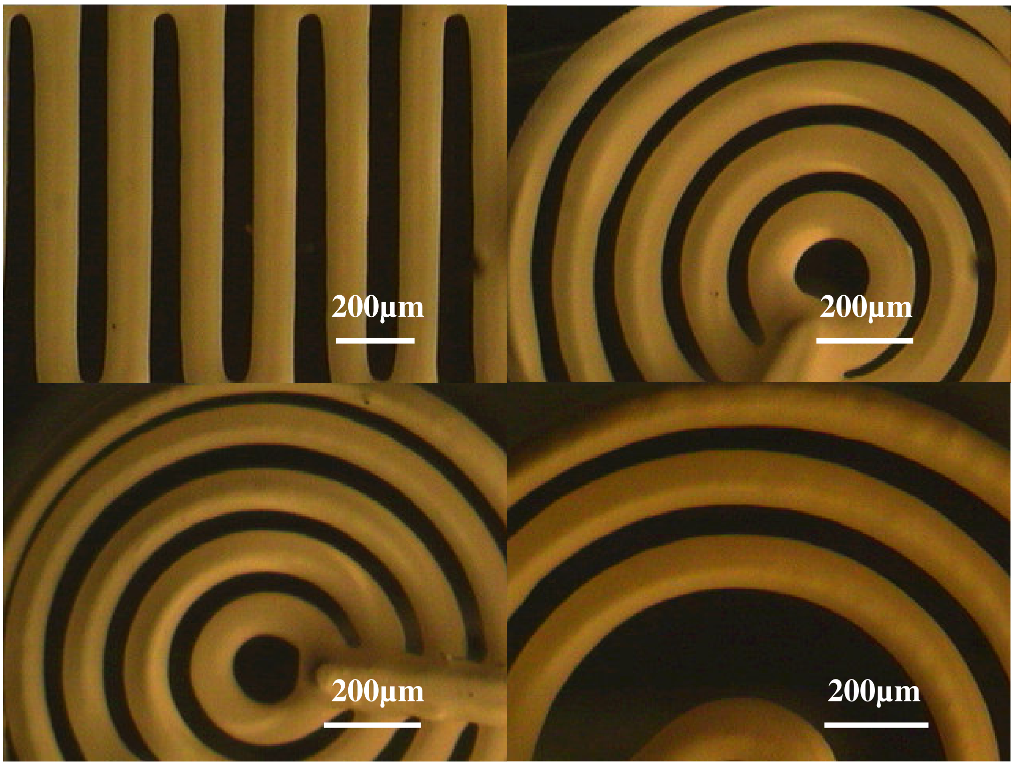

Figure 6.24. Two dimensional shapes produced by robocasting.

Similarly, pictures of three dimensional lattices fabricated by different PMN inks are shown in Figure 6.25 to 6.34. Structures produced by PMN inks which contain adequate amount of PEI kept their shape during deposition (see Figure 6.25). Results showed that it was possible to create well shaped, uniform lattices having rod sizes in the range of 100 μm to 500 μm using PMN ink in the presence of 0.04 or 0.06 mg/m^2 PEI (Figures 6.25 to 6.27). At a PEI concentration of 0.08 mg/m^2 the yield stress of the PMN ink was too high therefore, at this concentration the flow properties of the ink was poor. Above this value some difficulties were observed in shape retention (see Figure 6.28) due to decrease in destabilization of PMN inks. Figure 6.28 depicts the structure of the square lattices prepared by ionic strength modification method. Similar to structures prepared by PEI addition method, this method was also adequate to produce defect free structures. Results showed that deposition of the inks prepared by ΔpH method (at pH 8) was also successful but some difficulties were observed adjusting the gel properties Figures 6.29 and 6.30 demonstrate the structures produced using inks prepared by ΔpH method. Furthermore, in ΔpH method leaching of Pb^{+2} and Mg^{+2} at pH values lower than 6 was a significant problem as described in Chapter three. Therefore, deposition of radial structures using PMN inks prepared by PEI method were better compared to the PMN inks prepared by ΔpH method (Figures 6.31 and 6.32). Consequently, in the study PEI addition and ionic strength modification methods were observed to produce better results and therefore they were preferred to prepare PMN inks for robocasting.

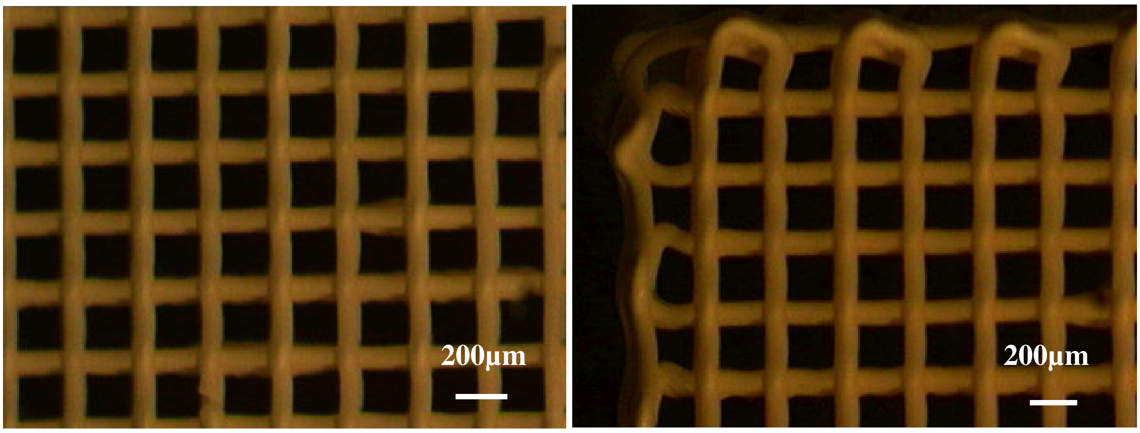

Figure 6.25. Optical microscope images of the structures produced by ink which contains 0.04 mg/m^2 PEI. 5mm x 5mm, 100 µm tip size.

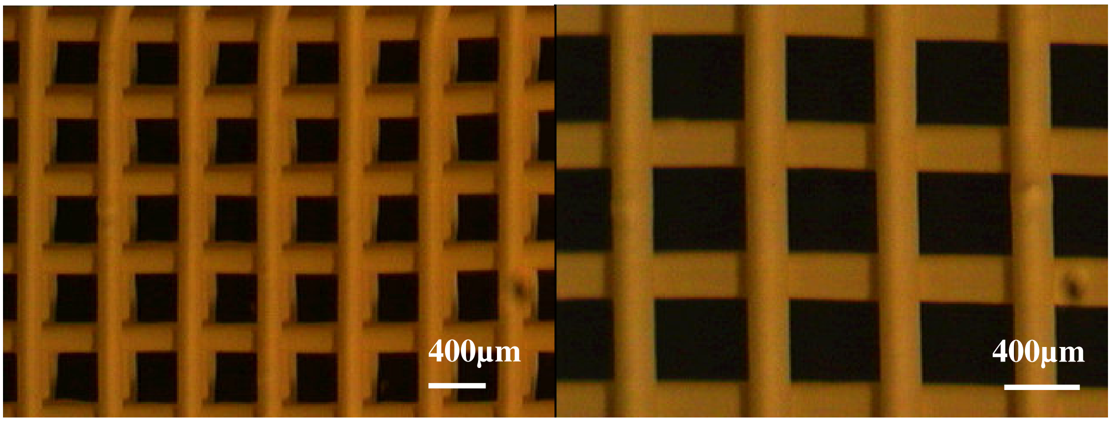

Figure 6.26. Optical microscope images of the structures produced by ink which contains 0.06 mg/m^2 PEI. 10mm x10mm, tip size 200 µm.

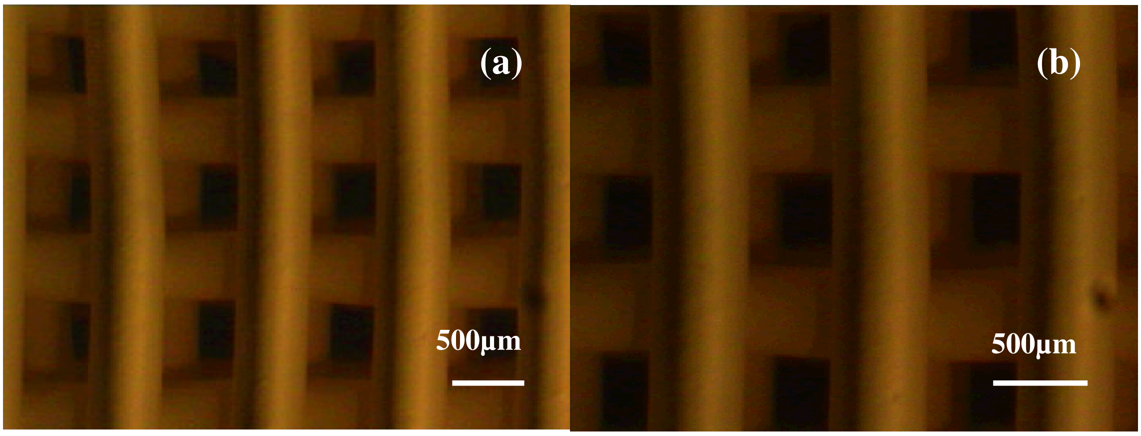

Figure 6.27. Optical microscope images of the structures produced by ink a) contains PEI 0.06 mg/m^2 b) pH 8 (tip size 500 µm).

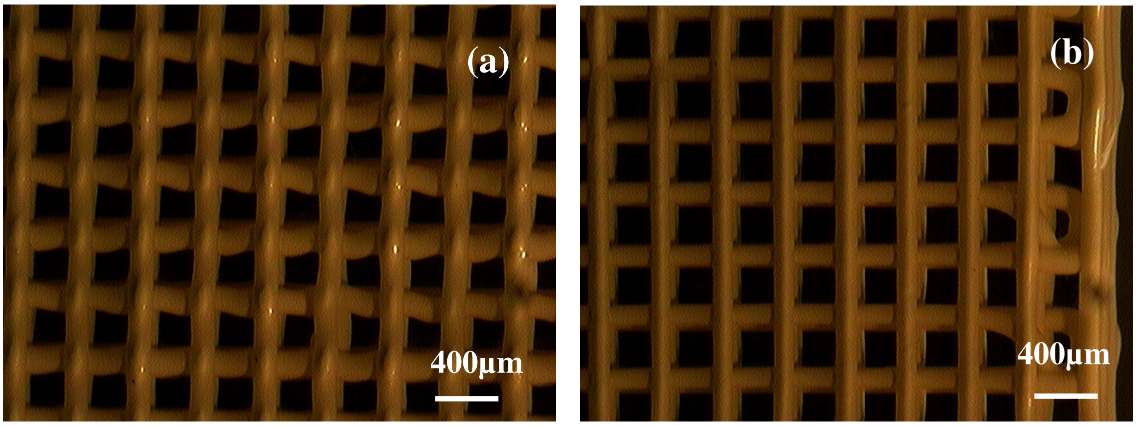

Figure 6.28. Optical microscope images of the robocast structures produced by ink which contains a) 0.2 mg/m^2 PEI. b) 0.02 M MgCl$_2$ (10mm x10mm, tip size 200 µm).

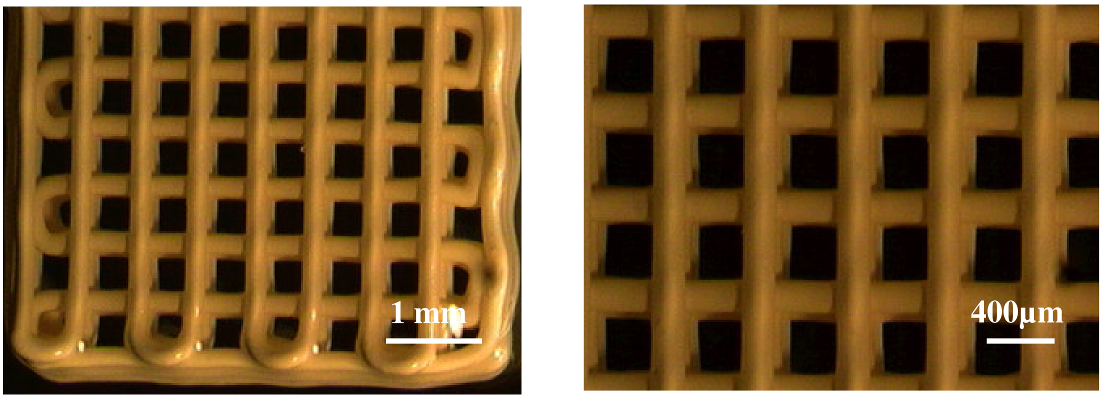

Figure 6.29. Structures produced by PMN ink prepared using ΔpH method (pH 7). 5mm x 5mm, tip size 200 µm.

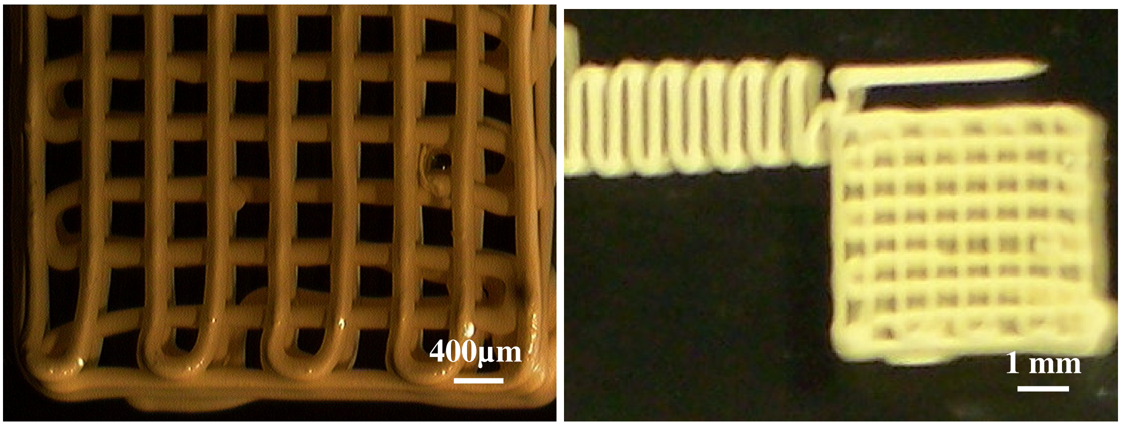

Figure 6.30. Structures produced by PMN ink prepared using ΔpH method (pH 8). 5mm x 5mm, tip size 200 µm.

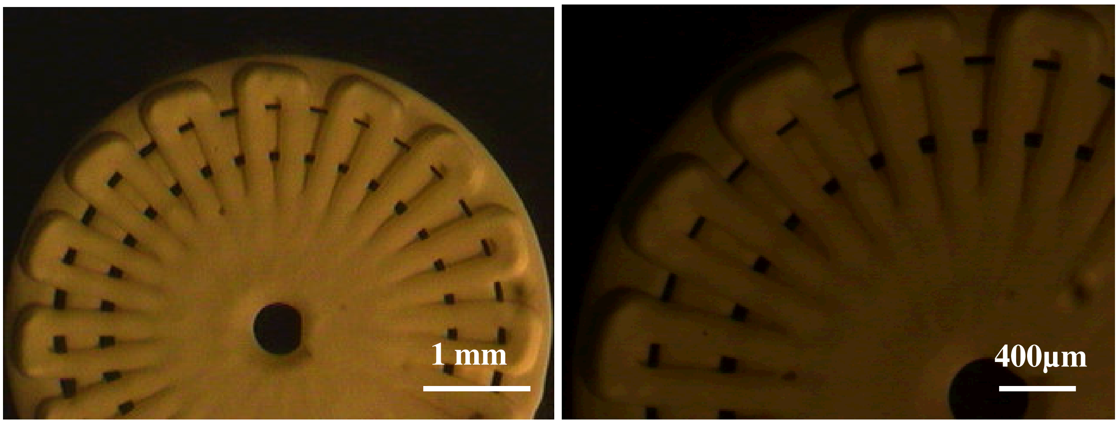

Figure 6.31. Optical microscope images of the structures produced by ink containing 0.06 mg/m^2 PEI.D: 5 mm, 200 μm tip size.

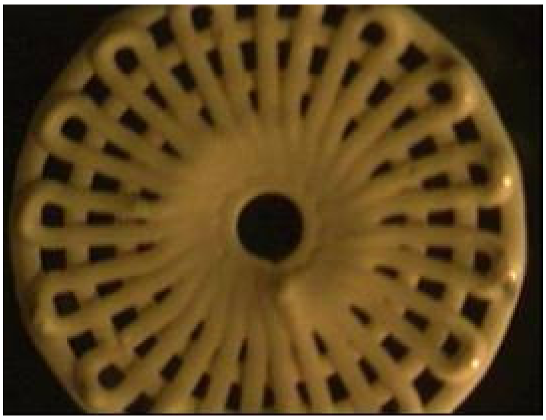

Figure 6.32. Optical microscope image of the structure produced by PMN ink prepared using ΔpH method (pH 8).D :5 mm, 200 μm tip size.

As it is discussed in previous section rheological behavior and the viscosity of PMN inks is crucial during robotic deposition. Figure 6.33 show the structures obtained by PMN inks that contain too much PEI. Above a critical concentration PEI act as a cationic dispersant since it creates a second layer on the particle surface. Therefore, viscosity of the ink decreases due electrostatic repulsion between the like charged particles. On the other hand, viscosity is not the only parameter that may affect the deposition process. The pressure applied during deposition has also a significant importance on the final structure. Figure 6.34 (a) demonstrates the 3-D periodic lattice deposited at very low pressure. As it is clearly seen from the figure that at very low pressures deposition of rod like shapes could not achieved. Similarly, applying too high pressure during deposition is also cause formation of similar defects and non-uniform shapes. The other factor that may influence the shape formation is the rod spacing. For the simple tetragonal lattices, the rod spacing (*L*) depends on the rod size and z-spacing (or lattice constant). Very low rod spacing values (compared to the rod size) or z height may cause formation of structures that is shown in Figure 6.34 (b).

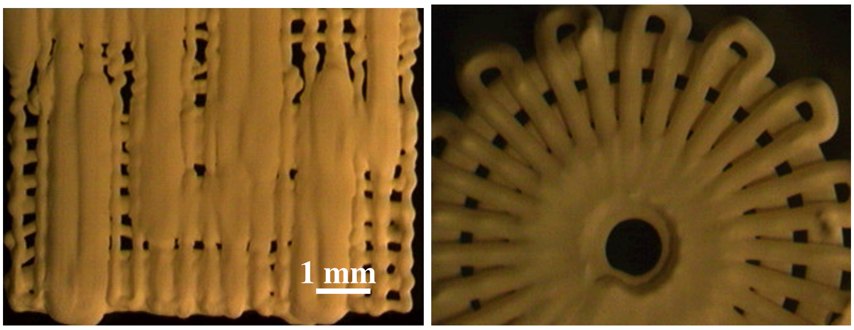

Figure 6.33. Optical microscope images of the robocast structures produced by ink which contains 0.5 mg/m^2 PEI. 5x5mm, tip size 100 μm.

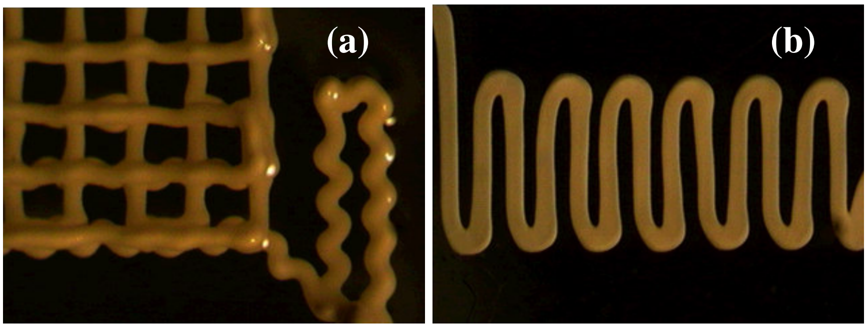

Figure 6.34. a) Deposition pressure is too low b) Height in z direction is too low.

6.3.6. Drying and Sintering

In printing process, structures were dried under ambient conditions for 24 hours after the oil was slowly drained from the deposition reservoir. Then samples were dried in a low temperature furnace at 80 ºC for over night. Dried pieces were sintered in an electric furnace at different temperatures. Any crack formation was not observed during drying. Samples were not removed from the oil container that they were deposited into during this period to avoid possible cracking in green state. Figure 6.35 presents optical microscope images of 3-D structures after drying.

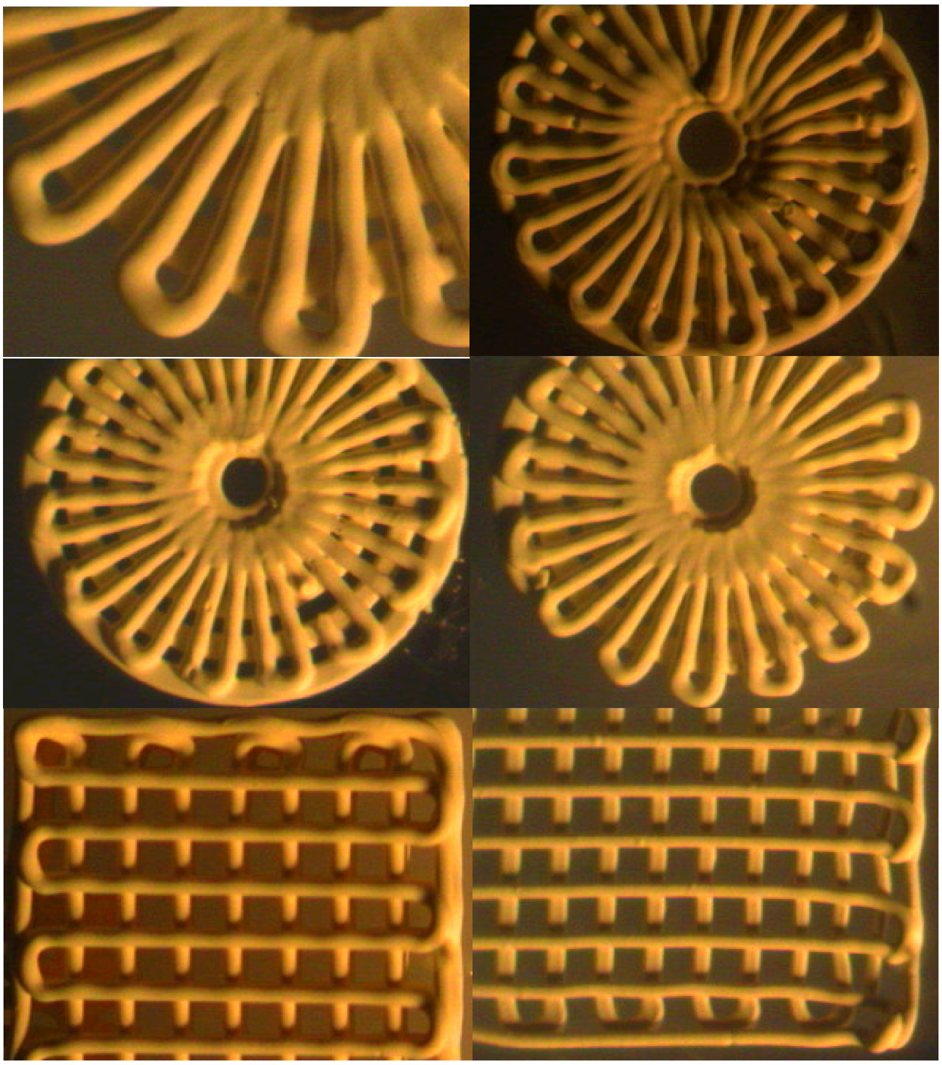

Figure 6.35. Pictures of radial and square lattices after drying.

Microstructure of the dried samples were investigated using SEM. Figure 6.36 show the surface view and the cross section of the samples produced by robocasting. SEM micrographs reveal that samples contain some degree of porosity although they contain negligible amount of binder. Significant difference was not observed between the microstructures of the samples prepared from different type of inks.

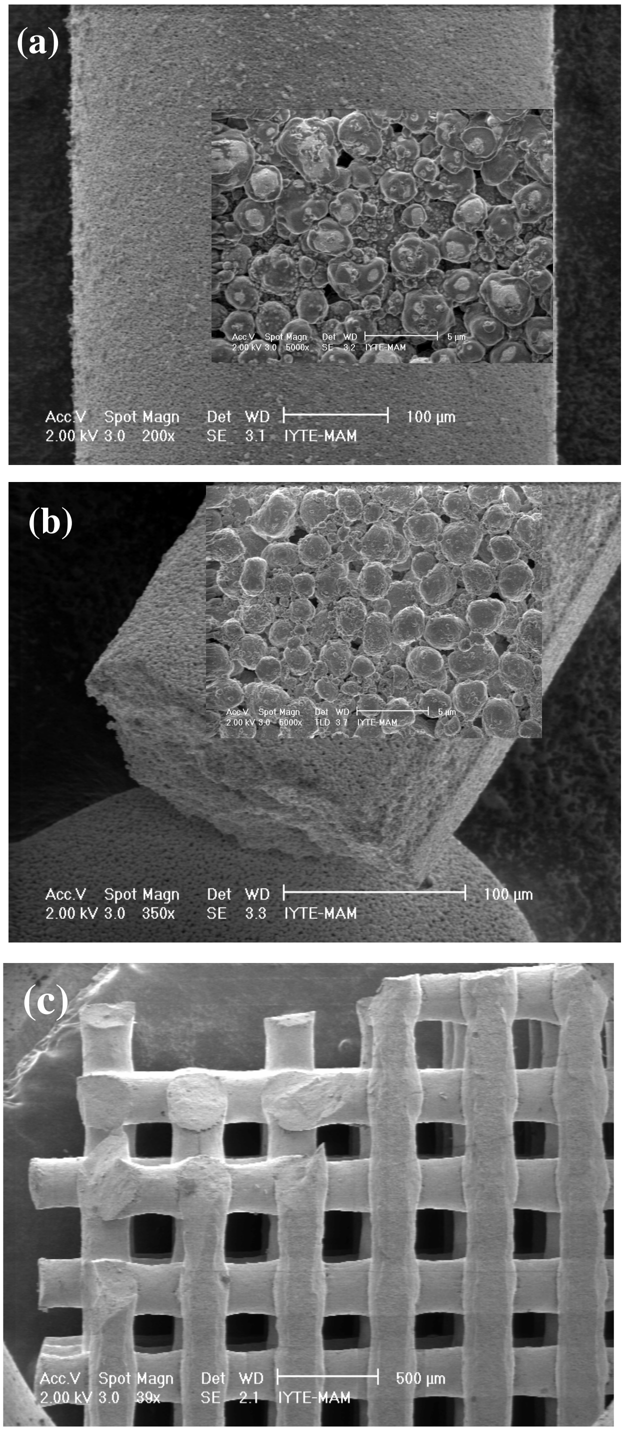

Figure 6.36. Microstructures of the green samples produced by robocasting (a) ΔI method, (b) PEI method, (c) ΔI method.

Heat treatment was applied to the dried samples in order to achieve full densification. Figure 6.37 show the pictures of the samples before and after heat treatment. Some of the samples were directly placed to the furnace without removing the sample container to avoid the deformation. At elevated temperatures these plastic containers melts and the samples can be easily removed.

On the other hand, it is well known that it is necessary to create a lead rich atmosphere in the furnace to compensate the lead loss occurs at high temperatures (>1000 ºC). Therefore, it is obligatory to use an additional lead source inside the furnace to increase lead vapor pressure. To use in the furnace atmosphere $PbZrO_3$ powder was prepared using solid state reactions as it is described in Chapter 5. Three dimensional lattices produced by robocasting was placed in $PbZrO_3$ powder bed as shown in Figure 6.37 (a) and they were covered by alumina crucibles to minimize the lead loss. Samples were sintered at different temperatures in the range of 1000 to 1300 °C. Figure 6.37 (b) show the pictures of the samples that were sintered using the following heating schedule: 25-700 ºC with 1 ºC/min wait for 1 hour, 700-1300 ºC with 3 ºC/min wait for 2 hours.

Similarly, Figure 6.38 shows the optical microscope images of the samples sintered at 1300 °C. Samples have totally a yellow color which is the indication of a lead loss occur during high temperature treatment. SEM pictures in Figure 6.39 demonstrate that samples have a heterogeneous microstructure and contain high amount of pyrochlore. Formation of pyrochlore can be attributed to the very high sintering temperature which causes high amount of lead loss. Microstructure of the PMN samples sintered at various temperatures is shown in Figure 6.40. SEM micrographs reveal that samples calcined at 1000 °C have very high porosity. On the other hand, sintering at 1180 °C produced a homogeneous, low porosity and single phase structure. Above that temperature (e.g. 1250 °C) significant grain growth was observed.

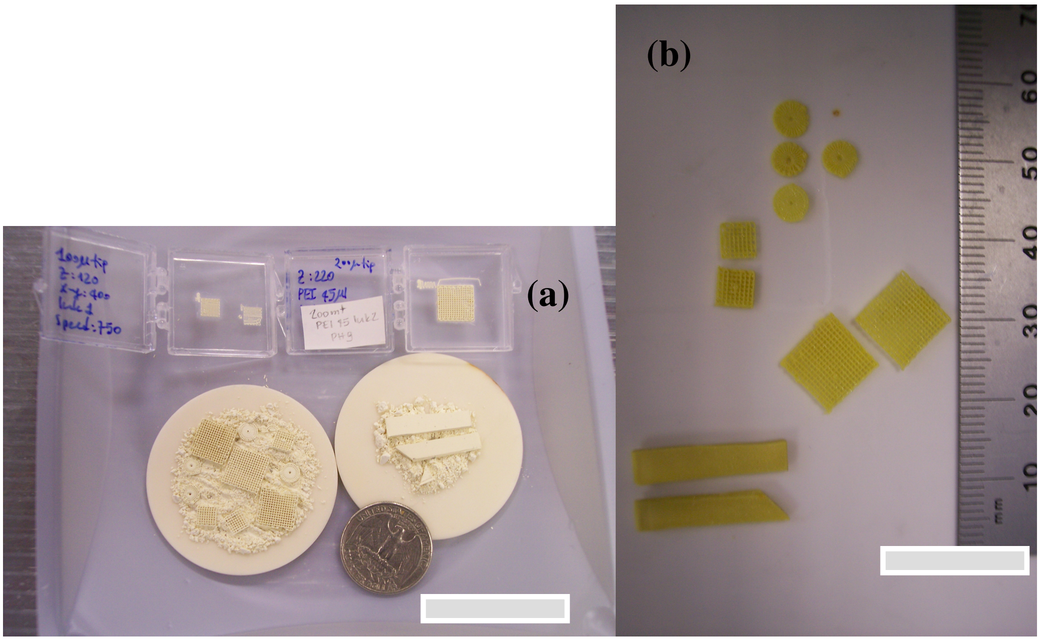

Figure 6.37. Various lattices fabricated by robocasting a) before and b) after sintering.

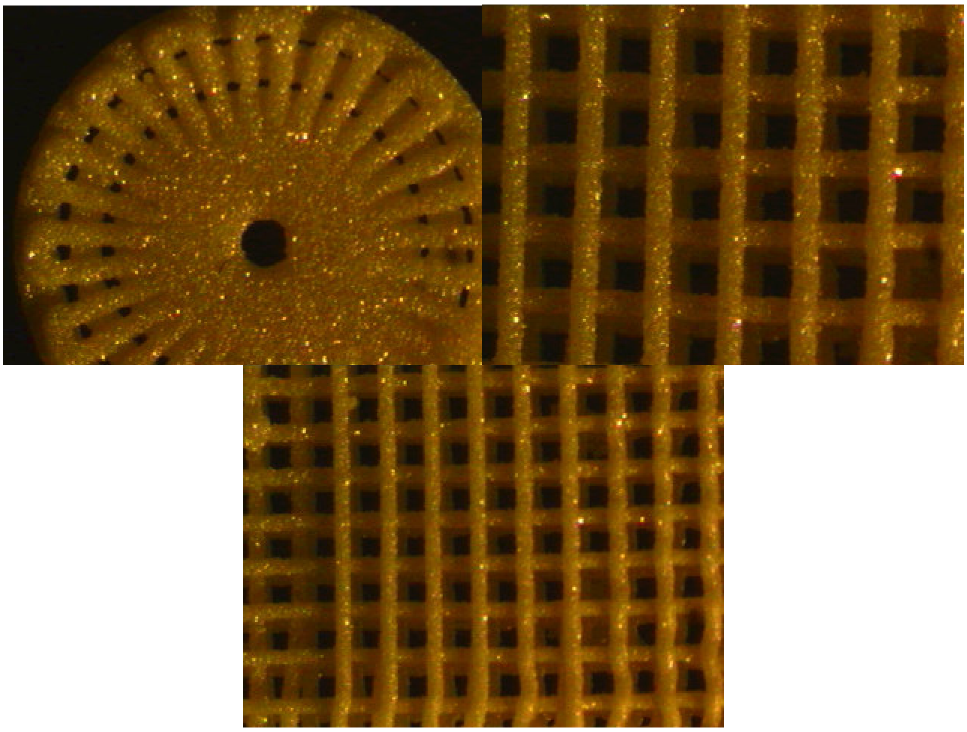

Figure 6.38. PMN 3-D shapes after sintering at 700 ºC for 1 hour and 1300 ºC for 2 hours.

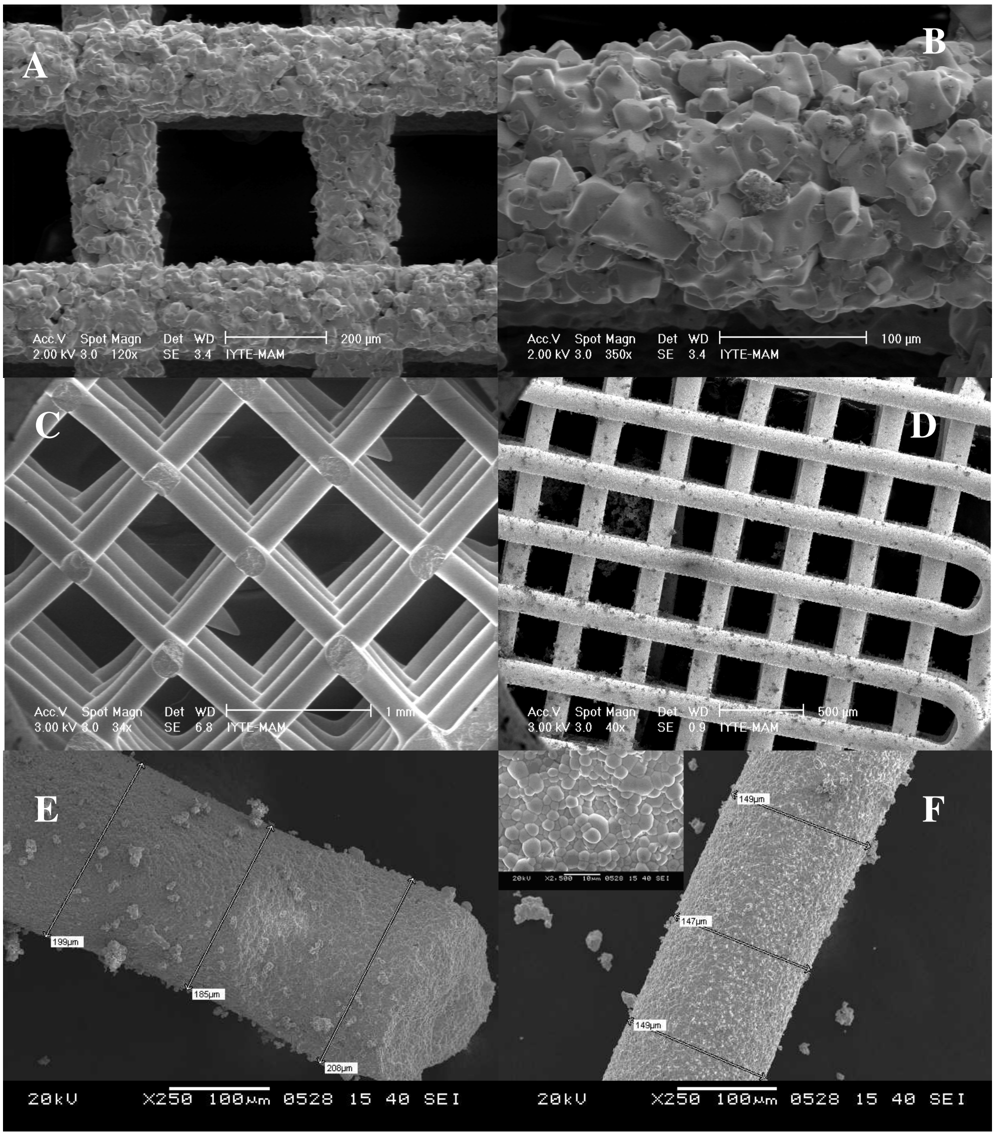

Figure 6.39. SEM micrographs of the samples sintered at (a) and (b) 700 ºC for 1 hour followed by 1300 ºC for 2 hours (c) 1150 °C for 2 hours (d), (e) and (f) 1180 °C 2 hours.

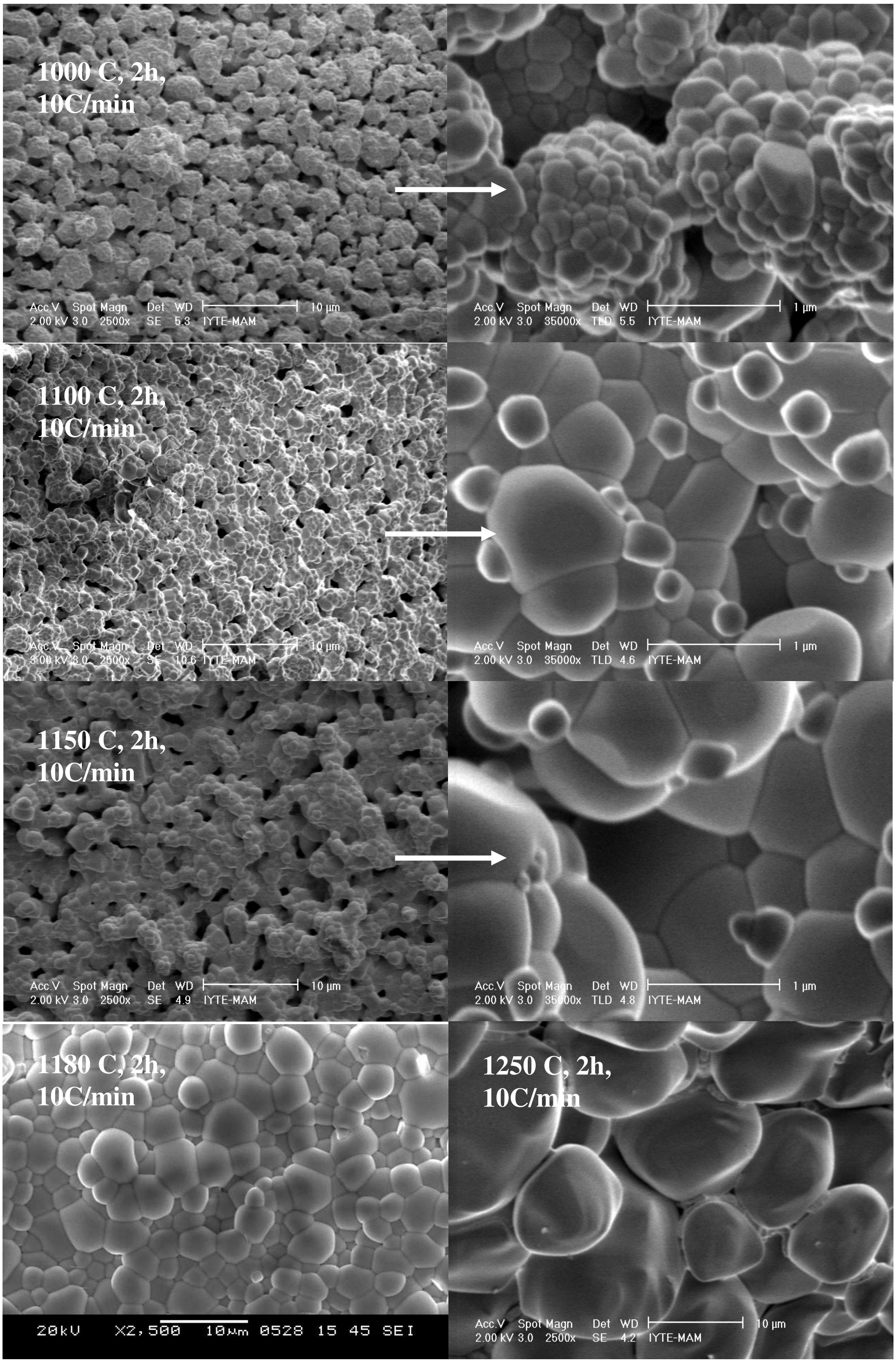

Figure 6.40. SEM micrographs of PMN samples sintered at various temperatures.

CHAPTER 7

CONCLUSIONS AND SUGGESTIONS FOR FUTURE WORK

7.1. Conclusions

Based on the results of this study following conclusions can be drawn: Surface properties of the lead magnesium niobate powders in aqueous medium have been investigated. It has been found that the isoelectric point of this multi-component oxide is depended on the solids loading. At low particle concentrations, such as below 1 vol% IEP was determined to be pH 5 to pH 6. At higher solids loadings such as 20 vol% or above IEP was at pH 9 to pH 10. This behavior was explained by the solubility characteristics of the PMN in water. It was found that Pb^{+2} and Mg^{+2} ions dissolve from PMN surface especially in the acidic pH region. Cation dissolution showed a gradual decrease as the pH increased. Dissolution of Pb^{+2} and Mg^{+2} increases with decreasing pH whereas Nb^{+5} dissolution were negligible under the same conditions. It was concluded that Pb-Mg-Nb-H_2O system undergoes incongruent dissolution with selective leaching of the Pb^{+2} and Mg^{+2} ions in the pH range between pH 2 to 10. The positive surface charge of PMN was attributed to protonation of the amphoteric oxide groups and also dissolution and re-adsorption of the dissolved cations from solution phase to the PMN surface.

In this study, the effect of PAA and PAA/PEO comb polymers on the stability and flow behavior of PMN suspensions was also investigated. PAA experienced large conformational changes as a function of solution pH and the ionic strength. However, PAA/PEO comb polymers imparted stability over a wide range of polymer concentration, pH and ionic strength.

One possible explanation regarding how the PAA/PEO comb polymers increase the stabilization between the suspended PMN particles is the adsorption of like negative charged comb polymers attached onto the particles and formation of a protective shield. The repulsive forces generated by the adsorbed comb polymers are believed to reduce the tendency of the particles to aggregate, thus, counteracting the attractive van der Waals forces.

Effect of comb polymer architecture on the stability was also tested in the study. Results showed that the presence of PEO teeth in few monomer units (i.e. 360 g/mol) was sufficient to protect the PAA/PEO from aggregation even in the presence of divalent ions. Additionally, PAA/PEO species containing longer PEO teeth did not aggregate in solution in the presence of either divalent or trivalent ions.

Adsorption behavior of PAA and PAA/PEO onto PMN surface was determined in aqueous solutions and the influence of pH and ionic strength was investigated. Results showed that adsorption of PAA or PAA/PEO increased with decreasing pH of the suspension. The increase in the ionic strength or the presence of divalent cations caused an increase in the maximum adsorbed amount of PAA and PAA/PEO comb polymers. It was observed that adsorption reaches a maximum when PAA is fully complexed in solution. On the other hand, the increase in the adsorption of PAA/PEO onto PMN in the presence of monovalent or divalent salt was attributed to the decrease in the electrostatic forces rather than complex formation with the divalent metal ions in solution. Because turbidity measurements showed that there is no complex formation between the divalent metal ions and PAA/PEO comb polymers due to shielding effect of the PEO teeth.

In the project Pb^{+2} and Mg^{+2} ion leaching from PMN surface was also studied. Measurements were performed as a function of polyelectrolyte concentration. Results showed that Pb^{+2} and Mg^{+2} concentrations become significant immediately after powder addition. However, upon further treatment Pb^{+2} concentration decreases while Mg^{+2} concentration increases with time. In the presence of comb polymer and at pH 9 Pb^{+2} concentrations in suspension was nearly 10 times higher compared to that in the suspensions which contained no dispersant. On the other hand, it was observed that cation dissolution from PMN surface was inhibited due to an increase in adsorption under acidic conditions in the presence of polyelectrolytes.

In this work, aqueous PMN slurry formulations were also successfully developed for the tape casting applications. The slurries were prepared using a PAA/PEO comb polymer as the dispersant, nonionic acrylic latex as the binder phase and hydroxyl propyl methyl cellulose as the wetting agent. Concentrated PMN suspensions of 55 vol% and 60 vol% were tape cast onto a silicone-coated mylar carrier film. PMN films having a green body thickness of 10 μm to 250 μm were manufactured using the doctor blade technique. Results showed that it was possible to prepare flexible, crack free PMN thick films employing highly concentrated suspensions in the presence of acrylic latex as the binder without using any plasticizer.

In the study, periodic lattices having the rod sizes in the rage of 100 to 500 μm with square and radial geometries were successfully assembled using robocasting technique. For this purpose, stable PMN suspensions (55 vol%) were prepared in the presence of polyacrylic acid. An aliquot of hydroxyl propyl methyl cellulose (HPMC) stock solution was added to yield a final cellulose concentration of 5 mg/ml to bring about thickening of the suspension for increasing the solution viscosity and reducing flocculation kinetics. HPMC also served as the binder phase. Gelation was achieved using three different methods. In the first method, coagulated inks were prepared by adding polyethyleneimine. In the second approach the pH of the system was reduced below pH 9 to obtain a strong gel network. In the last method monovalent and divalent salts were introduced to the system and their ability to construct a gel network was evaluated. Rheological measurements were performed to characterize the gelation behavior of concentrated suspensions and to optimize the viscoelastic properties. Results showed that addition of divalent salts such as zinc acetate or magnesium chloride caused gelation by bridging flocculation whereas monovalent salt addition only increased the ionic strength and did not result in increase in suspension viscosity. Oscillatory measurements revealed that addition of PEI at a specific concentration produced a strong gel network. Similarly, the pH modification was used as an alternative method to induce gelation but controlling of the viscoelastic properties with this method was difficult. Therefore, it was concluded that addition of poly (ethylene imine) and the use of multivalent salts are the most suitable methods to induce gelation in stable PMN suspensions in the presence of PAA.

7.2. Suggestions for Future Work

Future work related with this study may include the following items:

Regarding the solubility and surface properties of PMN powders in water, a detailed analysis can be performed to identify the dissolution reactions in the PMN/water system. Surface groups on the PMN surface should be studied as a function of dissolution kinetics. This will lead to a better understanding of the surface properties of PMN in aqueous suspensions.

Dispersion mechanisms of PAA/PEO comb polymers were discussed in detail in this thesis. Their stabilization mechanism was reported as electrosteric similar to the most other type of charged polymers. On the other hand, adsorption studies showed that PAA/PEO comb polymers exhibited low affinity for the PMN surface. Therefore, some kind of a depletion interaction may have been also responsible for the stability of these systems.

Concerning the PMN ink preparation for the robocasting, biphasic colloidal inks should be prepared in the presence of both PAA/PEO comb polymers and the PAA. In the current study, suspensions were stabilized using only PAA. A gel-like structure was achieved through modifications in pH, ionic strength and also by the addition of cationic polyelectrolyte to the system. Since the ionization degree of PAA is very sensitive to the pH changes and salt concentration, gelation was reached by means of PAA alone. On the other hand, stability of PAA/PEO comb polymers is not affected by the pH or ionic strength modifications. Results showed that PAA/PEO comb polymers imparted stability to PMN suspensions over a wide range of pH and ionic strength where the pure PAA fails. Therefore, it is difficult to induce gelation in the presence of PAA/PEO. On the other hand, PMN inks in the presence of PAA showed high moduli and some difficulties were observed in processing on these inks with the tips having diameter less than 30 µm. To solve this problem, biphasic colloidal inks can be prepared in the presence of PAA/PEO comb polymers and the PAA. Figure 7.1 describes the structure of the suspension in the presence of both PAA and PAA/PEO. Introduction to the stable phase to the system may be helpful in extrusion process and may change the ink structure.

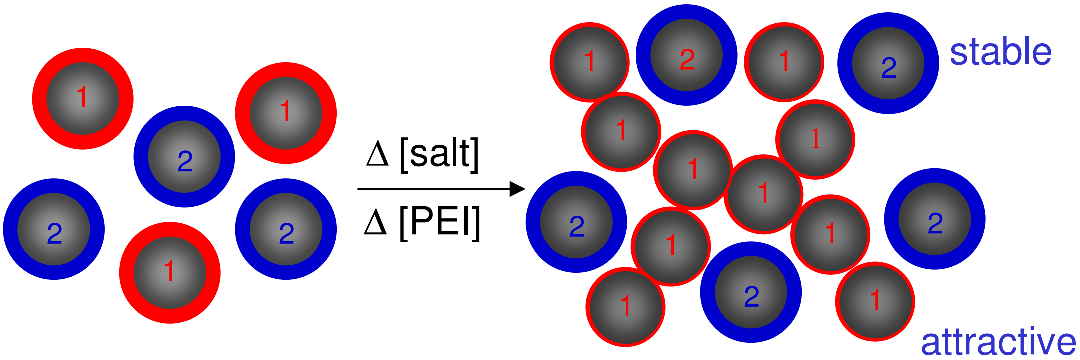

Figure 7.1. Schematic presentation of the gelation mechanism in biphasic PMN inks (1) PAA coated PMN particles (2) PAA/PEO coated PMN particles.

Effect of rare earth metal salts on the gelation behavior of PMN inks and their effect on the final microstructure after sintering should be investigated. Previous studies have demonstrated that some rare earth elements, such as Lanthanium, inhibit the grain growth in PMN ceramics. Therefore, it may be interesting to test the ability of rare earth metal salts to induce gelation in PMN system and their effect on the microstructural evolution during sintering.

In the current study, electrical characterization of the samples produced by robocasting could not been performed. Since the main application area of the radial PMN structures are actuators, strain versus applied electric field data should be obtained to investigate the electrostrictive response of the samples.

REFERENCES

Açıkbaş, N.Ç., Suvacı, E. and Mandal, H. 2006. “Fabrication of Functionally Graded Sialon Ceramics by Tape Casting”, *Journal of the American Ceramic Society*. Vol. 89, No.10, p. 3255-3257.

Adair, J.H., Crampo, J., Mandanas, M.M. and Suvaci, E. 2006. “The Role Material Chemistry in Processing $BaTiO_3$ in Aqueous Suspensions”, *Journal of the American Ceramic Society.* Vol. 89, p. 1853-1860.

Agarval, V., Chahal, P., Tummala, R.R. and Allen, G.M. 1998. “Improvements and Recent Advances in Nanocomposite Capacitors Using a Colloidal Technique”, IEEE, Proceedings of the Electronic Components and Technology Conference, p. 165-170.

Allahverdi, M. and Safari, A. 2004. “Direct Write of PZT Thick Films”, IEEE, Proceedings of the International Ultrasonics, Ferroelectrics, and Frequency Control Joint 50th Anniversary Conference, p.250-253.

Andersson, K. and Bergstrom, L. 2000. “Effect of the Cobalt Ion and Polyethyleneimine Adsorption on the Surface Forces between Tungsten Oxide and Cobalt Oxide in Aqueous Media”, *Journal of the American Ceramic Society*. Vol. 85, No.10, p. 2404-2408.

Babooram, K., Tailor, H. and Ye, Z-G. 2004. “Phase Formation and Dielectric Properties of $0.90Pb(Mg_{1/3}Nb_{2/3})O_3$-$0.10PbTiO_3$ Ceramics Prepared by A New Sol-Gel Method”, *Ceramics International*. Vol. 30, p. 1411-1417.

Bandyopadhyay, A., Panda, R.K., Janas, V.F., Agarwala, M.K., Danforth, S.C., and Safari, A. 1997. “Processing of Piezocomposites by Fused Deposition Technique”, *Journal of the American Ceramic Society.* Vol. 80, No.6, p. 1366-72.

Barnes, H.A., Hutton, J.F. and Walters F.R.S. 1993. *An Introduction to Rheology,* (Elsevier, Netherlands).

Bellaiche, L. 2002. “Piezoelectricity of Ferroelectric Perovskites from First Principles”, *Current Opinion in Solid State and Materials Science.* Vol. 6, p. 19–25.

Beng, Ng W., Wang, J., Choon, Ng S. and Gan, L.M. 1999. ”Processing and Characterization of Microemulsion-Derived Lead Magnesium Niobate”, *Journal of the American Ceramic Society.* Vol. 82, No.3, p. 529.

Bergstrom, L. 1997. “Hamaker Constants of Inorganic Materials”, *Advances in Colloid and Interface Science*. Vol. 70, p. 125-69.

Bhalla, A.S., Guo, R. and Ray, R. 2000. “The Perovskite Structure- A Review of its Role in Ceramic Science and Technology”, *Material Research Innovation.* Vol. 4, p. 3-26.

Bitterlich, B., Lutz, C. and Roosen A. 2002. "Rheological Characterization of Water-Based Slurries for the Tape Casting Process", *Ceramics International.* Vol. 28, p. 675 –683.

Blackman, K.A. 1996. "Processing of Non-Aqueous Tape Cast Ceramic Layers", *MSc. Thesis, University of Illinois at Urbana Champaign.*

Blackwood, G.H. and Ealey, M.A. 1993. "Electrostrictive Behavior in Lead Magnesium Niobate (PMN) actuators Part I: Materials Perspective", *Smart Materials and Structures.* Vol. 2, p. 124-133.

Bouhamed, H., Boufi, S. and Magnin, A. 2005. "Alumina Interaction with AMPS-PEG Random Copolymer II. Stability and Rheological Behavior", *Colloids and Surfaces A: Physicochemical and Engineering Aspects*. Vol. 253, p. 145-153.

Bourikas, K., Kordulis, C., and Lycourghiotis, A. 2005. "Differential Potentiometric Titration: Development of a Methodology for Determining the Point of Zero Charge of Metal (hydr) Oxides by One Titration Curve", *Environmental Science and Technology.* Vol. 1, No.39, p. 4100-8.

Brailenau, A., Ianculescu, A., Zaharescu, M., Pasuk, I., Preda, S., Madarasz, J. and Pokol, G. 2004. "Phase Formation Study of La-modified Lead Magnesium Niobate", *Key Engineering Materials.* Vol. 1309, p. 264-268.

Brennan, R.E., Turcu, S., Hall, A., Hagh, N.M. and Safari A. 2003. "Fabrication of Electroceramic Components by Layered Manufacturing", *Ferroelectrics.* Vol. 293, p. 3-17.

Brown, G.L.and Garrett, B.S. 1959. "Latex Thickening: Interactions Between Aqueous Polymeric Dispersions and Solutions", *Journal of Applied Polymer Science.* Vol. 1, p. 283-295.

Burton, B.P. 2000. "Why $Pb(B_{1/3}B_{2/3}O_3)$ Perovskites Disorder More Easily Than $Ba(B_{1/3}B_{2/3}O_3)$ Perovskites and the Thermodynamics of 1:1-Type Short-Range Order in PMN", *Journal of Physics and Chemistry of Solids.* Vol. 61, p. 327-333.

Buscall, R., Mills, P. and Gates, G. 1986. "Viscoelastic Properties of Strongly Flocculated Polystyrene Latex Dispersions", *Colloids and Surfaces A: Physicochemical and Engineering Aspects.* Vol. 18, p. 341-358.

Calvert, P. 2001. "Ink Jet Printing for Materials and Devices", *Chemistry of Materials.* Vol. 13, p. 3299-3305.

Calvert, P. and Crockett, R. 1997 "Chemical Solid Freeform Fabrication: Making Shapes without Molds", *Chemistry of Materials.* Vol. 9, p. 650-663.

Cesarano III, J. and Aksay, I.A. 1988a. "Processing of Highly Concentrated Aqueous α-Alumina Suspensions Stabilized with Polyelectrolytes", *Journal of the American Ceramic Society.* Vol. 71, No.12, p. 1062-1067.

Cesarano III, J. and Aksay, I.A. 1988b. “Stability of Aqueous α-Alumina Suspensions with Poly(methacrylic acid) Polyelectrolyte”, *Journal of the American Ceramic Society*. Vol. 71, No.4, p. 250-55.

Cesarano III, J., Segalman, R. and Calvert, P. 1998. “Robocasting Provides Moldless Fabrication from Slurry Deposition”, *Ceramic Industry*. Vol. 148, p. 4.

Chartier, T. and Rouxel, T.1997. “Tape Cast Alumina-Zirconia Laminates: Processing and Mechanical Properties”, *Journal of the European Ceramic Society.* Vol. 17, No.2, p. 299-308.

Chartier, T., Hinczewski, C. and Corbel S. 1999. “UV Curable Systems for Tape Casting”, *Journal of the European Ceramic Society*. Vol. 19, No.1, p. 67-74.

Chibowski, S. and Paszkiewicz, M. 2006. “Polyacrylic Acid (Paa) Adsorption onAlumina Surface: Influence of Sodium Dodecyl Sulfide (SDS) on Adsorption in PAA-SDS-Al_2O_3 System”, *Physicochemical Problems of Mineral Processing*. Vol. 40, p. 175-184.

Chiu, R.C. and Cima, M.J. 1993. “Drying of Granular Ceramic Films: II, Drying Stress, Saturation Uniformity”, *Journal of the American Ceramic Society.* Vol. 76, p. 2769-2777.

Chiu, R.C., Garino, T.J. and Cima, M.J. 1993. “Drying of Granular Ceramic Films: I, Effect of Processing Variables on Cracking Behavior”, *Journal of the American Ceramic Society. Vol.* 76, p. 2257-64.

Cho, Y.S., Pilgrim, S.M. and Giesche, H. 2000. “Dielectric and Electromechanical Properties of Chemically Modified PMN-PT-BT Ceramics”, *Journal of the American Ceramic Society.* Vol. 83, p. 2473-80.

Chu, T.-M.G., Halloran, J.W., Hollister, S.J. and Feinberg, S.E. 2001. “Hydroxyapatite Implants with Designed Internal Architecture”, *Journal of Materials Science: Materials in Medicine.* Vol. 12, p. 471-478.

Clendenning, S.B., Aouba, S., Rayat, M.S., Grozea, D., Sorge, J.B., Brodersen, P.M., Rana Sodhi, R.N.S., Lu, Z.H., Yip, C.M., Freeman, M.R., Ruda, H.E. and Manners, I. 2004. “Direct Writing of Pattern Ceramics Using Electron- Beam Lithography and Metallopolymer Resists”, *Advanced Materials*. Vol. 16, No.3, p.215-219.

Cohen, D.L., Malone, E., Lipson, H. and Bonassar L. 2006. “3D Direct Printing of Heterogeneous Tissue Implants”, *Tissue Engineering.* Vol. 12, No.5, p. 1325-1335.

Cohen, R.E. 2000. “Theory of Ferroelectrics: A vision for the Next Decade and Beyond”, *Journal of the Physics and Chemistry of Solids.* Vol. 61, p. 139-146.

Cohen-Stuart, M.A., Cosgrove, T. and Vincent B. 1986. “Experimental Aspects of Polymer Adsorption of Solid/Solution Interfaces”, *Advances in Colloid and Interface Science*. Vol. 24, p. 143-239.

Cohen-Stuart, M.A., Weajen, F.H.L.H., Cosgrove, T., Vincent, B. and Croculey, T. 1984. “The Hydrodynamic Thickness of Adsorbed Polymer Layers”, *Macromolecules*. Vol. 17, p. 1825-1830.

Costa, A.L., Galassi, C., Fabri, G., Roncari, E., Capiani, C. 2001. “Pyrochlore Phase and Microstructure Development in Lead Magnesium Niobate Materials”, *Journal of the European Ceramic Society*. Vol. 21, No.9, p. 1165-1170.

Cui, X., Ouyang, S., Yu, Z., Wang, C. and Huang, Y. 2003. ”A Study on Green Tapes for LOM with Water Based Tape Casting Pprocesses”, *Materials Letters*. Vol. 57, p. 1300-1304.

Das, B.P., Choudhary, R.N.P and Mahapatra, P.K. 2003. “Effect of Europium (Eu) on Structural, Dielectric and Electrical Properties of Pb($STiO_3$) Ferroelectric Ceramics”, *Materials Science and Engineering*. Vol. B104, p. 96-105.

Das, K.K. and Somasundaran, P. 2001. “Ultra Low Dosage Flocculation of Alumina Using Polyacrylic Acid”, *Colloids and Surfaces B: Physicohemical and Engineering Aspects*. Vol. 182, No.1-3, p. 25-33.

Das, S. and Hollister, S. 2002. “Tissue Engineering Scaffolds”, *Encyclopedia of Materials-Science and Technology*. Edited by K.H.J. Buschow, R.W. Cahn, M.C. Flemings, B. Ilschner, E.J. Kramer and S. Mahajan (Elsevier).

Deegan, R.D., Bakajin, O., Dupont, T.F., Huber, G., Nagel, S.R. and Witten, T.A. 1997. “Capillary Flow as the Cause of Ring Strains from Dried Liquid Drops”, *Nature*. Vol. 389, p. 827-829.

Desai, P.R., Jain, N.J., Sharma, R.K., Bahadur, P. 2001. “Effect of additives on the micellization of PEO/PPO/PEO block copolymer F127 in aqueous solution”, *Colloids and Surfaces A: Physicochemical and Engineering Aspects*. Vol. 178, No. 1-3, p.57-69.

Dimos, D., King, B.H. and Yang, P. 1999. “Direct Write Fabrication of Integrated Multilayer Passive Components”, *International Symposium of Advanced Packing Materials*. p. 187-190.

Dobbie, J.W., Robert, E., Gibson, D.V., Smitham, J.B. and Napper, D.H. 1973. “Enhanced Streic Stabilization”, *Journal of Colloid and Interface Science*. Vol. 45, No.3, p.557-565.

Doreau, F., Tari, G., Pagnoux, C., Chartier, T. and Ferreira J.M.F. 1998. “Processing of Aqueous Tape Cating of Alumina with Acrylic Emulsion Binders“, *Journal of the European Ceramic Society*. Vol. 18, No.4, p. 311-318.

Dorey, R.A. and Whatmore, R.W. 2004.”Electroceramic Thick Film Fabrication for MEMS”, *Journal of Electroceramics.* Vol. 12, p. 19-32.

Dupont, L., Foissy, A., Mercier, R. and Mottet, B. 1993. Effect of Calcium Ions on the Adsorption of Polyacrylic Acid onto Alumina”, *Journal of the Colloid and Interface Science.* Vol. 161, p. 455-464.

Dutta, D., Prinz, F.B., Rosen, D. and Weiss, L. 2001. “Layered Manufacturing: Current Status and Future Trends“, *Transactions of the ASME, Journal of Computing and Information Science in Engineering.*. Vol. 1, p.60-71.

Egami, T., Teslic, S., Dmowski, W., Davies, P.K., Chen, H. and Chen, I-W. 1998. “Microscopic Origin of Relaxor Ferroelectricity in PMN”, *Journal of the Korean Physical Society.* Vol. 32, p. 935-938.

Ewais, E., Zaman, A. and Sigmund, W. 2002. “Temperature Induced Forming of Zirconia from Aqueous Slurries: Mechanism and Rheology”, *Journal of the European Ceramic Society.* Vol. 22, No.16, p. 2805-2812.

Fanning, D.M. 2000. “Structure Property Relations in Ferroelectric Materials”, *PhD Thesis, University of Illinois at Urbana Champaign.*

Fengbing, S., Qiang, L., Haisheng, Z., Chunhong, L., Shix, Z. and Dezhong, S. 2004. “Phase Formation and Transitions in the Lead Magnesium Niobate-Lead Titanate System”, *Materials Chemistry and Physics.* Vol. 83, p. 135-139.

Fitzgerald, J.J., Prasad, S., Huang, J. and Shore, J.S. 2000. “Solid-State ^{93}Nb NMR and ^{93}Nb Nutation Studies of Polycrystalline $Pb(Mg_{1/3}Nb_{2/3})O_3$ and (1-x) $Pb(Mg_{1/3}Nb_{2/3})O_3/xPbTiO_3$ Solid-Solution Relaxor Ferroelectrics”, *Journal of the American Chemical Society.* Vol. 122, No.11, p. 2556-2566.

French, H.R. 2000. “Origins and Applications of London Dispersion Forces and Hamaker Constants in Ceramics”, *Journal of the American Ceramic Society.* Vol. 83, No.9, p. 2117-46.

Galassi, C., Roncari, E., Capiani, C. and Pinasco, P. 1997. “PZT Based Suspensions for Tape Casting”, *Journal of the European Ceramic Society.* Vol. 17, p. 367-371.

Gardon, J.L. 1963. “Peel Adhesion I. Some Phenomenological Aspects of the Test”, *Journal of Applied Polymer Science.* Vol. 7, p. 625-641.

Gauckler, L.J, Graule, T. and Baader, F. 1999. “Ceramic Forming Enzyme Catalyzed Reactions”, *Materials Chemistry and Physics.* Vol. 2509, p. 1-25.

Geissler, M. and Xia, Y. 2004. “Patterning: Principles and Some New Developments”, *Advanced Materials.* Vol.16, No 15, p.1249-1269.

Gentil, S., Damjanoviç, D. and Setter, N. 2004. “$Pb(Mg_{1/3}Nb_{2/3})O_3$ and (1-x)$Pb(Mg_{1/3}Nb_{2/3})O_3$-$xPbTiO_3$ Relaxor Ferroelectric Thick Films: Processing and Eelectrical Characterization”, *Journal of Electroceramics.* Vol. 12, p. 151-161.

Goel, T.C. and Tripathi, A.K. 2001. "Ferroelectric Films and Micro Devices", *Journal of Indian Institute of Science*. Vol. 81, p. 637-643.

Gratson, G.M. 2005. "Colloidal and Polyelectrolyte Inks for Direct-Write Assembly of 3D Periodic Structures", *PhD thesis University of Illinois at Urbana Champaign*.

Gratson, G.M. and Lewis, J.A. 2005. "Polyelectrolyte Inks for Direct-Write Assembly of 3D Microperiodic Scaffolds", *Langmuir*. Vol. 21, No.1, p. 457-464.

Gratson, G.M., Garcia-Santamaria, F., Lousse, V., Xu, M., Fan, S., Lewis, J.A. and Braun, P.V. 2006. "Direct Write Assembly of Three Dimensional Photonic Crystals: Conversion of Polymer Scaffolds to Silicon Hollow Woodpile Structures", *Advanced Materials*. Vol. 18, p. 461-465.

Grau, J.E., Uhland, S.A., Moon, J., Cima, M.J. and Sachs, E.M. 1999. "Controlled Craking of Multilayer Ceramic Bodies", *Journal of the American Ceramic Society*. Vol. 82, No.8, p. 2080-86.

Graule, T., Gauckler, L.J. 1993. "Electrophoretic Mobilities of Ceramic Slurries Characterized by Electrokinetic Sonic Amplitude (ESA)", *Ceramica Acta*. Vol. 5, No.3, p. 5-12.

Griffith, M.L.and Halloran, J.W. 1996. "Freeform Fabrication of Ceramics via Stereolithography", *Journal of the American Ceramic Society.* Vol. 79, No.10, p. 2601-2608.

Gu, H. 2003. "Processing of $Pb(Mg_{1/3}Nb_{2/3})O_3$-$PbTiO_3$ by a Novel Coating Approach", *PhD Thesis, Drexel University.*

Guo, D., Cai, K. Huang, Y., Li, L. and Gui, Z. 2003. "Water Based Gel Casting of Lead Zirconate Titanate", *Materials Research Bulletin.* Vol. 38, p. 807-816.

Gutierrez, C.A. and Moreno, R. 2001. "Influence of Slip Preparation and Casting Conditions on Aqueous Tape Casting of Al_2O_3", *Materials Research Bulletin.* Vol. 36, p. 2059–2072.

Hackley, V.A. 1997. "Colloidal Processing of Silicon Nitride with Poly(acrylic acid): Adsorption and Electrostatic Interactions", *Journal of the American Ceramic Society*. Vol. 80, No.9, p. 2315-25.

Heartling, H.G. 1999. "Ferroelectric Ceramics: History and Technology", *Journal of the American Ceramic Society.* Vol. 82, No.4, p. 797-818.

Hesselink, F.T., Vrij, A. and Overbeek, J.T.G. 1971. "On the Theory of Stabilization of Dispersions by Adsorbed Macromolecules: II Interaction between Two Flat Particles", *Journal of Physical Chemistry.* Vol. 75, No: 14, p.2094-2103.

Holmberg, K., Shah, D.O. and Schwuger, M.J. 2002. *Handbook of Applied Surface and Colloid Chemistry*, (John Wiley and Sons) Vol. 2

Hood, A.A. 1996. “Control System Design for Active Vibration Control of a Turning Process Using PMN Actuators”, *MSc Thesis, University of Maryland.*

Hoogeveen, N.G., Stuart, C.A.M. and Fleer, G.J. 1996. “Polyelectrolyte Adsorption onto Oxides: Kinetics and Adsorbed Amount”, *Journal of Colloid and Interface Science*. Vol. 182, p.133-145.

Hotza, D. and Greil, P. 1995. “Review: Aqueous Tape Casting of Ceramic Powders“, *Materials Science and Engineering.* Vol. A202, p. 206-217.

Houbenov, N. 2005. “Adsorption and Grafting of Polyelectrolytes at Solid-Liquid Interfaces”, *PhD Thesis, Technischen Universität.*

Hough, D. and Lee, W. 1980. “The Calculation of the Hamaker Constants from Lifshitz Theory with Applications to Wetting Phenomena”, *Advances in Colloid and Interface Science*. Vol.14, p. 3-41.

Hu, H. and Larson, R.G. 2005. “Analysis of the Microfluid Flow in an Evaporating Sessile Droplet”, *Langmuir*. Vol. 21, p. 3963-3971.

Hu, M., Du, H., Ling, S.F., Zhou, Z. and Li, Y. 2004. “Motion Control of an Electrostrictive Actuator”, *Mechatronics.* Vol. 14, p. 153–161.

Huei, F.J. and Dogan, F. 2000. “Aqueous Processing and Mechanical Properties of PLZT Green Tapes”, *Materials Science and Engineering*. Vol. A 283, p. 56-64.

Hunter, R.J. 1995. *Foundations of Colloid Science*, (Oxford, UK).

Israelachvili, J. 1991. *Intermolecular & Surface Forces*, (Academic Press Limited, San Diego).

Jablonski, E., Learner, T., Hayes, J. and Golden, M. 2004. “Conservation Concerns for Acrylic Emulsion Paints: A literature Review”, *Tate papers.* Vol. 2, p.1-15.

Jadidian, B., Allahverdi, M., Mohammadi, F. and Safari, A. 2002. “Processing and Characterization of Oval Piezoelectric Actuators”, *Applied Physics Letters.* Vol. 80, No.11, p. 1981-1983.

Jantunen, H., Hu, T., Uusimaki, A. and Vuori, S.L. 2004. “Tape Casting of Ferroelectric, Dielectric, Piezoelectric and Ferromagnetic Materials”, *Journal of the European Ceramic Society*. Vol. 24, No.6, p. 1077–1081.

Jing, Y. and Luo, J. 2005. “Structure and Electrical Properties of PMN-PZT Microactuator Deposited by Tape Casting Process”, *Journal of Materials Science: Materials in Electronics.* Vol. 16, p. 287-294.

Jingxian, Z., Dongliang, J., Weisensel, L. and Greil, P. 2004 “Deflocculants for Tape Casting of TiO_2 Slurries”, *Journal of the European Ceramic Society.* Vol.24, No.8, p. 2259-2265.

Joanny, J.F. 1999. "Polyelectrolyte Adsorption and Charge Inversion", *European Physics Journal.* Vol. B9, p. 117-122.

Jordan, T.L. and Qunaies, Z. 2001. "Piezoelectric Ceramic Characterization", ICASE, NASA/CR 211225, Report. No: 28, p.1-22.

Kahn, M., Burks, D.P., Burn, I. and Schulze, W.A. 1988. "Ceramic Capacitor Technology", *Electronic Ceramics, Properties, Devices and Applications,* edited by Levinson (Marcel Dekker Inc., USA).

Kelly, J., Leonard, M., Tantigate, C. and Safari, A. 1997. "Effect of Composition on the Electromechanical Properties of $(1\text{-}x)Pb(Mg_{1/3}Nb_{2/3})O_{3}$- $xPbTiO_3$ Ceramics", *Journal of the American Ceramic Society*. Vol. 80, 4, p. 957-64.

Kiennemann, J., Chartier, T., Pagnoux, C., Baumard, J.F., Huger, M. And Lamerant, J.M. 2005. "Drying Mechanism and Stress Development in Aqueous Alumina Tape Casting", *Journal of the European Ceramic Society.* Vol. 25, No.9, p.1551-1564.

Kim, B-K. and Cha, S-B. 1997. "Synthesis and Cationic Ordering Structure of Samarium-Doped Lead Magnesium Niobate Ceramics", *Materials Research Bulletin.* Vol. 32, p. 743-747.

Kim, S-R. 1994. "Flow and Stability of Nonaqueous Dispersions", *PhD Thesis, Swinburne University of Technology.*

Kingery, W.D., Bowen, H.K. and Ulhmann, D.R. 1976. *Introduction to Ceramics*, (Wiley & Sons, Canada).

Kirby, G.H. 2003. "PAA/PEO Comb Polymer Effects on the Rheological Property Evolution in Concentrated Cement Suspensions", *PhD Thesis University of Illinois at Urbana Champaign.*

Kirby, G.H. and Lewis, J.A. 2004. "Comb Polymer Architecture Effects on the Rheological Property Evolution of Concentrated Cement Suspensions", *Journal of the American Ceramic Society*. Vol. 87, No.9, p. 1643-1652.

Kirby, G.H., Daniel, H., Qi, L. and Lewis, J.A. 2004. "Polyacrylic Acid-Polyethylene Oxide Comb Polymer Effects on $BaTiO_3$ Nanoparticle Suspension Stability", *Journal of the American Ceramic Society*, Vol. 87, No.2, p. 181-186.

Kircher, O. and Bohmer, R. 2002. "Aging, Rejuvenation, and memory Phenomena in a Lead-Based Relaxor Ferroelectric", *European Physical Journal.* Vol. B 26, p. 329-338.

Kishi, H., Mizuno, Y. and Chazono, H. 2003. "Metal Electrode-Multilayer Ceramic Capacitors : Past, Present and Future Perspectives", *Japanese Journal of Applied Physics*. Vol. 42, p. 1-15.

Kobune, M., Yamakawa, K., Yamashiki, T. and Akamatsu, T. 2004. "Effects of Depressor Addition on the Electrical Properties of $Pb(Mg_{1/3}Nb_{2/3})O_{3}$- $PbTiO_3$ Dielectric Ceramics", *Journal of the European Ceramic Society*. Vol. 24, No.6, p. 1485-1488.

Kofod, G. 2001. "Dielectric Elastomer Actuator", *PhD Thesis, Technical University of Denmark.*

Kosmulski, M. 1993. "Standard Enthalpies of Ion Adsorption onto Oxides from Aqueous Solutions and Mixed Solvents", *Colloids and Surfaces A: Physicochemical and Engineering Aspects*. Vol. 83, p. 237-243.

Kosmulski, M. 1997. "Attempt to Determine Pristine Points of Zero Charge of Nb_2O_5, Ta_2O_5, and HfO_2", *Langmuir*. Vol. 13, No.23, p. 6315-6320.

Kiratzis, N.E. and Luckham, P.F. 1999. "The Rheology of Aqueous Alumina Suspensions in the Presence of Hydoxycellusose as Binder", *Journal of the European Ceramic Society*. Vol. 19, No.15, p. 2605-2612.

Kristofferson, A., Roncari, E. and Galassi, C. 1998. "Comparison of Different Binders for Water Based Tape Casting of Alumina", *Journal of the European Ceramic Society*. Vol. 18, No.14, p. 2123-2131.

Kristoffersson, A. and Carlström, E. 1997. "Tape Casting of Alumina in Water with an Acrylic Latex Binder", *Journal of the European Ceramic Society*. Vol. 17, No.2, p. 289-297.

Krsmanovic, J.L. 2003. "Adsorption of Novel Block Copolymers for Steric Stabilization and Flocculation of Colloidal Particles in Aqueous Environments", *PhD Thesis, State University of the Virginia Polytechnic Institute.*

Kumar, P., Santosa, J.K., Beck, E. and Das, S. 2004. "Direct-Write Deposition of Fine Powders Through Miniature Hopper-Nozzles For Multi-Material Solid Freeform Fabrication", *Rapid Prototyping Journal*, Vol. 10, No.1, p.14-23.

Kwon, S. and Messing, G.L. 1997. "The Effect of Particle Solubility on the Strength of Nanocrystalline Agglomerates: Boehmite", *Nanostructured Materials*, Vol. 8, No.4, p. 399-418.

Kwon, S., Sabolsky, E.M. and Messing, G.L. 2001. "Low Temperature Reactive Sintering of 0.65PMN-0.35PT ", *Journal of the American Ceramic Society*. Vol. 84, No.3, p.648.

Lane, R. and Craig, B. 2000. "An introduction to Smart Materials", *Advanced Materials, Manufacturing and Testing Information Analysis Center*, *The AMPTIAC Quarterly*. Vol. 7, No 2, p. 9-13.

Lange, F.F. 2001. "Shape Forming of Ceramic Powders by Manipulating the Interparticle Pair Potential", *Chemical Engineering Science*. Vol. 56, p. 3011-3020.

Larson, G.R. 1999. *The Structure and Rheology of Complex Fluids*, (Oxford University Press).

Lau, S.T., Lam, K.H., Chan, H.L.W., Choy, C.L., Luo, H.S., Yin, Q.R. and Yin, A.W. 2005. "Piezoelectric PMN-PT Fibre Hydrophone Forultrasonic Transducer Calibration", *Journal of Applied Physics*. Vol. A 80, p. 105-110.

Lewis, J.A. 2000. "Colloidal Processing of Ceramics", *Journal of the American Ceramic Society*. Vol. 83, No.10, p. 2341-59.

Lewis, J.A. 2002. "Direct-Write Assembly of Ceramics from Colloidal Inks", *Current Opinion in Solid State and Materials Science*. Vol. 6, p. 245-250.

Lewis, J.A. 2006 "Direct Ink Writing of 3D Functional Materials", *Advanced Functional Materials*. Vol. 16, p. 2193-2204.

Lewis, J.A. and Gratson, G.M. 2004. "Direct Writing in Three Dimensions", *Materials Today*. Vol. July/August, p. 32-39.

Lewis, J.A., Kirby, G., Cheung, J.Ho-Wah and Jeknavorian, A.A. 2006a. "Controlled Dispersion of Colloidal Suspension by Comb Polymers", *US Patent*. No 7053125.

Lewis, J.A., Smay, J.E., Stuecker, J. and Cesarano III, J. 2006b. "Direct Ink Writing of Three Dimensional Ceramic Structures", *Journal of the American Ceramic Society*. Vol. 89, No.12, p. 3599-3609.

Li, C.C. and Jean, J.H. 2002. "Dissolution and Dispersion Behavior of Barium Carbonate in Aqueous Solutions", *Journal of the American Ceramic Society.* Vol. 85, No.12, p. 2977-2983.

Li, Q. 2005. "Nanoparticle Inks for Direct Write Assembly of 3D Periodic Structures", *MSc Thesis, University of Illinois at Urbana-Champaign.*

Li, Q. and Lewis, J.A. 2003. "Nanoparticle Inks for Directed Assembly of Three Dimensional Periodic Structures", *Advanced Materials*. Vol. 15, No: 19, p.1639-43.

Lopez, B.M.C., Rand, B. and Riley, F.L. 1997 "The Properties of Aqueous Phase Suspensions of Barium Titanate", *Journal of the European Ceramic Society*. Vol. 17, p. 281-287.

Lopez, B.M.C., Rand, B. and Riley, F.L. 2000. "The Isoelectric Point of $BaTiO_3$", *Journal of the European Ceramic Society*. Vol. 20, No.2, p. 108-118.

Lucas, P. and Petuskey, W. 2001. "Phase Equilibria Lead-Magnesium-Niobium-Oxygen System at 1000°C", *Journal of the American Ceramic Society.* Vol. 84, No.9, p. 2150-52.

Luo, H. 2005. "Colloidal Processing of PMN-PT Thick Films for Piezoelectric Sensor Applications", *PhD Thesis, Drexel University.*

Ma, J., Zhang, R., Liang, C.H. and Weng, L. 2003. “Colloidal Characterization and Electrophoretic Deposition of PZT“, *Materials Letter.* Vol. 57, p. 4648-4654.

Macosko, C.W. 1994. *Rheology, Principles, Measurements and Applications*, (Wiley-VCH).

Martinez, C.J. 2002. “Structure and Property Evolution during Film Formation from Binary Colloidal Suspensions”, *PhD Thesis, University of Illinois at Urbana Champaign.*

Martinez, C.J. and Lewis, J. 2002. “Rheological Structural and Stress Evolution of Aqueous Al_2O_3: Latex Tape Cast Layers”, *Journal of the American Ceramic Society*. Vol. 85, No.10, p. 2409-16.

Mathan, N., Husson, E., Gaucher, P. and Morell, A. 1990. “Modification of the B-site Order of PMN Ceramics by Thermal Annealing or La-Doping”, *Materials Research Bulletin*, Vol. 25, p. 427-434.

Mathur, S. and Moudgil, B.M. 1997. “Adsorption Mechanism(s) of Poly (Ethylene Oxide) on Oxide Surfaces”, *Journal of Colloid and Interface Science.* Vol. 196, p. 92-98.

Mchenry, D.A. 1992. “Optical and Eelectroptical Properties of Lead Magnesium Niobate-Lead Titanate”, *Dissertation Abstracts International.* Vol 53-05, Section B, p.2492 .

Meier, P.L., Urech L. and Gauckler, L.J. 2004. “Tape Casting of Nanocrystallize Ceria Gadolinia Powder”, *Journal of the European Ceramic Society*. Vol. 24, No.15, p. 3753-3758.

Mistler, R.E. 1998. “Tape Casting: Past, Present, Potential”, *American Ceramic Society Bulletin*.Vol.77, No.10, p. 82-86.

Mistler, R.E., Shenefield, D.J. and Runk, R.B. 1978. “Tape Casting Ceramics”, Ceramic Processing before Firing, edited by G.Y. Onada and L.L. Hench (John Wiley, printed in USA), p.411-448.

Mohan, D., Prasad, R. and Banerjee, S. 2001. “Dielectric Properties of Lead Magnesium Niobate and Lead Iron Niobate Prepared by the Semiwet Hydroxide Route”, *Journal of the American Ceramic Society.* Vol. 84, No.9, p. 2126-2128.

Morissette, S.L. 1999. “Compositional Effects on the Chemorheological Properties and Forming Behaviour of Aqueous Alumina-Poly Vinly Alcohol Gel Casting Suspensions”, *PhD Thesis, University of Illinois at Urbana Champaign.*

Morissette, S.L. and Lewis, J.A. 2001. “Direct Write Fabrication of $Pb(Nb,Zr,Ti)O_3$ Devices: Influence of Paste Rheology on Print Morphology and Component Properties”, *Journal of the American Ceramic Society*, Vol. 84, No.11, p. 2462-68.

Morissette, S.L., Cesarano III, J., Lewis, J.A. and Dimos, D.B. 2002. “Solid Freeform Fabrication Using Chemically Suspensions”, *US Patent.* No: 6454972.

Mott, M. and Evans, J.R.G. 1999. “Zirconia/Alumina Functionally Graded Material Made by Ceramic Ink Jet Printing”, *Materials Science and Engineering*, Vol. A271, p. 344-352.

Moulson, J.A. and Herbert, J.M. 1990. *Electroceramics Materials Properties and Applications,* (Chapman & Hall).

Myers, D. 1999. *Surfaces, Interfaces and Colloids Principles and Applications. (John Wiley and Sons)*

Nadkarni, S.S. and Smay, J.E. 2006. “Concentrated Barium Titanate Colloidal Gels Prepared by Bridging Flocculation for Use in Solid Freeform Fabrication”, *Journal of the American Ceramic Society*. Vol. 89, No.1, p. 96-103.

Nahass, P., Pober, R.L., Rhine, W.E., Robbins, W.L. and Bowen, H.K. 1992. “Prediction and Explanation of Aging Shrinkage in Tape Cast Ceramic Green Sheets”, *Journal of the American Ceramic Society.* Vol. 75, No.9, p. 2372-2378.

Napper, D.H. 1977. “Steric Stabilization”, *Journal of Colloid and Interface Science.*Vol. 58, No.2, p.390-407.

Navarro, A., Alcock, J.R. and Whatmore, R.W.2004. “Aqueous Colloidal Processing and Green Sheet Properties of Lead Zirconate Titanate (PZT) Ceramic Made by Tape Casting”, *Journal of the European Ceramic Society*, Vol. 24, No.6, p. 1073-1076.

Nesbitt, W.H., Bancroft, M.G., Fyfe, S.W., Karkhanis, H.S. and Nishijima, A. 1981. “Thermodynamic Stability and Kinetics of Perovskite Dissolution”, *Nature*. Vol. 289, No.29, p. 358-362.

Netz, R.R. and Andelman, D. 2003. “Neutral and Charged Polymers at Interfaces”, *Physics Reports*. Vol. 380, p. 1-95.

Neubrand, A., Lindner, R. and Hoffmann, P. 2000. “Room Temperature Solubility Behavior of Barium Titanate in Aqueous Media“, *Journal of the American Ceramic Society*. Vol. 83, No.4, p. 860-64.

Newnham, E.R. and Amin, A. 1999. “Smart Sytems: Microphones, Fish Farming and Beyond”, *Chemical Innovation*. Vol. 29, No.12, p. 38-46.

Newnham, E.R. and Ruschau, G.R. 1991. “Smart Electroceramics”, *Journal of the American Ceramic Society.* Vol.74, No.3, p.463.

Ogden, A.L. 1996. “The Influence of Nonadsorbed Polymer on the Behavior of Weakly Flocculated Suspensions”, *PhD Thesis, University of Illinois at Urbana Champaign*.

Ogitani, S., Bidstrup-Allen, S. and Kohl, P. 1998. “Development of High-K Photo-Definable Epoxy Composites for Embedded Capacitors” IEEE.,lCPMT Proceedings of International Electronics Manufacturing Technology Symposium, p.199-205.

Orth, J., Meier, M.H., Bellmann, C. and Wegner, G. 1997. "Stabilization of Aqueous Alpha Alumina Suspensions with Block Copolymers", *Acta Polymerica*. Vol. 48, p. 490-501.

Overbeek, T.J.H. 1977. "Recent Developments in Understanding of Colloid Stability", *Journal of Colloid and Interface Science*. Vol. 58, No.2, p.408-422.

Pagnoux, C., Chartier, T., Granja, F., Doreau, F., Ferreira, J.M.and Baumard, J.F. 1998. "Aqueous Suspensions for Tape Casting Based on Acrylic Binders", *Journal of the European Ceramic Society*. Vol. 18, No.3, p. 241-247.

Paik, U. and Hackley, A.V. 2000. "Influence of Solids Concentration on the Isoelectric Point of Aqueous Barium Titanate", *Journal of the American Ceramic Society*. Vol. 83, No.10, p. 2381-2384.

Paik, U., Hackley, A.V., Lee, J.and Lee, S. 2003. "Effect of Poly(acrylic acid) and Poly(vinyl alcohol) on the Solubility of Colloidal $BaTiO_3$ in an Aqueous Medium", *Journal of Materials Research*. Vol 8, No.5, p.1266-1274.

Paik, U., Lee, S. and Hackley, A.V. 2003. "Influence of Barium Dissolution on the Electrokinetic Properties of Colloidal $BaTiO_3$ in an Aqueous Medium", *Journal of the American Ceramic Society*. Vol. 86, No.10, p. 1662-68.

Paik, U., Yeo, J.G., Lee, M.H., Hackley, A.V. and Jung, Y.G. 2002. "Dissolution and Precipitation of Barium at the Particulate $BaTiO_3$-Aqueous Solution Interface", *Materials Research Bulletin* Vol. 37, p.1623-1631.

Palmqvist, M.L., Lange, F.F., Sigmund, W. and Sindel, J. 2000. "Dispersion and Consolidation of Alumina Using a Bis-Hydrophilic Diblock Copolymer", *Journal of the American Ceramic Society*, Vol. 83, No.7, p. 1585-91.

Pan, Z., Campbell, A. and Somasundaran, P. 2001. "Polyecrylic Acid Adsorption and Conformation in Concentrated Alumina Suspensions", *Colloids and Surfaces, A: Physicochemical and Engineering Aspects.* Vol. 191, No.1-2, p. 71-78.

Pashley, R.M. and Karaman, M.E. 2004. *Applied Surface and Colloid Chemistry* (Wiley and Sons, printed in U.K.).

Pedersen-Guldberg, H. and Bergstrom, L. 2000. "Stabilizing Ceramic Suspension Using Anionic Polyelectrolyte: Adsorption Kinetics and Interparticle Forces", *Acta Materialia.* Vol. 48, p. 4563-4570.

Pithan, C., Hennings, D. and Waser, R. 2005. "Progress in the Synthesis of Nanocrystalline $BaTiO_3$ Powders for MLCC", *International Journal of Applied Ceramic Technology.* Vol. 2, p. 1-14.

Polat, M. and Polat H. 2000. "A Review of the Theory of Interactions between Particles Dispersed in Aqueous Media, II. Vander Waals Interactions", *Ore Dressing*. Vol. 3, p. 21-48.

Prasad, S.E., Ahmed A. and Wheat, T.A. 1998. “The Role of Smart Materials and Structure in Robotics”, *Smart Materials and Structures.* p. 133-147.

Rahaman, M.N. 1995. *Ceramic Processing and Sintering*, (Marcel Dekker Inc., USA).

Rak, Z.S. 2000. “Advanced Forming Techniques in Ceramics”, Proceedings of the Polish Ceramics Conference, Spala. (www.ecn.nl/docs/library/report/2000).

Rao, R.B., Krafcik, K.L., Morales, A.M. and Lewis J.A. 2005. “Microfabricated Deposition Nozzles for Direct-Write Assembly of Three Dimensional Periodic Structures”, *Advanced Materials.* Vol. 17, No.3, p.289-293.

Ravez, J. 2000. “Ferroelectricity in Solid State Chemistry”, *Solid State Chemistry and Crystal Chemistry.* Vol. 3, p. 267-283.

Reed, J.S. 1995. *Principles of Ceramic Processing*, Chapter 26, Tape Casting, (Wiley, USA.).

Rezvan, K. 2005. “ProteinTreated Aqueous Colloidal Oxide Particle Suspensions: Driving Forces for Protein Adsorption and Conformational Changes”, *PhD Thesis, Swiss Federal Institute of Technology.*

Riedl, Z., Szklenarik, G., Zelko, R., Marton, S. And Racz, I. 2000. “The Effect of Temperature and Polymer Concentration on Dynamic Surface Tension and Wetting Ability of Hydroxypropylmethylcellulose Solutions”, *Drug Development and Industrial Pharmacy.* Vol. 26, No.12, p. 1321-1323.

Rueb, C.J. and Zukoski, C.F. 1997. “Viscoelastic Properties of Colloidal Gels”, *Journal of Rheology.* Vol. 41, No.2, p. 197-218.

Sabate, R., Gallardo, M. and Estelrich, J. 2000. “Electrophoretic Properties of Dodecyltrimethyl Ammonium Bromide Micelles in KBr Solution” *Electrophoresis.* Vol. 21, p. 481-485.

Sadar, M.J. 1998. *Turbidity Science*, (Technical Information Series Booklet, Hach Company, USA), No 11, p.1-18.

Safari, A., Allahverdi, M. and Akdogan, E.K. 2006. “Solid Freeform Fabrication of Piezoelectric Sensors and Actuators”, *Journal of Materials Science.* Vol. 41, p. 177-198.

Safari, A., Cesarano, J., Clem, P.G. and Bender, B. 2002. “Fabrication of Advanced Functional Electroceramics Components by Layered Manufacturing (LM) Methods”, Proceedings of the 13th IEEE International Symposium on Applications of Ferroelectrics, Japan, p. 1-6.

Safari, A., Panda, R. and Janas, V. 1996. “Ferroelectric Ceramics: Processing, Properties and Applications”, *Advanced Ceramic Materials: Key Engineering Materials.* Vol.122-124, p. 35-71.

Şakar-Deliormanlı, A., Çelik, E. and Polat, M. “Phase Formation and Microstructure of Nd^{+3} Doped $Pb(Mg_{1/3}N_{2/3})O_3$ Prepared by Sol-Gel Method”, *Journal of Materials Science: Materials in Electronics*. In press.

Sato, T. and Ruch, R. 1980. “Stabilization of Colloidal Dispersions by Polymer Adsorption”, *Surfactant Science Series,* (Marcel Dekker, USA), Vol. 9.

Scherer, G.W. 1988. “Aging and Drying of Gels”, *Journal of Non-Crystalline Solids*. Vol. 100, p. 77-92.

Scherer, G.W. 1990. “Theory of Drying”, *Journal of the American Ceramic Society.* Vol. 73, No.1, p. 3-14.

Schwartz, R.W. 1997. “Chemical Solution Deposition of Perovskite Thin Films”, *Chemistry of Materials.* Vol. 9, No.11, p. 2325-2340.

Seal, A., Chattopadhyay, D., Sharma, D.A., Sen, A. and Maiti H.S. 2004. ”Influence of Ambient TempErature on the Rheological Properties of Alumina Tape Casting Slurry”, *Journal of the European Ceramic Society.* Vol. 24, No.8, p. 2275-2283.

Seerden, K.A.M., Reis, N., Evans, J.R.G., Grant, P.S., Halloran, J.W. and Derby, B. 2001. “Ink Jet Printing of Wax-Based Alumina Suspensions”, *Journal of the American Ceramic Society*. Vol. 84, No.11, p. 2514-20.

Shankar, N. and Hom, C.L. 2000 “An Acoustic/Thermal Model for Self-Heating in PMN Sonar Projectors”, *Journal of Acoustic Society of America.* Vol. 108, p. 2151-2158.

Shaw, D.J. 2003. *Introduction to Colloid and Surface Chemistry* (Butterworth-Heinemann, Elsevier science, printed in Great Britain)

Shih, W.Y., Shih, W.H. and Aksay A.I. 1999. “Elastic and Yield Behavior of Strongly Flocculated Colloids”, *Journal of the American Ceramic Society.* Vol. 82, No.3, p. 616-624.

Shqau, K. 2004. “Electrosteric Dispersant Used in the Colloidal Processing of Ceramics”, *Report, Ohio State University,* 04043/CISM/KSh. p. 1-17.

Sindel, J., Bell, N.S. and Sigmund, W.M. 1999. “Electrolyte Effects on Nonionic Steric Layers: Bis-Hydrophilic PMAA-PEO Diblock Copolymers, Adsorbed on Barium Titanate”, *Journal of the American Ceramic Society.* Vol. 82, No.11, p. 2953-2957.

Slilaty, R.M. 1995. “The Effects of Suspension Stability and Rheology on the MicroStructure of As-Cast Alumina-Poly (vinyl butyral) Tapes”, *MSc thesis, University of Illinois at Urbana Champaign.*

Smay, J.E. 2002. “Directed Colloidal Assembly and Characterization of PZT Polymer Composites”, *PhD thesis, University of Illinois at Urbana Champaign.*

Smay, J.E. and Lewis, J.A. 2001. “Structural and Property Evolution of Aqueous Based Lead Zirconate Titanate Tape Cast Layers”, *Journal of the American Ceramic Society*. Vol. 84, No.11, p. 2495-500.

Smay, J.E., Cesarano III, J. and Lewis, J.A. 2002a. “Colloidal Inks for Directed Assembly of 3-D Periodic Structures”, *Langmuir*. Vol. 18, No.14, p. 5429-5437.

Smay, J.E., Gratson, G.M., Shepherd, R.F., Cesarano III, J. and Lewis, J.A. 2002b. “Directed Colloidal Assembly of 3D Periodic Structures”, *Advanced Materials*. Vol. 14, No.18, p.1279-83.

Song, J.K., Um, W-S., Lee, H-S., Chung, K-W. and Park, J-H. 2000. “Effect of Polymer Moleculer Weight Variations on PZT Slip for Tape Casting“, *Journal of the European Ceramic Society*. Vol. 20, No.6, p. 685-688.

Steeg, G.M.H. van de, Cohen-Stuart, A.M., Keizer, A. and Bijsterbosch, B.H. 1992. “Polyelectrolyte Adsorption: A Subtle Balance of Forces”, *Langmuir.* Vol. 8, p. 2538-2546.

Stumm, W. 1992. *Chemistry of the Solid-Water Interface Processes at the Mineral-Water and Particle-Water Interface in Natural Systems, (*John Wiley and Sons Inc, printed in USA).

Su, B., Pearce, D.H. and Button, T.W. 2001. “Routes to Net Shape Electroceramic Devices and Thick Films”, *Journal of the European Ceramic Society.* Vol. 21, No.10, p. 2005–2009.

Su, B.1997. “Novel Fabrication Processing For Improved Lead Zirconate Titanate (PZT) Ferroelectric Ceramic Materials” *PhD thesis, Faculty of Engineering, University of Birmingham (UK).*

Sun, J., Bergstrom, L. and Gao, L. 2001. “Effect of Magnesium Ions on the Adsorption of Polyacrylic acid onto Alumina”, *Journal of the American Ceramic Society*. Vol. 84, No.11, p. 2710-12.

Swartz, S.L. 1990. “Review: Topics in Electronic Ceramics”, *IEEE Transactions on Electrical Insulation.* Vol. 25, No. 5, p.935-980.

Tadros, T.F. 1986. “Control of the Properties of Suspensions”, *Colloid and Surfaces*. Vol. 18, p. 137-173.

Teng, K.F., Azadpour, M.A. and Yang, H.Y. 1988. “Rapid Prototyping of Multichip Packages Using Computer Controlled Ink-Jet Direct Write”, IEEE Proceedings of the 38th Electronics Components Conference, p.326-329.

Terrones, G., Smith, P.A., Armstrong, T.R. and Soltesz, T.J. 1997. “Applications of the Carreau Model to Tape-Casting Fluid Mechanics”, *Journal of the American Ceramic Society.* Vol. 80, 12, p. 3151-56.

Therriault, D., Shepherd, R.E., White, S.R. and Lewis, J.A. 2005. “Fugitive Inks for Direct Write Assembly of Three Dimensional Microvascular Networks”, *Advanced Materials.* Vol. 17, No.4, p.395-399.

Tian, T., Jiang, D., Zhang, J. and Lin, Q. 2007. “Aqueous Tape Casting Process for Hydroxyapatite”, *Journal of the European Ceramic Society.* Vol. 27, No.7, p. 2671–2677.

Tsang, W.S., Chan, K.Y., Mark, C.L. and Wong, K.H. 2003. “Spectroscopic Ellipsometry Study of Epitaxially Grown $Pb(Mg_{1/3}Nb_{2/3})O_3$-$PbTiO_3$/MgO/TiN/Si Heterostructures”, *Applied Physics Letters.* Vol. 83, No.8, p.1599-1601.

Tzou, H.S., Lee, H.J. and Arnold, S.M. 2004. “Smart Materials, Precision Sensors/Actuators, Smart Structures, and Structronic Systems”, *Mechanics of Advanced Materials and Structures*. Vol. 11, p. 367-393.

Uchino, K. 1986. “Piezoelectric and Electrostrictive Actuators”, IEEE Proceedings of the 6th International Symposium on Applications of Ferroelectrics, p. 610-618

Ushifusa, N. and Cima, M.J. 1991. “Aqueous Processing of Mullite-Containing Green Sheets”, *Journal of the American Ceramic Society.* Vol. 74, No.10, p. 2443-47.

Vasanthakumari, K.G., Denny, A.P., Sasidharan, K., Unnikrishnan, G. and Raghu, N. 2005. “Pizoelectric and Electrostrictive Multilayer Actuators”, Proceedings of ISSN, International Conference on Smart Structures and Systems, p. 129-136.

Vermohlen, K., Lewandowski, H., Narres, H.D. and Schwuger, M.J. 2000. “Adsorption of Polyelectrolytes onto Oxides-the Influence of Ionic Strength, Molar Mass and Ca^{+2} Ions”, *Colloids and Surfaces A: Physicochemical and Engineering Aspects*. Vol. 163, No.1, p. 45-53.

Vikhnin, V.S., Blinc, R. and Pirc, R. 2003. “Mechanisms of Electrostriction and Giant Piezoelectric Effect in Relaxor Ferroelectrics”, *Journal of Applied Physics.* Vol. 93, p. 9947-9952.

Vincent, B. 1974. “The Effect of Adsorbed Polymers on Dispersion Stability”, *Advances in Colloid and Interface Science*. Vol. 4, p. 193-277.

Vincent, B., Edwards, J., Emmett, S. and Jones, A. 1986. “Depletion Flocculation in Dispersions of Sterically Stabilized Particles”, *Colloids and Surfaces.* Vol. 18, p. 261-81.

Vincent, B., Luckham, P.F. and Waite, F.A. 1980. “The Effect of Free Polymer on the Stability of Sterically-Stabilized Dispersions”, *Journal of Colloid Interface Science.* Vol.73, p.508.

Wan, X., Xu, H., He, T., Lin D., and Luo, H. 2003. “Optical Properties of Tetragonal $Pb(Mg_{1/3}Nb_{2/3})O_{0.62}Ti_{0.38}O_3$ Single Crystals”, *Journal of Applied Physics*. Vol. 93, No.8, p. 4766-4768.

Wang, G., Sarkar, P. and Nicholson, S.P. 1999. "Surface Chemistry and Rheology of Electrostatically (Ionically) Stabilized Alumina Suspensions in Polar Organic Media", *Journal of the American Ceramic Society*. Vol. 82, No.4, p. 849-56.

Wang, X.Y., Lu, S.W., Lee, B.I. and Mann, L. 2000. "Dispersion and Aging behavior of $BaTiO_3$ and PZT in Water", *Materials Research Bulletin*. Vol. 35, p. 2555-2563.

WEB_1, 2007. Ecertec Ltd.`s web site, 2007. http://www.ecertec.com

WEB_2, 2007. Morganelectroceramics web site, 2007. http://www.morganelectroceramics.com/pzbook.html#pdf1

WEB_3, 2007. Malvern web site, 2007. http://www.malvern.com

WEB_4, 2007.Shimadzu web site, 2007. http://www.shimadzu.com

WEB_5, 2007.Novo Control web site, 2007. http://www.novocontrol.de/html/index analyzer.htm

WEB_6, 2007. Desautels-Lee R., Theory of van der Waals Forces as Applied to Particulate Materials, 2007. http://www.erpt.org/051Q/Leed-00.htm

Whitby, C.P., Scales, P.J., Grieser, F., Healy, T.W., Kirby, G., Lewis, A.J. and Zukoski, C.F. 2003. "PAA/PEO Comb Polymer Effects on Rheological Properties and Interparticle Forces in Aqueous Silica Suspensions", *Journal of Colloid and Interface Science*. Vol. 262, p. 274-281.

White, L.R. 1992. "Capillary Rise in Powders", *Journal of Colloid and Interface Science*. Vol. 90, p. 536-538.

Windlass, H., Markondeya, P.J. and Balamaran, D. 2001. "Colloidal Processing of Polymer Ceramic Nanocomposites for Integral Capacitors" International Symposium on Advanced Packaging Materials Proceedings, p. 393-398.

Windlass, H., Raj, P.M., Balaraman, D., Bhattacharya, S.K. and Tummala, R.R. 2003. "Polymer-Ceramic Nanocomposite Capacitors for System-On-Package (SOP) Applications", *IEEE Transactions on Advanced Packaging*. Vol. 26, No.1, p.10-16.

Wu, B.M., Borland, S.W., Giordano, R.A., Cima, L.G., Sachs, E.M. and Cima, M.J. 1996. "Solid Free-Form Fabrication of Drug Delivery Devices", *Journal of Controlled Release*. Vol. 40, No: 1, p. 77-87.

Wu, L. and Lion, Y-C. 1995. "The Effect of Heating Rate on the Properties of PMN Relaxor Ceramics", *Ceramics International*. Vol. 21, p. 335-338.

Xiaogang, L., Lei, F., Seunghun, H., Dravid, V.P. and Mirkin, C.A. 2002. "Arrays of Magnetic Nanoparticles Patterned via Dip Pen Nanolithography", *Advanced Materials*. Vol. 14, No: 3, p.231-234.

Yamada, K., Takahashi, T., Hanehara, S. and Matsuhisa, M. 2000. “Effects of Chemical Structure on the Properties of Polycarboxylate-type Superplasticizers”, *Cement and Concrete Research*, Vol. 30, p. 197-207.

Yan, Y., Pennycook, S.J., Xu, Z. and Viehland, D. 1998. “Determination of the Ordered Structures of $Pb(Mg_{1/3}Nb_{2/3})O_3$ and $Ba(Mg_{1/3}Nb_{2/3})O_3$ by Atomic Resolution Z-Contrast Imaging”, *Applied Physics Letters.* Vol. 72, p. 3145-3147.

Yanez, J., Shikata, T., Lange, F., Pearson, D.S. 1996. “Shear Modulus and Yield Stress Measurements of Attractive Alumina Particle Networks in Aqueous Slurries”, *Journal of the American Ceramic Society,* Vol. 79, No.11, p. 2917-2924.

Yoo, J., Cima, M., Scahs, E., Suresh, S. 1995. “Fabrication and Microstructural Control of Advanced Ceramic Components by Three Dimensional Printing”, *Ceramic Engineering and Science Proceedings.* Vol. 16, p. 755-762.

Yoon, H.-D. and Lee, B.I. 2004. “Processing of Barium Titanate Tapes with Different Binders for MLCC Applications –Part II: Comparison of the Properties”, *Journal of the European Ceramic Society.* Vol. 24, No.5, p.753-761.

Yoshioka, K., Sakai, E., Daimon, M. and Kitahara, A. 1997. “Role of Steric Hindrance in the Performance of Superplasticizers for Concrete”, *Journal of the American Ceramic Society.* Vol. 80, No.10, p. 2667-71.

Yuping, Z., Dongliang, J. and Greil, P. 2000. “Tape Casting of Aqueous Al_2O_3 Slurries”, *Journal of the European Ceramic Society.* Vol. 20, No.11, p. 1691-1697.

Zeng, Y-P., Zimmermann, A., Zhan, L. And Aldinger, F. 2004. “Tape Casting of PLZST Tapes Via Aqueous Slurries“, *Journal of the European Ceramic Society.* Vol. 24, No.2, p. 253-258.

Zhang, Y. and Binner, J. 2002. “Tape Casting Aqueous Alumina Suspensions Containing A Latex Binder”, *Journal of Materials Science.* Vol. 37, p. 1831-1837.

Zhong, N., Xiang, P-H., Sun, D-Z and Dong, X-L. 2005. “Effect of Rare Earth Additives on the Microstructure and Dielectric Properties of $0.67Pb(Mg_{1/3}Nb_{2/3})O_3$-$0.33PbTiO_3$ Ceramics”, *Materials Science and Engineering B.* Vol. 116, p. 140-145.

Zhou, X.Y., Wei, X.J., Fedkin, M.V., Strass, K.H. and Lvov, S.N. 2003. “Zetameter for Microelectrophoresis Studies of the Oxide/Water Interface at Temperatures up to 200 °C”, *Review of Scientific Instruments.* Vol. 74, No. 4, p. 2501-2506.

Zosel, A. 1993. “Studies of the Wetting Kinetics of liquid Drops on Solid Surfaces”, *Colloid and Polymer Science.* Vol. 271, p. 680-687.

Zupancic, A., Lpasin, R., and Kristoffersson, A. 1998. “Influence of Particle Concentration on Rheological Properties of Aqueous α-Alumina Suspensions”, *Journal of the European Ceramic Society.* Vol. 18, No.5, p. 467-477.

APPENDIX A

DETERMINATION OF HAMAKER FUNCTION

In literature there are different methods to determine the Hamaker constants of materials. They can be divided into three main categories; (*i)* microscopic approach (e.g. Gregory equation) *(ii)* macroscopic approach (Liftshitz theory) *(iii)* experimental (e.g. surface tension measurement) (Polat M and Polat H. 2000). For the calculation of the non-retarded Hamaker constant for two identical particles (1), interacting across a medium (3), the Tabor and Winterton equation can be used (Bergstrom 1997):

$$A_{131} = \frac{3}{4}kT\left(\frac{\varepsilon_1 - \varepsilon_3}{\varepsilon_1 + \varepsilon_3}\right)^2 + \frac{3h\nu_e}{16\sqrt{2}}\frac{\left(n_1^2 - n_3^2\right)^2}{\left(n_1^2 + n_3^2\right)^{3/2}} \tag{A.1}$$

The first term on the right hand side represents static contribution (Keesom and Debye polarization terms) and the second term represents the dispersive contribution (London dispersion) and n_1 and n_3 is the refractive index of the material and the medium respectively, ε is the static dielectric constant of the material and νe is the ultraviolet absorption frequency (Bergstrom 1997, Larson 1999, Hough and Lee 1980).

In this study, non-retarded Hamaker constant of PMN/water system is calculated to be ≈ 24.154×10^{-20} J using the equation (A.1). Through the calculations following parameters were used: ε_1=11000 (measured using impedance analyzer, see Chapter 5) and ε_3=79 are the low frequency dielectric constants for PMN and water, respectively, n_1 = 2.5219 is the refractive index for PMN (McHenry 1992), n_3=1.33 is the refractive index of water, $\nu_e = 3 \times 10^{15}$ s^{-1} is the estimated electronic absorption frequency, and *h* is Plank's constant.

However, non-retarded Hamaker constant is valid only at small particle separations (generally < 5nm). On the other hand in the case s
tericly stabilized suspensions the particle separations can be higher than 5nm. In this case it is necessary to consider the effect of this separation on the Hamaker function. In this study, Hamaker function is calculated using the following set of equations (Kirby 2003, Martinez 2002, French 2000, Bergstrom 1997):

$$\frac{A_{121}}{kT} = \frac{3(\varepsilon_{10} - \varepsilon_{30})(\varepsilon_{20} - \varepsilon_{30})}{4(\varepsilon_{10} + \varepsilon_{30})(\varepsilon_{20} + \varepsilon_{30})}(1 + 2\kappa h)e^{-2\kappa h} + \frac{3}{2}\sum_{n=1}^{\infty}\Delta_{13}^{*}\Delta_{23}^{*}(r_n + 1)e^{-r_n} \tag{A.2}$$

$$\varepsilon_j = \begin{cases} 1 + C_j/(1 + (\xi_n/\varpi_j)^2) & \text{for } \xi_\mathrm{n} > 0 \\ \varepsilon_{j0} & \text{for } \xi_\mathrm{n} = 0 \end{cases} \tag{A.3}$$

$$\Delta_{jk}^{*} = \frac{\varepsilon_j(i\xi_\mathrm{n}) - \varepsilon_k(i\xi_\mathrm{n})}{\varepsilon_j(i\xi_\mathrm{n}) + \varepsilon_k(i\xi_\mathrm{n})} \tag{A.4}$$

$$r_n = 2h\xi_n\varepsilon_3^{1/2}/c \tag{A.5}$$

$$\xi_n = 2\pi nkT/h \tag{A.6}$$

Where ε_{jo} is the static dielectric constant for material k (k:1 or 2) or solvent (k:3) and ε_j is the frequency dependent dielectric constant approximated by the value of C_j at a characteristic absorption peak value, ωj. The term $\xi_n = 2\pi nkT/h$ at room temperature is about 2.5x10^{14} Hz which is in the IR range. Here h is the Planck`s constant, k is the Boltzman constant, T is the absolute temperature and the n=0,1,2,3…..is an integer. The complex dielectric constant of a material is:

$$\varepsilon(\omega) = \varepsilon'(\omega) + i\varepsilon''(\omega) \tag*{A.7)}$$

Where ω is the angular frequency, ε' and ε'' are the real and imaginary parts of the dielectric constant. But the determination of the dielectric constants for the entire spectrum is only available for a limited number of materials. Then the imaginary dielectric response function can be given as:

$$\omega(i\xi) = 1 + \frac{C_{IR}}{1 + (\xi/\omega_{IR})^2} + \frac{C_{UV}}{1 + (\xi/\omega_{UV})^2} \tag{A.8}$$

Where C_{IR} and C_{UV} are the materials absorption strengths and ω_{IR} and ω_{UV} are the absorption frequencies in the IR and UV range, respectively. In the UV range Cuv and ωuv were determined from the intercept and slope of the plot of (n^2-1) versus $\omega^2(n^2-1)$, known as a Cauchy plot (French 2000, Ogden 1996, Bergstrom 1997, WEB_6 2007).

$$n^2(\omega)-1=(n^2(\omega)-1)\frac{\omega^2}{\omega^2 uv}+C_{uv} \tag{A.9}$$

Through the calculations refractive index spectra of PMN was used. Using the experimental data of Tsang et al. and Wan et al., $n^2(\omega)$-1 are plotted against $(n^2(\omega)-1)$ ω (Figure A.1) (Tsang et al. 2003, Wan et al. 2003). The slope of the linear fitting is $1/\omega uv^2$ and the intercept on the y axis is $C_{uv.}$ Results are tabulated in Table A.1.

Table A.1. Parameters used in the calculation of Hamaker function.
(Source: Tsang et al. 2003)

	n	ε	ω_{UV} (Hz)	C_{UV}
Water	1.33	79.7	1.992×10^{16}	-
PMN	2.52	11.000	8.56×10^{15}	4.99

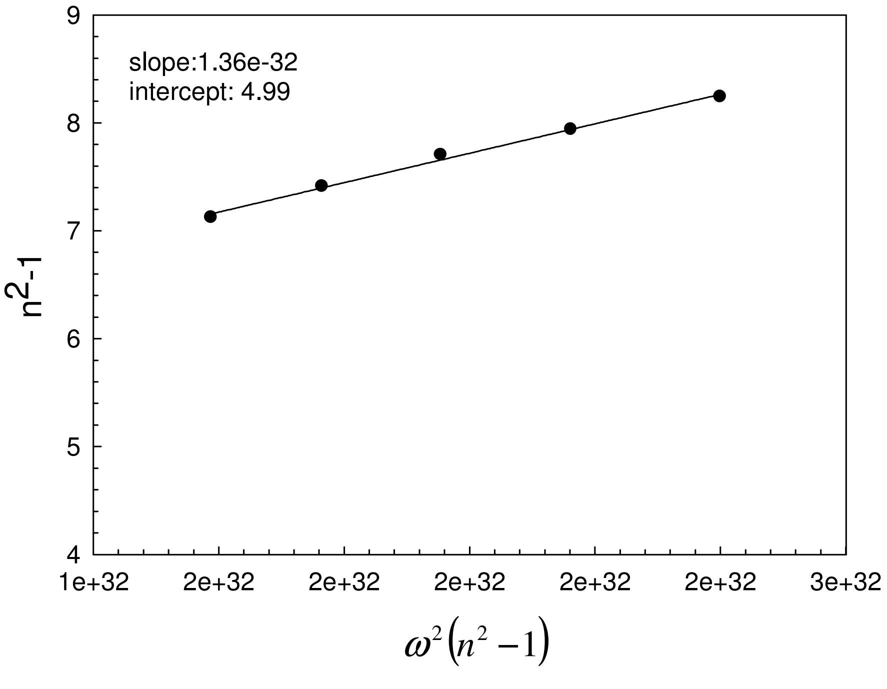

Figure A.1. Cauchy plot for PMN.

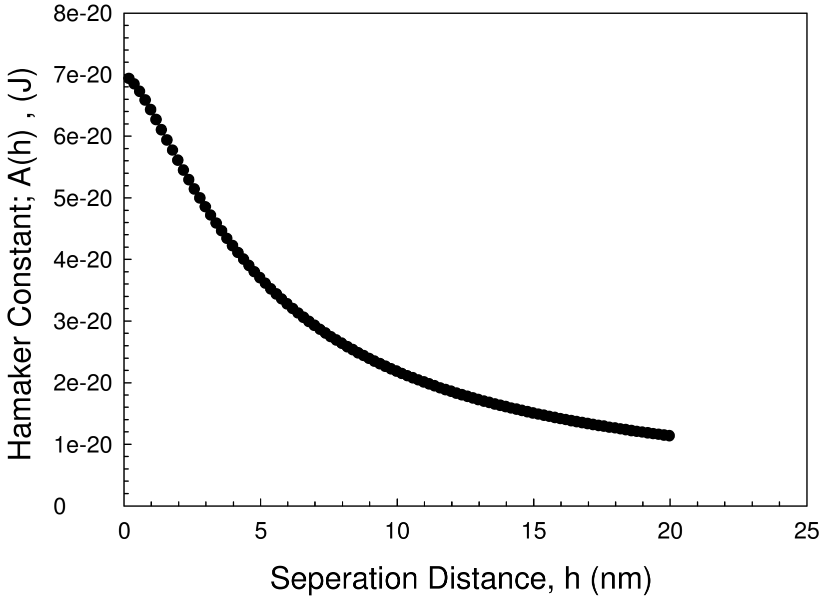

Figure A.2. Retarded Hamaker function of PMN as a function of separation distance.

The Figure A.2 shows variation in Hamaker function, A(h), as a function of separation distance. The value of the Hamaker function at h=0 was calculated to be 6.96×10^{-20} J. However, results indicates that the value of retarded Hamaker function at h=0 is lower than the value of the non-retarded Hamaker constant, that is calculated using equation (A.1). This difference may be attributed to the absence of the IR term effects in the oscillator model equation. To substitute IR terms to the equation C_{IR} can be calculated as:

$$C_{IR} = \varepsilon(0) - C_{UV} - 1 \quad (A.10)$$

The absorption frequency, ω_{IR} , can be defined as the frequency of the major absorption peak in the IR spectrum. But the ω_{IR} spectrum for the PMN could not been obtained. On the other hand the magnitude of dispersive interactions depends mainly on the ultraviolet relaxations for many materials. Therefore, in most cases retarded Hamaker function is calculated for the UV range. But in our case, the dielectric constant of the materials is very high and the elimination of the IR term in the calculations may cause such a difference. Previous studies on the same area also showed that the values obtained using macroscopic procedure are generally higher than those obtained with the microscopic procedures (Hunter 1995).

APPENDIX B

MODEL INTERACTION POTENTIAL CALCULATIONS FOR LEAD MAGNESIUM NIOBATE

Total interaction potential for the colloidal systems can be calculated by the sum of the following contributions (Hunter 1995, Israelachvili 1991):

$$V_{total} = V_{VDW} + V_{elec} + V_{steric} + V_{dep} \tag{B.1}$$

where V_{VDW} is the attractive potential energy due to long-range van der Waals interactions between particles, V_{elec}, is the repulsive potential energy arising from electrostatic interactions between charged particle surfaces, V_{steric} is the repulsive potential energy arising from steric interactions between particles coated with adsorbed polymers, and, V_{dep} is the potential energy created by the presence of nonadsorbed polymeric species in solution.

A.1. Electrostatic Forces and DLVO Model Calculations

DLVO model developed by Derjaguin and Landau in 1941, Verwey and Overbeek in 1948. The model calculations consider the long range attractive Van der Waals and electrostatic interactions between two identical bodies. For spherical particles of equal size, V_{VDW} is given by the Hamaker expression:

$$V_{VDW} = -\frac{A_{132}(h)}{6}\left(\frac{2}{s^2-4} + \frac{2}{s^2} + \ln\frac{s^2-4}{s^2}\right) \tag{B.2}$$

where $s = (2a + h)/a$, h is the minimum separation distance between the particle surfaces, a is the particle radius, and A_{132} is the non-retarded Hamaker constant. Retarded and non-retarded Hameker constants of PMN were calculated in this study and results are given Appendix A. However, in this section non-retarded Hamaker constant was used for the model calculations since the some of spectral data for PMN are not available to calculate the Hamaker function.

When two identical particles of radius a, approach each other under conditions of constant potential, the electrostatic repulsive potential can be calculated using the following equations (Hunter 1995):

$$V_R = 64\pi a n_0 kT \left(\tanh \frac{ze\psi_0}{4kT} \right)^2 \frac{1}{\kappa^2} \exp(-\kappa h) \qquad \text{(B.3)}$$

If the surface potential is small it follows that (Wang et al. 1999):

$$V_{elect} = 2\pi\varepsilon_r\varepsilon_o a \psi_0^2 \ln(1+ \exp(-\kappa h)) \qquad \{\kappa a > 10 \qquad \text{(B.4)}$$

$$V_{elect} = 2\pi\varepsilon_r\varepsilon_o a \psi_0^2 \exp(-\kappa h) \qquad \{\kappa a < 5 \qquad \text{(B.5)}$$

where, ε_r is the dielectric constant of the solvent (78.5), ε_0 is the permittivity of vacuum (8.8542×10^{-12} $C^2/N.m^2$), ψ_0 is the surface potential (estimated as the zeta potential), h is the separation distance, a is the particle radius, and κ^{-1} is the Debye Huckel screening length given by:

$$\kappa^{-1} = \left(\frac{2F^2[I]}{\varepsilon_r \varepsilon_0 kT} \right)^{-1/2} \qquad \text{(B.6)}$$

where kT is the thermal energy, F is the Faraday's constant (96500 C) and [I] is the ionic strength . The ionic strength is calculated by summing individual contributions from each of the dissolved ions using the following equation:

$$[I] = \frac{1}{2} \sum_i c_i z_i^2 \qquad \text{(B.7)}$$

where c_i and z_i are the concentration and valency of the ionic species "i". For the ionic strength calculations concentration of Pb^{+2} and Mg^{+2} ions in suspension were also taken into account. Concentration of ionic species in solution was measured by inductively coupled plasma spectroscopy. Results of the measurements and a detailed discussion related to this subject can be found in Chapter 3. Zeta potential measurements were performed using a zetasizer (Malvern HA 3000, UK). Results are reported in Chapters 3 and 4.

Total interaction potential energy curves (van der Waals attractive and electrostatic repulsive forces) of aqueous PMN suspensions in the presence of 10^{-3} M KNO_3 is shown with respect to separation distance in Figure B.1. Through the calculations dissolved ions from PMN were also taken into account to determine the exact ionic strength of the suspension. According to the Figure B.1 it is clear that long range attractive van der Waals interactions are much stronger than electrostatic repulsion and this cause aggregation in the system.

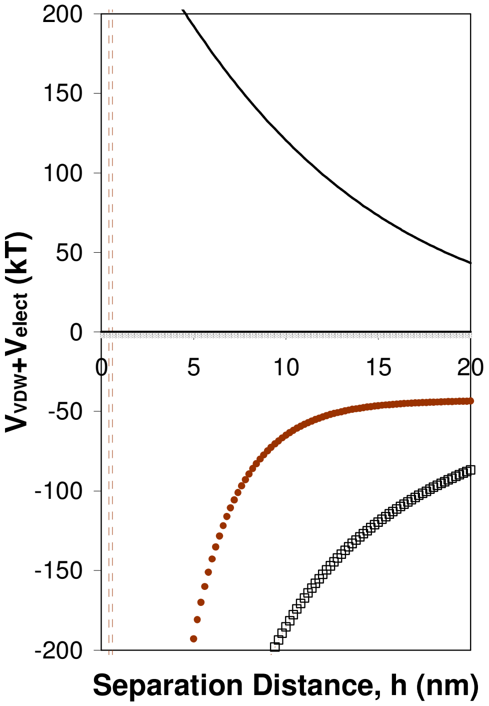

Figure B.1. Calculated interaction potential energy as a function of interparticle separation distance for PMN suspensions in absence of dispersant, 10^{-3} M KNO_3, 20 vol%, pH 9, ξ : -12 mV, ionic strength $2.55\text{x}10^{-3}$ M . (- V_{elect}, ○V_{tot}, □ V_{vdw}).

Similarly total interaction potential ($V_{total}= V_{VDW} + V_{elec}$) for PMN/water system in the presence of comb polymer PAA/PEO (2000) and PAA was calculated. The values tabulated in Table B.1 were used to calculate the separation distance between two particles covered by the PAA/PEO comb polymers. DLVO model calculations for PAA coated PMN suspensions were carried out in a similar way (δ_{PAA} adsorbing block: 4.2 nm).

Table B.1. Some of the parameters used in the DLVO model calculations.

$\delta_{PAA\text{-}PEO\ (2000)}$	8.0 nm
$\delta_{PAA\text{-}PEO}$ adsorbing block	4.9 nm
$\delta_{PAA\text{-}PEO}$ adsorbing block/$\delta_{PAA\text{-}PEO}$	0.61δ
PMN radius (PAA/PEO coated)	1004.9 nm

Total interaction potential (van der Waals and electrostatic) of aqueous PMN suspensions in the presence of PAA/PEO comb polymer and PAA is shown in Figure B.2 with respect to separation distance.

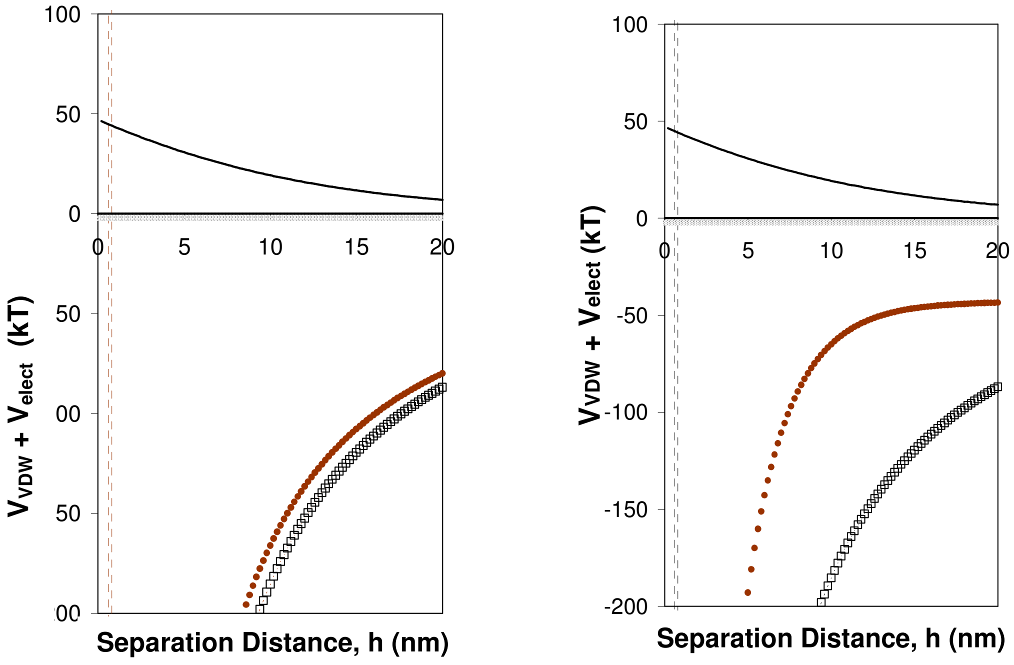

(a) (b)

Figure B.2. Calculated interaction potential energy as a function of separation distance for PMN suspensions in presence of (a) PAA/PEO (b) PAA, 20 vol%, pH 9 (- V_{elect}, ○V_{tot}, □ V_{vdw}).

Results showed that in the presence of polyelectrolytes the magnitude of the net interaction potential between particles were very high and negative which means that electrostatic repulsion has a very little effect on the stability of PMN particles suspended in water.

A.2. Steric Interactions

In this study the steric interaction potential is calculated using the equation developed by Vincent and coworkers for spherical particles with adsorbed polymer layers. Adsorbed layer thickness (δ) is estimated as the hydrodynamic radius in dilute solution (Vincent et al.1980, 1986). Hydrodynamic radius of the polymers used was measured by dynamic light scattering technique and results are given in Chapter 4.

The pseudo-homopolymer and pseudo-tail models are used to describe the mixing interactions in the range $\delta<h<2\delta$. On the other hand for smaller particle separations ($h<\delta$) uniform segment model can be used. The equation for the pseudo-homopolymer model can be given as (Vincent et al. 1986):

$$V_{steric,mix} = \frac{32\pi\, akT\left(\overline{\phi}_2^{\,a}\right)^2 (0.5-\chi)}{5v_1\delta^{\,4}}\left(\delta-\frac{h}{2}\right)^6 \qquad \text{(B.8)}$$

Where the ν1 is the solvent molar volume (0.018 L/mol), χ is the solvent parameter (0.4), $\overline{\phi}_2^{\,a}$ is the average volume fraction of segments in the adsorbed layer, estimated by the following equation:

$$\overline{\phi}_2^{\,a} = \frac{a^3 A_s \Gamma_p\, \rho/\rho_2}{(a+\delta)^3 - a^3} \qquad \text{(B.9)}$$

Where A_s is the surface area of the PMN particle (1.168 m^2/g) , ρ is the density of the particle (7.967 g/cm^3) , ρ_2 is the polymer density (~ 1.1 g/cm^3 for PAA/PEO and PAA) and Γ_p is the amount of polymer adsorbed calculated by total organic carbon analyzer ($\Gamma_{PAA/PEO}$: 1.25 mg/m^2 , Γ_{PAA} :0.6 mg/m^2). Comprehensive information regarding the adsorption of polyelectrolytes onto PMN surface can be found in Chapter

4. The average volume fraction of segments in the adsorbed layer $\overline{\phi}^{\mathrm{a}}_{2\,\mathrm{PAA/PEO}}$ and $\overline{\phi}^{\mathrm{a}}_{2\,\mathrm{PAA}}$ are calculated to be 0.56 and 0.40 for the PAA/PEO and PAA, respectively.

The pseudo-homopolymer model counts only the chain conformations for adsorbed polymers. Therefore, it can be used the model interaction of homopolymers like PAA. On the other hand, the pseudo-tail model also accounts the effect of tails and therefore more suitable to describe PMN interactions in the presence of PAA-PEO comb polymers (Vincent et al. 1986, Sato and Ruch 1980, Kirby 2003).

$$V_{steric} = \frac{32\pi\, akT\left(\overline{\phi}^{\mathrm{a}}_{2}\right)^{2}(0.5-\chi)}{15 v_1 \delta^{4}}\left(10\delta^{2}\left(\delta-\frac{h}{2}\right)^{4}-12\delta\left(\delta-\frac{h}{2}\right)^{5}+3\left(\delta-\frac{h}{2}\right)^{6}\right) \quad \text{(B.10)}$$

For the smaller particle separations (h<δ) steric potential is the sum of the mixing and elastic contributions. In this case following equations can be used (Vincent 1974).

$$V_{steric,mix} = \frac{4\pi\, a\delta^{2} kT\left(\overline{\phi}^{\mathrm{a}}_{2}\right)^{2}(0.5-\chi)}{v_{1}}\left(\frac{h}{2\delta}-\frac{1}{4}-\ln\frac{h}{\delta}\right) \quad \text{(B.11)}$$

$$V_{steric,\, elastic} = \frac{2\pi\, akT\delta^{2}\rho_{2}\overline{\phi}^{\mathrm{a}}_{2}}{M_{2}^{a}}\left\{\frac{h}{\delta}\ \ln\left[\frac{h}{\delta}\left(\frac{3-h/\delta}{2}\right)^{2}\right]-6\ln\left(\frac{3-h/\delta}{2}\right)+3\left(1-\frac{h}{\delta}\right)\right\} \quad \text{(B. 12)}$$

where ρ_2 is the polymer density and M_2^{a} is the molecular weight of the adsorbed species. M_2^{a} values of 5000 and 25800 g/mole are used for PAA and PAA/PEO2000, respectively.

Figure B.3 show the steric potential energy for PMN suspensions in the presence of PAA/PEO(2000) comb polymer and PAA. The osmotic and the mixing contribution of the steric stabilization are also given in Figure B.4. The osmotic repulsion curve becomes effective at a higher separation distance than the volume restriction (elastic) repulsive curve since it begins at the point of initial overlap of the polymeric regions. Similarly, the electrosteric potential curve which is combination of the DLVO potential and the steric repulsion potential is shown in Figure B.5 (b).

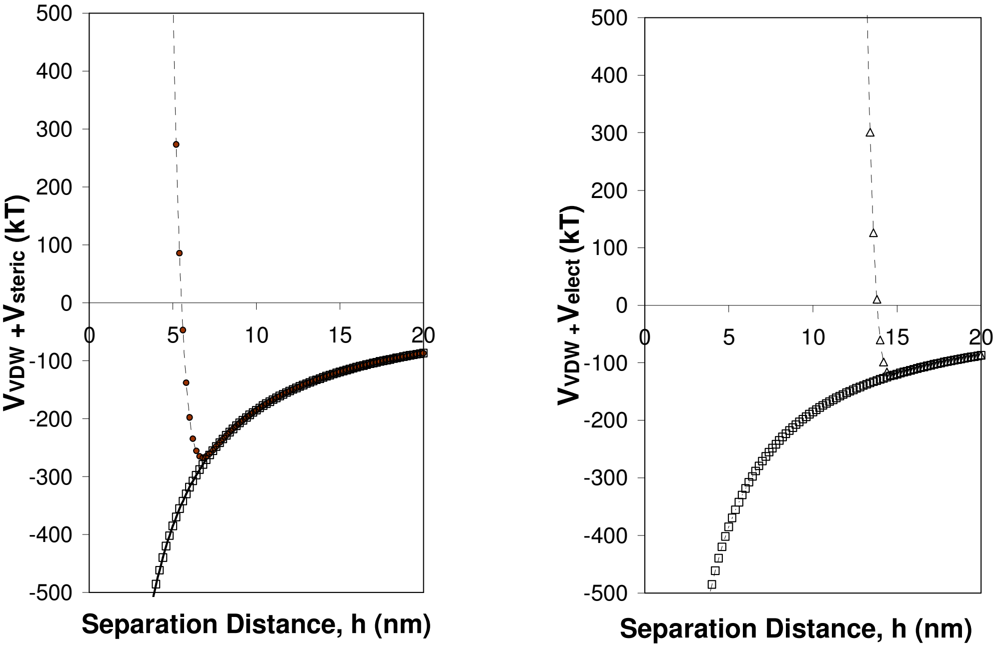

(a)

(b)

Figure B.3. Steric interaction potential energy as a function of separation distance for PMN suspensions in presence of a) PAA b) PAA/PEO.

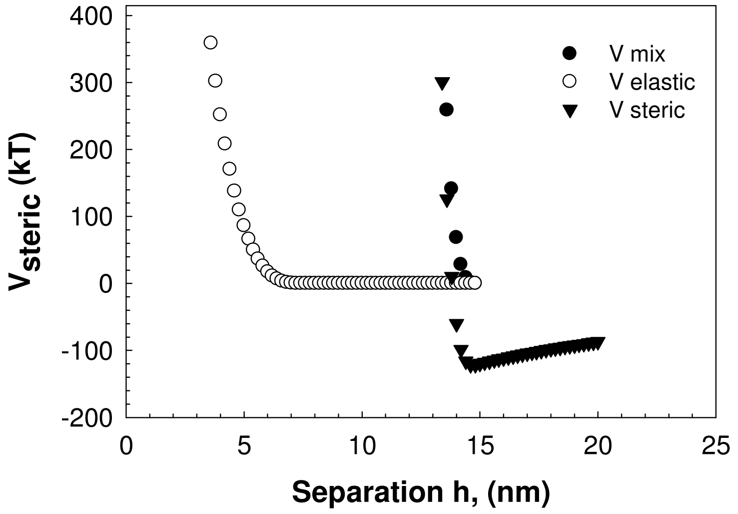

Figure B.4. Total steric interaction potential energy for PMN suspensions showing elastic and enthalpic (mix) component.

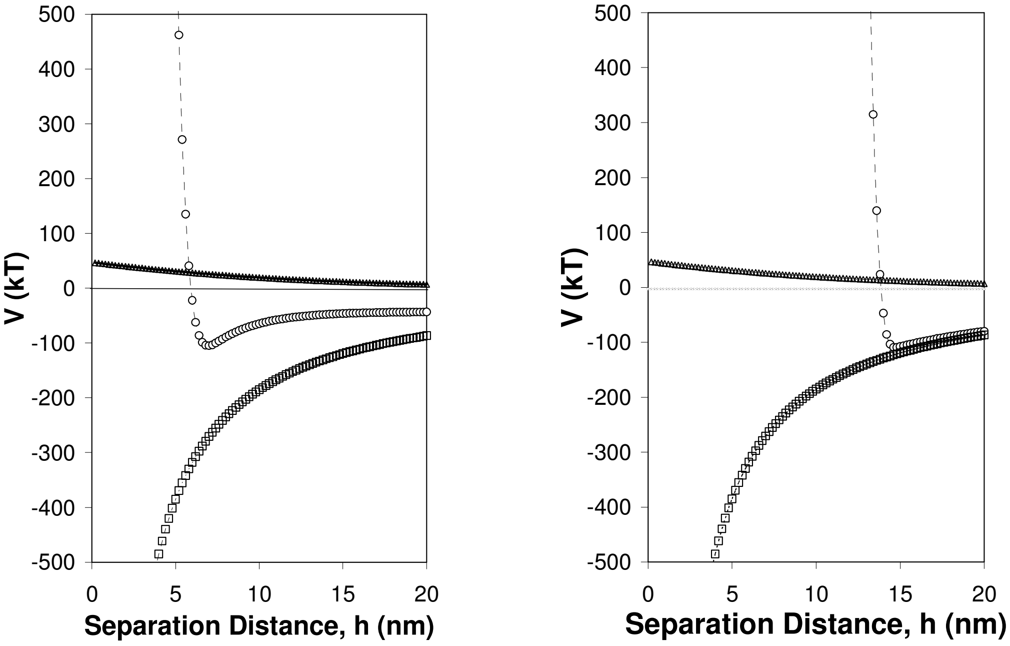

(a) (b)

Figure B.5. Electrosteric energy as a function of separation distance for PMN suspensions in presence of a) PAA and b) PAA/PEO, (-V_{elect}, ○V_{steric}, □ V_{vdw}).

Results showed that polymer coated PMN particles flocculate in a weak attractive minima, unlike the pure PMN suspensions. The depletion interaction potential was neglected in these interparticle potential calculations. However, non-adsorbed fraction of the polymers may have important effects on the stability mechanism of these systems. Adsorption experiments showed that especially PAA/PEO comb polymers shows low affinity type adsorption onto PMN surface at pH 9. Therefore, excess free polymer should exist in the suspension. On the other hand, non-adsorbed fraction of comb polymer had little effect on the colloidal stability of PMN particles as evidenced by rheological measurements. At critical weight fraction of the polymer added, nearly Newtonian behavior was observed. Upon increasing the polymer addition above the critical weight fraction the amount of non-adsorbed species increased but no further improvement in flow behavior was observed.

VITA

Name : Aylin M.Deliormanlı
Date/Place of Birth : March 30, 1971, İzmir-Turkey

Education

MSc	İzmir Institute of Technology, Department of Materials Science and Engineering (2000)
BSc	Ege University, Department of Chemical Engineering (1994)

Selected Publications

- Şakar-Deliormanlı, A., Polat, H., Çiftçioğlu, M. 2004 "Alumina/water suspensions in the presence of PEO/PPO/PEO triblock copolymers" *Journal of the European Ceramic Society.* Vol. 24, p. 3063-3072.
- Şakar-Deliormanlı, A., Yayla, Z. 2004 "Effect of calcium hydroxide on slip casting behaviour" *Applied Clay Science.* Vol. 24, p. 237-243.
- Şakar-Deliormanlı, A., Çiftçioğlu, M., Polat, M. 2004 "Effects of mechanical treatment on the formation of α-alumina from gibbsite" *Key Engineering Materials.* Vol. 264-268, p. 65-69.
- Wyss, H., Deliormanlı, M.A., Tervoort, E., Gauckler, L.J. 2005 "Influence of Microstructure on the Rheological Behavior of Dense Particle Gels" *American Institute of Chemical Engineers Journal, AIChE Journal.* Vol. 51.
- Şakar-Deliormanlı, A., Güden, M. 2006 "Microhardness and Fracture Toughness of Dental Materials by Indentation Method" *Journal of Biomedical Materials Research: Part B Applied Biomaterials.* Vol. 76-B, p. 257-264.
- Şakar-Deliormanlı, A. 2007 "Synergistic effect of polymer-surfactant mixtures on the stability of aqueous silica suspensions " *Journal of the European Ceramic Society.* Vol. 27, p. 611-618.
- Şakar-Deliormanlı, A., Çelik, E., Polat, M."Phase formation and Microstructure of Nd^{+3} doped Lead Magnesium Niobate (PMN) Prepared by Sol-Gel Method" *Journal of Materials Science : Materials in Electronics* (In press).
- Şakar-Deliormanlı, A., Çelik, E., Polat, M."The Isoelectric Point of Lead Magnesium Niobate" *Journal of the American Ceramic Society* (In press).
- Şakar-Deliormanlı, A., Çelik, E., Polat, M."Adsorption of Anionic Polyelectrolytes onto lead magnesium niobate" *Colloids and Surfaces A* (In press).